Electrically Detected Magnetic Resonance on Fullerene-Based Organic Semiconductor Devices and Microcrystals

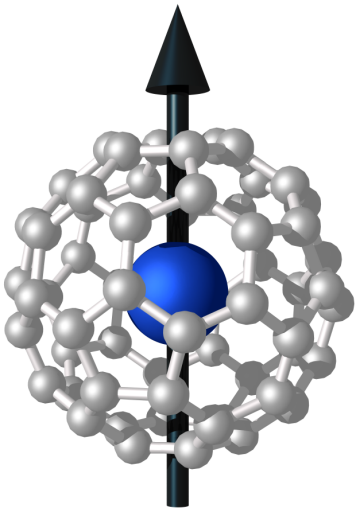

Dissertation

zur Erlangung des akademischen Grades
"Doktor der Naturwissenschaften"
im Promotionsfach Chemie

dem Fachbereich Chemie, Pharmazie und Geowissenschaften der Johannes Gutenberg-Universität Mainz vorgelegt von

Michael Eckardt
geboren in Bad Salzungen

Mainz, September 2016

JOHANNES GUTENBERG UNIVERSITÄT MAINZ

This dissertation was supervised by [redacted] in cooperation with [redacted] and was carried out at the Institut of Physical Chemistry at the Johannes Gutenberg-Universität Mainz from April 2013 to September 2016.

D77 (Dissertation Johannes Gutenberg-Universität Mainz)

Dean of the Faculty	[redacted]
1st Report	[redacted]
2nd Report	[redacted]
Submitted:	September 29th, 2016
Oral Examination:	November 16th, 2016

Abstract

This thesis deals with electrically detected magnetic resonance (EDMR) – a technique that probes spin-dependent electronic transport processes by a combination of highly sensitive current detection and electron paramagnetic resonance (EPR) – and its application to organic semiconductor microcrystals and solar cell devices. The ability to directly observe and identify spin-dependent processes makes EDMR especially useful for the device analysis in the field of organic solar cells, where charge carrier recombination is one of the limiting factors and particularly hard to quantify.

The design and implementation of a compact setup for measuring EDMR, which is based on a commercially available benchtop EPR spectrometer, is presented first. Using a silicon-based reference sample, the setup's performance is compared to a state-of-the-art instrument. It is concluded that the EDMR spectra recorded with the new spectrometer are quantitatively comparable in all spectroscopic dimensions with those obtained in the "large-scale" setup. The system is capable of nearly simultaneous collection of EDMR and current-voltage data, opening up the way to rapid research cycles and measurement series.

The benefits of close proximity between device fabrication and spectroscopic characterization offered by the new setup are then used to record EDMR spectra of microcrystals made from pure, oxidized, and N@C_{60}-doped Buckminsterfullerene. These environment-sensitive objects have not been studied in EDMR before. An evidence for strongly dipolar-coupled spin pairs in the N@C_{60}-doped material is presented. Although an unambiguous quantitative modeling of the presented data is not possible due to the limited signal-to-noise ratio, a symmetric structure in the obtained spectra is clearly visible. The performed experiments give a first spectroscopic evidence for strongly dipolar-coupled spin pairs, never reported before in EDMR. This result illustrates that using microcrystals and paramagnetic doping can significantly enhance the EDMR resolution.

Making use of the presented benchtop EDMR system, the recombination in freshly prepared P3HT:PC_{61}BM solar cells is studied and the observed EDMR signals are assigned to P3HT-related species and processes. The spin-dependent recombination currents measured by EDMR are quantitatively correlated to the current-voltage characteristics of the device, systematically varying both optical and electronic operating conditions. A strong voltage dependence of the signal shape and intensity is revealed, with a characteristic maximum at the quasi flat-band conditions (corresponding to an inflection point in the voltage-dependent photocurrent). Two clearly distinct bias regimes can be distinguished, in which the recombination is dominated by either photo-generated or injected charge carriers. It is disclosed that the spin-independent recombination in this study is a bimolecular process (Langevin type) and that the observed spin-dependent recombination is monomolecular in nature (Shockley-Read-Hall type).

Finally, a brief EDMR study on a degraded P3HT:PC_{61}BM solar cell device is presented. It is concluded that the degradation does not change the species actively involved in the spin-dependent processes, but that the injection-current-related EDMR signal component is suppressed, most probably due to the oxidation of the top contact.

Abstract (German)

Die vorliegende Arbeit beschäftigt sich mit der elektrisch detektierten magnetischen Resonanz (EDMR) - eine Technik, mit deren Hilfe spinabhängige Transportprozesse durch eine Kombination aus hochsensitiver Stromdetektion und Elektronenspinresonanz (ESR) untersucht werden können - sowie ihrer Anwendung auf Mikrokristalle aus organischen Halbleitermaterialien und Solarzellen. Durch die Möglichkeit spinabhängige Prozesse direkt zu beobachten und zu identifizieren, ist die EDMR besonders zur Analyse organischer Solarzellen geeignet, in welchen die Rekombination von Ladungsträgern einen limitierenden und schwer zu quantifizierenden Verlustprozess darstellt.
Zunächst wird das Design und die technische Realisierung eines kompakten EDMR Spektrometers basierend auf einem kommerziell verfügbaren ESR-Tischspektrometer vorgestellt. Unter Verwendung einer Referenzsolarzelle auf Siliziumbasis wird die Leistungsfähigkeit des neuen Systems mit derjenigen eines typischen Großgerätes verglichen. Es wird gezeigt, dass die im EDMR-Kompaktspektrometer aufgenommenen Spektren in allen spektroskopischen Parametern quantitativ mit denjenigen des Großgerätes vergleichbar sind. Das vorgestellte EDMR-System ermöglicht ferner nahezu simultane EDMR- und Strom-Spannungs-Messungen durchzuführen und unterstützt damit schnelle Entwicklungszyklen und systematische Messreihen.
Die Vorteile der räumlichen Nähe zwischen Probenherstellung und -analyse werden im Anschluss dazu genutzt, Mikrokristalle bestehend aus reinen, oxidierten und mit $N@C_{60}$ dotierten Buckminsterfullerenen zu untersuchen. Hierbei handelt es sich um Proben, welche aufgrund ihrer Empfindlichkeit gegenüber Umwelteinflüssen bisher nicht mittels EDMR untersucht wurden. Die Studien ermöglichen es, eine starke Dipolkopplung zwischen den Partnern eines Spinpaares innerhalb des mit $N@C_{60}$ dotierten Materials zu präsentieren. Obwohl aufgrund des eingeschränkten Signal-zu-Rausch-Verhältnisses keine eindeutige quantitative Modellierung der Daten möglich ist, kann deutlich eine symmetrische Struktur innerhalb der erhaltenen Spektren erkannt werden. Damit liefern diese Experimente einen ersten spektroskopischen Beweis für das Vorhandensein stark dipolgekoppelter Spinpaare, welche bisher in der EDMR nicht beobachtet werden konnten. Dieses Ergebnis macht deutlich, dass unter Verwendung von Mikrokristallen und paramagnetischem Doping die erzielbare Auflösung der EDMR-Methode signifikant gesteigert werden kann.
Weiterhin wird das vorgestellte EDMR-Kompaktgerät dazu genutzt, die Rekombination in frisch präparierten P3HT:PC_{61}BM Solarzellen zu untersuchen. Die erhaltenen EDMR-Signale lassen sich dabei verschiedenen P3HT-Spezies sowie ihnen zugehörigen Prozessen zuordnen. Die systematische Variation von Spannungs- und Beleuchtungswerten führt zu EDMR-Daten, die in eine quantitative Übereinstimmung mit den entsprechenden Strom-Spannungskurven der Solarzelle gebracht werden können. Generell zeigt sich eine starke Abhängigkeit der Signalform und Signalintensität vom gewählten Biaspunkt. Die EDMR Daten durchlaufen dabei ein gemeinsames Maximum, welches in etwa dem Spannungswert der Quasiflachbandbedingung (Wendepunkt des spannungsabhängigen Photostroms) entspricht. Insgesamt lassen sich zwei deutlich unterschiedliche Bereiche ausmachen, in welchen das EDMR-Signal durch Photo- bzw. injizierte Ladungsträger dominiert wird. Ferner kann gezeigt werden, dass in dieser Studie die nicht-spinabhängige Rekombination bimolekular, d.h. vom Langevin-Typ ist, während die spinabhängige Rekombination eine monomolekulare Charakteristik aufweist (Shockley-Read-Hall Mechanismus).
Abschließend wird eine kurze EDMR Studie an einer degradierten Solarzelle vorgestellt. Während die an den Rekombinationsprozessen beteiligten Spezies hierbei unverändert auftreten, ist das zu den durch injizierte Ladungsträger korrespondierende EDMR-Signal, mutmaßlich aufgrund der auftretenden Kontakdegradation, unterdrückt.

Wenn wir unser wahres Ziel nicht für immer aufgeben wollen, dann dürfte es nur den einen Ausweg aus dem Dilemma geben: daß einige von uns sich an die Zusammenschau von Tatsachen und Theorien wagen, auch wenn ihr Wissen teilweise aus zweiter Hand stammt und unvollständig ist – und sie Gefahr laufen, sich lächerlich zu machen.

— Erwin Schrödinger

This thesis is dedicated to [redacted], for her kindness and devotion, and for her endless support during all these years.

This thesis was typset using LaTeX 2_ε. Marvin was used for drawing, displaying and characterizing chemical structures, substructures and reactions, Marvin 14.7.14, 2014, ChemAxon (http://www.chemaxon.com).

Preface

Investigating the world of organic electronics using one of the most fascinating analytical techniques based on the electron spin, this thesis is both dedicated to the world of physical chemistry and material science. Being always curious what science looks like on the other side, the topic of electrically detected magnetic resonance gave me the opportunity to look on a specific problem from many sites - be it chemistry, physics or engineering - and I am very glad about this. From building up an analytical system and synthesizing a remarkable fullerene-based material to the investigation of state-of-the-art organic solar cells I was given the freedom to cross many boundaries. At this point, I would like to express my special appreciation and thanks to the people that made all this possible:

I am very grateful to [redacted] for encouraging my research, taking care of the first report and for giving me the opportunity to conduct my Ph.D. in her group. I would like to express my special appreciation and thanks to [redacted] whose support and guidance made my thesis work possible. I appreciate all his contributions of time, ideas and IGOR PRO knowledge. Furthermore, I like to thank him for taking care of the second report. I am grateful to [redacted] and [redacted] for their support and willingness to be part of the examination board.
I have appreciated the camaraderie and expertise of my colleague and friend [redacted] who was of enormous help not only during my Ph.D. but also in all the years of my studies. He encouraged me and always gave a helping hand. I am very grateful for his motivation, enthusiasm and the active interest he showed in my work. I also want to thank [redacted] and [redacted] for sharing their knowledge and having a good time. For fruitful discussions I am grateful to [redacted]. My preparation lab partners [redacted] and [redacted] provided a great work environment, I also thank them for their help and chats. The technicians of our group - [redacted] - supported my work with all those uncountable little and big things a lab day comes up with, their help is much appreciated. I thank [redacted] as well as [redacted] for their skill in spreading cheerfulness and the daily joke.

The experiments on the new benchtop-system would not have been possible without [redacted] - especially [redacted] contributed significantly during the design and implementation of the system, as well as the adaption of the MS400 control interface. The help of [redacted] and [redacted] during the validation and calibration of the system using a µc-Si:H sample has been invaluable. For a very fruitful collaboration on organic solar cells I like to thank [redacted] and [redacted], especially [redacted] who carefully build the solar cells used in this work. The fabrication of the used micro-structured substrates would have been impossible without the support of [redacted] and [redacted] and [redacted]. I would like to acknowledge [redacted], especially [redacted], who always were of enormous help during the design of custom lab equipment. Without their commitment and enthusiasm many experiments could not have been be performed. I am also very grateful to [redacted] for their continuous support and help during my years in Mainz.

The financial support by the Deutsche Forschungsgemeinschaft (DFG) within the Priority Programme 1601 NewFrontiers in Sensitivity for EPR Spectroscopy: From Biological Cells to Nano Materials and by the VolkswagenStiftung within the funding initiative Integration of Molecular Components in Functional Macroscopic Systems is also gratefully acknowledged.

Beyond this thesis, I owe particular thanks to [redacted] and [redacted] for introducing me to the world of analytical chemistry and the possibility to experience Canada in a very special way. Words cannot express how grateful I am to [redacted] and [redacted] for all their love, encouragement and support in all my pursuits. At the end I would like to thank [redacted] for all of the sacrifices that she has made on my behalf - you always were my support in the moments when there was no one to answer my queries. Thank you.

Mainz
September 27th, 2016
Michael Eckardt

Contents

List of Abbreviations

CW-EDMR	Continuous Wave Electrically Detected Magnetic Resonance
CW-EPR	Continuous Wave Electron Paramagnetic Resonance
dynLLIP	Dynamic Liquid-Liquid Interfacial Precipitation
EDMR	Electrically Detected Magnetic Resonance
ENBW	Equivalent Noise Bandwidth
EPR	Electron Paramagnetic Resonance
ESR	Electron Spin Resonance
FFT	Fast Fourier Transform
HOMO	Highest Occupied Molecular Orbital
HPLC	High-Performance Liquid Chromatography
ITO	Indium Tin Oxide
IUPAC	International Union of Pure and Applied Chemistry
KSM	Kaplan, Solomon and Mott
LEPR	Light-Induced Electron Paramagnetic Resonance
LLIP	Liquid-Liquid Interfacial Precipitation
LUMO	Lowest Unoccupied Molecular Orbital
MEH-PPV	Poly[2-methoxy-5-(2'-ethylhexyloxy)-1,4-phenylenevinylene]
MPP	Maximum Power Point
NMR	Nuclear Magnetic Resonance
P3HT	Poly(3-hexylthiophene-2,5-diyl)
$PC_{61}BM$	[6,6]-Phenyl-C_{61}-butyric acid methyl ester
pEDMR	Pulsed Electrically Detected Magnetic Resonance
PEDOT:PSS	Poly(3,4-ethylenedioxythiophene) polystyrene sulfonate
PSD	Phase Sensitive Detection
QCM	Quartz Crystal Microbalance
RF	Radio Frequency
SNR	Signal-to-Noise Ratio
SRH	Shockley-Read-Hall
TCO	Transparent Conductive Oxide
TEMPO	(2,2,6,6-Tetramethyl-piperidin-1-yl)oxyl
TMP	Turbomolecular Pump
UPS	Uninterrupted Power Supply

Introduction and Motivation

Organic electronics, i.e. the application of carbon-based organic small molecules and polymers for the construction of electronic devices, has become a very active field of research in recent years, since it opens up the way to next generation devices like organic light emitting diodes and organic solar cells.[1] The virtually unlimited supply with carbon-based semiconductor materials, as well as the possibility to deposit these substances at low temperatures in a solution-based process, e.g. via coating or even printing, on flexible and transparent substrates makes this technology very appealing for industrial applications.[2,3]
The major drawbacks of organic devices are the limited device efficiency and the lack of long-term stability under the influence of moisture and oxygen.[4–6] Some processes that are at the heart of organic electronics, like charge carrier recombination, are still not fully understood and hamper further device optimizations. The small thickness of the active layer in organic devices is responsible for their above mentioned advantages compared to silicon-based systems, but at the same time can become problematic when it comes to device analysis. For example, small amounts of defects in the active layer or imperfections at the interfaces of an organic photovoltaic device can influence the power conversion efficiency, but may not be observable using bulk-sensitive analysis methods. In order to gain a deeper understanding of the limiting processes, it is necessary to investigate fully functional devices at realistic operating conditions, which is problematic using ultra-sensitive techniques like electron or scanning probe microscopy. Hence, an inefficient trial-and-error approach is still often used in the development process of organic electronics.
Electrically detected magnetic resonance (EDMR) – a technique that probes spin-dependent electronic transport processes, like hopping or charge carrier recombination, by a combination of highly sensitive current detection and electron paramagnetic resonance – can be used in order to extend our knowledge about organic devices like polymer-based photovoltaic cells. The ability to directly observe and identify spin-dependent processes makes EDMR particularly useful for the device analysis in the field of organic optoelectronics. However, due to a lack of compact and affordable equipment, EDMR is much less widely spread amongst material researchers compared to other analysis methods, like photoluminescence and absorption spectroscopy. Up to now, EDMR is mostly used by research groups focusing specifically on the development of magnetic resonance techniques, and only few reports on EDMR on organic semiconductors exist. Interestingly, the applied electrical bias conditions in those reports are often dissimilar, e.g. OLED-mode at 15 K,[7] forward bias at ambient-temperature,[8] short-circuit at 5 K,[9] or reverse bias at 10 K,[10] and the dependence of the EDMR signal on the operating conditions of the device have not yet been studied systematically. Furthermore, opposing views as to how the EDMR signal is generated at the microscopic level in organic devices continue to be published so far.[8,10,11]

The brief introduction given above leads to the following conclusions: a) The EDMR technique is still evolving and a deeper understanding about the signal generation and how it is connected to the spin-dependent processes inside a device is needed. b) The method has a large potential and can be a valuable tool in the area of semiconductor research, but it needs to be more easily accessible in order to become more widely used. Thus, the aim of this work is to design a flexible benchtop EDMR system that can be used by researchers working in the field of material sciences as an easy to handle tool and to investigate the species and processes that are actively involved in spin-dependent recombination events inside organic semiconductor materials and fully functional organic photovoltaic devices.

Thesis Structure

In the first part of this thesis, we will introduce the theoretical foundations of EDMR and present the design and implementation of a compact EDMR setup, which is based on a commercially available electron paramagnetic resonance spectrometer. Due to its small footprint, the presented unit is highly mobile and can in particular be operated inside cleanrooms or even glove boxes. The calibration and validation of the setup will be shown and we will compare the new benchtop spectrometer with a state-of-the-art instrument.

In the second part of this work, we will introduced a class of samples to EDMR, namely fullerene microcrystals, that was not investigated so far, due to its delicate nature. This approach aims to further the understanding of how EDMR works and to explore its sensitivity. Furthermore, we will incorporate the paramagnetic dopant N@C_{60} into the fullerene host matrix. This molecule gives rise to a characteristic hyperfine pattern, which is identifiable even on a large and broad background and can thus significantly increase the spectral resolution of EDMR.

In the third part, we will use EDMR to directly investigate and distinguish different species and recombination processes in polymer-fullerene bulk-heterojunction solar cells during device operation. A systematic study with varying bias and illumination conditions will be used to show how combining EDMR and "classical" current-voltage analysis helps forming a picture of spin-dependent processes that limit the charge carrier lifetimes. In this context, a quantitative model, directly connecting both photo- and dark current of the device to the EDMR signal will be developed. Finally, an outlook is given on how the application of EDMR as a tool for the investigation of device degradation can help to understand the processes that eventually lead to a failure of the solar cell device.

Part I.

Benchtop-EDMR Spectrometer

Focus and objective: This first part deals with the design and implementation of a compact electrically detected magnetic resonance setup based on a commercially available benchtop electron paramagnetic resonance spectrometer. After introducing the theoretical foundations of both electron paramagnetic resonance (EPR) and electrically detected magnetic resonance (EDMR) the changes and extensions to the commercial setup's hard- and software will be explained in detail. Later on, the calibration and validation of the setup will be shown. At the end of this part the benchtop setup will be compared to a "large scale" spectrometer using a solar cell based on microcrystalline silicon as a reference system.

The following part of this thesis has partially been published in a peer-reviewed journal: M. Eckardt, J. Behrends, D. Münter, W. Harneit, Compact electrically detected magnetic resonance setup, *AIP Adv.* **2015**, *5*, 047139. Chapters based on this article are indicated by a †.

1. Basics of EPR Spectroscopy

EPR spectroscopy, which is sometimes referred to as electron spin resonance (ESR), is an analytical method based on the physical properties of the electron spin. Therefore, it is particularly useful for the investigation of paramagnetic substances. Using EPR allows not only to gain structural informations but also to quantify the number of unpaired electrons in a given sample. All investigations in this work were performed using what is called an X-band spectrometer, applying microwave frequencies of 9 GHz to 10 GHz (corresponding to a wavelength of about 3 cm) making it a low energy method.

1.1. The Electron Spin in a Magnetic Field

The interaction between the magnetic moment of the electron and the externally applied magnetic field is at the heart of EPR spectroscopy. It was P. Zeeman in 1896 who observed the splitting of spectral lines if a static magnetic field was applied during the acquisition of optical spectra.[12] This observation, together with the experiments of Stern and Gerlach in 1920, eventually led to the concept of the electron spin formulated by Goudsmit and Uhlenbeck in 1925 as an "intrinsic angular momentum".[13–15] The corresponding spin quantum number parameterizing the spin has the value $s = 1/2$ and the relationship between the angular momentum operator of the electron spin $\hat{\boldsymbol{S}}$ and the operator of the magnetic moment $\hat{\boldsymbol{\mu}}_{\mathbf{s}}$ is given by

$$\hat{\boldsymbol{\mu}}_{\mathbf{s}} = -\gamma \hat{\boldsymbol{S}} \tag{1.1}$$

with γ as the gyromagnetic ratio. For a free electron, this ratio is given by

$$\gamma = -g_{\mathrm{e}} \mu_{\mathrm{B}} / \hbar \tag{1.2}$$

in angular frequency units (rad/s T) with μ_{B} as the Bohr magneton, $\hbar$ as the reduced Planck's constant and the electron g-factor $g_{\mathrm{e}} = -2.002\,319\,304\,361\,53(53)$.[16] In this thesis we will follow a convention often used in atomic physics, were the electron spin g-factor is defined as $g_{\mathrm{s}} = -g_{\mathrm{e}}$. For some calculations it is convenient to express equation 1.2 in frequency units and define the reduced gyromagnetic ratio

$$\gamma = \frac{\gamma}{2\pi} = \frac{g_{\mathrm{s}} \mu_{\mathrm{B}}}{h} \approx 28.025\,\mathrm{MHz/mT} \tag{1.3}$$

in analogy to $\hbar = h/2\pi$.

The Hamiltonian of a magnetic moment in an external magnetic field $\boldsymbol{B}$ is given by

$$\hat{H} = -\hat{\boldsymbol{\mu}}_{\mathbf{s}}\boldsymbol{B} \tag{1.4}$$

which transforms into equation 1.5 if the magnetic field is applied only along the z-axis.

$$\hat{H}_{\mathrm{z}} = \frac{g_{\mathrm{s}}\mu_{\mathrm{B}}}{\hbar} B_{\mathrm{z}} \hat{S}_{\mathrm{z}} \tag{1.5}$$

Here, $\hat{S}_{\mathrm{z}}$ denotes the corresponding component of the angular momentum operator. For a quantum state $|\psi\rangle$ with $\langle\psi\,|\,\psi\rangle = 1$, the expectation value for the energy of this systems is then simply given by

$$E = \left\langle \psi \,\middle|\, \hat{H}_{\mathrm{z}} \,\middle|\, \psi \right\rangle = m_{\mathrm{s}}\, g_{\mathrm{s}}\, \mu_{\mathrm{B}}\, B_{\mathrm{z}} \tag{1.6}$$

with $m_{\mathrm{s}} = \pm 1/2$ as the magnetic spin quantum number. Hence, the energy difference between the two possible spin states depends on the value of the applied magnetic field and is given by equation 1.7. This also defines the resonance condition and thus sets the frequency ν_{L}, called the Larmor frequency, at which the system can absorb radiation to drive the transition between the spin states. Additionally, this transition is constrained by the selection rule $|\Delta m_{\mathrm{s}}| = 1$, as can be deduced from time-dependent perturbation theory for a non-vanishing transition moment integral.[17]

$$\Delta E = g_{\mathrm{s}}\, \mu_{\mathrm{B}}\, B_{\mathrm{z}} = h\nu_{\mathrm{L}} = \hbar\omega_{\mathrm{L}} \tag{1.7}$$

The resonance absorption can be detected with a suitable setup and gives rise to the EPR signal, as will be shown in the following sections. According to equation 1.7 it is equally possible to either "sweep" the magnetic field or the frequency in order to record an EPR spectrum. However, as will be shown in section 1.4, the requirement of a resonance cavity results in the use of a magnetic field sweep in most practical cases.

1.2. The EPR Spin Hamiltonian

After introducing the very basic principle of EPR in the previous section, we will now have a closer look to the chemical environment of the electron spin in resonance. It is the sensitivity to its surrounding that makes EPR such a powerful analytical tool in both chemistry and physics. First of all, one can observe an interaction between the spin and orbit angular momentum (spin-orbit coupling) leading to a deviation of the g-factor compared to the "free" electron value g_{s}. This g-factor shift can often be used as a fingerprint for the paramagnetic species. Furthermore, the magnetic moment of the considered spin can interact with other magnetic moments in the sample which may arise from other electrons or nuclei. Such an interaction can lead to an analyzable splitting pattern in the observed EPR spectrum.
As pointed out by Abragam and Pryce,[18] the electronic level separations are much larger compared to the ones addressed in an EPR experiment at the usual experimental temperatures. For the transition energies, it is therefore acceptable to only consider states within the electronic ground state of a paramagnetic species (higher excited states can, however, have an effect on spin-relaxation). Thus, the EPR Hamiltonian of a particular unpaired electron in a system with serveral nuclei is given by

$$\hat{H}_{\mathrm{EPR}} = \hat{H}_{\mathrm{EZ}} + \hat{H}_{\mathrm{NZ}} + \hat{H}_{\mathrm{HF}} + \hat{H}_{\mathrm{ZF}} + \hat{H}_{\mathrm{NQ}} \tag{1.8}$$

with $\hat{H}_{\mathrm{EZ}}$: the electron Zeeman interaction; $\hat{H}_{\mathrm{NZ}}$: the nuclear Zeeman interactions; $\hat{H}_{\mathrm{HF}}$: the hyperfine couplings between the electron spin and the nuclear spins; $\hat{H}_{\mathrm{ZF}}$: the zero-field splitting

for systems with strongly interacting unpaired electrons; and $\hat{H}_{\mathrm{NQ}}$: the nuclear quadrupole interactions. Additionally, if the considered system shows a weak coupling between two electrons on neighboring atoms a spin-spin interaction according to equation 1.9 has to be taken into account.

$$\hat{H}_{\mathrm{EPR}}(S_1, S_2) = \hat{H}_{\mathrm{EPR}}(S_1) + \hat{H}_{\mathrm{EPR}}(S_2) + \hat{H}_{\mathrm{EE}}(S_1, S_2) \tag{1.9}$$

In the following, the different parts of $\hat{H}_{\mathrm{EPR}}$ will be briefly described. A more detailed explanation of the individual constituents can be found in the literature.[17,19–23]

1.2.1. Electron Zeeman Interaction

If the unpaired electron can be described by a state $|\psi_0\rangle$ with zero orbital angular momentum, $\hat{\boldsymbol{L}} = \left(\hat{L_{\mathrm{x}}}, \hat{L_{\mathrm{y}}}, \hat{L_{\mathrm{z}}}\right)$, the interaction between the considered electron and the external magnetic field is described by the electron Zeeman interaction and the Hamiltonian is given by equation 1.5. However, in a more complex system (i.e. a molecule) this interaction can be anisotropic due to spin-orbit coupling. Therefore, the g-factor has to be replaced by the symmetric tensor $\boldsymbol{g}$. If the molecular coordinate system is considered to be the principal axes system of this tensor, it becomes

$$\boldsymbol{g} = \begin{pmatrix} g_{\mathrm{x}} & 0 & 0 \\ 0 & g_{\mathrm{y}} & 0 \\ 0 & 0 & g_{\mathrm{z}} \end{pmatrix} \tag{1.10}$$

with g_{x}, g_{y} and g_{z} as the principal values. In the case of organic radicals the g-anisotropy is usually very small and equation 1.11 often gives a good approximation for the isotropic g-factor.[24]

$$g_{\mathrm{iso}} = {}^1\!/_3 \left(g_{\mathrm{x}} + g_{\mathrm{y}} + g_{\mathrm{z}}\right) \tag{1.11}$$

The source of the spin-orbit coupling effect is a mixing of the ground state $|\psi_0\rangle$ with exited magnetic states $|\psi_n\rangle$. Thus, the spin-orbit coupling has to be added to the free electrons' Zeeman term (see equation 1.5) to get a general expression for the electron Zeeman interaction. Equation 1.12 shows the result of this consideration introducing λ_{LS} as the magnitude of the spin-orbit coupling.

$$\hat{H}_{\mathrm{EZ}} = \hat{H}_{\mathrm{z}} + \hat{H}_{\mathrm{LS}} = \frac{\mu_{\mathrm{B}}}{\hbar} \boldsymbol{B} \left(\hat{\boldsymbol{L}} + g_{\mathrm{s}} \hat{\boldsymbol{S}}\right) + \lambda_{\mathrm{LS}} \hat{\boldsymbol{L}} \hat{\boldsymbol{S}} \tag{1.12}$$

A second order perturbation theory approach for this term leads to the new expression

$$\boldsymbol{g} = g_{\mathrm{s}}\, \mathbb{1} + \boldsymbol{\Delta g} \tag{1.13}$$

for the g-tensor.[21] Here, $\boldsymbol{\Delta g}$ is the symmetric g-shift tensor, whose elements are given by

$$\Delta g_{ij} = 2\, \lambda_{\mathrm{LS}} \sum_{n \neq 0} \frac{\langle \psi_0 | \hat{L_i} | \psi_n \rangle \langle \psi_n | \hat{L_j} | \psi_0 \rangle}{E_0 - E_n} \tag{1.14}$$

with $|\psi_0\rangle$ as the ground state and $|\psi_n\rangle$ as the n^{th} exited state of the system. The corresponding energies are given by E_0 and E_n, respectively. With this considerations, the electron Zeeman interaction for an unpaired electron in a molecule is given as shown in equation 1.15.

$$\hat{H}_{\mathrm{EZ}} = \frac{\mu_{\mathrm{B}}}{\hbar} \boldsymbol{B}\, \boldsymbol{g}\, \hat{\boldsymbol{S}} \tag{1.15}$$

The calculation of g-shifts with respect to the free electron value is in principle possible using equation 1.14. However, since for such an evaluation comprehensive information about the

involved excited states (i.e. energy, symmetry and occupation) is necessary, it is difficult to give a general rule of thumb. As pointed out by Carrington and McLachlan,[22] the sign of $(E_0 - E_n)$ depends on ψ_n and changes from an occupied to an unoccupied orbital. Thus, if everything else can be considered equal, the filled and empty states give opposite contributions to the observed g-shift. Models have been proposed for inorganic systems with a delocalized unpaired electron, as well as for aromatic hydrocarbons by A.J. Stone.[25,26] For aromatic radicals he found a linear dependence of the observed g-shift on the Hückel energy of the singly occupied π-orbital, resulting in a positive deviation of g compared to g_s for both cations and anions.[23,27] Stone's approach has proven to be successful for non-degenerate ground states, but extensions for vibronic coupling (associated with the Jahn-Teller effect) and ion pairing need to be taken into account if a degenerate (or almost degenerate) ground state, like in the benzene anion, is involved.[28–30] This illustrates the difficulties in formulating a straight forward rule on g-value shifts valid for more than certain special cases. However, g-values can still be used to compare different experimental results on the same species.

1.2.2. Nuclear Zeeman Interaction

For atomic nuclei with non-zero nuclear spin an interaction with the external magnetic field analogous to equation 1.1 can be formulated.

$$\hat{\boldsymbol{\mu}}_\mathbf{n} = \gamma_\mathrm{n} \hat{\boldsymbol{I}} \tag{1.16}$$

Here γ_n represents the gyromagnetic ratio for the nucleus and $\hat{\boldsymbol{I}}$ the nuclear spin angular momentum operator. Thus, the Hamiltonian of the nuclear Zeeman interaction is given by

$$\hat{H}_\mathrm{NZ} = -\frac{\mu_\mathrm{n}}{\hbar} \boldsymbol{B}\, \boldsymbol{g}_\mathbf{n}\, \hat{\boldsymbol{I}} \tag{1.17}$$

with μ_n as the nuclear magneton and $\boldsymbol{g}_\mathbf{n}$ as the nuclear g-tensor taking into account the orientation dependence. However, due to the conservation of the total angular momentum after absorbing a photon the selection rules for EPR become: $|\Delta m_\mathrm{s}| = 1$ and $\Delta m_\mathrm{i} = 0$. Hence, the nuclear Zeeman interaction has usually little influence in EPR and can be neglected. It may only become relevant for systems with large nuclear quadrupole momentum, or if it reaches the same order of magnitude as the hyperfine interaction.[19]

1.2.3. Hyperfine Interaction

According to equation 1.16 nuclei with non-zero nuclear spin possess a magnetic moment. This moment can interact with the corresponding magnetic moment of the electron, which is called the hyperfine interaction. The Hamiltonian describing this interaction is given by

$$\hat{H}_\mathrm{HF} = \hat{\boldsymbol{S}} \boldsymbol{A} \hat{\boldsymbol{I}} \tag{1.18}$$

with $\hat{\boldsymbol{S}}$ and $\hat{\boldsymbol{I}}$ as the operators for the electron and nuclear angular momentum, respectively. Using the identity operator $\mathbb{1}$, the interaction tensor $\boldsymbol{A}$ can be written as

$$\boldsymbol{A} = a_\mathrm{iso} \cdot \mathbb{1} + \boldsymbol{T} \tag{1.19}$$

where the first term symbolizes the Fermi contact interaction characterized by the isotropic coupling constant a_iso.[19]

$$a_\mathrm{iso} = \frac{2}{3} \frac{\mu_0}{\hbar} g_\mathrm{s}\, \mu_\mathrm{B}\, g_\mathrm{n}\, \mu_\mathrm{n}\, |\psi_0\,(0)|^2 \tag{1.20}$$

In equation 1.20, μ_0 denotes the magnetic vacuum permeability and $|\psi_0(0)|^2$ is the electron spin density at the nucleus. From its definition and name it can be deduced that a_{iso} represents the non-zero probability of finding the electron occupying an s-orbital at the nucleus. Electrons occupying p- ,d- or f-orbitals can contribute to the spin density at the nucleus via configuration interaction or spin polarization mechanisms and thus show an influence on the isotropic hyperfine coupling constant.[31]
The second term in equation 1.19 is the electron-nuclear dipole-dipole interaction tensor $\boldsymbol{T}$. If only the wavefunction of the ground state ψ_0 is considered, it is a traceless, symmetric tensor whose elements are given by

$$T_{ij} = \frac{\mu_0}{4\pi\hbar} g_{\mathrm{s}}\,\mu_{\mathrm{B}}\,g_{\mathrm{n}}\,\mu_{\mathrm{n}} \left\langle \psi_0 \left| \frac{3r_i r_j - \delta_{ij} r^2}{r^5} \right| \psi_0 \right\rangle \tag{1.21}$$

with r as the distance between the electron and the nucleus and δ_{ij} as Kronecker's delta.[19] Assuming only a small g-tensor anisotropy and switching to the hyperfine principal axes system the diagonalized tensor can be written as

$$\boldsymbol{T} = \frac{\mu_0}{4\pi\hbar} \frac{g_{\mathrm{s}}\,\mu_{\mathrm{B}}\,g_{\mathrm{n}}\,\mu_{\mathrm{n}}}{R^3} \begin{pmatrix} -1 & 0 & 0 \\ 0 & -1 & 0 \\ 0 & 0 & 2 \end{pmatrix} = \begin{pmatrix} -T & 0 & 0 \\ 0 & -T & 0 \\ 0 & 0 & 2T \end{pmatrix} \tag{1.22}$$

with R as the distance between the nucleus and the center of the atomic orbital occupied by the unpaired electron.[19] Anisotropic interactions are averaged out due to fast movement of the molecules for EPR spectra recorded in solution or gaseous phase. Hence, only the isotropic part of $\boldsymbol{A}$ has to be considered for such samples.

1.2.4. Zero-Field Splitting

For systems with more than one unpaired electron, electron-electron couplings can sometimes be observed in EPR. While weak electron-electron couplings are characterized best by their individual spins (see section 1.2.6), strongly interacting electrons are usually described by a "group spin". In systems of non-cubic symmetry the electron dipole-dipole coupling lifts the $(2S+1)$-fold degeneracy of the ground state $|\psi_0\rangle$ even in the absence of an external magnetic field. Therefore, this effect is called zero-field splitting and described by the Hamiltonian given in equation 1.23.

$$\hat{H}_{\mathrm{ZF}} = \hat{\boldsymbol{S}}\boldsymbol{D}\hat{\boldsymbol{S}} \tag{1.23}$$

Here, $\hat{\boldsymbol{S}}$ denotes the angular momentum operator of the total electron spin and $\boldsymbol{D}$ is the symmetric and traceless, i.e. $\mathrm{tr}(\boldsymbol{D}) = D_{\mathrm{xx}} + D_{\mathrm{yy}} + D_{\mathrm{zz}} = 0$, zero-field interaction tensor. Since it is traceless, $\boldsymbol{D}$ can be characterized by two independent parameters: $D = {}^3/_2 D_{\mathrm{zz}}$ and $E = {}^1/_2 (D_{\mathrm{xx}} - D_{\mathrm{yy}})$.[21] The parameters D and E are named "axial zero-field splitting parameter" and "rhombic zero-field splitting parameter". Using these parameters and switching to the principal axes system of $\boldsymbol{D}$, equation 1.23 becomes

$$\hat{H}_{\mathrm{ZF}} = D_{\mathrm{xx}}\hat{S}_{\mathrm{x}}^2 + D_{\mathrm{yy}}\hat{S}_{\mathrm{y}}^2 + D_{\mathrm{zz}}\hat{S}_{\mathrm{z}}^2 = D\left(\hat{S}_{\mathrm{z}}^2 - \frac{1}{3}\hat{S}^2\right) + E\left(\hat{S}_{\mathrm{x}}^2 - \hat{S}_{\mathrm{y}}^2\right) \tag{1.24}$$

with $\hat{S}_{\mathrm{x}}$, $\hat{S}_{\mathrm{y}}$ and $\hat{S}_{\mathrm{z}}$ as the components of the spin angular momentum operator.[21] If $D = E = 0$ (cubic symmetry) no zero-field splitting can be observed. For $D \neq 0, E = 0$ the system shows axial and for $D \neq 0, E \neq 0$ rhombic symmetry.

1.2.5. Nuclear Quadrupole Interaction

Atomic nuclei with a nuclear spin $I > 1/2$ possess an electric nuclear quadrupole moment, describing the deviation of the charge distribution from spherical symmetry. This nuclear quadrupole moment can interact with the electrical field gradient at the nucleus, thus the Hamiltonian is given by

$$\hat{H}_{\mathrm{NQ}} = \hat{\boldsymbol{I}}\boldsymbol{P}\hat{\boldsymbol{I}} \tag{1.25}$$

where $\hat{\boldsymbol{I}}$ is the nuclear angular momentum operator and $\boldsymbol{P}$ is the nuclear quadrupole interaction tensor. Nuclear quadrupole interactions lead to shifts in allowed resonance lines and may also result in the appearance of usually forbidden transitions in an EPR spectrum.[19] Because these second-order effects are small and therefore difficult to observe in EPR, they will not be further discussed.

1.2.6. Weak Electron-Electron Interactions

As mentioned in section 1.2.4, weakly coupled electron spins can be described by a spin-spin interaction Hamiltonian

$$\hat{H}_{\mathrm{EE}} = \hat{H}_{\mathrm{Ex}} + \hat{H}_{\mathrm{DD}} = \hat{\boldsymbol{S}}_{\mathbf{1}}\boldsymbol{J}_{\mathbf{ex}}\hat{\boldsymbol{S}}_{\mathbf{2}} + \hat{\boldsymbol{S}}_{\mathbf{1}}\boldsymbol{J}_{\mathbf{dd}}\hat{\boldsymbol{S}}_{\mathbf{2}} \tag{1.26}$$

where $\hat{H}_{\mathrm{Ex}}$ characterizes the Heisenberg exchange coupling and $\hat{H}_{\mathrm{DD}}$ the electron-electron dipole-dipole interaction. Here $\hat{\boldsymbol{S}}_{\mathbf{1}}$ and $\hat{\boldsymbol{S}}_{\mathbf{2}}$ are the electron-spin operators for electrons 1 and 2, respectively.
The Heisenberg exchange term becomes relevant if radical species approach each other close enough, so that the orbitals of the two spins overlap and the unpaired electrons can be exchanged. In solid samples an exchange may be observed if the two unpaired electrons are closer than about 1.5 nm, which can be exceeded in strongly delocalized systems.[32] For organic radicals, the anisotropic part of $\boldsymbol{J}_{\mathbf{ex}}$ can usually be neglected,[19] resulting in the isotropic exchange interaction

$$\hat{H}_{\mathrm{Ex,iso}} = J_{\mathrm{iso}}\hat{\boldsymbol{S}}_{\mathbf{1}}\hat{\boldsymbol{S}}_{\mathbf{2}} \tag{1.27}$$

with J_{iso} as the corresponding coupling constant, which to a first approximation is given by

$$J_{\mathrm{iso}} = -2\left\langle \psi_{\mathrm{a}}(1)\psi_{\mathrm{b}}(2)\left|\frac{e^2}{4\pi\epsilon_0 r_{12}}\right|\psi_{\mathrm{a}}(2)\psi_{\mathrm{b}}(1)\right\rangle \tag{1.28}$$

where ψ_{a} and ψ_{b} are the wavefunctions of the different spatial molecular-orbitals, ϵ_0 is the electric vacuum permittivity, and r_{12} the inter-electron distance.[21]
The electron-electron dipole-dipole interaction is analogous to the dipole-dipole coupling between the electron and the nuclear spin discussed in section 1.2.3. In its principal axes frame the coupling tensor $\boldsymbol{J}_{\mathbf{dd}}$ becomes

$$\boldsymbol{J}_{\mathbf{dd}} = \frac{\mu_0}{4\pi\hbar}\frac{g_1\, g_2\, \mu_{\mathrm{B}}^2}{r_{12}^3}\begin{pmatrix}-1 & 0 & 0\\ 0 & -1 & 0\\ 0 & 0 & 2\end{pmatrix} = \begin{pmatrix}-J_{\mathrm{dd}} & 0 & 0\\ 0 & -J_{\mathrm{dd}} & 0\\ 0 & 0 & 2J_{\mathrm{dd}}\end{pmatrix} \tag{1.29}$$

with g_1 and g_2 as the isotropic g-factors of the two electron spins and r_{12} as their distance. This expression is only valid if the anisotropy of the g-tensor can be neglected and the energy splitting of the electron spin levels is large enough that direct mixing of spin wavefunctions by hyperfine coupling can be neglected (so called "high-field approximation", where only the $\hat{S}_{\mathrm{z}}$ component of $\hat{\boldsymbol{S}}$ is retained).

1.3. Signal Shape in CW-EPR Spectroscopy

The previous sections introduced the basic principles of electron paramagnetic resonance with respect to the resonance condition. Thus, the static aspects of EPR were considered so far only. We will now investigate the dynamics of EPR by introducing the concept of spin-relaxation. This will lead us to an expression for the line-shape of an EPR signal, before the components of a typical EPR setup are explained in section 1.4.

1.3.1. Magnetization and Static Susceptibility

Before we can turn to the dynamic aspects of EPR spectroscopy, we need to introduce the concept of magnetization first. If a material is exposed to an external magnetic field $\boldsymbol{B}_{\mathbf{ext}}$ its response to this field, i.e. its magnetization $\boldsymbol{M}$, can be characterized by the magnetic susceptibility χ. The magnetic susceptibility is positive ($\chi > 0$) for paramagnetic materials and negative for diamagnetic ones ($\chi < 0$). For constant temperature and volume it is given by equation 1.30.

$$\chi = \mu_0 \left(\frac{\partial M}{\partial B_{\text{ext}}} \right)_{T,V} \tag{1.30}$$

The magnetization is defined as the magnetic moment $\boldsymbol{m}$ per volume V. For a solid the total magnetic moment is given by the sum over all atomic moments $\boldsymbol{\mu}$ as shown in equation 1.31.

$$\boldsymbol{M} := \frac{\boldsymbol{m}}{V} = \frac{1}{V} \sum_i \boldsymbol{\mu_i} \tag{1.31}$$

Thus, if a static external magnetic field $B_0 = B_\mathrm{z}$ is applied along the z-axis, the corresponding magnetization M_0 becomes

$$M_0 = \frac{N_\mathrm{s}}{V} \langle \mu_\mathrm{z} \rangle = -n_\mathrm{s}\, g_\mathrm{s}\, \mu_\mathrm{B} \langle m_\mathrm{s} \rangle \tag{1.32}$$

with N_s as the total number of spins, the corresponding spin density n_s, and $\langle \mu_\mathrm{z} \rangle$ as the expected value for its corresponding random variable: the magnetic moment in z-direction. In the two-state quantum system of the electron spin the Boltzmann distribution describes the probability of finding the electron in a certain state, i.e. $m_\mathrm{s} = +1/2$ or $m_\mathrm{s} = -1/2$ with corresponding energies E_+ and E_- (given by equation 1.6), respectively. For m_s being a discrete variable, the corresponding expected value is given by

$$\langle m_\mathrm{s} \rangle = \sum_{m_\mathrm{s}=-1/2}^{m_\mathrm{s}=+1/2} m_\mathrm{s} P_{m_\mathrm{s}} = -\frac{1}{2} \frac{\mathrm{e}^{+\mu_\mathrm{eff} B_\mathrm{z}/k_\mathrm{B}T} - \mathrm{e}^{-\mu_\mathrm{eff} B_\mathrm{z}/k_\mathrm{B}T}}{\mathrm{e}^{+\mu_\mathrm{eff} B_\mathrm{z}/k_\mathrm{B}T} + \mathrm{e}^{-\mu_\mathrm{eff} B_\mathrm{z}/k_\mathrm{B}T}} = -\frac{1}{2} \tanh\left(\frac{\mu_\mathrm{eff} B_\mathrm{z}}{k_\mathrm{B}T} \right) \tag{1.33}$$

with k_B as the Boltzmann constant, P_{m_s} as the Boltzmann probability for a certain spin state and $\mu_\mathrm{eff} = 1/2\, g_\mathrm{s}\, \mu_\mathrm{B}$. For $\mu_\mathrm{eff} B_\mathrm{z}/k_\mathrm{B}T \ll 1$ the hyperbolic tangent can be approximated using a series expansion, yielding equation 1.34.

$$\langle m_\mathrm{s} \rangle \approx -\frac{1}{2} \frac{\mu_\mathrm{eff} B_\mathrm{z}}{k_\mathrm{B}T} \tag{1.34}$$

Using equations 1.30, 1.32 and 1.34 the static susceptibility can be calculated. In thermal equilibrium, it is given by equation 1.35.

$$\chi_0 = \mu_0 \left(\frac{\partial M_0}{\partial B_0} \right)_{T,V} = \mu_0 \cdot \frac{n_\mathrm{s}\ g_\mathrm{s}^2\, \mu_\mathrm{B}^2}{4\, k_\mathrm{B}T} \tag{1.35}$$

1.3.2. Relaxation, Bloch Equations and Energy Absorption

If a static magnetic field B_0 along the z-axis is applied to a paramagnetic sample, the spins will precess about this field, and a finite magnetization M_z along the z-direction can be observed. The net magnetization depends on the strength of the magnetic field and the temperature as was shown in the previous section. The system will reach (or restore) its thermal equilibrium magnetization M_0 with a characteristic time constant, called the spin-lattice relaxation time T_1, due to an energy exchange between the spin system and its surrounding.
However, for each precessing spin there is also a component of the magnetic moment rotating in the xy-plane, i.e. perpendicular to B_0. Because there is no phase coherence among the spins in the ensemble, the corresponding net magnetizations M_x and M_y will be zero in thermal equilibrium. If a suitable perturbation is applied to the spin system by a magnetic field perpendicular to B_0 the sample will acquire a transverse magnetization rotating or oscillating in the xy-plane. After the perturbation is switched off, this magnetization components will again decay to zero because the spin system loses its coherence with the characteristic spin-spin relaxation time T_2. In contrast to the spin-lattice relaxation, the spin-spin relaxation does not involve transitions between the two energy levels E_+ and E_- and, in general, T_1 and T_2 are different from each other.
The equations of motion for the components of the magnetization - called Bloch equations - where originally derived by Felix Bloch in 1946 for nuclear magnetic resonance but can easily be rewritten for EPR purposes.[33] The classic equation of motion for a magnetic moment $\boldsymbol{\mu_\mathrm{s}}$ can be derived from the rate of change of the angular momentum, which is the torque $\boldsymbol{T}$.

$$\boldsymbol{T} = \frac{\mathrm{d}\boldsymbol{S}}{\mathrm{d}t} = \boldsymbol{\mu}_\mathrm{s} \times \boldsymbol{B} \tag{1.36}$$

Using equation 1.1, the rate of change for the magnetic moment becomes

$$\frac{\mathrm{d}\boldsymbol{\mu_\mathrm{s}}}{\mathrm{d}t} = -\gamma \frac{\mathrm{d}\boldsymbol{S}}{\mathrm{d}t} = -\gamma \left(\boldsymbol{\mu_\mathrm{s}} \times \boldsymbol{B}\right) \tag{1.37}$$

with γ being the gyromagnetic ratio of an electron. Going from a single magnetic moment $\boldsymbol{\mu_\mathrm{s}}$ to the sample magnetization $\boldsymbol{M}$ this expression transforms into equation 1.38.

$$\frac{\mathrm{d}\boldsymbol{M}}{\mathrm{d}t} = -\gamma \left(\boldsymbol{M} \times \boldsymbol{B}\right) \tag{1.38}$$

In addition to the static component along the z-axis, B_0, a time dependent field component B_1, rotating at the angular frequency ω in the xy-plane, is used to perturb the spin ensemble in a magnetic resonance experiment. The total external magnetic field $\boldsymbol{B}$ in equation 1.38 is thus given by

$$\boldsymbol{B} = \boldsymbol{e_\mathrm{x}} B_1 \cos\omega t + \boldsymbol{e_\mathrm{y}} B_1 \sin\omega t + \boldsymbol{e_\mathrm{z}} B_0 \tag{1.39}$$

with $\boldsymbol{e_\mathrm{x}}$, $\boldsymbol{e_\mathrm{y}}$ and $\boldsymbol{e_\mathrm{z}}$ as the unit vectors along the x-, y- and z-axis, respectively. The famous Bloch expressions (1.40) can be derived from equation 1.38 and 1.39 by phenomenologically adding decay terms for the longitudinal (spin-lattice) and transversal (spin-spin) relaxation mechanisms.[33]

$$\begin{aligned}
\frac{\mathrm{d}M_\mathrm{x}}{\mathrm{d}t} &= -\gamma \left(M_\mathrm{y} B_0 - M_\mathrm{z} B_1 \sin\omega t\right) - \frac{M_\mathrm{x}}{T_2} \\
\frac{\mathrm{d}M_\mathrm{y}}{\mathrm{d}t} &= -\gamma \left(M_\mathrm{z} B_1 \cos\omega t - M_\mathrm{x} B_0\right) - \frac{M_\mathrm{y}}{T_2} \\
\frac{\mathrm{d}M_\mathrm{z}}{\mathrm{d}t} &= -\gamma \left(M_\mathrm{x} B_1 \sin\omega t - M_\mathrm{y} B_1 \cos\omega t\right) - \frac{M_\mathrm{z} - M_0}{T_1}
\end{aligned} \tag{1.40}$$

Solving this system of equations is more convenient in a coordinate system rotating at angular frequency ω around the z-axis. Introducing the substitutions $M_\mathrm{x} = M_\mathrm{u}\cos\omega t - M_\mathrm{v}\sin\omega t$ and $M_\mathrm{y} = M_\mathrm{u}\sin\omega t + M_\mathrm{v}\cos\omega t$, as well as the shorthands $\omega_\mathrm{L} = \gamma B_0$ and $\omega_1 = \gamma B_1$, the system of equations in 1.40 transforms into [23]

$$\begin{aligned}
\frac{\mathrm{d}M_\mathrm{u}}{\mathrm{d}t} &= (\omega - \omega_\mathrm{L})\, M_\mathrm{v} - \frac{M_\mathrm{u}}{T_2} \\
\frac{\mathrm{d}M_\mathrm{v}}{\mathrm{d}t} &= -(\omega - \omega_\mathrm{L})\, M_\mathrm{u} - \omega_1 M_\mathrm{z} - \frac{M_\mathrm{v}}{T_2} \\
\frac{\mathrm{d}M_\mathrm{z}}{\mathrm{d}t} &= \omega_1 M_\mathrm{v} - \frac{M_\mathrm{z} - M_0}{T_1}
\end{aligned} \tag{1.41}$$

with M_u and M_v being in phase and $\pi/2$ out of phase with B_1, thus describing the in-phase and out-of-phase magnetization components, respectively. If the resonance experiment is performed in the slow-passage regime, i.e. the magnetic field is varied slowly and does not change significantly during the period of a Lamor precession, all time derivatives can be set to zero to find the static solution for this system given by the equations in 1.42. [23]

$$\begin{aligned}
M_\mathrm{u} &= -M_0\, \frac{\omega_1 T_2^2\,(\omega - \omega_\mathrm{L})}{1 + \omega_1^2\, T_1 T_2 + T_2^2\,(\omega - \omega_\mathrm{L})^2} \\
M_\mathrm{v} &= -M_0\, \frac{\omega_1 T_2}{1 + \omega_1^2\, T_1 T_2 + T_2^2\,(\omega - \omega_\mathrm{L})^2} \\
M_\mathrm{z} &= M_0\, \frac{1 + T_2^2\,(\omega - \omega_\mathrm{L})^2}{1 + \omega_1^2\, T_1 T_2 + T_2^2\,(\omega - \omega_\mathrm{L})^2}
\end{aligned} \tag{1.42}$$

So far, the external magnetic field $\boldsymbol{B}$ introduced in equation 1.39 was taken to be circular polarized. However, EPR spectrometers usually use linear polarized microwave radiation resulting in a linear polarized microwave magnetic field.

$$\boldsymbol{B} = \boldsymbol{e}_\mathbf{x} 2B_1 \cos\omega t + \boldsymbol{e}_\mathbf{y} 0 + \boldsymbol{e}_\mathbf{z} B_0 \tag{1.43}$$

The change in the sample's energy due to the microwave irradiation, $\mathrm{d}E = {}^1\!/_{\mu_0} B\,\mathrm{d}M$, can be used to calculate the microwave power absorption P during a period [23]

$$P = \frac{\omega}{2\pi} \int_0^{2\pi/\omega} \frac{\mathrm{d}E}{\mathrm{d}t}\mathrm{d}t = \frac{\omega}{2\pi} \int_0^{2\pi/\omega} \frac{1}{\mu_0} 2B_1 \cos\omega t\, \frac{\mathrm{d}M_\mathrm{x}}{\mathrm{d}t}\mathrm{d}t = -\frac{1}{\mu_0}\omega B_1 M_\mathrm{v} = -\frac{2}{\mu_0^2}\omega B_1^2\, \chi'' \tag{1.44}$$

with χ'' as the radio frequency (RF) susceptibility, which is defined analogous to the static susceptibility given by equation 1.35.

$$\chi'' = \frac{\mu_0}{2} \left(\frac{\partial M_\mathrm{v}}{\partial B_1}\right)_{T,V} \tag{1.45}$$

Using the result given in equation 1.42, the RF susceptibility becomes

$$\chi'' = -\frac{1}{2}\chi_0\, \omega_\mathrm{L}\, \underbrace{\frac{T_2}{1 + \omega_1^2\, T_1 T_2 + T_2^2\,(\omega - \omega_\mathrm{L})}}_{f(\omega)} \tag{1.46}$$

with ω_L as the angular Larmor frequency. Looking at $f(\omega)$ in equation 1.46 it becomes clear that, if $\omega_1^2 T_1 T_2 \ll 1$, this is the equation of a Lorentzian line with its maximum at $\omega = \omega_\mathrm{L}$. Because $f(\omega)$ decreases for large $\omega_1 = \gamma B_1$ and long $T_1 T_2$, $Z = 1 + \omega_1^2 T_1 T_2$ is sometimes called the saturation parameter (see section 1.3.3).[23]
For the usual narrow-band EPR transitions, the approximation $\omega \approx \omega_\mathrm{L}$ can be used to obtain a final expression for the absorbed power by plugging equation 1.46 in 1.44 and using equation 1.35.

$$P = \frac{n_\mathrm{s} \hbar^2 \gamma^2 B_0^2}{4\, kT \mu_0} \frac{\omega_1^2 T_2}{1 + \omega_1^2 T_1 T_2 + T_2^2 (\omega - \omega_\mathrm{L})} \tag{1.47}$$

1.3.3. Saturation, Linewidth and Broadening Effects

From the last section it is known that the EPR absorption signal can - in the absence of broadening effects - be described by a Lorentzian shape function. Furthermore, the signal is influenced by many instrumental variables like gain, modulation amplitude, cavity quality factor and so on. Combining all these variables in a proportionality factor Λ the EPR absorption signal is given by[23]

$$S^\mathrm{EPR} = \Lambda \cdot B_1^\kappa \chi'' = \Lambda \cdot B_1^\kappa \chi_0 \omega_\mathrm{L} \frac{T_2}{Z + T_2^2 (\omega - \omega_\mathrm{L})^2} \tag{1.48}$$

with the saturation parameter $Z = 1 + \omega_1^2 T_1 T_2 = 1 + \gamma^2 B_1^2 T_1 T_2$. Depending on the characteristics of the detector used, the EPR signal is observed to be proportional to either B_1 (linear detector) or B_1^2 (square-law detector). The exponent κ in equation 1.48 accounts for this difference. For a linear detector, used in most modern EPR spectrometers, $\kappa = 1$ and the detected signal is proportional to the transversal magnetization. However, in some cases like EDMR the detector - which is the sample itself in case of EDMR - acts like a square-law detector with $\kappa = 2$ and the observed signal is proportinal to the absorbed power P (cf. equation 1.47). For quantification purposes it is more precise to use the area under the resonance signal given by equation 1.49 instead of its height to account for broadening effects.[23]

$$A^\mathrm{EPR} = \int_0^\infty S^\mathrm{EPR}\, \mathrm{d}\omega = \Lambda \cdot B_1^\kappa \chi_0 \omega_\mathrm{L} \pi Z^{-1/2} \tag{1.49}$$

By investigating the saturation behavior of the EPR signal area – i.e. recording spectra for different microwave magnetic fields B_1 – estimates for the product of the time constants T_1 and T_2 can be obtained from Z. With these parameters available, the study of relaxation processes and what influences them becomes possible in both EPR and EDMR.
In general, there are two different types of line broadening that need to be considered. Effects summarized by the terminus **homogeneous broadening** are due to fluctuating fields originating from spin flips of spins with the same Larmor frequency and are sometimes called life-time effects. This broadening category is dominated by the spin-spin relaxation because T_2 is usually much smaller than T_1. In the absence of saturation effects, i.e. $\gamma^2 B_1^2 T_1 T_2 \ll 1$, the relation between the full width at half maximum of the Lorenzian-shaped signal, $\Delta\omega$, and T_2 is given by equation 1.50.[23]

$$\Delta\omega = \frac{2}{T_2} \tag{1.50}$$

However, the spin-lattice relaxation and power-saturation effects can also play a role in some samples, making the determination of T_2 more difficult.

On the other hand, effects leading to differences in the local magnetic field for different spins are summarized by the terminus **inhomogeneous broadening**. Because the resonance condition changes for some of the spins in the sample, they are no longer exited together but rather in different spin packets according to their Larmor frequency. As a result of the distribution of individual spin packets with different Larmor frequencies, the observed signal is often no longer of Lorentzian but of Gaussian shape.[19] The main source of such local field inhomogeneities are unavoidable effects inside the sample like dipolar couplings to surrounding proton spins, unresolved hyperfine splittings, and g-tensor anisotropies. Additionally, local field inhomogeneities can arise from the spectrometer setup itself, for example due to the mounting of additional equipment, like dewars, inside the resonance cavity. This type of magnetic field distortion is, however, in principle avoidable.

1.4. A Typical CW-EPR Instrument

This section will introduce some more technical aspects of EPR spectroscopy by familiarizing the reader with a typical setup concept. In this context, only the continuous wave electron paramagnetic resonance (CW-EPR) technique is considered. Here, the amplitude and frequency of the microwave irradiation is kept constant in time. Beyond that, a variety of pulsed EPR techniques exists that lie outside the scope of this work.
Figure 1 shows a typical CW-EPR spectrometer setup. In principle two options of recording a spectrum exist. One can either vary the external magnetic field or the microwave excitation frequency to fulfill the resonance condition given by equation 1.7. Thus, it is equally possible to "sweep" the magnetic field or the frequency. In most practical cases, however, the field sweep

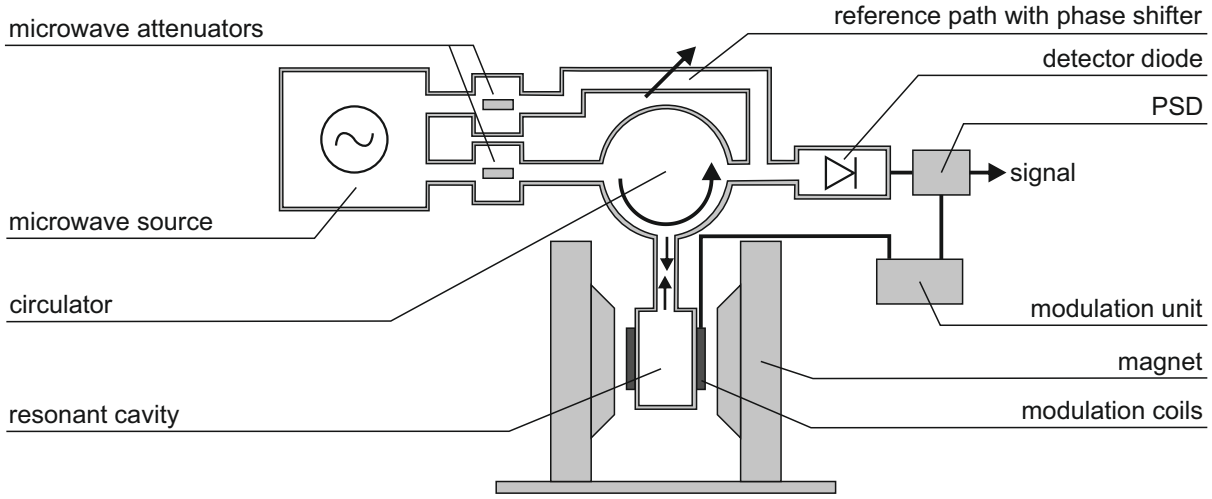

Fig. 1: Working principle and parts of a typical CW-EPR instrument. The central part of the spectrometer is the circulator ensuring that microwaves exiting the source can only travel to the sample in the resonant cavity and only reflected radiation reaches the detector. After the microwave radiation gets converted to a corresponding current by the detector diode, the signal is processed by a phase sensitive detection (PSD). Other important parts are the microwave attenuators responsible for the adjustment of the microwave power and the modulation system consisting of the modulation coils and the modulation unit.

is used because the sample is placed in a resonant cavity responsible for the conversion of the microwave power P_{MW} to the corresponding magnetic field strength B_1. The efficiency of this

conversion process is characterized by the cavity conversion factor c given by equation 1.51.

$$c = \frac{B_1}{\sqrt{P_{\mathrm{MW}}}} \tag{1.51}$$

As introduced in section 1.3.2 it is the $\boldsymbol{B_1}$ field (which is perpendicular to the static magnetic field) that introduces the spin transitions detected in EPR. Producing a large enough microwave magnetic field at the sample's position is thus important to obtain a sufficient signal-to-noise ratio (SNR). The specific cavity used in the instrument will of course only be resonant for a particular microwave frequency making a frequency-sweep EPR unfavorable.

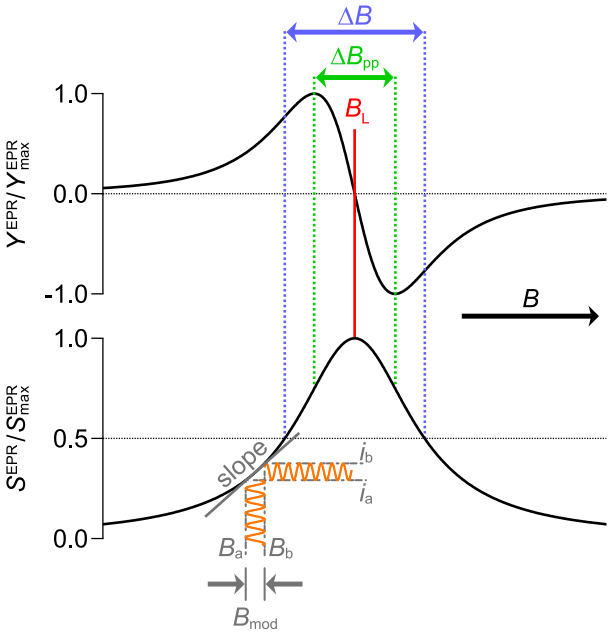

Fig. 2: EPR absorption and modulation principle. The EPR absorption signal S^{EPR} is detected as its first derivative Y^{EPR} due to the applied magnetic field modulation with amplitude B_{mod}. Here, i_{a} and i_{b} are the detector currents corresponding to B_{a} and B_{b}, respectively. The center of the absorption signal is given by B_{L} and has a full width at half maximum of ΔB corresponding to $\sqrt{3}\,\Delta B_{\mathrm{pp}}$.

The SNR can be greatly improved if the microwave detector diode is only irradiated in case of an absorption. This idea lies at the heart of the reflection cavity principle. Here, the whole system is balanced so that in absence of an absorption all microwave energy is stored (and dissipated) inside the cavity. If the sample begins to absorb energy from the $\boldsymbol{B_1}$ field, the system is no longer balanced out due to a change in the impedance of the cavity. Thus, the radiation gets reflected and eventually reaches the detector diode producing the EPR signal. The dimensions of the sample cavity depend on the wavelength used in the instrument. In this work, an X-band spectrometer utilizing a microwave frequency of about 9.4 GHz with corresponding resonator dimension of approximately 3 cm was used.
Typically, the microwave detector diode needs to be biased to be in its linear working regime but, as just discussed, should not be in a line with the microwave source. A reference path (also called bypass) is thus used to bias the detector diode at a particular level. Furthermore, a part of equipment called the circulator uses the fact the waves possess a traveling direction to separate the waves moving to the cavity from the ones reflected from it to ensure that only the latter reach the detector.
Figure 1 also contains a magnetic field modulation system consisting of the modulation unit, the modulation coils and the phase sensitive detection (PSD). These components are responsible for further improvement of the SNR. The change in the microwave absorption due to spin transitions in the sample is very small, and it is thus favorable to apply a lock-in detection scheme. Here, the modulation unit is responsible for producing a modulated current through the modulation coils (or rods) resulting in a magnetic field $\boldsymbol{B_{\mathrm{mod}}}$ parallel to the static external field $\boldsymbol{B_0} = \boldsymbol{e_z} B_0$. This oscillating field is characterized by its amplitude B_{mod} and frequency f_{mod}. As illustrated in figure 2, the modulation of the external magnetic field produces a modulation in the detector current i at f_{mod}. The PSD

then allows for the extraction of only those changes in the detector current occurring at f_{mod}. This makes an amplification of only the relevant signal component possible, which dramatically improves the achievable SNR.
Figure 2 illustrates an important side effect of this field modulation approach: Detecting the EPR absorption S^{EPR} using a field modulated by $\boldsymbol{B_{\mathrm{mod}}}$ results in recording the slope Y^{EPR} of S^{EPR} at any point – as long as the modulation amplitude B_{mod} is small compared to the full width at half maximum ΔB. Otherwise, the recorded first derivative Y^{EPR} is distorted and one observes what is referred to as "field over-modulation" leading to an increased peak-to-peak linewidth ΔB_{pp}. Typically, EPR spectra are shown as the first derivative Y^{EPR} being a function of the applied external magnetic field strength B because this greatly simplifies the determination of the important spectroscopic parameters. These are the peak-to-peak linewidth ΔB_{pp} and the magnitude of the resonance field B_{L} (often referred to in terms of the g-factor using equation 1.7). For Lorentzian lines, the relationship between the absorption, its first derivative, and the important spectroscopic parameters is shown in figure 2 where $\Delta B_{\mathrm{pp}} = {}^{1}\!/\!_{\sqrt{3}}\,\Delta B$. Using equation 1.50 the spin-spin relaxation time T_2 is given by

$$T_2 = \frac{2}{\Delta\omega} = \frac{2}{\gamma\sqrt{3}\,\Delta B_{\mathrm{pp}}} \tag{1.52}$$

with γ as the reduced gyromagnetic ratio in frequency units defined by equation 1.3.

2. Basics of EDMR Spectroscopy

In chapter 1 we introduced the basics of EPR spectroscopy and – as we soon shall see – also laid the groundwork for the electrically detected magnetic resonance (EDMR) technique used throughout this thesis. At the beginning of this chapter we will discuss the similarities and differences between EPR and EDMR and investigate what kind of processes inside a sample can be observed best using EDMR. This will be followed by the introduction of a system of rate equations leading to expressions for the relaxation times and signal shape in EDMR. Finally, a typical EDMR setup will be introduced.

2.1. From EPR to EDMR

In a nutshell, the EDMR method investigates the influence of a microwave magnetic field $\boldsymbol{B_1}$ on the current that flows through a sample. Thus, in contrast to the EPR method described in chapter 1 – where any kind of unpaired electron can in principle lead to a signal – EDMR is only sensitive to those spins involved in spin-dependent processes that affect the lifetimes and transport of elementary excitations. Due to this difference, EDMR has proven to be a powerful tool in semiconductor materials and electronic devices research in recent years.[8,34–38]
The macroscopic property changing during an EDMR experiment is the sample's conductivity σ, given by equation 2.1.

$$\sigma = e\,(\mu_{\mathrm{e}} n_{\mathrm{e}} + \mu_{\mathrm{h}} n_{\mathrm{h}}) \tag{2.1}$$

In this equation e is the elementary charge and μ_{e} and μ_{h} denote the mobility of electrons and holes, respectively. The corresponding number densities of electrons and holes are indicated by n_{e} and n_{h}. Hence, the observation of an EDMR signal can be due to a change in the mobility or in the number of the charge carriers inside a given sample.
In fact, Maxwell and Honig attributed the first EDMR signal in phosphorus doped silicon to spin-dependent scattering of charge carriers and thus to a change in μ.[39] A few years later, Lepine

discovered the first spin-dependent recombination path, i.e. he explained his observations in pure n-type silicon by a change in the number of carriers available.[40] For a transition between two charge carriers to take place, the Pauli exclusion principle needs to be obeyed as depicted in figure 3. The fully occupied final state has to be a singlet. If no spin-flip occurs during the transition, i.e. no magnetic interaction is involved, the spin-dependence is already determined by the initial state. Thus, if the initial state is a triplet (vivid picture: "parallel spins", exact definition see equation 2.4) the transition is forbidden. In contrast, if the initial state is a singlet (vivid picture: "anti-parallel spins") the transition can take place. This basic principle is at the heart of the following considerations regarding spin-dependent processes.

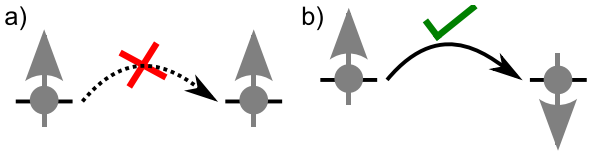

Fig. 3: Spin-dependent transitions are governed by the Pauli exclusion principle. a) Pauli forbidden transition between "parallel" spins. b) Pauli allowed transition between "anti-parallel" spins.

In an EDMR experiment, the microwave irradiation can induce spin-flips and therefore alter the triplet state density. If the transition is part of a recombination pathway, a quenching of the sample current can be observed. On the other hand, if the transition contributes constructively to the transport pathway (i.e. is part of a hopping mechanism) an enhancement is detected. To develop a more precise picture than just the simple "parallel" and "anti-parallel" spin alignment analogy, we need to look at the transition moment integral and its connection to the transition rate $r_{i\to S}$ for an initial state $|i\rangle$ and a final state, which is by prerequisite a singlet state $|S\rangle$. Equation 2.2 shows this relationship.

$$r_{i\to S} \propto |\langle S \,|\, i\rangle|^2 \tag{2.2}$$

If the initial state is itself a singlet, the transition moment integral is given by $|\langle S \,|\, S\rangle|^2 = 1$ and the corresponding transition rate is denoted r_S. For a triplet initial state $|T\rangle$ the result is $|\langle S \,|\, T\rangle|^2 = 0$ due to the orthogonality of the spin wave functions with corresponding transition rate r_T. Although the triplet transitions are called "forbidden", spin-orbit coupling can result in $r_\mathrm{T} > 0$ and therefore at least partly allow for recombinations from such a state. Often, this effect can be considered to be only small and thus $r_\mathrm{S} >> r_\mathrm{T}$. Summing up, it is essential for the magnitude of the transition rate what exact configuration the initial state $|i\rangle$ possesses.

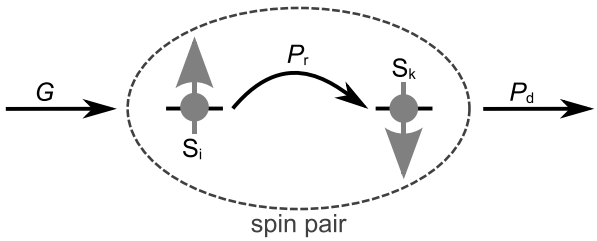

Fig. 4: KSM model spin pair. The spin pair composed of S_i and S_k is generated with rate G and can either recombine with probability P_r or dissociate with probability P_d. Recombination with other spins can not take place during the pair's lifetime.

In the first picture introduced by Lepine,[40] the spin-dependent recombination depends on the thermal polarization of the charge carriers which leads to a difference in the singlet-triplet ratio from its equilibrium value 1/3. This model predicts a maximum EDMR effect of $\Delta\sigma/\sigma \approx 10^{-6}$. Furthermore, it shows a quadratic dependence on the magnetic field. In fact, experimental data not only revealed that a much larger EDMR effect is possible,[40,41] but also that the prediction regarding the magnetic field could not be confirmed.[42]

Kaplan, Solomon and Mott were able to overcome the difficulties of the Lepine model in

their approach (frequently referred to as the KSM model) introducing a spin pair as the key element.[42] Figure 4 illustrates the basic KSM idea using a spin pair composed of S_i and S_k. The KSM model anticipates the formation of such a spin pair with generation rate G, which can then either recombine with probability P_r or dissociate again with probability P_d, but will not recombine with other spins in the system during its lifetime. Here, in contrast to the Lepine model, the microwave induced spin-flip happens during the lifetime of the spin pair so that the system can not reach thermal equilibrium. Thus, the probability for a transition depends on the symmetry of the spin pair. In the Zeeman basis for a system with two particles of spin 1/2: $|\uparrow\uparrow\rangle$, $|\uparrow\downarrow\rangle$, $|\downarrow\uparrow\rangle$, $|\downarrow\downarrow\rangle$ the system's Hamiltonian (see equation 1.9) is non-diagonal if exchange or dipolar couplings are present.[43,44] It can, however, be diagonalized by an unitary transformation, leading to the new basis:[44]

$$\begin{aligned} |T_+\rangle &:= |1\rangle = |\uparrow\uparrow\rangle \\ |\tilde{S}_A\rangle &:= |2\rangle = \cos\alpha\,|\uparrow\downarrow\rangle - \sin\alpha\,|\downarrow\uparrow\rangle \\ |\tilde{S}_B\rangle &:= |3\rangle = \sin\alpha\,|\uparrow\downarrow\rangle + \cos\alpha\,|\downarrow\uparrow\rangle \\ |T_-\rangle &:= |4\rangle = |\downarrow\downarrow\rangle \end{aligned} \tag{2.3}$$

where the angle α depends on the coupling strength between the two spins. Here, $|T_+\rangle$ and $|T_-\rangle$ are pure triplet states with inhibited recombination, whereas the two states $|\tilde{S}_A\rangle$ and $|\tilde{S}_B\rangle$ are mixed states with singlet content where recombination is partly allowed. If no coupling exists, i.e. $\alpha = 0$, the basis in equation 2.3 transforms back into the Zeeman basis. On the other hand, if the coupling is strong ($\alpha = \pi/4$) the basis transforms into

$$\begin{aligned} |T_+\rangle &= |1\rangle = |\uparrow\uparrow\rangle \\ |S_0\rangle &:= |2\rangle = 1/\sqrt{2}\,(|\uparrow\downarrow\rangle - |\downarrow\uparrow\rangle) \\ |T_0\rangle &:= |3\rangle = 1/\sqrt{2}\,(|\uparrow\downarrow\rangle + |\downarrow\uparrow\rangle) \\ |T_-\rangle &= |4\rangle = |\downarrow\downarrow\rangle \end{aligned} \tag{2.4}$$

with $|T_+\rangle$, $|T_-\rangle$ and $|T_0\rangle$ as pure triplet states and $|S_0\rangle$ as pure singlet, only from which recombination can occur.[44] Looking at equation 2.2 it becomes clear that, in general, the transition rate coefficient for the spin pair with initial state $|i\rangle$ is given by equation 2.5.[43]

$$r_i = r_S\,|\langle S|i\rangle|^2 + r_T\,|\langle T|i\rangle|^2 \tag{2.5}$$

The pure triplet states $|T_+\rangle$, $|T_-\rangle$ and $|T_0\rangle$ possess a rate coefficient r_T while for the pure singlet state $|S_0\rangle$ the rate coefficient is r_S. For the mixed states $|\tilde{S}_A\rangle$ and $|\tilde{S}_B\rangle$ in basis 2.3 the rate coefficient can be approximated by neglecting triplet recombination, as shown in equation 2.6.

$$r_{\tilde{S}} = 1/2(r_S + r_T) \approx 1/2\,r_S \tag{2.6}$$

Finally, we want to introduce the results obtained by KSM based on their above described model.[42] If the pair generation rate is denoted f and that one for the dissociation is d, the equilibrium recombination rate in the absence of resonant microwaves R_0 is given by

$$R_0 = f\left[1 - \frac{2d}{r_S}\ln\left(\frac{1+\frac{2d}{r_S}}{\frac{2d}{r_S}}\right)\right] \tag{2.7}$$

and the maximum recombination rate – determining the expected maximum EDMR effect – calculates to

$$R_{res} = \frac{f}{1+\frac{4d}{r_S}} \tag{2.8}$$

in resonance with the microwave irradiation. The spin-dependent recombination effect according to the KSM model is thus given by

$$\frac{\Delta R}{R} = \frac{R_{\mathrm{res}} - R_0}{R_0} \tag{2.9}$$

with a maximum of about 12 % for $d/r_{\mathrm{S}} = 0.14$. The basic KSM model has been revised with focus on a quantum mechanical description of the originally semi-classical theory and improvements have been published for certain special cases by different authors over the years.[44–47] Furthermore, work based on rate equations has been done to directly include assumptions regarding the charge carrier concentrations in equilibrium and in resonance with the microwave to calculate the EDMR signal amplitude.[48–50] An approach to combine EPR and EDMR theory based on such a system of rate equations was developed by Kanschat.[51] He was able to describe spectroscopic parameters like lineshape and linewidth based on the corresponding EPR expressions, and we will follow his approach in the next section.

2.2. Combining EPR and EDMR – The Rate Equation Model

The EDMR method is particularly useful for the study of spin-dependent processes in semiconductors. The selection rules that correspond to these processes can be quite strict even at room temperature, especially in organic materials, where they lead to relatively long-lived spin pair states. As introduced in the previous section, the pair partners, which may be photo-excited electrons and holes, preferably recombine when they are in a singlet pair state. Because such spin pairs can be found not only at grain boundaries between different crystalline parts or at contact interfaces of materials but also exist at deep levels due to the disorder in amorphous parts of a device, EDMR can be considered an ideal tool for understanding the basic charge transport and loss mechanisms in these devices. Thus, it would be of great benefit if we could use the well-known EPR theory to understand and describe EDMR processes as well. The theory of CW-EPR signal shape was already introduced in section 1.3 and we will now build a connection between these expressions and the EDMR theory introduced in section 2.1. Our approach will be based on a rate equation model introduced by Lips,[48] that was later refined by Kanschat in his doctoral thesis.[51]

If the interaction between the two partners that make up the spin pair can be considered weak, the eigenstates in basis 2.3 can be used to describe this spin system. In reality, on one hand, there may be a finite, if small, spin-spin interaction characterized by the parameter J containing both exchange and dipolar coupling. On the other hand, there is a significant singlet-triplet mixing due to differences in the Zeeman frequencies $\Delta\omega$ arising as a result of different g-factors and local hyperfine fields for the two pair partners. The parameter controlling the amount of singlet-triplet mixing, $\Delta\omega/J$, may usually be taken as large enough to justify the assumption of weakly coupled spins used hereinafter. It will be assumed that the capture and dissociation of a spin pair depends on one type of carrier mostly, e.g. on electrons, since the other type of carrier is less mobile and hence accumulated in the bulk and can be considered to play the role of a "recombination center". The rate equation model derived in the following can equally well be interpreted in terms of unipolar spin pairs, in which the recombination center is realized by a polaron of the same type. Coulombic repulsion will be neglected in this approach as the excess energy of diffusing polarons exceeds the Coulomb energy, at least right after their creation and before complete thermalization.[41]

The important processes on which the EDMR rate equation model is based on are illustrated in figure 5. Transport electrons n are generated at rate G by photoexcitation. Recombination

can then occur either spin independently via a recombination center **r** with capture time τ, or spin-dependently via a spin pair (**e**, **h**). These spin pairs are generated at rate f and can dissociate again at rate d. Here, depending on the eigenstate of the spin pair recombination occurs at rate r_T or $r_\tilde{\mathrm{S}}$ as introduced in equation 2.5 and 2.6. As for the approximation in equation 2.6, $r_\mathrm{T} << r_\mathrm{S}$ is assumed.

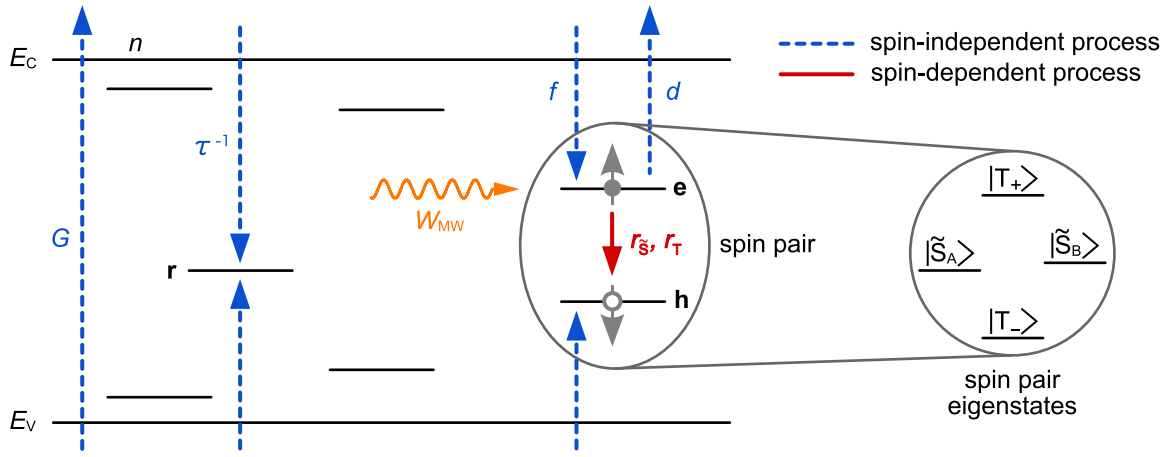

Fig. 5: Important processes for the EDMR rate equation model in an n-type photoconductor. Transport electrons n are generated at rate G by photoexcitation. Spin-independent recombination with capture time τ takes place via the recombination center **r**. Spin-dependent recombination occurs via the spin pair (**e**, **h**) formed with rate f. The spin pair can dissociate again with rate d or recombine with rate $r_\tilde{\mathrm{S}}$ or r_T, depending on its eigenstate (cf. basis given by equation 2.3).

With N_T and $N_\tilde{\mathrm{S}}$ as the density of pairs in the triplet and mixed state, respectively, the rate equation model following from figure 5 is given by equation 2.10.

$$\begin{aligned}
\dot{n} &= G - (f + 1/\tau)\, n + N_\tilde{\mathrm{S}}\, d + N_\mathrm{T}\, d \overset{!}{=} 0 \\
\dot{N}_\tilde{\mathrm{S}} &= \pi_\tilde{\mathrm{S}}\, f n - \left(d + r_\tilde{\mathrm{S}}\right) N_\tilde{\mathrm{S}} - W\left(N_\tilde{\mathrm{S}} - N_\mathrm{T}\right) \overset{!}{=} 0 \\
\dot{N}_\mathrm{T} &= \pi_\mathrm{T}\, f n - (d + r_\mathrm{T})\, N_\mathrm{T} + W\left(N_\tilde{\mathrm{S}} - N_\mathrm{T}\right) \overset{!}{=} 0
\end{aligned} \tag{2.10}$$

Here, polarization effects are captured by the parameter $\pi = P_\mathrm{e}\, P_\mathrm{h}$ with the spin polarization of the pair partners

$$P_j = (n_{j\uparrow} - n_{j\downarrow})/(n_{j\uparrow} + n_{j\downarrow}) \tag{2.11}$$

and thus

$$\begin{aligned}
\pi_\tilde{\mathrm{S}} &= (1 - P_\mathrm{e}\, P_\mathrm{h}) = (1 - \pi)/2 \\
\pi_\mathrm{T} &= (1 + P_\mathrm{e}\, P_\mathrm{h}) = (1 + \pi)/2
\end{aligned} \tag{2.12}$$

as the polarizations of the pairs in mixed and triplet state, respectively. The total spin-flip rate $W = W_0 + W_\mathrm{MW}$ covers spontaneous spin flips

$$W_0 = \frac{1}{2\,T_{1,P_\mathrm{e}}} + \frac{1}{2\,T_{1,P_\mathrm{h}}} \tag{2.13}$$

due to an energy exchange between the spin system and its surrounding (characterized by the time constant T_1, see section 1.3.2), as well as microwave induced spin flips occurring at W_MW.

The rate equation model given by equation 2.10 can be simplified by introducing the average recombination rate $r = \left(r_{\tilde{\mathrm{S}}} + r_{\mathrm{T}}\right)/2$, the excess recombination rate $\varrho = \left(r_{\tilde{\mathrm{S}}} - r_{\mathrm{T}}\right)/2$ as well as the total number density of spin pairs $N = N_{\mathrm{T}} + N_{\tilde{\mathrm{S}}}$ and the excess number density of triplet spin pairs $\Delta = N_{\mathrm{T}} - N_{\tilde{\mathrm{S}}}$. With these, we find that

$$\begin{aligned} Nr - \Delta\varrho &= N_{\tilde{\mathrm{S}}}\, r_{\tilde{\mathrm{S}}} + N_{\mathrm{T}}\, r_{\mathrm{T}} \\ N\varrho - \Delta r &= N_{\tilde{\mathrm{S}}}\, r_{\tilde{\mathrm{S}}} - N_{\mathrm{T}}\, r_{\mathrm{T}} \end{aligned} \tag{2.14}$$

and the rate equation model can be transformed into the one shown in equation 2.15.

$$\begin{aligned} \dot{n} &= G - (f + 1/\tau)\, n + Nd \stackrel{!}{=} 0 \\ \dot{N} &= fn - N\,(d + r) + \Delta\varrho \stackrel{!}{=} 0 \\ \dot{\Delta} &= \pi f n + N\varrho - \Delta\,(d + r + 2W) \stackrel{!}{=} 0 \end{aligned} \tag{2.15}$$

As introduced earlier, the macroscopic property changing during an EDMR experiment is the sample's conductivity σ (see equation 2.1). In analogy to the spin-dependent recombination effect predicted by the KSM model (cf. equation 2.9), the signal in an EDMR experiment is given by

$$S^{\mathrm{EDMR}} = \frac{\Delta\sigma}{\sigma} = \frac{n\,(W_{\mathrm{MW}}) - n_0}{n_0} \tag{2.16}$$

with n_0 as the off-resonant number of transport electrons. An infinitely high microwave spin-flip rate will thus define the maximum observable EDMR signal amplitude as shown in equation 2.17.

$$S^{\mathrm{EDMR}}_{\mathrm{max}} := \lim_{W_{\mathrm{MW}} \to \infty} \frac{\Delta\sigma}{\sigma} = \lim_{W_{\mathrm{MW}} \to \infty} \frac{n\,(W_{\mathrm{MW}}) - n_0}{n_0} \tag{2.17}$$

The general solution of the system of rate equations shown in expression 2.15 with respect to this limit is given by equation 2.18.

$$S^{\mathrm{EDMR}}_{\mathrm{max}} = -\frac{f\tau}{\left(1 + \frac{d}{r}\right) + f\tau} \cdot \frac{\left(\frac{\varrho}{r}\right)^2 + \pi\left(\frac{\varrho}{r}\right)\left(1 + \frac{d}{r}\right)}{1 + \frac{r}{d}\left(1 - \left(\frac{\varrho}{r}\right)^2\right) + \left(1 + \frac{d}{r}\right)\left(1 + 2\,\frac{W_0}{d}\right)} \tag{2.18}$$

The EDMR signal can now be derived from the corresponding expression for the EPR absorption line (equation 1.48) using $\kappa = 2$ to account for the square-law detection characteristics of the sample. The microwave induced spin-flip rate in resonance ($\omega = \omega_{\mathrm{L}}$) for a homogeneous line is given by equation 2.19.[52]

$$W_{\mathrm{MW}} = \gamma^2 B_1^2\, T_2 \tag{2.19}$$

With this, the EDMR signal can be expressed as

$$S^{\mathrm{EDMR}} = S^{\mathrm{EDMR}}_{\mathrm{max}} \cdot \frac{W_{\mathrm{MW}}\, T_1^{\mathrm{E}}}{1 + W_{\mathrm{MW}}\, T_1^{\mathrm{E}}} = S^{\mathrm{EDMR}}_{\mathrm{max}} \cdot \frac{W_{\mathrm{MW}}}{W_1 + W_{\mathrm{MW}}} \tag{2.20}$$

with T_1^{E} as the T_1 analog in an EDMR experiment. The system of rate equations shown in expression 2.15 can now be used together with equation 2.16, 2.18 and 2.20 to yield the following expression for T_1^{E}

$$\frac{1}{T_1^{\mathrm{E}}} = W_1 = W_0 + \frac{r}{2}\left(1 - \left(\frac{\varrho}{r}\right)^2\right) + \frac{d}{2}\left(1 + \frac{\left(\frac{\varrho}{r}\right)^2 - \pi\left(\frac{\varrho}{r}\right) f\tau}{\left(1 + \frac{d}{r}\right) + f\tau}\right) \tag{2.21}$$

with W_0 as the spontaneous spin-flip rate as introduced in equation 2.13.
To be able to fully treat the EDMR signal analog to the EPR signal with respect to its shape (cf. section 1.3) not only T_1^{E} has to be defined but also T_2^{E}, which is analog to the T_2 time constant in an EPR experiment, has to be derived. In an EPR experiment the T_2 time is generally limited by the lifetime of the spin state in resonance.[23] In analogy to this, T_2^{E} is limited by the lifetime of the spin pair T_{pair}. As pointed out by Kanschat,[51] the lifetimes of the final and initial state in an EDMR experiment differ and are in general proportional to the relative amounts of $|\tilde{S}\rangle$ and $|T\rangle$ contribution to the mixed states $\delta\,|\tilde{S}\rangle + (1-\delta)\,|T\rangle$. Averaging over a 180° spin-flip T_{pair} becomes[51]

$$\frac{1}{T_{\mathrm{pair}}} = \int_0^1 \delta\left(W_0 + r_{\tilde{\mathrm{S}}} + d\right) + (1-\delta)\left(W_0 + r_{\mathrm{T}} + d\right) d\delta = W_0 + r + d \tag{2.22}$$

with $r = \left(r_{\tilde{\mathrm{S}}} + r_{\mathrm{T}}\right)/2$ as the average recombination rate. T_2^{E} is then connected to the well-known T_2 time constant from EPR as shown in equation 2.23.

$$\frac{1}{T_2^{\mathrm{E}}} = W_2 = \frac{1}{T_2} + \frac{1}{T_{\mathrm{pair}}} \tag{2.23}$$

In summary, the re-interpretation of the well-known time constants T_1 and T_2 from EPR led to the corresponding EDMR expressions shown in equation 2.21 and 2.23, as well as to a general expression of the EDMR signal (equation 2.20) that corresponds to the EPR signal introduced in equation 1.48. Therefore, the signal characteristics derived for EPR signals can be equally interpreted for EDMR experiments. This is especially useful for the area under the resonance signal given by

$$A^{\mathrm{EDMR}} = \int_0^\infty S^{\mathrm{EDMR}}\,\mathrm{d}\omega \propto \frac{B_1^2}{1 + \gamma^2 B_1^2\, T_1^{\mathrm{E}}\, T_2^{\mathrm{E}}} \tag{2.24}$$

in analogy to the EPR expression shown in equation 1.49. Additionally, the derived expressions show that the EDMR signal is governed not only by the spin-lattice relaxation time T_1 and the spin-spin relaxation time T_2 (see section 1.3.2) but that the dissociation and recombination rates for the formed spin pair play an important role in EDMR. Furthermore, the presence of spin-independent processes can significantly influence the observable EDMR signal magnitude as shown in equation 2.18.
The determination of the $T_1^{\mathrm{E}}\,T_2^{\mathrm{E}}$ product is possible by studying the saturation behavior of the EDMR signal area. Thus, using equation 1.52 the T_2^{E} time constant can be estimated from the EDMR spectrum, making T_1^{E} calculable from the $T_1^{\mathrm{E}}\,T_2^{\mathrm{E}}$ product. Looking at equation 2.23 it becomes clear that, due to the pair lifetime T_{pair}, the EDMR linewidth is somewhat larger than the corresponding EPR linewidth.

2.3. A Typical CW-EDMR Instrument

This section will introduce some more technical aspects of EDMR spectroscopy by familiarizing a typical setup concept. As for the EPR setup, only the continuous wave electrically detected magnetic resonance (CW-EDMR) technique is considered. Here, amplitude and frequency of the microwave irradiation is kept constant in time. Beyond that, EDMR can also be carried out using a pulsed approach.[53] This, however, lies outside the scope of this work.
Figure 6 shows a typical CW-EDMR spectrometer setup. In contrast to EPR, where the detec-

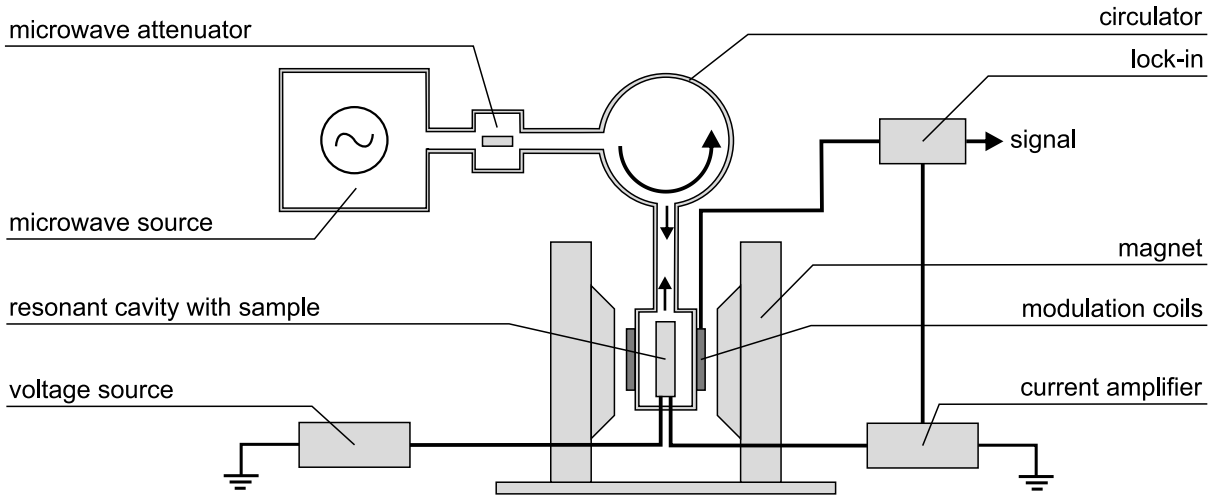

Fig. 6: Working principle and parts of a typical CW-EDMR instrument. In contrast to an EPR machine (cf. figure 1) the sample itself acts as the detector in an EDMR spectrometer. Therefore, no detector diode is used and the sample is connected to a voltage source responsible for biasing it during the experiment instead. The current flowing through the sample is enhanced using a current amplifier which is connected to the lock-in responsible for signal detection and magnetic field modulation. Besides the electrical detection pathway, the spectrometer consists of similar parts as the corresponding EPR setup.

tion is done using a microwave detector diode, the sample itself acts as a square-law detector (cf. section 1.3.3) in an EDMR experiment. The electrical detection pathway needed in an EDMR experiment consists of a high precision voltage source responsible for maintaining a certain bias voltage, a current amplifier that transforms the current flowing through the sample into a voltage signal and amplifies it and a lock-in amplifier which detects the EDMR signal and is also responsible for the field modulation characterized by the field modulation amplitude B_{mod} and frequency f_{mod} during the experiment. Besides this electrical detection pathway, the spectrometer consists of similar parts as the corresponding EPR setup and like in EPR the slope of the EDMR absorption signal is detected at any point of the spectrum due to the modulation principle as introduced in section 1.4 (see figure 2).
As for the EPR spectrometer, the resonant cavity is responsible for the conversion of the microwave power P_{MW} to the corresponding magnetic field strength B_1 and equation 1.51 applies. However, because the sample needs to be electrically contacted in an EDMR experiment the conversion efficiency may be somewhat lower as in the corresponding EPR experiment. To avoid major disturbances of the cavity tuning process, which may make a sample analysis impossible, the EDMR connection concept has to be carefully designed. In fact, the contacts introduced into the resonant cavity have to be thinner than the skin depth of the microwaves δ_{MW} for the used material.[54]

$$\delta_{\mathrm{MW}} = \sqrt{\frac{2\rho}{\omega_{\mathrm{MW}}\,\mu_0\,\mu_{\mathrm{r}}}} \tag{2.25}$$

Here, μ_0 and μ_{r} denote the magnetic vacuum permeability and the relative magnetic permeability of the material, respectively. The resistivity of the material is indicated by ρ and ω_{MW} is the angular frequency of the used microwave radiation. Using equation 2.25 the skin depth for gold contacts ($\rho_{\mathrm{Au,\,298\,K}} = 2.214 \times 10^{-8}\,\Omega\,\mathrm{m}$,[55] $\mu_{\mathrm{r,\,Au}} \approx 1$) in an X-band spectrometer operating at

9.42 GHz can for example be calculated to be $\delta_{\mathrm{MW,Au}} = 772\,\mathrm{nm}$.

3. Design and Implementation of a Benchtop EDMR System†

In the previous chapters we looked at the basics of both EPR and EDMR spectroscopy and introduced typical spectrometer concepts for both modes. Based on this theory we will now be concerned with the design and implementation of a compact EDMR setup based on a commercially available benchtop EPR spectrometer. At the beginning of this chapter, we will introduce the modifications that were necessary to implement an EDMR mode in an existing MS400 machine (Magnettech GmbH, Germany). This will also include the design of a special EMDR sample holder system suitable for quick, easy and precise sample change and positioning. Finally, the developed control software interface and EMDR Analysis Toolbox written in IGOR Pro will be presented.

3.1. Spectrometer Components and Modifications

In contrast to EPR, where the cavity-reflected microwave power gives rise to the detected signal, EDMR uses an electrical detection scheme to measure the spin-dependent currents as introduced in chapter 2. Since electric currents can be detected with very high accuracy, the electrical detection concept also leads to an increase in sensitivity over conventional EPR spectroscopy.[34] The EDMR setup introduced in this thesis is based on the commercially available benchtop EPR spectrometer MiniScope MS400 made by Magnettech GmbH (Berlin, Germany). Figure 7 illustrates the EDMR detection scheme as well as the necessary extensions made to this commercial machine in order to construct a benchtop EDMR spectrometer. In addition, one needs several new components, which will be described in the following.
For EDMR measurements, a stable and precise bias voltage V_{bias} has to be applied to the sample or device under test. To further investigate the sample by measuring its I/V characteristics, it is necessary to determine the current through the sample I_{sample}. Using a Keithley 2400 source measure unit (SMU), the sample's characteristics can be investigated very conveniently directly inside the spectrometer. Additionally, the determination of I_{sample} during an EDMR experiment opens up the possibility to set an offset current I_{offset} at the low-noise current preamplifier SR570 (Stanford Research) to compensate for the sample bias current, thus enabling sensitivity levels down to 1 pA/V. Furthermore, the SR570 preamplifier provides the ability to filter the input signal if desired, choosing from several different low-pass, high-pass and band-pass filters. As in conventional EPR spectroscopy, a signal modulation principle is beneficial to detect the rather small part of the total signal that is actually spin-dependent. In the EPR mode of the MS400 spectrometer, a fixed modulation frequency of 100 kHz is used for phase-sensitive detection. However, a lower modulation frequency is required for EDMR. Furthermore, both theory and experiment have shown a modulation frequency dependence for EDMR experiments.[56,57] It is therefore desirable to be able to freely select the modulation frequency over a wide range. For this purpose, an additional modulation amplifier for the frequency range 20 Hz – 20 kHz with suitable transformer, as well as a relay to switch between the EDMR and EPR mode, were installed inside the MS400 by Magnettech (cf. MS400 built-in EDMR extension in figure 7). Instead of the 100 kHz lock-in amplifier used in the EPR mode, an external dual phase lock-in amplifier

†This chapter has partially been taken from the peer-reviewed journal article published in advance: M. Eckardt, J. Behrends, D. Münter, W. Harneit, Compact electrically detected magnetic resonance setup, *AIP Adv.* **2015**, *5*, 047139.

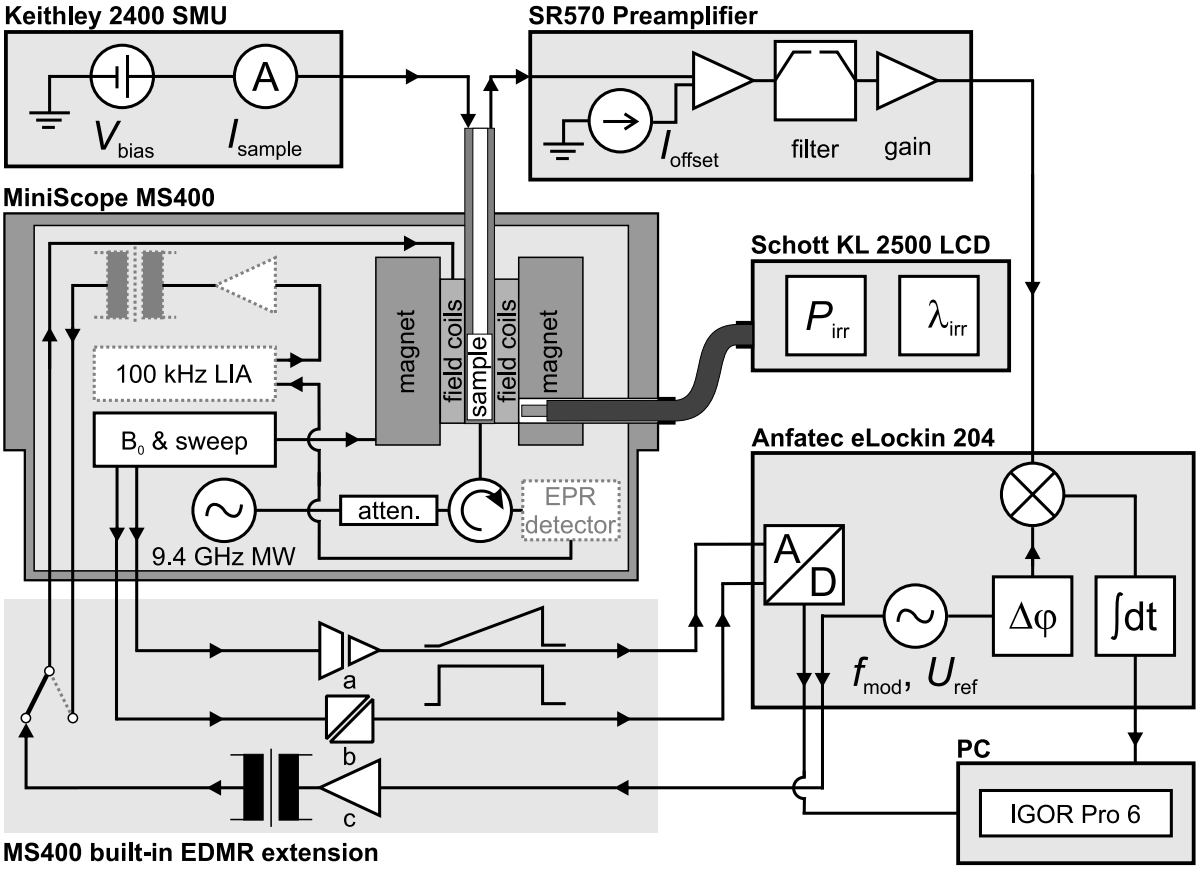

Fig. 7: Detection scheme and extensions for the EDMR setup. The sample is located inside the EPR resonance cavity and connected to a Keithley 2400 source measure unit (SMU) and a SR570 low-noise current preamplifier. The sample bias voltage V_{bias} is applied using the Keithley SMU which also measures the sample current I_{sample}. The SR570 current preamplifier is able to compensate for the sample's direct current via the offset current I_{offset}. Additionally, the SR570 offers several low-pass, high-pass and band-pass filters. Its variable gain can be set from 1 V/mA to 1 V/pA. The setup can operate in EPR or EDMR mode using either an internal fixed-frequency lock-in amplifier (LIA) at 100 kHz, the corresponding modulation amplifier and the microwave detector (dotted components), or the EDMR extension components, respectively. The newly modified B-field sweep generator creates a signal for the magnetic sweep ramp and a trigger signal. These signals are passed to the analog-to-digital converter of the lock-in amplifier (Anfatec eLockIn 204) via an isolation amplifier (a) and an optocoupler (b), respectively. In EDMR mode, the eLockIn reference sine generator output is used to drive the custom EDMR modulation amplifier (c) setting the desired modulation amplitude via the applied reference voltage amplitude U_{ref} at the chosen modulation frequency f_{mod}. All components are controlled via IGOR Pro 6, which also collects the x- and y-channel data, as well as the magnetic sweep ramp and the trigger signal from the eLockIn. Here, $\Delta\varphi$ is the phase shifter and $\int \mathrm{d}t$ symbolizes the time integration. The MS400 possesses a light port ending at the field modulation coils. This port holds an optical fiber with a diameter of 5 mm. A KL 2500 LCD halogen cold light source is used to control the amount of light P_{irr} illuminating the sample. The irradiation spectrum λ_{irr} can be changed using an appropriate filter.

with integrated reference signal generator covering the frequency range 20 Hz – 20 kHz is used in EDMR mode. Its reference output is used to drive the EDMR modulation amplifier setting the desired modulation amplitude B_{mod} via the amplitude of the applied reference voltage U_{ref} at the chosen modulation frequency f_{mod}. For synchronizing the EDMR measurement and detection, the generation of an analogue magnetic sweep ramp output, as well as a trigger signal was implemented in the B_0 & sweep generator of the MS400 by Magnettech. To enhance signal quality, the magnetic sweep ramp and the trigger signal are galvanically isolated via an isolation amplifier and an optocoupler, respectively. Both signals are fed into the analog-to-digital converter of the Anfatec eLockIn 204 and read out synchronously with the lock-in channel data containing the EDMR signal. Using the virtual instrument software architecture (VISA protocol) to address all setup components and the powerful and extensible scientific analysis capabilities of IGOR Pro 6 (WaveMetrics, Inc.), a highly customizable and freely accessible software interface for the EDMR setup was implemented, enabling all components to work seamlessly together. The details of this software interface are introduced together with the EMDR Analysis Toolbox in section 3.3.

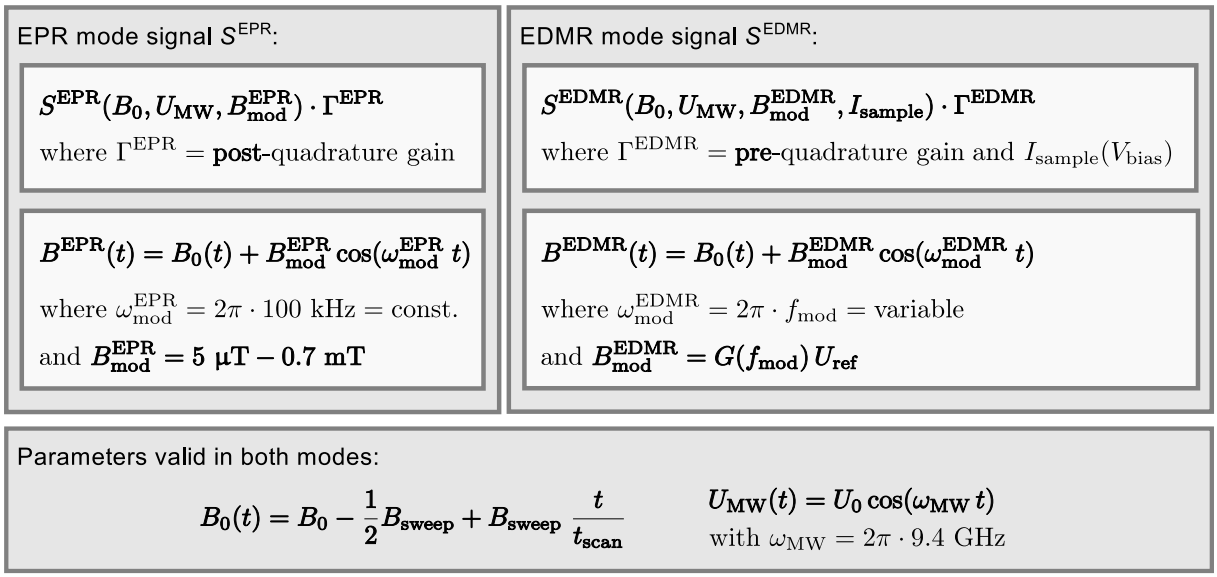

Fig. 8: Comparison between EPR and EDMR mode signal generation. The parameters are chosen in analogy to figure 7. Note the difference in gain Γ, as well as in the modulation amplitude B_{mod} for the different modes. The magnetic field B_0, as well as the microwave radiation U_{MW} are equal in both modes. For EDMR the relation $G(f_{\mathrm{mod}})$ has to be investigated experimentally to determine the modulation amplitude. See text for details.

Because the designed benchtop setup allows for EPR as well as EDMR measurements, it is useful to briefly summarize the commons and differences of both detection modes with respect to the signal generation at this point. Figure 8 shows a comparison between the signal generation in EPR (S^{EPR}) and EDMR (S^{EDMR}) mode. While the parameters for the magnetic field ramp $B_0(t)$ (with sweep width B_{sweep} and scan time t_{scan}), as well as the microwaves U_{MW} (with amplitude U_0 adjustable by means of the attenuator) remain unchanged in both measuring modes, the applied gain Γ and field modulation amplitude B_{mod} do not. Here, a key point is the different signal gain, which is applied post-quadrature as a linear gain in case of EPR but pre-quadrature by the current preamplifier in the EDMR mode. Beside the different gains, a sample bias voltage V_{bias} and corresponding bias current I_{sample} are present in EDMR mode as new parameters (cf.

figure 7). However, the most important aspect is the difference in the field modulation. For EPR there is only one modulation frequency (100 kHz) available in the MS400 tabletop spectrometer. The modulation system is resonantly tuned and optimized for that frequency, resulting in possible field modulation amplitudes of 5 µT to 0.7 mT. In contrast, the modulation frequency can be freely selected between 20 Hz and 20 kHz in the EDMR mode. Thus, the obtainable field modulation amplitude $B_{\mathrm{mod}}^{\mathrm{EDMR}}$ is a function of the modulation frequency f_{mod} and the applied reference voltage amplitude U_{ref}. To be able to select the desired field modulation amplitude in an EDMR experiment the modulation frequency dependency $G(f_{\mathrm{mod}})$ has to be determined during the calibration procedure as described in chapter 4, section 4.2.

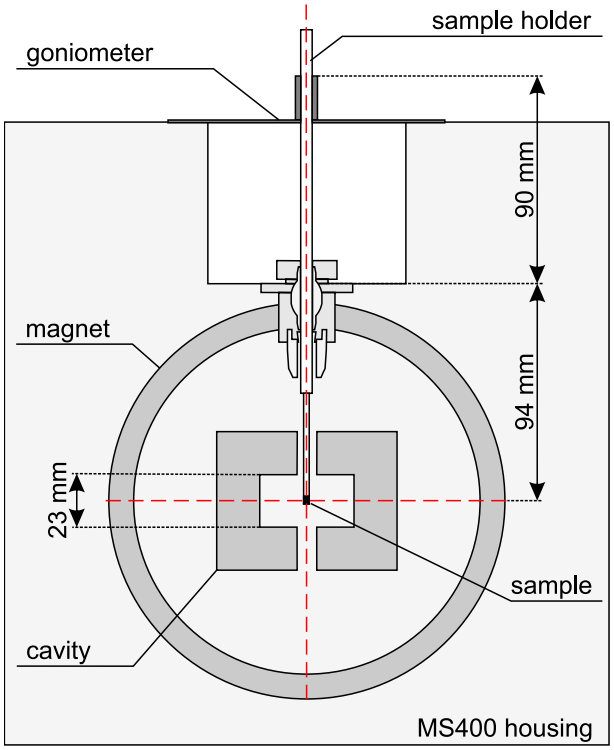

Fig. 9: EDMR sample positioning. The optimum sample position is located at the center of the resonant cavity (dotted red lines). Using the sample holder system introduced in section 3.2 in combination with the accompanying goniometer, the sample can precisely be adjusted using the distances given. [58]

As for any magnetic resonance spectrometer, the EDMR sample position has to be carefully controlled in order to get reproducible results. The optimum sample position is located at the center of the resonant cavity where the microwave magentic field $\boldsymbol{B_1}$ is maximum and at the same time the microwave electric field component has its minimum. Knowledge about the distance between some fix points is necessary to hit this spot. Figure 9 shows the distance between the fix points for the MS400, based on informations given by the manufacturer. [58] The sample can be fixed using a goniometer that at the same time allows for setting a specific angle between the sample and the light port of the spectrometer.

To quantitatively compare spectra obtained with different EDMR setups, the microwave conversion factor, which depends on the cavity's fill factor, quality factor and geometry must be known. For the rectangular TE_{102} resonator used in the Miniscope MS400 the quality factor of the empty cavity is specified as $Q = \nu/\Delta\nu \approx 6000$ where ν is the resonant frequency of the cavity and $\Delta\nu$ is the width at half height of the resonance. The corresponding conversion factor is then

$$c = \frac{B_1}{\sqrt{P_{\mathrm{MW}}}} = 0.20(2)\,\mathrm{mT}/\sqrt{\mathrm{W}} \qquad (3.1)$$

with B_1 as the amplitude of the microwave magnetic field and P_{MW} as the microwave power set for the experiment. Thus, the conversion factor is a measure for the efficiency of the power conversion inside the resonant cavity of the machine.

3.2. Sample Holder System

As mentioned above, a precise sample positioning is mandatory for reproducible EDMR results. Furthermore, rapid sample exchange can be beneficial if measurement series on different samples

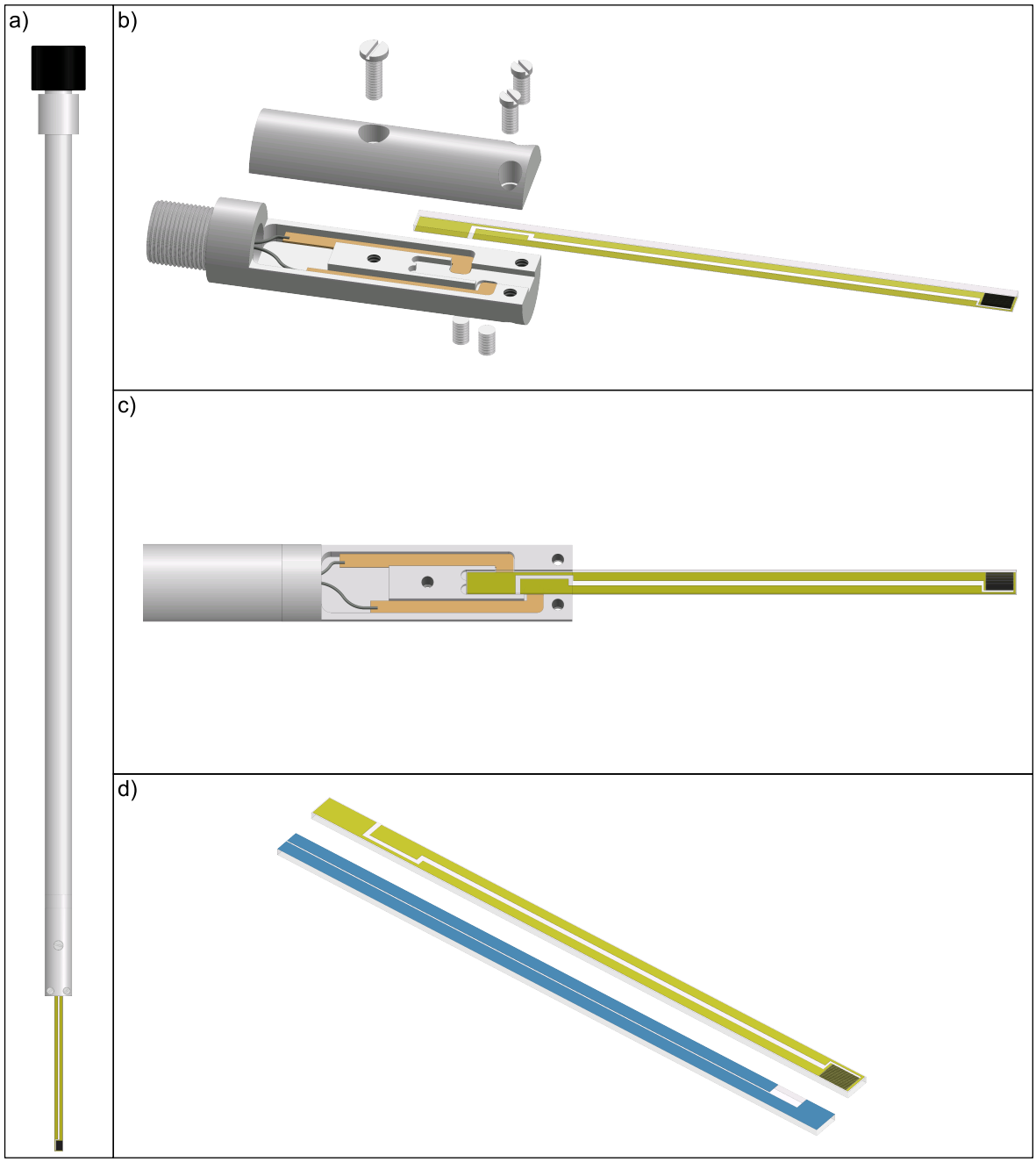

Fig. 10: Design of the EDMR sample holder. a) Overview of the assembled sample holder made from acrylic glass, consisting of (top to bottom): a thumbscrew for cable fixation (black), a hollow rod for sample positioning and a head for contacting and holding the sample substrate. b) Explosion drawing of the sample holder head. The assembling is done by the three screws shown on top together with the head's lid. The two grub screws are used to contact the sample substrate. c) Top view of the sample holder head showing the contact scheme and substrate positioning. d) Different sample substrates compatible with the sample holder system. Both types are based on coated glass substrates. The gold structure is used to contact organic microcrystals (see part II), the blue structure is made from indium tin oxide (ITO) and useful for organic solar cells (see part III).

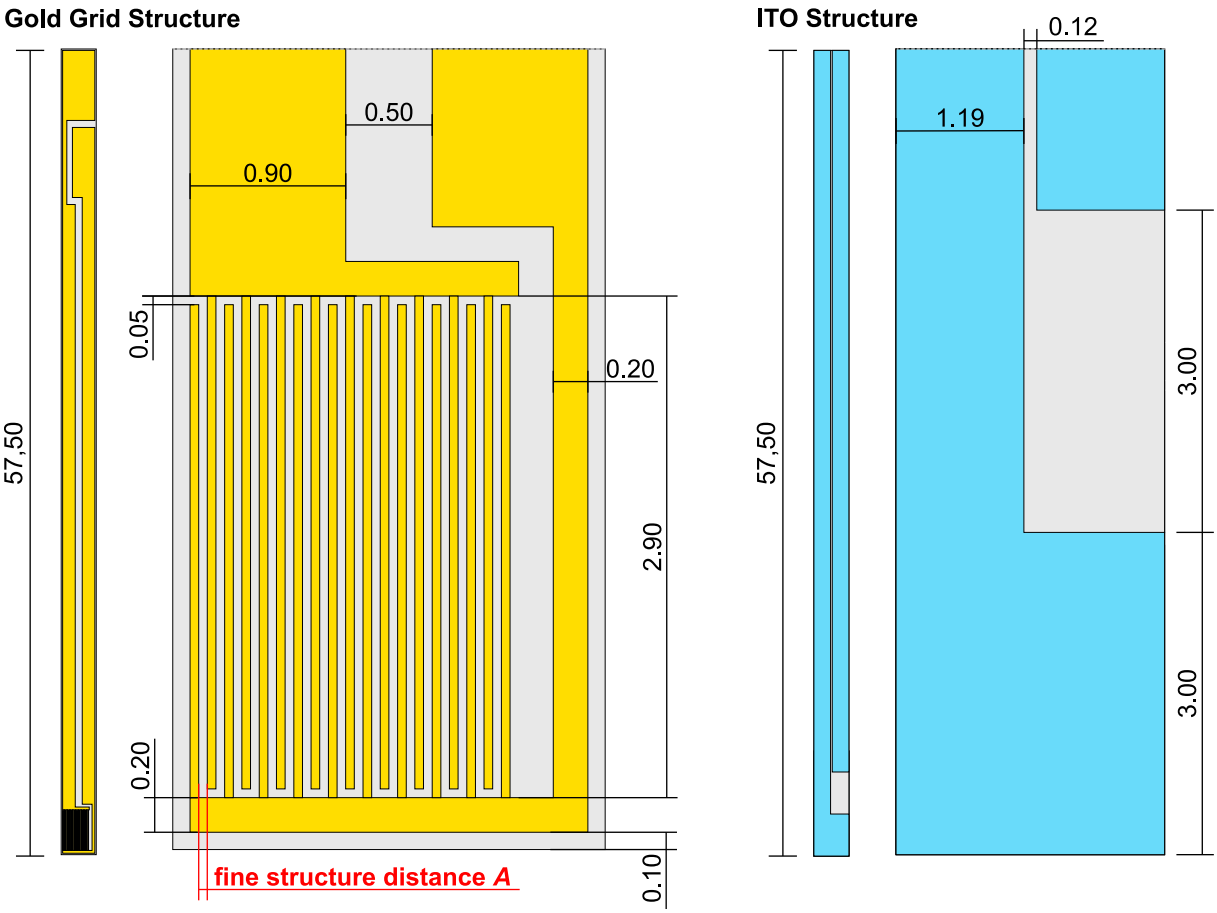

Fig. 11: Overview and details of the designed EDMR substrates (all measurements given in millimeters). Blue areas symbolize ITO coated glass, yellow areas indicate a chromium/gold coating. The glass itself is shown in gray. Both substrate types have outer dimensions of 57.50(5) mm × 2.50(5) mm. Details about the used material types, coatings and processing methods are given in Table 1. The gold grid structure possesses a fine structure distance A that could be varied during substrate processing. Structures with $A = 1\,\mu m$, $2\,\mu m$, $3\,\mu m$, $5\,\mu m$ and $10\,\mu m$ were manufactured at ZMN - Zentrum für Mikro- und Nanotechnologie (Technische Universität Ilmenau, Germany).

are to be performed. Various sample types, like organic microcrystals and organic solar cells, necessitate different substrates and a specific angle to the light source. To fulfill these requirements a special sample holder system completely made from acrylic glass was designed for the benchtop EDMR spectrometer. Figure 10 shows the design based on a hollow rod with a thumbscrew for cable fixation and a removable head that holds the sample substrate and contacts it. The head itself consist of a removable lid and the base holding the contacts, which are made from pure gold sheet. Shielded cables are used to connect the contacts to the Keithley 2400 SMU and the SR570 preamplifier (cf. figure 7). As can be seen from figure 9, the only part of the sample holder system that enters the resonant cavity is the EDMR sample substrate. Thus, the conductive layer of the substrates must not be thicker than the skin depth of the microwaves for the material used, as introduced in equation 2.25.

Tab. 1: Material types and processing methods for EDMR substrates. Both glass types where purchased from Präzisions Glas & Optik GmbH, Germany and processed by ZMN - Zentrum für Mikro- und Nanotechnologie at Technische Universität Ilmenau, Germany. The glass substrates had a thickness of 0.70(5) mm in both cases and the final dimensions: 57.50(5) mm × 2.50(5) mm.

Substrat Type	Glass Type	Coating	Processing Method
gold grid	borosilicate glas	none	coating: 10 nm Cr + 120 nm Au
ITO structure	low iron float glass	100 nm ITO	structure etching of ITO layer

Figure 10 d) shows the two fundamentally different substrate types that where used in this thesis: gold grids with varying fine structure and an ITO structure suitable for the preparation of organic solar cells. Details about the dimensions and the fine structure for both substrate types are shown in figure 11. Table 1 gives an overview of the used glass types, coatings and processing methods. The glass substrates were purchased from PGO (Präzisions Glas & Optik GmbH, Germany) and fully processed by ZMN (Zentrum für Mikro- und Nanotechnologie at Technische Universität Ilmenau, Germany). The ITO layer was specified by PGO to have a surface resistivity of $R \leq 20\,\Omega/\mathrm{sq}$.

3.3. Software Interface and EDMR Analysis Toolbox

Using the IGOR Programming Language a highly customizable software interface for the EDMR setup was implemented in IGOR Pro 6. Furthermore, IGOR Pro 6 was used to develop the EDMR Analysis Toolbox software package, which is used to analyze all EDMR spectra throughout this thesis. Both tools will be introduced briefly in the following sections.

3.3.1. EDMR Control Center

The EDMR Control Center is the software package that controls all EDMR equipment. Screenshots from this application can be found in the appendix on page 132 and 133 (figures A1 and A2). Due to its modular concept, some terms and expressions used in the control software differ from the ones introduced in section 3.1. Thus, were useful both designations are given. The EDMR Control Center consists of several stand-alone modules:

- **Keithley 2400 SourceMeter Control**
  This module is used to perform voltage and current sweeps in order to investigate the sample's current-voltage characteristics. During an EDMR experiment it is used to apply a voltage bias V_{bias} to the sample and log the corresponding sample current I_{sample}. This information can then be used to set the input offset current for the SR570 preamplifier, which makes working at a high sensitivity level possible. A compliance limit can be set for both sweep and bias mode to prevent damaging the sample due to too high a current. The module generates two graph displays: a current-voltage curve after performing a sweep (*KeithleyIVCurve*) and a life sample current display if value logging is enabled (*BiasGraph*). Furthermore, sweep and bias log results can be saved (and loaded) as *.ivs and *.ivb files, respectively.

- **Magnettech MS400**
  The Magnettech MS400 module is used to control the MiniScope MS400 in both EDMR and EPR mode. It is designed to act as a client for the MS400 instrument server (MiniScopeCtrl.exe) written by J. Tilgner (Magnettech GmbH, Berlin, Germany). Therefore, for this module to work properly the MS400 server has to be started beforehand, which is done by the module itself. Afterwards, all relevant parameters like the central field B_0, the sweep width $\Delta B = B_{\text{sweep}}$, the microwave attenuation, the scan time and the number of scans can be selected and transmitted to the instrument. In EPR mode, the modulation amplitude B_{mod} can directly be set in the MS400 module, while in EDMR mode this is conrolled via the Anfatec eLockin 204 setup's $U_{\text{ac}} = U_{\text{ref}}$ value and only displayed here. The linear gain is available as an additional parameter in EPR mode. In EDMR mode, this panel acts as the main control used to start the EDMR experiment as well as save and load results as *.pxp files.

- **FC400**
  The FC400 module is a rather small part of the EDMR Control Center. It is used to record the microwave frequency ν_{MW} during an EDMR experiment, which is measured by the frequency counter unit that accompanies the MS400 spectrometer. If used as a stand-alone tool the microwave frequency can be read out and saved based on a user selected time interval or on demand.

- **SR570 Preamplifier**
  This module is used to control the parameters used during signal conversion and amplification. The SR570 converts the current signal coming from the sample into a voltage signal that can be processed by the Anfatec eLockin 204. Using the sample current I_{sample} measured by the Keithley 2400 Source Meter the offset level can be set to compensate for this current. This way, the SR570 can be used in a more sensitive working range without overloading the circuits. Thus, after setting the desired bias voltage for the EDMR sample under investigation, the input offset current for the SR570 should be set either manually or automatically using the I_{sample} value supplied by the Keithley 2400. Only then should the sensitivity range and gain mode be selected at the software interface. Furthermore, the SR570 Preamplifier module can be used to select from a list of various low-pass, high-pass and band-pass filters.

- **Anfatec eLockin 204 setup**
  The *Anfatec eLockin 204 setup* panel is used to control the lock-in settings for signal detection as well as the field modulation during an EDMR experiment. The latter is set by means of the modulation frequency $f = f_{\text{mod}}$ and the reference output voltage $U_{\text{ac}} = U_{\text{ref}}$ that is converted to a B_{mod} value based on the calibration of the field modulation amplitude (see chapter 4, section 4.2) and displayed on the *Magnettech MS400* panel. The signal detection is controlled by the input range and coupling settings as well as the slope of the filter. The harmonic used for detection can be selected together with the corresponding time constant and reference phase shift. Additionally, using the second lock-in of the Anfatec eLockin 204 one can use two different harmonics for detection at the same time. The display and readout properties of the panel govern what channels are recorded and displayed in the corresponding graph (*eLockin204 Scope*) and details about this can be set at the *Anfatec eLockin 204 scope* panel.

The introduced modules can be called individually using the *Instruments* menu of the EDMR

Control Center software or all together using the *Open All Instruments* option. During an EDMR experiment, the progress can be observed using the *eLockin204 Scope* graph window.
After all EDMR scans have finished, the software averages the runs and displays the x- and y-channel data in a graph window (*EDMRGraph*). This window has some additional features to analyze the obtained spectrum without altering the raw data. First of all, the so called *Auto Phase* function tries to find the reference phase shift necessary to transfer all data into one single channel. To achieve this it maximizes the signal content in the x-channel. After this operation is completed it gives the new reference phase offset taking into account the actual value used during the measurement. Furthermore, the obtained data can be resampled using the *(Re)Average* button together with a reduced point number or filtered using a fast Fourier transform (FFT) approach.
The saved EDMR *.pxp file contains the x- and y-channel raw data for every scan together with the corresponding average and the used magnetic field ramp, as well as the microwave frequency and I_{sample} values. Additionally, the used instrument parameters for the above introduced modules are stored inside the experiment file together with an operator note. A screenshot of such an EDMR data file can be found in the appendix on page 134, figure A3.
The *Data Browser* window gives an overview over both package parameters for the individual modules and obtained data. All user communication is done using the history output and console window shown at the bottom of figure A2. Here, all standard IGOR Pro commands are directly available as well.

3.3.2. EDMR Analysis Toolbox

The EDMR Analysis Toolbox is a software package capable of deconvolute and analyze EDMR spectra. It was developed using the programming capabilities of IGOR Pro and can thus be loaded as a procedure in every IGOR Pro instance. The package adds the menu path *Macros* → *EDMR Analysis* with the following entries to the IGOR Pro menu bar:

- **Analysis Panel (Alt + F2)**
  Opens the *EDMR Signal Analysis* panel used to control the main part of the software.
- **Reset Analysis (Alt + F3)**
  Closes all program windows and resets the *EDMR Signal Analysis panel* to initial values.
- **Export Results (Alt + F4)**
  Writes the actual fit results into a semicolon-separated text file (*.csv) for external use.
- **Touch Up Version (Alt + F5)**
  Updates the results obtained with previous software versions to the latest patch level.
- **Load EDMR Series (Alt + F6)**
  Loads a series of EDMR measurements and averages their x- and y-channel data.

The software's main part is controlled via the *EDMR Signal Analysis* panel shown in figure 12. Its functionality will be briefly described in the following.
After opening an existing EDMR data file and loading the analysis panel using the menu bar, the *Folder* and *Wave to fit* controls are used to select the raw data that should be analyzed, e.g. the x-channel average. The software gets the microwave frequency used during the measurement from the parameters stored in the active experiment file (this value can be overridden by the user). The corresponding manganese-standard value (see chapter 4, section 4.1) can be loaded

or entered manually. The two controls labeled *B-Field/T* and *g-Factor* next to this act as a built-in calculator to convert between magnetic field values and corresponding g-factors in both directions. Using the *Add g-factor axis* button every active EPR and EDMR graph can be equipped with a g-factor top axis taking the manganese calibration value into account.

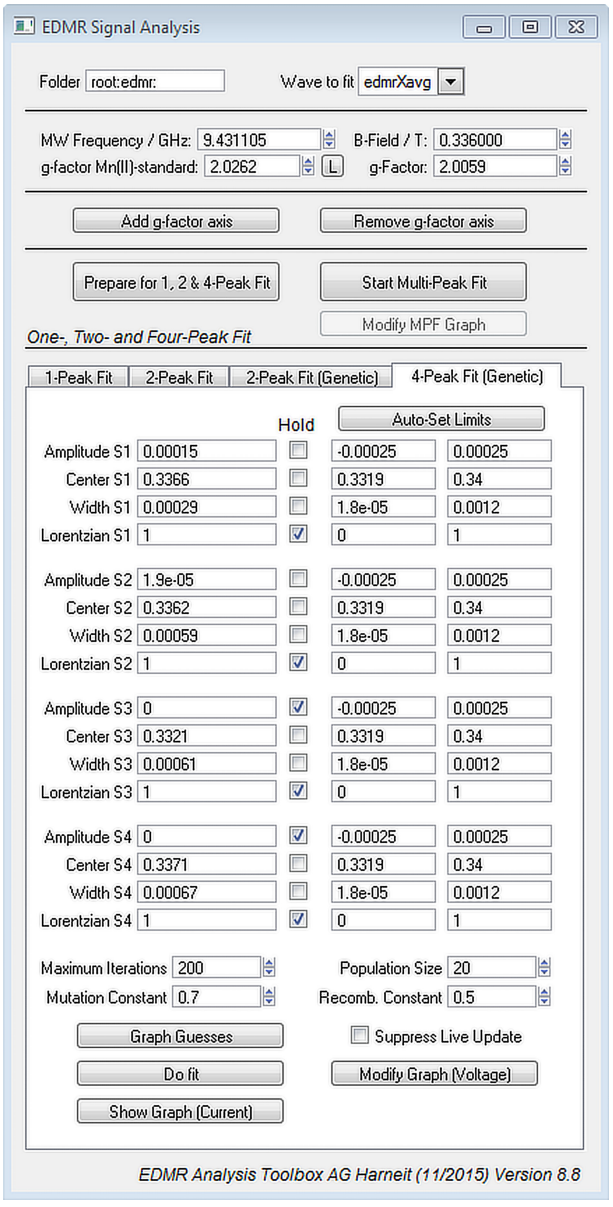

Fig. 12: Screenshot of the main panel of the developed EDMR Analysis Toolbox. Its functionality is explained in the text.

The EDMR Analysis Toolbox provides two fundamentally different methods for signal fitting. The first approach is available through the *Start Multi-Peak Fit* button. It simply calls the IGOR Pro built-in multi-peak fit routine, which acts well on absorption signals but is not readily able to fit in dispersion mode, i.e. work with the "derivative" line shapes typical for EPR and EDMR spectroscopy. Thus, the EDMR Analysis Toolbox integrates the raw data first, before passing it on to IGOR's multi-peak fit routine. The corresponding *Modify MPF Graph* button can be used to add a g-factor axis, as well as label the resulting multi-peak fit graph. The second method, on the other hand, is designed to work well on typical EPR and EDMR signals, i.e. do fits in dispersion mode. This approach is very useful for both EPR and EDMR spectroscopy and was applied to all samples throughout this thesis. Furthermore, the EDMR Analysis Toolbox is able to directly calculate all relevant spectroscopic results, like linewidth and g-factor automatically using this method. Thus, it will be described in more detail in the remainder of this section.

Prior to the actual analysis process, an offset correction has to be performed and the graphical user interface needs to be extended by a fit preview window. These operations are done using the *Prepare for 1, 2 & 4-Peak Fit* button. For the actual fitting process, the user can choose between a one-, two- and four-peak fit and whether a genetic algorithm is to be used. Setting the amplitude of a peak to zero and select to hold this parameter, the user can reduce the number of signal components used for the fit process. Thus, the four tabs available at the *EDMR Signal Analysis* panel (see figure 12) are very similar and the four-peak fit tab can in principle be used for every task. However, in case only a one- or two-peak fit should be performed it is somewhat more convenient to make use of the preconfigured tabs.

The EDMR Analysis Toolbox provides two different fit algorithms, the standard Levenberg-

Marquardt method and the Genetic Optimization as an alternative. The Levenberg-Marquardt algorithm is often used to solve non-linear least squares problems,[59] e.g. least squares curve fitting. To find a global solution for a problem this algorithm, however, needs to have good starting parameters otherwise it will fall into a local minimum or even fail. To provide a more robust method of fitting EPR and EDMR spectra the genetic curve fit procedure (GenCurveFit XOP) introduced to IGOR Pro by Andrew Nelson and the Australian Nuclear Science and Technology Organisation was implemented.[60] The GenCurveFit XOP enables IGOR Pro to use an evolutionary algorithm called "Differential Evolution" introduced by Storn & Price to curvefit data.[61,62] In contrast to the Levenberg-Marquardt algorithm this method is able to find global best fits even if the starting guesses for the fit are poor. The Differential Evolution algorithm starts with an initial population of randomly generated parameter vectors and attempts to find the best solution for the problem by a repeated cycle of mutation, recombination and selection. Here, mutation means exploring new points in the parameter space by making small random changes to the parameters, while recombination means exploiting the information discovered so far by combining two parameter vectors from the previous generation.[63] Hence, the user has to specify the number of *Maximum Iterations* and empirically select the *Population Size*, *Mutation Constant* and *Recombination Constant* for all tabs on the main panel that involve the genetic approach. If the number of iteration steps was insufficient to find a proper solution the EDMR Analysis Toolbox will create a warning message. Furthermore, the processor load on the used machine can be reduced by suppressing live updates during the fit process by selecting the corresponding option on the *EDMR Signal Analysis* panel. Supplying the algorithm with a reasonable parameter space is mandatory for the genetic optimization and the user can do this by using the *Auto-Set Limits* button, which suggests suitable values by analyzing the raw data given, or by manually entering the low and high boundaries.
Independent from the algorithm used the user has to provide an initial guess for the fit. The EDMR Analysis Toolbox uses derivatives of pseudo-Voigt functions (linear combination of Gauss and Lorentz shape) for each signal component. Hence, the guess consists of a value for the amplitude Θ (from zero), the center B_{L}, the peak-to-peak linewidth ΔB_{pp} and the weight of the Lorentzian ϵ. One or more of these parameters can be hold during the fit. As mentioned earlier, setting the amplitude for a peak to zero and selecting hold will disable it and thus reduce the number of available signal components for the fit. The total fit function for m signal components used by the EDMR Analysis Toolbox is given by

$$Y_{\mathrm{Fit}} = \sum_{n=1}^{m} \left[\epsilon_n \, Y_{\mathrm{dLor},n} + (1-\epsilon_n) \, Y_{\mathrm{dGauss},n}\right] \tag{3.2}$$

with $Y_{\mathrm{dLor},n}$ as the Lorentzian derivatives given by

$$Y_{\mathrm{dLor},n} = -2\Theta_n \cdot \frac{B - B_{\mathrm{L},n}}{\Delta B_{\mathrm{pp},n}} \cdot \frac{16}{\left(3 + \frac{4\left(B-B_{\mathrm{L},n}\right)^2}{\Delta B_{\mathrm{pp},n}^2}\right)^2} \tag{3.3}$$

and $Y_{\mathrm{dGauss},n}$ as the Gaussian derivatives given by

$$Y_{\mathrm{dGauss},n} = -2\Theta_n \cdot \frac{B - B_{\mathrm{L},n}}{\Delta B_{\mathrm{pp},n}} \cdot \exp\left(\frac{1}{2} - \frac{2\left(B - B_{\mathrm{L},n}\right)^2}{\Delta B_{\mathrm{pp},n}^2}\right) \tag{3.4}$$

with equal line width $\Delta B_{\mathrm{pp},n}$ for the Gaussian and Lorentzian fraction of the total signal Y_{Fit}. The *Graph Guesses* button will add graphical representations of the guesses to the fit window,

afterwards the fit procedure can be started using the *Do fit* button. After the fit procedure finished successfully, the obtained spectroscopic parameters and a g-factor axis can automatically be added to the graph window by pressing the button *Modify Graph (Voltage)*. The results from the fitting procedure are evaluated "per signal component". While the peak-to-peak linewidth of a component, ΔB_{pp}, is directly obtained from the fit as a parameter, the g-factor has to be calculated. Applying equation 1.7, the g-factor for a component is determined by

$$g = \frac{h\,\nu_{\mathrm{MW}}}{\mu_{\mathrm{B}}\,B_{\mathrm{L}}} \cdot K \tag{3.5}$$

with B_{L} as the center of the absorption (cf. figure 2) and ν_{MW} as the corresponding microwave frequency. The factor K is a correction taking the manganese g-factor calibration into account (see chapter 4, section 4.1, equation 4.1). The EDMR Analysis Toolbox is also capable of providing a figure of merit by calculating the SNR for the total signal. For this, the noise is determined as the σ parameter of a gaussian fit to a histogram of the fit residuum. It is important to point out that the software reports the 1σ-noise, thus omitting noise spikes that lie outside of a 68.3 % interval of the noise distribution. Based on this value, the 2σ-noise was calculated and used in this thesis, taking into account the 95.5 % interval of the noise distribution. Additionally, the software calculates the ratio between the noise area and the signal area and reports this as "area SNR". However, this value is not very meaningful and thus never used in this thesis.
EDMR spectroscopy not only allows for the determination of spectroscopic parameters like linewidth and g-factor, but is also able to quantify the spin-dependent currents flowing through the sample. The quantification process is started by pressing the button *Show Graph (Current)*. First, the software calculates the used EDMR gain

$$\Gamma^{\mathrm{EDMR}} = \frac{\Gamma^{\mathrm{PA}}}{B_{\mathrm{mod}}} \tag{3.6}$$

where Γ^{PA} is the sensitivity (inverse gain) set at the SR570 current preamplifier and B_{mod} is the used magnetic field modulation amplitude. With this, the EDMR raw data recorded in voltage units can be converted as shown in equation 3.7.

$$\frac{Y^{\mathrm{EDMR}}}{\mathrm{A\,T^{-1}}} = \frac{Y^{\mathrm{EDMR}}_{\mathrm{raw}}}{\mathrm{V}} \cdot \frac{\Gamma^{\mathrm{EDMR}}}{\mathrm{A\,V^{-1}\,T^{-1}}} \tag{3.7}$$

Furthermore, the software uses Γ^{EDMR} to calculate and report the amplitude obtained from the fit as peak-to-peak value ($2\Lambda_n$, see equation 3.2 - 3.4) for each signal component together with the peak-to-peak amplitude of Y_{Fit} ("total-signal amplitude") and the noise level (based on the 1σ value from the SNR determination, see above). After the conversion of $Y^{\mathrm{EDMR}}_{\mathrm{raw}}$ is done, the software integrates the EDMR spectrum with respect to the magnetic field to obtain S^{EDMR} (cf. figure 2).

$$S^{\mathrm{EDMR}} = \int_{B_{\mathrm{start}}}^{B_{\mathrm{end}}} Y^{\mathrm{EDMR}}\,\mathrm{d}B \tag{3.8}$$

With the integration limits $B_{\mathrm{start}} = B_0 - \frac{1}{2}B_{\mathrm{sweep}}$ and $B_{\mathrm{end}} = B_0 + \frac{1}{2}B_{\mathrm{sweep}}$. The amplitude of S^{EDMR} is determined and reported by the EDMR Analysis Toolbox for every signal component individually. This value is called "spin-dependent EDMR current" and denoted ΔI^{EDMR} throughout this thesis. Using the average of the sample current I_{sample}, the EDMR effect

$$\xi^{\mathrm{EDMR}}_{\mathrm{sd}} = \frac{\Delta I^{\mathrm{EDMR}}}{\overline{I_{\mathrm{sample}}}} \tag{3.9}$$

is calculated and reported by the software. The quality of this value of course depends on the stability of the sample current during the measurement. However, for most samples investigated in this thesis the current was pretty stable and $\xi_{\mathrm{sd}}^{\mathrm{EDMR}}$ could be determined with sufficient precision. For samples were this was not the case, the calculation was done manually using $I_{\mathrm{sample}}(B_{\mathrm{L}})$ in equation 3.9. In some situations, e.g. if the linewidth of a signal component changes during experiments, the interpretation of a series of measurements is best done using the area under the component instead of its amplitude. In EDMR, a double integration needs to be done to determine the peak area, i.e. S^{EDMR} has to be integrated again using the same integration limits as in equation 3.8.

$$A^{\mathrm{EDMR}} = \int_{B_{\mathrm{start}}}^{B_{\mathrm{end}}} S^{\mathrm{EDMR}}\,\mathrm{d}B \tag{3.10}$$

The EDMR Analysis Toolbox determines and reports the EDMR double integral (A^{EDMR}) for each signal component individually. Additionally, the double integral for the EDMR raw data and for the 'total fit' are reported.
A visual impression of the EDMR Analysis Toolbox software during the fit and analysis process of a sample consisting of the *EDMR Signal Analysis* panel, the EDMR raw data (*EDMR Graph*), the fit preview window including the residuum (*EDMRanaGraph*), the results summary window (*FitResults*) and the final EDMR graph window (*EDMRanaGraphCurrent*) can be found in the appendix on page 135 in figure A4.
If the EDMR signal can not be transferred to only one channel (i.e. the x-channel) by shifting the reference phase, it is desirable to be able to fit both x- and y-channel data in one single analysis file. This can also be beneficial if a series of measurements is to performed at a fixed reference phase shift, while the distribution of the signal components may change during the series. The EDMR Analysis Toolbox is able to perform as many fits in a single experiment file as desired. To start a new fit data set in an experiment file, the user simply needs to close the *EDMR Signal Analysis* panel and re-open it using either the menu or the shortcut Alt+F2. The software will start saving all fit parameters and results in a new data set and label graph and result windows accordingly. An example for a fit of both x- and y-channel data and their resulting graphs and separate result windows can be found in the appendix on page 136 in figure A5.

4. Calibration of the Benchtop EDMR System[†]

In the preceding chapter the design and implementation of a compact EDMR setup based on a commercially available benchtop EPR spectrometer was described. Furthermore, the developed control software interface and EMDR Analysis Toolbox were introduced in some detail. However, for the EDMR setup to produce reproducible and correct data some components need to be characterized and calibrated. In this chapter, the necessary procedures for the calibration of the g-factor, the field sweep generator and the field modulation amplitude will be discussed. The chapter will finish with a description of the calibration procedure for the light source intensity of the used Schott KL 2500 LCD.

[†]This chapter has partially been taken from the peer-reviewed journal article published in advance: M. Eckardt, J. Behrends, D. Münter, W. Harneit, Compact electrically detected magnetic resonance setup, *AIP Adv.* **2015**, *5*, 047139.

4.1. Calibration of the *g*-Factor and the Field Sweep Generator

After implementing the EDMR modifications (see chapter 3, section 3.1) the $\boldsymbol{B}$-field sweep generator of the MiniScope MS400 needs to be recalibrated in order to obtain accurate results.

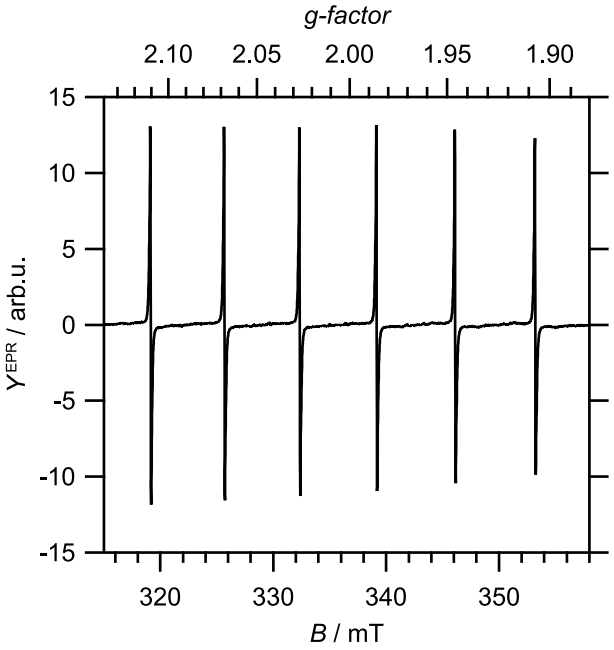

Fig. 13: EPR spectrum of the used manganese standard ($^{55}Mn^{2+}$ in ZnS). Possessing a nuclear spin of $I = 5/2$, the powder spectrum consists of six hyperfine lines. The g-factor for this standard is certified to be $g = 2.0024(3)$, see text for further details.

For each mode, the instrument settings and calibration data is stored in a separate configuration file (EDMR mode: *MiniScopeCtrl.ini*, EPR mode: *miniscope.ini*). However, the calibration data for the $\boldsymbol{B}$-field sweep generator is identical in both versions and can be adjusted using the fifth parameter of the *Middle* (g-factor) and *Range* (hyperfine line distance) value in the *Polynom* section.

To calibrate the MS400, a certified managnese EPR standard (Magnettech GmbH, Berlin, Germany) with well-known spectroscopic properties was used. The powder sample consists of $^{55}Mn^{2+}$ ions with electron configuration $3d^5$ and a ^6S ground state in zinc sulfide (ZnS) crystals. The natural abundance of the manganese isotope ^{55}Mn is 100 % and it possesses a nuclear spin of $I = 5/2$. Thus, its EPR powder spectrum consists of six hyperfine lines as shown in figure 13. The g-factor for this sample is certified to be $g = 2.0024(3)$. However, for the calibration process the third hyperfine line with apparent $g = 2.0267(2)$ was used due to the ease of determination. Besides this, the peak-to-peak distances between the six hyperfine lines and the peak-to-peak linewidth of the standard were determined.

The adjustment of the $\boldsymbol{B}$-field sweep generator was done by comparing the experimentally obtained values for the manganese standard with the ones given on the accompanying certificate (see table 2) and performing a linear readjustment of the old parameters in the configuration files. As a result of this calibration procedure, all spectral parameters of the standard were found to be within the specifications given by the manufacturer.

While the hyperfine distances and the peak-to-peak linewidth normally only change if the spectrometer hardware was altered or serviced, the g-factor (i.e. the magnetic field accuracy) changes somewhat with time. Thus, a recalibration of the g-factor has to be performed on a regularly basis. In principle, the above introduced calibration procedure can be used to adjust the magnetic field accuracy in the forefront of every EPR or EDMR measurement. However, since the g-factor depends linearly on the magnitude of the resonance field (see equation 1.7), a correction factor K can be used to compensate for changes in the magnetic field accuracy (see equation 3.5). Hence, an EPR spectrum covering only the third hyperfine line of the manganese standard was recorded after each experimental series (usually once a day). This was then used during the

Tab. 2: Spectral properties of the certified manganese standard ($^{55}Mn^{2+}$ in ZnS, Magnettech GmbH, Berlin, Germany). The values given are taken from the certificate that accompanied the standard. The MiniScope MS400 was recalibrated after implementing the EDMR modifications using these.

Apparent *g*-factor	**Hyperfine Lines No.**	**Certified Distance / mT**
3rd hyperfine line: 2.0267(2)	1 ↔ 2	6.53
	2 ↔ 3	6.67
Peak-to-Peak Linewidth	3 ↔ 4	6.81
0.08 mT	4 ↔ 5	6.95
	5 ↔ 6	7.09

analysis of the actual experiment to calculate K and compensate for the changes.

$$K = \frac{g_{\mathrm{Mn^{2+},\ 3^{rd}\ hfl,\ certified\ value}}}{g_{\mathrm{Mn^{2+},\ 3^{rd}\ hfl,\ measured}}} \tag{4.1}$$

This process is fully integrated into the *EDMR Signal Analysis* panel shown in figure 12. The button labeled L is used to load the EPR spectrum of the third hyperfine line of the manganese standard, calculate K and display the determined value for $g_{\mathrm{Mn^{2+},\ 3^{rd}\ hfl,\ measured}}$.

4.2. Calibration of the Field Modulation Amplitude

As mentioned in chapter 3, section 3.1 (see figure 8) the field modulation amplitude B_{mod} for the EDMR mode depends on the applied modulation voltage amplitude U_{ref} and the transfer characteristics of the used modulation transformer expressed as $G(f_{\mathrm{mod}})$.

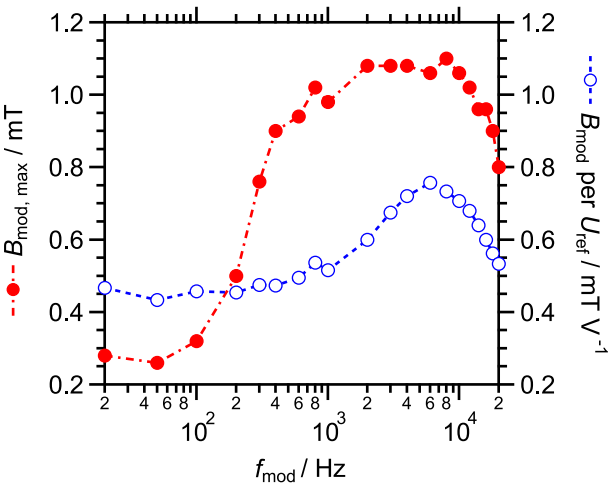

Fig. 14: Characterization of $G(f_{\mathrm{mod}})$ for EDMR mode: Maximum field modulation amplitude $B_{\mathrm{mod,\ max}}$ and calibration factor $B_{\mathrm{mod}}/U_{\mathrm{ref}}$ as functions of the applied modulation frequency f_{mod}.

To characterize the modulation path for the EDMR mode, the maximum possible modulation voltage amplitude $U_{\mathrm{ref,\ max}}$ for the modulation amplifier as well as the resulting current through the modulation rods as a function of f_{mod} were measured carefully. To prevent the modulation amplifier to get damaged due to too high a voltage, $U_{\mathrm{ref,\ max}}$ was programed into the EDMR Control Center software as an interlock for the reference output voltage U_{ac} at a given modulation frequency. Afterwards, the field modulation amplitude B_{mod} was determined using a Hall effect magnetometer in alternating current mode, precisely positioned at the sample location in the resonance cavity at different modulation frequencies f_{mod} for an applied modulation voltage amplitude of $U_{\mathrm{ref}} = 1\,\mathrm{V}$. Since the resulting magnetic field strength is directly proportional to the current flowing through the modulation rods,

it was possible to determine the maximum modulation amplitude $B_{\mathrm{mod,\,max}}$ as a function of the modulation frequency f_{mod}. Figure 14 shows the results of this characterization together with the calibration factor $B_{\mathrm{mod}}/U_{\mathrm{ref}}$ used by the EDMR Control Center to calculate the modulation amplitude for a specific EDMR experiment. As expected, the achievable field modulation amplitude depends on frequency. A modulation amplitude of $B_{\mathrm{mod}} > 0.25\,\mathrm{mT}$ can be applied to the EDMR sample over the whole frequency range. For modulation frequencies between 400 Hz and 18 kHz the maximum field modulation amplitude lies above 0.9 mT.
It is important to note that even though $B_{\mathrm{mod,\,max}}$ could be determined over the whole frequency range shown in figure 14, the developed EDMR setup was not able to operate closely around $f_{\mathrm{mod}} = 2\,\mathrm{kHz}$ since at that frequency the tuning of the resonant cavity is hindered by acoustic couplings. Besides that, the modulation frequency could be freely selected and no further restrictions were discovered during operation of the instrument.

4.3. Calibration of the Light Source Intensity

One major aspect of the experiments performed and discussed in this thesis is the dependence of the EDMR signals on the used light intensity. In this context, a relative measure between the different illumination levels selectable at the Schott KL 2500 LCD halogen cold light source is of great importance. Furthermore, it is desirable to be able to give the used light intensity for

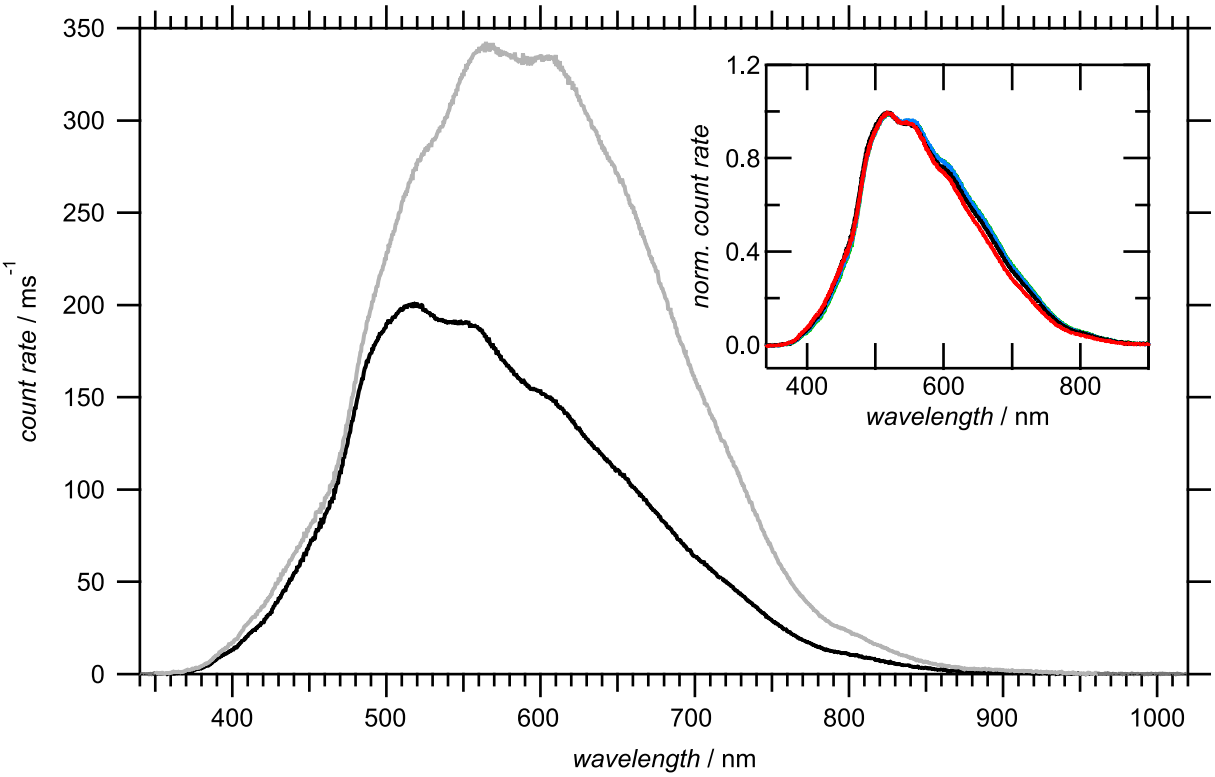

Fig. 15: Comparison of the spectra emitted by the Schott KL 2500 LCD halogen cold light source with (black line) and without (gray line) the daylight filter at *Level* 4, *Aperture* E (abrev. 4E). The inset shows normalized spectra obtained at settings 3E (green), 4D (blue), 4E (black) and 6C (red) using the daylight filter. Due to the use of this filter and the built-in light source stabilizer, all spectra – even for different *Level* settings – are comparable.

an experiment in a standard unit of measure. Because part III of this thesis is all about EDMR on organic solar cells, it was chosen to give the light intensity in *suns* throughout this work. In solar cell research *one sun* corresponds to a standard illumination of $1\,\mathrm{kW\,m^{-2}}$.[64]
The light intensity of the used KL 2500 LCD cold light source can be altered using different combinations of the *Level* (1-6) and *Aperture* (A-E) selectors on the device. While the first one electronically adjusts the light intensity by varying the voltage, the latter only changes the diameter of an orifice, thus adjusting the intensity at a constant color temperature. A daylight filter (#258 306, Schott, Germany) was used for all experiments to give an application-oriented light spectrum. Figure 15 compares the spectra emitted without using any filter and with the daylight filter applied. Due to the use of the daylight filter and the built-in light source stabilizer of the KL 2500 LCD the resulting light spectra were comparable even for different *Level* settings, as can be seen in the inset of figure 15.
An increment for each *Level* and *Aperture* setting of the KL 2500 LCD was determined by recording spectra for nine different combinations covering *Level* settings 1 to 4 and 6, as well as *Aperture* settings A to E and calculating the corresponding spectral count rate for each combination by integrating over the wavelength range from 339 nm to 1025 nm. These increments were then used to calculate a relative measure for the light intensity for all light source settings possible. Furthermore, a commercial silicon-based solar cell (Osram SFH2400) was used to convert this relative unit of measure into a standard one. For this purpose, the current resulting from the Osram solar cell at an applied bias voltage of $-1.00\,\mathrm{V}$ was recored when precisely placed at the sample location inside the MiniScope MS400 and illuminated using the 4E setting of the KL 2500 LCD through the spectrometer light port. The resulting current was compared with the one obtained from the same Osram solar cell at the same bias level when placed in a commercial sun simulator (LOT Oriel, available at the Max Planck Institute for Polymer Research in Mainz) operating at 0.961 suns as validated using a Czibula & Grundmann RS-OD-1 reference solar cell. This way, the resulting effective number of suns at the sample location in the presented benchtop EDMR setup for every setting of the used KL 2500 LCD light source could be determined.
In summary, the presented setup is able to illuminate samples with as little as 7.0×10^{-3} suns up to a maximum of 5.0×10^{-1} suns. A detailed overview of the resulting effective light intensity for all selectable combinations of the *Level* and *Aperture* selectors can be found in the appendix on page 137, table A1.

5. Comparison with a Large Scale Spectrometer[†]

In the preceding chapters of this first thesis part the theoretical foundations of both EPR and EDMR were introduced, followed by the changes and extensions made to the hard- and software of a commercially available benchtop EPR spectrometer in order to build a compact EDMR setup. Furthermore, the necessary calibration of g-factor, field sweep generator, field modulation amplitude and light source intensity were discussed in detail. In this last chapter of the first part we will validate the results obtained with the new EDMR spectrometer using a well-known reference sample. Afterwards, the setup's performance will be compared to the one of a "large scale" spectrometer including the signal-to-noise ratio.

[†]This chapter has partially been taken from the peer-reviewed journal article published in advance: M. Eckardt, J. Behrends, D. Münter, W. Harneit, Compact electrically detected magnetic resonance setup, *AIP Adv.* **2015**, *5*, 047139.

5.1. EDMR Characteristics of the Reference Silicon Solar Cell

To characterize and validate the new benchtop EDMR setup, a hydrogenated microcrystalline silicon (µc-Si:H) pin solar cell with well-known spectroscopic properties and reasonable EDMR signal at room temperature even without illumination was used.[65,66] Since this type of sample is only used to validate the introduced benchtop EDMR setup, we will not go into much detail regarding spin-dependent processes other than the one observed here. A comprehensive overview of spin-dependent processes in microcrystalline silicon was published by Stutzmann *et al.*[38]

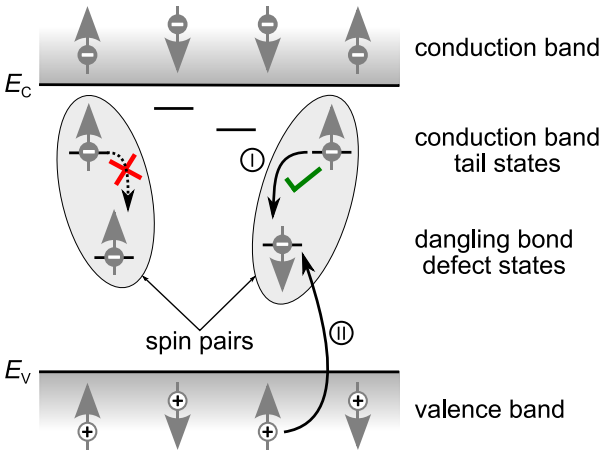

Fig. 16: Schematic representation of a spin-dependent recombination process via a dangling-bond defect state in a semiconductor device. Excess electrons may be captured by conduction band tail states from where they can move further into energetically lower lying dangling bond states only if this process is allowed for the formed spin pair according to the Pauli exclusion principle. Changing the relative spin orientation via EPR results in the transformation of a triplet (left) into a singlet pair (right) leading to charge accumulation at the dangling bond state. This charge then attracts a hole from the valence band in the second step and eventually undergoes charge carrier recombination.

The µc-Si:H pin solar cell used in this chapter was prepared and kindly provided by F. Finger, O. Astakhov, A. Lambertz and S. Haas at the Forschungszentrum Jülich. The µc-Si:H layers were prepared by plasma enhanced chemical vapor deposition using optimized standard deposition conditions.[67] Similar solar cells comprising hydrogenated amorphous silicon and µc-Si:H were previously studied by EDMR spectroscopy, and the spectroscopic properties of the current-influencing paramagnetic centers are known to a large extent.[65,66,68] Figure 16 illustrates the basic principle of a spin-dependent recombination process via a dangling-bond defect state in such a semiconductor device. An excess electron that may get captured by a conduction band tail state takes part in the formation of a spin pair with an electron occupying an energetically lower lying dangling-bond defect state. This spin-pair formation can be described using the model by Kaplan, Solomon and Mott introduced in chapter 2, section 2.1.[42] Although it would be energetically favorable for both electrons to occupy the lower lying state, this is allowed only if both spins are antiparallel according to the Pauli exclusion principle. Therefore, altering the relative spin orientation of the spin pair by driving an EPR transition on either of the two constituents produces a singlet spin-pair state and thus allows for the initially forbidden transition to take place. The resulting charge accumulation at the dangling-bond state then attracts a hole from the valence band and eventually results in charge carrier recombination. This recombination process macroscopically influences the sample conductivity (see equation 2.1) and thus alters the spin-dependent current which is – as we know from the previous chapters already – the observable in an EDMR experiment.

To determine the sample's EDMR characteristics the dependence of the signal area on microwave power was checked first. Moreover, the apparent peak-to-peak linewidth was recorded as a function of the modulation field amplitude B_{mod}. All experiments were carried out in the dark at an

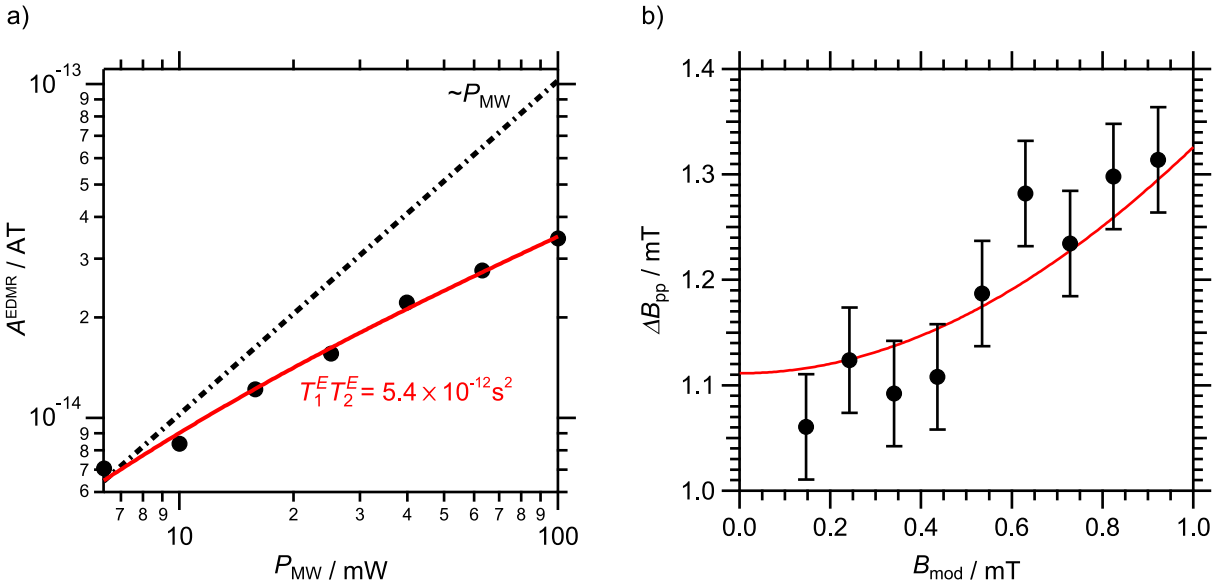

Fig. 17: EDMR characteristics of the investigated µc-Si:H type thin-film solar cell. a) Dependence of the EDMR signal area (A^{EDMR}) on the applied microwave power (P_{MW}). The dash-dotted line illustrates what a linear dependence on P_{MW}, and thus $A^{\mathrm{EDMR}} \propto B_1^2$ (cf. equation 3.1) would look like. The experimental data (black points) was fitted (red line) using equation 2.24, yielding a $T_1^{\mathrm{E}}\,T_2^{\mathrm{E}}$ product of $5.4 \times 10^{-12}\,\mathrm{s}^2$. b) Dependence of the apparent linewidth ΔB_{pp} on B_{mod}. ΔB_{pp} was fitted (red line) using Poole's equation for a modulation-broadened linewidth (equation 5.1), yielding an intrinsic linewidth of $\Delta B_{\mathrm{int}} = 1.11(5)\,\mathrm{mT}$.

identical reverse bias condition of $V_{\mathrm{bias}} = -0.32\,\mathrm{V}$ and a modulation frequency of $f_{\mathrm{mod}} = 625\,\mathrm{Hz}$. As shown in figure 17 a), the EDMR signal area A^{EDMR} is not proportional to P_{MW} and thus not to B_1^2. Instead, the signal area shows saturation over the whole experimental range. Using equation 2.24 the experimental data was fitted yielding a $T_1^{\mathrm{E}}\,T_2^{\mathrm{E}}$ product of $5.4 \times 10^{-12}\,\mathrm{s}^2$. As mentioned in chapter 1 (section 1.3.3), disentangling the two time constants is only possible in the absence of saturation effects, i.e. if $\gamma^2 B_1^2\,T_1^{\mathrm{E}} T_2^{\mathrm{E}} \ll 1$, because only then equations 1.50 and 1.52 are valid. However, since this is clearly not the case here we need to gain additional informations from elsewhere. So far, no experimental data for the EDMR relaxation times in µc-Si:H at ambient temperature is available but, following the approach by J. Behrends,[69] it is assumed that the values for µc-Si:H are comparable to those of hydrogenated amorphous silicon (a-Si:H). In his thesis J. Behrends applies $T_1 \approx T_2 \approx 5\,\mu\mathrm{s}$, which was determined in pulsed EPR measurements of a-Si:H done by M. Fehr and reported to J. Behrends in a private communication.[69] Furthermore, measurements of the spin-lattice relaxation time in a-Si:H revealed $T_1 \approx 10\,\mu\mathrm{s}$ for the dangling bond states at ambient temperature.[70] With this, the approximation $T_1^{\mathrm{E}} \approx T_2^{\mathrm{E}} \approx 2.3 \times 10^{-6}\,\mathrm{s}$ yields relaxation times that are somewhat smaller compared to the corresponding EPR values. However, looking at equations 2.21 and 2.23 this is to be expected due to the recombination rates and the pair lifetime in EDMR.

Figure 17 b) shows the increase of the apparent linewidth from about 1.1 mT to 1.3 mT with increasing B_{mod}. This is in accordance with a modulation broadening, given the performed B_{mod} calibration (cf. chapter 4, section 4.2) and an intrinsic inhomogeneous linewidth of 1.11(5) mT

according to Poole's equation for a modulation-broadened linewidth [54]

$$\Delta B_{\mathrm{pp}} = \sqrt{4\Delta B_{\mathrm{int}}^2 + B_{\mathrm{mod}}^2} - \Delta B_{\mathrm{int}} \tag{5.1}$$

with ΔB_{pp} as the apparent and ΔB_{int} as the intrinsic linewidth. This value is reasonable for dangling bond states in microcrystalline silicon, for which the reported g-factors are in the range of 2.004 – 2.006 depending on the deposition conditions. [71–73] The g-factors observed here are also within this range (see section 5.2). Finally, within the experimental accuracy given by the manganese standard (see chapter 4, section 4.1), it was observed that the g-factor does not depend at all on bias conditions or other experimental parameters, which is consistent with a single spin-dependent process prevailing in this sample.
In summary, the EDMR signal in µc-Si:H at ambient temperature without illumination can be attributed to spin-dependent recombination of injected charge carriers via silicon dangling bonds, as sketched in figure 16.

5.2. Quantitative Comparison with a "Large Scale" Spectrometer

To demonstrate the new benchtop setup's performance, spectra acquired both with the new setup and using a state-of-the-art "large scale" EDMR spectrometer (lab-built transient X/Q-band setup based on Bruker components, situated at the Berlin Joint EPR Lab) are compared in the following. Unlike in the remainder of this thesis, EDMR raw data ($Y_{\mathrm{raw}}^{\mathrm{EDMR}}$, cf. equation 3.7) is used here for direct comparison between setups running different acquisition software. Figure 18 presents results obtained for the same sample measured in both setups, which is very similar in characteristics to the one investigated in figure 17. The experimental data were fitted using

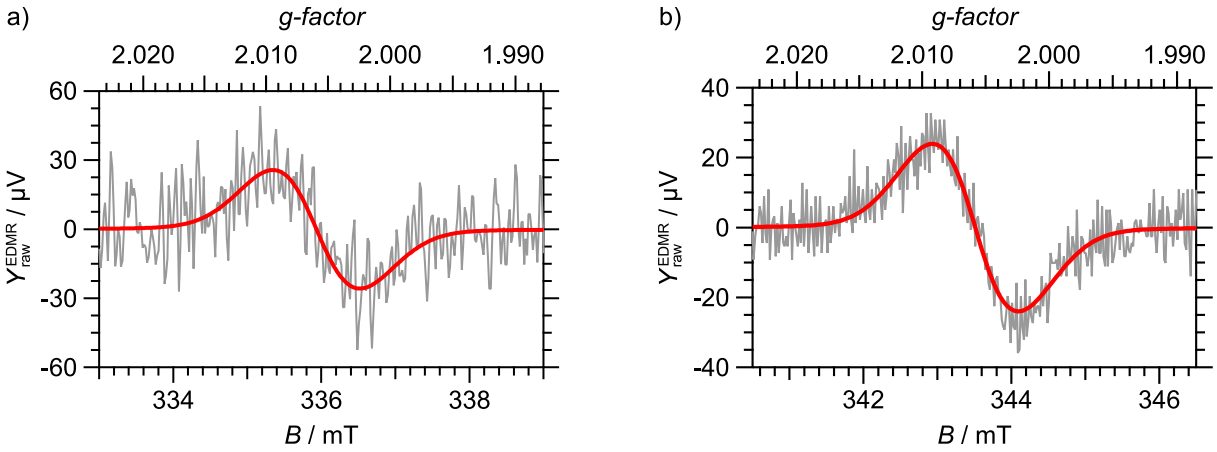

Fig. 18: EDMR spectra of the same µc-Si:H solar cell measured in a) the new benchtop EDMR setup introduced in this thesis and b) a state-of-the-art "large-scale" EDMR setup. The data were acquired at identical forward bias conditions $V_{\mathrm{bias}} = 320\,\mathrm{mV}$. All scan parameters, including equivalent noise bandwidth of the lock-in amplifier and scan time, were chosen as similar as technically possible. The modulation frequency was set to 9876 Hz. The experimental data were fitted (red line) using a pseudo-Voigt profile.

the EDMR Analysis Toolbox software package presented in chapter 3 (section 3.3.2) utilizing a pseudo-Voigt profile. For the benchtop spectrometer, a g-factor of 2.0059(3) was observed and the peak-to-peak linewidth was determined to be 1.18(5) mT. For the "large" spectrometer, a

g-factor of 2.0058(3) was obtained while the signal had a peak-to-peak linewidth of 1.15(5) mT. Therefore, both results are equal within the experimental errors, demonstrating the correct operation of the new setup.
Furthermore, the observed signal magnitudes are comparable under nominally identical conditions. In particular, the spectrum in figure 18 a) was recorded using five times the microwave source power compared to the one shown in figure 18 b). However, the resonant cavities have different fill factor, quality factor Q, geometry, and hence different conversion factor c as introduced in equation 1.51. For the rectangular TE_{102} resonator of the benchtop machine, we found that the quality factor of the empty cavity, $Q \approx 6000$, decreases by about 10 % upon introduction of the sample. The conversion factor was characterized to be $c = 0.20(2)\,\mathrm{mT}/\sqrt{\mathrm{W}}$ in chapter 3, section 3.1 for the MiniScope MS400. The dielectric ring resonator ER 4118 X-MD-5 of the "large" setup is specified as TE_{011}, $Q \approx 4000$ and $c = 0.42\,\mathrm{mT}/\sqrt{\mathrm{W}}$ by the manufacturer (Bruker Corporation). Thus, the effective magnetic field strength of the microwave, B_1, is estimated to be less than 10 % larger in figure 18 a) than in figure 18 b). All scan parameters (including the equivalent noise bandwidth of the lock-in amplifier and the scan time) were chosen as similar as technically possible on both spectrometers. The spectra were acquired in forward bias condition with $V_{\mathrm{bias}} = 320\,\mathrm{mV}$ using a modulation frequency of $f_{\mathrm{mod}} = 9876\,\mathrm{Hz}$ and a field modulation amplitude $B_{\mathrm{mod}} = 0.5\,\mathrm{mT}$ in both cases. Hence, the obtained signal magnitude should be comparable, which is in good accordance with the experimental results shown in figure 18.
In summary, it can be stated that the spectroscopic parameters of the used µc-Si:H solar cell could be successfully determined using the designed benchtop EDMR and that the obtained signal strength is comparable to the "large scale" machine.

5.3. Signal-to-Noise Ratio

During the µc-Si:H sample characterization shown in figure 17, a wide range of parameters for the effective microwave amplitude B_1 and the modulation amplitude B_{mod} was investigated. Within this range, no discernible dependence of the g-factor and linewidth, and also almost constant noise was found.
A comparison of the noise levels in figure 18 a) and 18 b) shows that the new benchtop EDMR setup exhibits somewhat higher noise. Thus, a careful experimental noise analysis and optimization was carried out. The somewhat surprising result of this analysis was that the detected EDMR signal in the new setup is limited by noise generated within the sample itself. Extrinsic noise sources such as the used amplifiers and the bias source can be disregarded. There is a finite, if small, coupling to environmental "lab noise" due to imperfections in the cable shielding used for contacting the sample. Due to the lock-in detection employed in EDMR, this noise is, however, efficiently filtered out by setting a small enough equivalent noise bandwidth (ENBW, inversely related to the lock-in time constant). Furthermore, the Anfatec lock-in amplifier used in the benchtop EDMR allows measuring the noise spectrum over arbitrary frequency intervals, so that one can conveniently choose a modulation frequency at which the lab noise is marginal. The modulation frequency and the electrical bias conditions, however, show a great impact on the signal-to-noise ratio. This is to be expected when considering the EDMR model introduced in chapter 2, section 2.2. Even in the simplest case, where only one spin-dependent transport channel like recombination contributes to the spin-dependent EDMR current ΔI^{EDMR}, it is still in competition with all spin-independent transport mechanisms that contribute to the total current I_{sample}. Hence, for rectifying devices like diodes and solar cells, it may be advantageous to measure under reverse-bias conditions where the unwanted, spin-independent, current is small.

Tab. 3: Summary of the obtained results for the µc-Si:H solar cell used in Figures 18 a) and 19. The preamplifier gain was set to $1\,\mathrm{V\,\mu A^{-1}}$, the modulation amplitude was $B_{\mathrm{mod}} = 0.5\,\mathrm{mT}$ and the microwave source power was set to 100 mW. ΔI^{EDMR} is the spin-dependent EDMR current, $\xi_{\mathrm{sd}}^{\mathrm{EDMR}}$ the EDMR effect and I_{noise} is the 2σ-noise current, these figures were introduced in chapter 3, section 3.3.2.

Figure	$\frac{f_{\mathrm{mod}}}{\mathrm{Hz}}$	$\frac{V_{\mathrm{bias}}}{\mathrm{V}}$	$\frac{I_{\mathrm{sample}}}{\mu\mathrm{A}}$	$\frac{\Delta I^{\mathrm{EDMR}}}{\mathrm{pA}}$	$\frac{I_{\mathrm{noise}}}{\mathrm{pA}}$	$\left\lvert\frac{I_{\mathrm{noise}}}{I_{\mathrm{sample}}}\right\rvert$	$\xi_{\mathrm{sd}}^{\mathrm{EDMR}}$	SNR
18 a)	9876	+0.32	13.0	52.9	35.2	2.7×10^{-6}	4.1×10^{-6}	1.5
19	625	−0.32	−0.112	−14.1	2.71	2.4×10^{-5}	1.3×10^{-4}	5.2

To illustrate this effect, figure 19 shows an EDMR spectrum of the same µc-Si:H sample as investigated in figure 18 a), but under reverse bias. The modulation frequency was changed to $f_{\mathrm{mod}} = 625\,\mathrm{Hz}$. All other parameters including the equivalent noise bandwidth of the lock-in amplifier as well as the scan time remained unchanged. Table 3 gives a summary of the obtained results from both measurements. It should be noted that the bias current I_{sample} is two orders of magnitude lower (and opposite in polarity) for the measurement shown in figure 19.

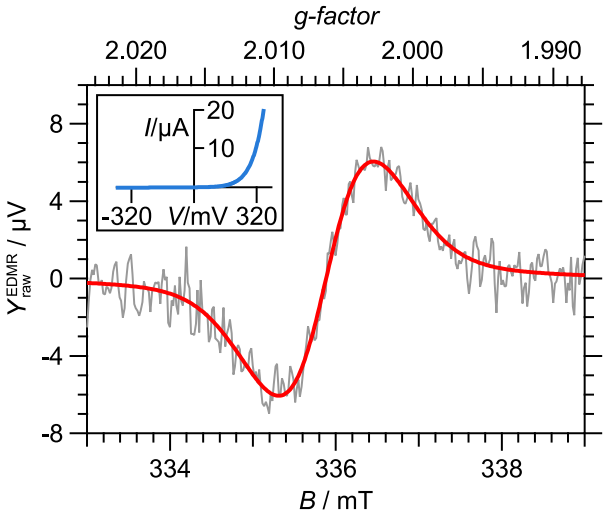

Fig. 19: EDMR spectrum of the same sample as shown in figure 18 a), but under reverse bias condition $V_{\mathrm{bias}} = -320\,\mathrm{mV}$ and at $f_{\mathrm{mod}} = 625\,\mathrm{Hz}$. The data were fitted (red line) using a pseudo-Voigt profile ($g = 2.0062(3)$, $\Delta B_{\mathrm{pp}} = 1.14(5)\,\mathrm{mT}$). The inset shows the I/V characteristic of the sample.

At the same time, the spin-dependent EDMR current, ΔI^{EDMR}, has decreased only by a factor of 3.8, and the noise reduction is about a factor of 13, leading to an enhanced signal-to-noise ratio of SNR = 5.2 in figure 19 as compared to SNR = 1.5 in figure 18 a). The noise is thus strictly proportional neither to the total bias current nor to the EDMR signal, suggesting that other noise sources may be present.

To summarize, the detected noise level may vary by as much as a factor of 13 depending on biasing conditions and modulation frequency alone. Looking at Figures 18 and 19, it is interesting to note that the modulation frequency dependence of the signal-to-noise ratio is different when measuring the same sample in both EDMR setups, even when using nominally similar biasing conditions. Since the sample and the manner of contacting it were the same in both cases, sample-related parasitic capacitances etc. can be excluded. Also, care was taken not to introduce artificial damping factors due to filters in the amplifier chain and to chose settings as similar as technically possible. Due to technical reasons, however, the total bias current value in the "large" setup could not be ascertained with the same accuracy as in the benchtop measurements. It may

well have been smaller in figure 18 b) than the value $I_{\text{sample}} = 13\,\mu\text{A}$ in figure 18 a), which could account for some of the additional noise.
A significant difference in the EDMR setups used here remains the resonance cavity, regarding both signal strength (i.e. B_1) and excess noise introduced by the electrical field component of the microwaves (i.e. E_1). It was recently shown that rectification effects of E_1 in silicon devices can dominate the noise measured in EDMR.[36] For both aspects, the dielectric ring resonator offers more favorable characteristics due to the higher field separation and concentration. At present, this translates to a somewhat larger noise floor for the benchtop spectrometer, which is, however, difficult to quantify due to the complicated bias dependency. This example shows that for each EMDR setup, choosing the optimum bias point and modulation frequency may lead to gains in SNR that are potentially large and similar to the difference between the two spectrometers.

6. Summary of Part I

In this first part, the foundations of both EPR and EDMR spectroscopy were introduced. The basic EPR theory concepts discussed in chapter 1, like spin Hamiltonian and signal shape functions, including saturation and linewidth, were successfully applied to the EDMR technique using the EDMR rate equation model introduced in chapter 2. The design and implementation of a benchtop EDMR system, including a special sample holder system ready for rapid sample exchange, as well as a comprehensive software interface to control the machine and analyze the recorded data, was presented in chapter 3. This was followed by the calibration and validation of the compact EDMR system using well-known samples in chapters 4 and 5.

In summary, a compact setup for measuring electrically detected magnetic resonance of semiconductor devices that yields consistent and highly reproducible results was built. Using a standard silicon solar cell for a detailed comparison with a typical "large-scale" setup, it could be shown that the EDMR spectra are quantitatively comparable in all spectroscopic dimensions with those obtained in a state-of-the-art spectrometer.
The introduced setup allows the study of processes in dark EDMR as well as under illumination. The current-voltage characteristic of the device under test can be investigated with the sample still inside the spectrometer's resonant cavity, allowing for rapid research cycles and measurement series. Furthermore, measurements at low temperatures are possible using the available dewar unit for the spectrometer. Thus, the presented setup can be used for complete semiconductor device characterization at different operating conditions.
Due to its small footprint, the unit is highly mobile and can in particular be operated inside cleanrooms or even glove boxes, which is beneficial for studies on organic materials and devices. Finally, although the spectrometer itself is compact and closed, the electrical detection pathway is entirely accessible to the researcher in order to study recently discussed phenomena like the dependence of the signal phase of EDMR signals on the modulation frequency.[56]

The benefits of close proximity between device fabrication and spectroscopic characterization possible with the compact EDMR setup presented here, will be used in the next part of this thesis to record EDMR spectra of C_{60} microcrystals, a class of samples never before investigated in EDMR.

Part II.

EDMR on Pure and Doped Fullerene Microcrystals

Focus and objective: This second part utilizes the EDMR technique to investigate both pure and doped fullerene based organic microcrystals. This type of sample is – like most organic semiconductors – prone to undergo a rapid degradation process if no proper encapsulation is used. However, because the encapsulation material itself can interfere with the active material and unintentionally influence the device characteristics, the study of unencapsulated systems is indicated. With time being a critical variable in unencapsulated devices, the experiments shown in this part benefit greatly from the close proximity between device fabrication and spectroscopic characterization possible with the new compact EDMR setup presented in part I. After introducing some basic properties of the Buckminsterfullerene C_{60}, we will look at the synthesis and purification of the endohedral compound N@C_{60} as well as its stability.‡ Afterwards, EPR and EDMR results on C_{60} microwires and microdisks are presented followed by the investigation of crystals made from $C_{60}O$. Finally, the first evidence for strongly dipolar-coupled spin pairs in N@C_{60}-doped Buckminsterfullerene observed via EDMR is presented.

The following part of this thesis has partially been published in a peer-reviewed journal: M. Eckardt, J. Behrends, D. Münter, W. Harneit, Compact electrically detected magnetic resonance setup, *AIP Adv.* **2015**, *5*, 047139. The chapter based on this article is indicated by a †.

7. Fullerenes and Fullerene Materials

The performance of electronics greatly improved over the past decades due to ever-smaller silicon-based devices. However, both scientific and technical limitations will soon make it impossible to follow down this pathway anymore. Thus, alternative device technologies are needed, and carbon-based molecular electronics are a promising approach to the post-silicon age as demonstrated recently with the discovery of unconventional molecule-resolved current rectification in diamondoid-fullerene hybrids.[74]
Charge transport in organic molecules differs from the one in inorganic materials like silicon. So far, most materials and devices for organic electronics are made and improved by a trial-and-error like approach. Here, the EDMR technique could be used to directly gain new insights on charge transport and recombination phenomena limiting the performance of optoelectronics. Before we will study recombination processes in fullerene-based organic solar cells in part III of this thesis, we will focus on the investigation of pure and doped fullerene microcrystals in the remainder of this part. First, the Buckminsterfullerene C_{60} will be introduced, followed by its endohedral derivative N@C_{60}. We will than look at the quantification, purification, and stability of fullerene materials and how to produce EDMR compatible microcrystals. Afterwards, EDMR results obtained on pure C_{60} microcrystals and oxidized fullerene species will be compared. Lastly, we will discuss and analyze the coupling pattern observed in EDMR experiments on N@C_{60}-doped crystals using a computer simulation approach.

7.1. The Buckminsterfullerene C_{60}

Following its discovery by Kroto *et al.* in 1985,[75] the spherical molecule C_{60} – made of twenty carbon hexagons and twelve carbon pentagons – attracted considerable attention for its fascinating geometry. Resembling the geodesic domes of architect Richard Buckminster Fuller it

‡A more comprehensive study on the stability of C_{60} and N@C_{60}, which is outside the scope of this thesis, has been published: M. Eckardt, R. Wieczorek, W. Harneit, Stability of C_{60} and N@C_{60} under thermal and optical exposure, *Carbon* **2015**, *95*, 601-607.

became eponymous for a whole related class of molecules, the fullerenes. The structure of the C_{60} molecule is depicted in figure 20. Typically, double bonds between hexagons are called [6,6] double bonds and those between pentagons and hexagons are referred to as [5,6] double bonds. Interestingly, no [5,6] double bonds at all exist in the C_{60} molecule and even though, in principle, there is more than one structural isomer for fullerenes with more than 70 carbon atoms, stable fullerenes obey what is known as the isolated-pentagon rule, which states that the pentagons do not make direct contact with each other.[76]

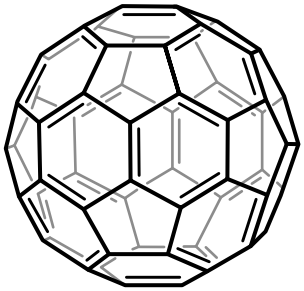

Fig. 20: Structure of the Buckminsterfullerene C_{60}. The molecule consists of twenty carbon hexagons and twelve carbon pentagons. Each pentagon is surrounded by five hexagons. Double bonds are located between hexagons, single bonds are located between the pentagons and hexagons only.

The diameter of C_{60} has been determined to be about 700 pm using nuclear magnetic resonance (NMR).[77,78] This results in a van der Waals diameter for the molecule of about 1 nm, taking into account the size of the π-electron cloud surrounding the carbon atoms on the C_{60} framework.[77] In contrast to other carbon allotropes, fullerenes are soluble in aromatic solvents like toluene and 1,2-dichlorobenzene giving intensively colored solutions (e.g. violet for C_{60} and burgundy for C_{70} dissolved in toluene). Solid C_{60} forms a face-centered-cubic structure at ambient temperature and solid-state NMR measurements revealed an almost free rotation of the constituting C_{60} molecules.[77,79]

Due to its remarkable structure, the C_{60} molecule has become a promising candidate for the fabrication of organized nanostructures.[80–82] Furthermore, with its electronic properties ranging from semiconductivity to superconductivity,[83,84] the construction of remarkable organic electronics seems feasible. The production of macroscopic quantities of Buckminsterfullerene C_{60} can basically be done by two different approaches. The first one is the so-called resistive heating of graphite – also known as the Krätschmer-Huffman method – which generates large quantities of a fullerene-containing carbon soot.[85] This soot is then extracted using toluene yielding about 10 % to 15 % fullerenes.[86] The second approach is the combustion of hydrocarbons like benzene in oxygen-argon flames as first reported by Howard *et al.*[87] Although this method only gives low fullerene yields (about 0.3 %), it is of commercial interest due to its scalability and the fact that it can be operated as a continuous process.[86]

As this part of the present thesis is about EDMR on pure and doped fullerene microcrystals, it is worthwhile to briefly discuss charged C_{60} species. In fact, its electron-accepting ability is one of the most characteristic chemical properties of the Buckminsterfullerene. It arises directly from the electronic structure of the molecule, which was calculated to have a triply degenerate lowest unoccupied molecular orbital (LUMO) of comparatively low energy, lying about 2 eV above the highest occupied molecular orbital (HOMO),[88,89] making C_{60} fairly electronegative and reducible up to the hexaanion.[90,91] EPR spectra of fulleride anion $C_{60}^{\bullet -}$ revealed a characteristically low g-factor between 1.994 and 2.000 at low temperatures.[92] However, the linewidth of the signal is strongly temperature dependent above about 77 K and increases with increasing temperature.[92] This broadening is due to strong spin relaxation, which eventually even makes the EPR signal too broad for detection at ambient temperatures.[93]

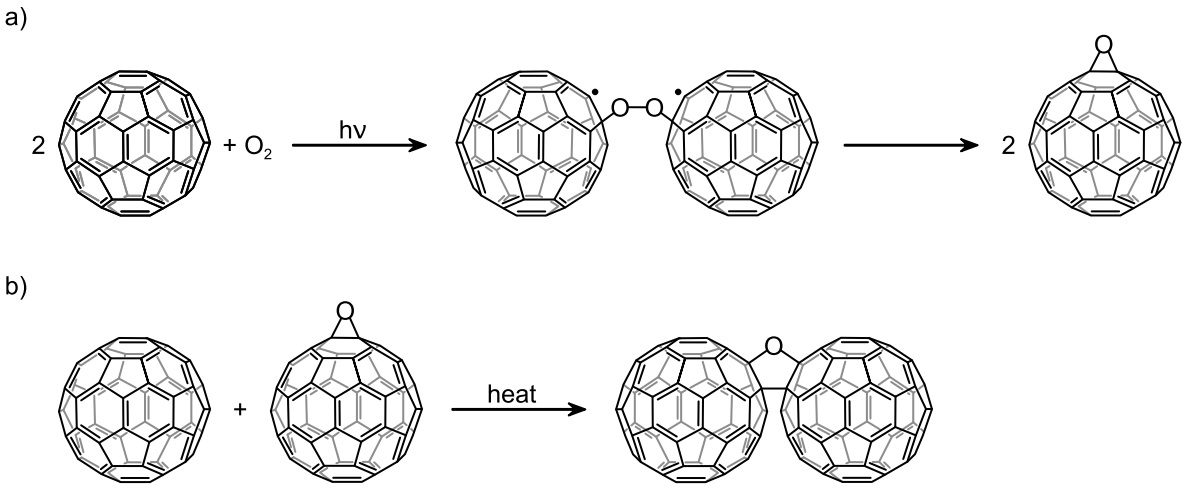

Fig. 21: Reaction scheme for the formation of $C_{120}O$ using C_{60} as starting material. a) The photochemical formation of $C_{60}O$ probably proceeds via the paramagnetic reaction intermediate $^{-\cdot}C_{60}{-}O{-}O{-}C_{60}{}^{\cdot-}$,[97] making fullerene materials somewhat sensitive to light and air. b) The formed $C_{60}O$ can react with an unmodified C_{60} molecule, yielding the dimer $C_{120}O$ often observed as an impurity in Buckminsterfullerene material.[99]

In addition to the reduction, the oxidation of C_{60} to the corresponding cation $C_{60}{}^{\cdot+}$ is possible, although this reaction occurs less willingly due to the comparatively high first oxidation potential of the Buckminsterfullerene.[89,91,94] EPR spectroscopy on $C_{60}{}^{\cdot+}$, prepared by different methods, has been carried out and the reported g-factors and linewidths show a broad distribution.[89] The reported differences in the spectroscopic properties may arise from subsequent reaction of the produced fullerene cation with nucleophiles present due to the synthesis route choosen. This, however, leaves doubt about whether $C_{60}{}^{\cdot+}$ was actually spectroscopied or some undefined reaction product.[89] The most reliable value so far is probably the one reported by Reed *et al.* ($g = 2.0022$, $\Delta B_{\mathrm{pp}} = 0.3\,\mathrm{mT}$ at $105\,\mathrm{K}$), obtained on fullerene carbocations synthesized from C_{60} and the superacid $H(CB_{11}H_6Cl_6)$.[95]
When considering oxidation reactions, C_{60} can not only undergo an electrochemical oxidation but also an oxygenation leading to the formation of $C_{60}O$ as depicted in figure 21 a). This reaction can be initiated by irradiating a fullerene solution with UV light, also forming $C_{60}O_n$ (with $n = 2, 3, 4, 5$) to a lesser amount.[96] The paramagnetic reaction intermediate $^{-\cdot}C_{60}{-}O{-}O{-}C_{60}{}^{\cdot-}$ occurring in this reaction scheme was first proposed by P. Paul *et al.*,[97] and later observed in own stability experiments.[98] The $C_{60}O$ molecule can further react with unmodified C_{60} to form the dimer $C_{120}O$, opening up a synthesis route to this molecule as depicted in figure 21 b).[99] The oxygenation of C_{60} does not only take place in targeted synthesis like this, but is a common problem when storing fullerene materials. Thus, $C_{120}O$ is often present as an impurity in C_{60}-samples.[97,100,101] Hence, fullerenes and fullerene materials should generally be stored away from light and air.
The so far described reactions are the more important ones with respect to this thesis. However, the C_{60} molecule has a rich chemistry including nucleophilic additions (e.g. cyclopropanation via the Bingel-Hirsch reaction),[102] hydrogenation,[103] halogenation,[104] and the formation of transition metal complexes.[105] Furthermore, cycloadditions can be performed making important molecules like $PC_{61}BM$ – a widely used electron-acceptor material in solar cell research that will be discussed in more detail in part III of this thesis – accessible.[106]

7.2. The Endohedral Fullerene N@C_{60}

A whole subclass of fullerene derivatives not discussed so far are the so-called "endohedrals" – tailor-made molecules enclosing ions, atoms, or clusters inside the near spherical hollowspace of a host fullerene. We will use a member of this class of substances, namely N@C_{60}, to produce doped fullerene microcrystals later in this chapter and thus introduce its properties, synthesis, as well as a suitable quantification method in the following. Afterwards, we will look at a preparative purification method for this material in chapter 7.3.

7.2.1. Nomenclature, Discovery and Properties

Soon after the discovery of the substance class of fullerenes itself, a molecule with the empirical formula LaC_{60} was obtained from a lanthanum chloride impregnated carbon source that was subjected to the Krätschmer-Huffman process.[107] Detailed studies of this material revealed that the lanthanum atom is located inside the closed shell of the fullerene host molecule.[108] This fullerene subclass is called "endohedral fullerenes" and the notation M@C_n is widely used, even though the IUPAC Nomenclature of Organic Chemistry suggests to use [n]fullerene-*incar*-M, which is denoted *i*MC_n.[109] Thus, the introduced lanthanum complex is usually written as La@C_{60}. This syntax will also be used throughout this thesis. Numerous endohedral fullerenes with one or more metal atoms are known, all of which are formed by capturing metal atoms during the fullerene-cage formation. Additionally, endohedral fullerenes containing the noble gases can be produced by forcing the noble gas atom into an existing fullerene molecule using high temperature and high pressure.[112] However, using an ion-implantation technique even the endohedral fullerenes of reactive group 15 elements like nitrogen and phosphorus can be synthesized.[113,114] In both cases, the reactive endohedral atom is stabilized inside the fullerene cage and does not undergo a reaction or a charge transfer with the surrounding carbon framework. This is supported by calculations,[115,116] showing no intermixing of the wavefunctions for the central atom with those of the fullerene host molecule, as well as by EPR spectroscopy,[113,114,117] revealing a quartet ground state with three unpaired electrons (total electron spin $S = 3/2$).

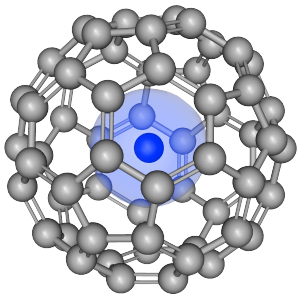

Fig. 22: Structure of the endohedral fullerene N@C_{60}. The nitrogen atom (depicted in blue) with atomic diameter 130 pm and van der Waals diameter 310 pm (transparent blue) is surrounded by carbon atoms (atomic diameter 140 pm) making up the fullerene molecule (van der Waals diameter ≈ 1 nm).[77,78,110,111]

The molecule of interest for this thesis, N@C_{60}, is shown in figure 22. The endohedral nitrogen atom has an atomic radius of 65 pm and a corresponding van der Waals radius of 155 pm.[110,111] For the surrounding carbon atoms the atomic radius is 70 pm with a specified van der Waals radius of 170 pm.[110,111] Due to the perfect shielding of the endohedral nitrogen atom and the resulting, fully retained electron spin, the N@C_{60} molecule is an interesting candidate for a molecular qubit model system.[118]

With two naturally occurring isotopes that possess a different nuclear spin, EPR spectra of

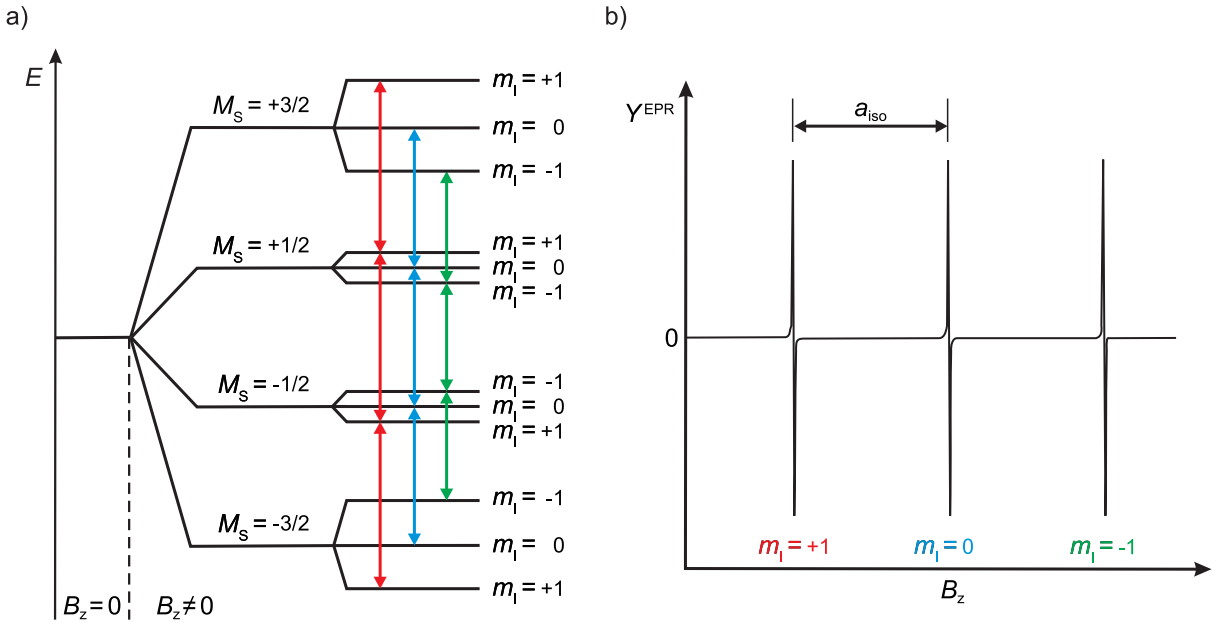

Fig. 23: Term diagram a) and resulting EPR spectrum b) for N@C_{60} in solution. The Zeeman splitting for a spectral line in presence of an external magnetic field for the magnetic quantum number of the total electron spin M_S ($M_S = -S, -S+1, \cdots, S-1, S$), together with the hyperfine interaction – characterized by the isotropic coupling constant a_{iso} – leads to a total of 12 energy sublevels. The transitions corresponding to a particular nuclear spin quantum number m_I are degenerate, resulting in the three-line EPR spectrum shown in b).

N@C_{60} are in principle a superpositions of two different spectra. However, since the two nitrogen isotopes have a very different natural abundance (^{14}N: 99.64 %, ^{15}N: 0.36 %),[55] only ^{14}N with nuclear spin $I = 1$ is considered in the remainder of this thesis.[113]
The effective EPR Hamiltonian for the N@C_{60} system in solution can be derived from equation 1.8 by omitting the non-resolvable nuclear Zeeman and nuclear quadrupole interactions (cf. chapter 1, sections 1.2.2 and 1.2.5) and the zero-field splitting (unobservable due to fast rotational averaging). With the magnetic field only applied along the z-axis, the Hamiltonian becomes

$$\hat{H}_{\text{eff, iso}} = \hat{H}_{\text{EZ}} + \hat{H}_{\text{HF}} = \frac{\mu_B}{\hbar} g_{\text{iso}} B_z \hat{S}_z + a_{\text{iso}} \hat{S}_z \hat{I}_z \tag{7.1}$$

with g_{iso} being the isotropic g-factor and a_{iso} as the isotropic coupling constant introduced in equation 1.20. Figure 23 illustrates the resulting term diagram and EPR spectrum. Experimentally, a g-factor of 2.0024(3), a peak-to-peak linewidth of $\Delta B_{pp} = 14(2)\,\mu$T and an isotropic hyperfine interaction of $a_{iso} = 0.56(1)$ mT was found for the N@C_{60} material used in this thesis. These spectroscopic parameters are in accordance with own results obtained on earlier produced material,[98] as well as those reported by other groups.[113,115]

7.2.2. Synthesis by Ion Implantation

As mentioned in the last section, the synthesis of N@C_{60} is possible using the ion-implantation technique introduced by Almeida Murphy *et al.* in 1996.[113] To produce the endohedral material needed for the experiments presented in this thesis, an implantation setup mainly based on

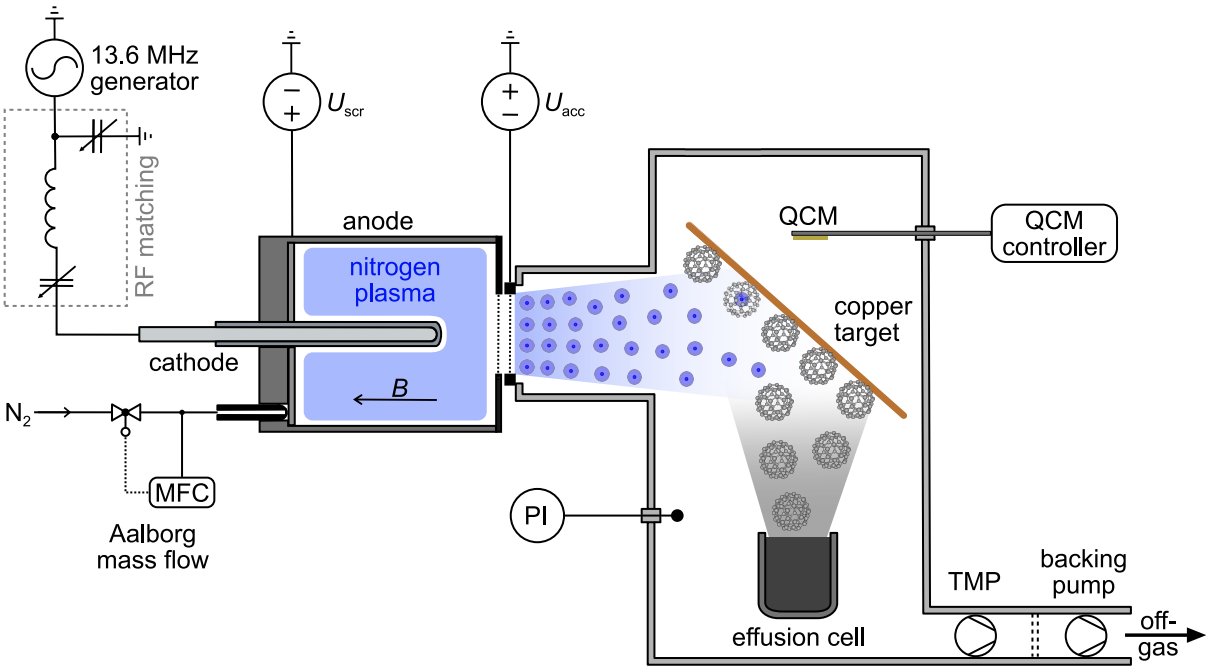

Fig. 24: Schematic diagram of the implantation setup used to synthesize N@C_{60}. Nitrogen ions having an energy of $E_{\text{ion}} = q(U_{\text{scr}} - U_{\text{acc}})$ move from the capacitively coupled ion source operating at 13.6 MHz towards the liquid-nitrogen cooled copper target. The necessary nitrogen mass flow is adjusted and maintained by an Aalborg mass flow controller (MFC). Fullerenes are sublimed from the resistively heated boron nitride effusion cell and meet with the nitrogen ions at the cold copper surface, generating the endohedral species. The fullerene sublimation is monitored by means of a quartz crystal microbalance (QCM). The chamber pressure is maintained by the turbomolecular pump (TMP) in combination with a backing pump. An emergency gate valve (dotted lines) between the two pumps protects the TMP in case of a mains failure. The pressure in the implantation chamber is monitored using a wide range gauge (PI).

equipment already available in the lab from an earlier production of the molecule was built. Figure 24 shows a schematic diagram of the used ion implantation system. The setup's composition, together with a picture of the assembled equipment (figure A6) can be found in the appendix on page 138. The general operation procedure used to synthesize N@C_{60} from a commercially available, cost efficient fullerene mix consisting of about 80 % C_{60} and 20 % C_{70} is described below.

The fullerene material is pelletized, filled in the boron nitride effusion cell and sublimed towards the liquid-nitrogen-cooled copper target. At the same time, the ion source is used to produce nitrogen ions in a plasma. An ion-beam containing N^+ ions (amongst other species) is extracted by the ion optics. These ions possess the energy $E_{\text{ion}} = q(U_{\text{scr}} - U_{\text{acc}})$. A certain ion proportion interacts with the sublimed fullerenes in front of and on the target itself, forming N@C_{60} and N@C_{70}. Furthermore, some of the fullerenes fragment or polymerize due to the ion beam and form insoluble byproducts. In order to increase the mean free path of ions and fullerenes, the system is operated under reduced pressure. The continuous fullerene evaporation is monitored using a quartz crystal microbalance (QCM). Both sides of the copper target can be used during the implantation process. Afterwards, the target is removed from the ion implantation's main

Tab. 4: Determined optimum operating conditions for the ion implantation setup. The typical pressure in the main chamber during an implantation run was about 3×10^{-4} mbar. The effusion cell temperature can be varied between 720 K and 910 K in order to obtain the necessary effusion rate.

Equipment	Parameter	Value
ion source	magnetic coil current	8.00 A
	average coupled power	25 W
	screen voltage U_{scr}	120 V
	acceleration voltage U_{acc}	−12 V
	nitrogen mass flow	9.5 mL/ min
effusion cell	effusion rate	~ 0.7 Å/ min
copper target	temperature	~ 130 K

chamber using a lock and the implanted fullerene material, which forms a solid black layer of a few microns in thickness, can be collected and further processed as needed.
As can be seen from figure 24, the ion implantation setup has many tunable parameters like average coupled power level, screen voltage (U_{scr}), acceleration voltage (U_{acc}), magnetic coil current, effusion rate, nitrogen mass flow, target temperature and chamber pressure. However, not all of these parameters can be chosen independently. For example the magnitude of U_{acc} has to be about 10 % of that of U_{scr} for the plasma to work smoothly. Furthermore, nitrogen mass flow and chamber pressure are of course linked and the plasma generator's average coupled power level together with the magnetic coil current and U_{acc} determines the ion beam density. Hence, there are basically three different parameters that can be set independently: the fullerene effusion rate, the ion energy and the target temperature. The latter one was not varied in the experiments conducted, but it is assumed that a low target temperature is beneficial for the N@C_{60} synthesis, since the C_{60} molecule gained vibration energy after being hit by a nitrogen ion and this excess energy needs to be dissipated. According to C. Meyer, the copper target should thus be cooled below about 230 K.[119] The following observations were made by varying the two other parameters:

- The ion-irradiation time per fullerene molecule has to be as short as possible to prevent fragmentation and polymerization. Thus, the effusion rate is a critical parameter. Too low an effusion rate can result in a total production loss. On the other hand, a high effusion rate leads to an increased adsorption of the starting material onto the inner chamber walls and therefore lowers the production efficiency.
- While – in theory – there should be an optimum for the ion energy, none could be observed experimentally. Although the ion energy was varied over the whole experimentally accessible range from about 1 eV up to 400 eV. Thus, the N@C_{60} formation seems to be limited by another (yet unknown) process and U_{scr} and U_{acc} can just be selected to yield a stable nitrogen plasma.

These observations led to the optimal implantation parameters summarized in table 4. Running the ion implantation under these conditions for about 2.5 h per target side typically yielded about

1.3 g of crude C_{60}/N@C_{60} material with a solubility of about 70 % and an implantation yield of 1.6×10^{-4}, corresponding to about 145 µg of pure N@C_{60}. During this thesis, a total amount of roughly 2 mg of N@C_{60} was synthesized using the described ion implantation setup.
However, as mentioned above, the used fullerene mix also contained about 20 % of C_{70} and some of the fullerene material is destroyed due to fragmentation and polymerization in the implantation process. Thus, the implanted material had to be purified before the synthesized N@C_{60} could be investigated using EDMR. This purification process is described in detail in section 7.3.

7.2.3. Quantification by EPR and HPLC

To assess the ion implantation process and later on the purification of the N@C_{60} material a valid quantification method is needed. However, the quantitative spin determination inside a given EPR sample is a non-trivial task, because not only a suitable spin standard has to be found but also a large number of parameters influencing the result have to be controlled carefully. Thus, the used spin standard, as well as the spectrometer have to be characterized adequately.[21]
As introduced in equation 1.44, the microwave absorption is inversely proportional to the sample's RF susceptibility, which itself is inversely proportional to the static susceptibility of the sample (cf. equations 1.35 and 1.46). With this, the relation between the number of spins N in two different EPR samples shown in equation 7.2 can be derived.[54]

$$\frac{N_1}{N_2} = \frac{A_1^{\mathrm{EPR}}}{A_2^{\mathrm{EPR}}} \cdot \sqrt{\frac{P_2}{P_1}} \cdot \frac{B_{\mathrm{mod},2}}{B_{\mathrm{mod},1}} \cdot \frac{g_2}{g_1} \cdot \frac{T_1}{T_2} \cdot \frac{S_2(S_2+1)}{S_1(S_1+1)} \cdot \frac{D_1}{D_2} \tag{7.2}$$

The subscripts are used to distinguish between sample 1 and 2. A^{EPR} is the EPR area (double integral of the EPR absorption signal Y^{EPR}, see figure 2) with multiplicity $D = 2I + 1$, due to the interaction of the total electron spin S with the nuclear spin I. P is the microwave source power and B_{mod} the modulation amplitude used. The g-factor, as well as the temperature T has to be known for both samples.
Two very important parameters with respect to quantification in EPR are the sample volume and positioning.[120] The details needed for the latter can be extracted from figure 9. For all EPR samples investigated in this thesis, a precisely adjusted sample positioning tool was used to ensure correct and reproducible results. The sample volume was strictly kept at 50 µL for all liquid samples. For solid-state samples, an equivalent sample-tube-filling height was ensured to provide a comparable cavity filling factor.
For the use as an easy-to-handle and reliable spin standard, the commercially available paramagnetic compound (2,2,6,6-tetramethyl-piperidin-1-yl)oxyl, commonly known as TEMPO, with $S = 1/2$ was successfully applied in a previous work.[120] For the calibration of the MiniScope MS400 spectrometer used in this thesis, a sample tube containing 15.5(5) mg TEMPO was prepared. The corresponding EPR signal area was determined by averaging over 30 repeated measurements, resulting in a relative error of 0.8 % at a significance level of $\alpha = 0.05$. Furthermore, a reliable quantification can only be performed if no saturation effects occur in both sample and standard. For this reason, the microwave power was kept as low as 10 µW in all quantitative experiments.
Since the N@C_{60} samples and the spin standard were measured in close temporal sequence, the temperature term in equation 7.2 can be omitted. Additionally, the g-factor of N@C_{60} and TEMPO are close and neglecting the corresponding term in equation 7.2 results in a error of about 0.2 % only.[113,121] These simplifications lead to equation 7.3, which was used for all

quantitative measurements presented here.

$$N_1 = N_2 \cdot \frac{A_1^{\mathrm{EPR}}}{A_2^{\mathrm{EPR}}} \cdot \sqrt{\frac{P_2}{P_1}} \cdot \frac{B_{\mathrm{mod},2}}{B_{\mathrm{mod},1}} \cdot \frac{S_2(S_2+1)}{S_1(S_1+1)} \cdot \frac{2I_1+1}{2I_2+1} \tag{7.3}$$

Herein, the used subscripts 1 and 2 identify the sample and the TEMPO standard, respectively.

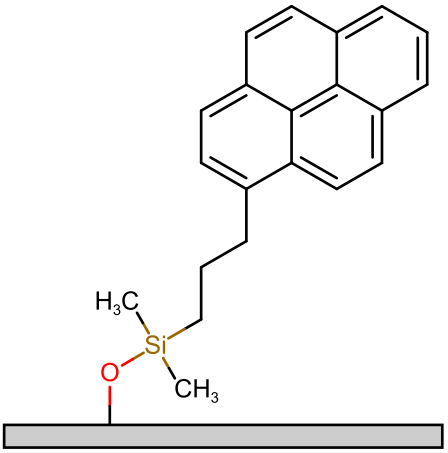

Fig. 25: Chemical structure of the stationary Buckyprep HPLC phase used in this thesis. The commercially available Buckprep material (Nacalai Tesque Inc., Japan) is made of [3-(1-pyrenyl)propyl]silyl modified silica. The fullerene-stationary-phase interaction is a result of the pyrene unit's ability of forming π-π interactions.The propyl unit links the functional group to the silica substrate resulting in a good overall pyrene coverage.[122]

In order to provide a figure for the N@C_{60} content of a given sample, not only the nitrogen filled molecules but also the empty C_{60} has to be quantified. With only paired electrons, the C_{60} molecule is of course EPR silent and another analytical method has to be used. In this thesis, high-performance liquid chromatography (HPLC) was applied for this task. HPLC itself is a separation technique rather than a quantification method. Only with a suitable, carefully calibrated detector can a quantification be done. The substance mixture to be separated is dissolved in the so-called liquid phase and moved across the so-called stationary phase, which typically is a solid in a column. Stationary and mobile phases have to be matched and further need to be compatible with the substances that should be separated. The interaction of these substances with both mobile and stationary phase lies at the very heart of the HPLC technique. This interaction leads to a distribution of the solutes between the two phases, described by an equilibrium constant. With different substances possessing different equilibrium constants, a separation is finally achieved after a repeated establishment of the equilibrium in a column of sufficient length. The substances exit the separation column successively, characterized by their individual retention time. The retention time is not a matter constant but rather depends on the specific parameters used in the separation like temperature and flow rate of the mobile phase. However, for a specific separation setup operated under constant conditions, the retention time for a chemical compound is a characteristic value. Using a known reference standard, this can be used to identify the component in question. A detailed description of the HPLC method and the variety of stationary and mobile phases that have been used over the years for different separation problems, however, lies outside the scope of this work and can rather be found in textbooks on analytical chemistry.[123]

In this work, commercially available HPLC columns with Buckprep as a stationary phase especially developed for fullerene separation (Nacalai Tesque Inc., Japan) were used. Figure 25 illustrates the chemical structure of this material. The necessary fullerene-stationary-phase interaction is a result of the pyrene unit's ability of forming π-π interactions with the fullerene molecules. In order to quantify the amount of fullerenes in a sample, the material was dissolved in toluene, which was also used as the HPLC's mobile phase running at a volume flow rate of

$1.0\,\mathrm{mL\,min^{-1}}$. 20 µL of the sample solution were injected in the analytical HPLC setup equipped with an UV detector operating at a wavelength of $\lambda = 320\,\mathrm{nm}$ (a detailed composition of the used setup can be found in the appendix on page 139, table A2). The calibration of this detector was done running 11 reference samples with known C_{60} content covering the concentration window from $0.006\,\mathrm{mg\,mL^{-1}}$ to $1.3\,\mathrm{mg\,mL^{-1}}$ and performing a linear regression on the resulting HPLC signal areas. It is important to note, that the UV detection can not distinguish between N@C_{60} and C_{60}, since the UV absorption of the molecule is not altered due to the perfectly shielded endohedral atom.
Finally, with HPLC being sensitive to all fullerene molecules – no matter if endohedral or vacant – and EPR being sensitive only to the paramagnetic N@C_{60} material, a figure of merit for the ion implantation and later on the N@C_{60} purification can be defined.

$$q = \frac{N_{\mathrm{N@C_{60}}}}{N_{\mathrm{C_{60}}}} = \frac{N_{\mathrm{N@C_{60}}}}{N_{\mathrm{total}} - N_{\mathrm{N@C_{60}}}} \tag{7.4}$$

In equation 7.4, $N_{\mathrm{N@C_{60}}}$ is the number of endohedral and $N_{\mathrm{C_{60}}}$ the number of vacant C_{60} molecules. N_{total} is the sum of both species available from a HPLC analysis. As mentioned in section 7.2.2, the implanted material produced for this thesis typically had $q \approx 1.6 \times 10^{-4}$.

7.3. Preparative Purification of Fullerene Materials

The stationary HPLC phase Buckyprep introduced in the previous section can not only be used in analytical size columns. Furthermore, it is commercially available in preparative size guard and separation columns with dimensions up to 28 mm × 250 mm. Using Buckyprep columns, a separation of C_{60} species from higher fullerenes can easily be achieved, as shown in figure 26.

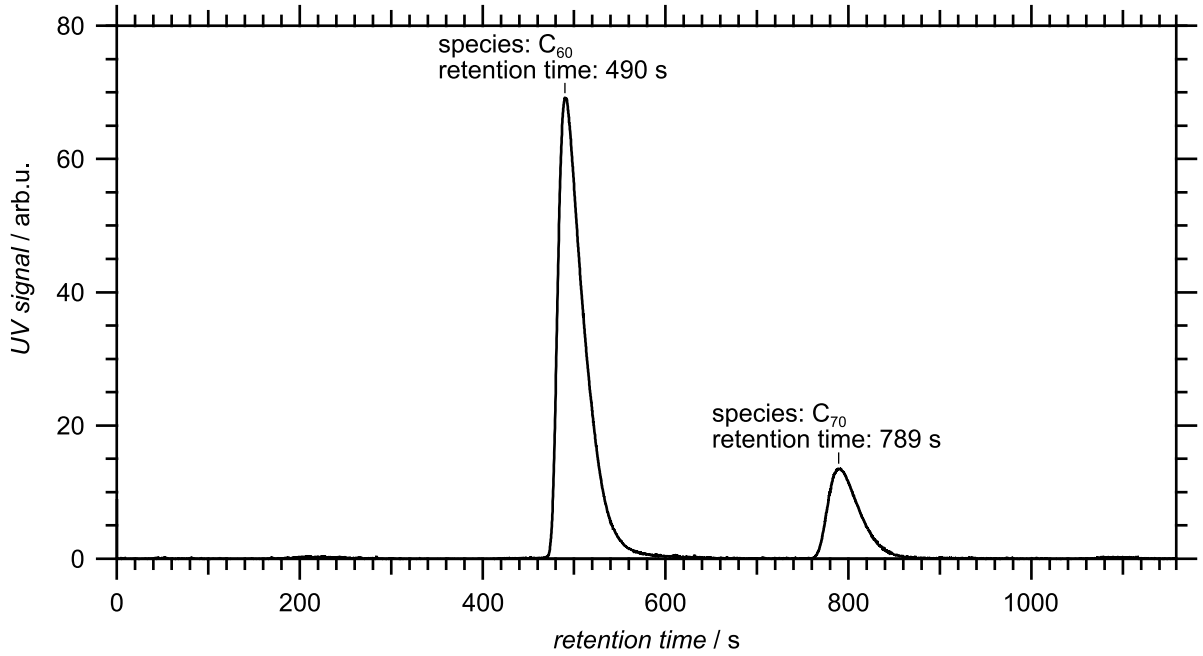

Fig. 26: Example chromatogram of a fullerene mixture containing C_{60} and C_{70} recorded using the analytical HPLC equipment. The retention time of C_{70} and higher fullerenes is significantly increased with respect to C_{60}, making the separation on Buckyprep easy.

While the separation of C_{60} and $N@C_{60}$ from higher fullerene species can in principle be done using preparative style Buckyprep HPLC columns, their price tag of about $40,000 per preparative column (28 mm × 250 mm) circumvents using them for the large amounts of material produced in the ion implantation process. Due to the difference in the number of constituting carbon atoms, a stationary phase with far less separation efficiency is sufficient to selectively separate C_{60} from higher fullerenes as demonstrated by Scrivens *et al.* using a mixture of silica and activated charcoal as the chromatographic plug in a flash chromatography.[124] This method was sucessfully used to separate a $C_{60}/N@C_{60}$ mixture from higher fullerene species after the ion implantation process in the past.[120] However, the composition of the chromatographic plug has to be adequately optimized to reduce the endohedral loss that could otherwise be as much as 39 %.[125] Using a design of experiments approach, Wieczorek identified not only the amount of activated charcoal but also the flow rate of the mobile phase (toluene) as a critical parameter in the flash chromatography process.[125] The latter can be adjusted be means of the used silica amount when preparing the slurry for the chromatographic plug. Based on the mass of the C_{60} species in the material, $m_{C_{60}}$, the amount of activated charcoal, $m_{\text{a.c.}}$, can be calculated using equation 7.5.

$$m_{\text{a.c.}} = \frac{m_{C_{60}}}{0.014} \tag{7.5}$$

This mass then determines the amount of silica (equation 7.6) to be used at the global optimum, resulting in a recovery for the C_{60} species of 98(2) %.[125]

$$m_{\text{silica}} = 21 \cdot m_{\text{a.c.}} \tag{7.6}$$

To purify the implanted material used in this thesis, the solid fullerene material obtained from the ion implantation process was dissolved in toluene, giving a brownish liquid with a fullerene mass concentration of about $0.75\,\text{g}\,\text{L}^{-1}$. This liquid was then filtered to remove insoluble reaction by-products and processed using the flash chromatography method (activated charcoal: Acros Organics NORIT SA 2, silica: Fluka silica gel 60, glass frit: typical porosity level 4). The endpoint detection in this process was done visually, since C_{60} solutions in toluene are colored deep purple, while C_{70} solutions possess a burgundy color. Care was taken not to drain the chromatographic plug, since even small cracks in the column result in an insufficient separation. The obtained $C_{60}/N@C_{60}$ solution was concentrated using a rotary evaporator to yield a mass concentration of about $1\,\text{g}\,\text{L}^{-1}$.

While the flash chromatography method is suitable to separate C_{60} and $N@C_{60}$ from other fullerene species, its separation efficiency is not high enough to separate or enrich $N@C_{60}$. However, as shown in figure 26, the Buckyprep phase has a high separation efficiency for fullerenes. It was successfully used to purify $N@C_{60}$ in earlier experiments,[120] as well as in the studies of others.[125–127] Figure 27 shows the preparative HPLC setup used to purify the material necessary for the experiments conducted in this work. The $N@C_{60}$ enrichment process is based on the fractionated collection of the HPLC eluate. A detailed composition of the used setup can be found in table A3 of the appendix on page 139. The most critical parameters for the preparative enrichment of $N@C_{60}$ are the column temperature and the length of the separation path. Increasing the latter one will of course result in an ever better chromatographic resolution but also drive up the systems flow resistance. Hence, the number of Buckprep columns that can be used in a practical sense is limited to three for the high pressure pump used here. For the separation temperature on the other hand, an optimum should exist. This separation sweet spot was found to be at 28 °C for the setup used in the present work.[125] It should be noted that no distinct $N@C_{60}$ peak can be observed in the preparative HPLC for material with $q \lesssim 1.3 \times 10^{-3}$

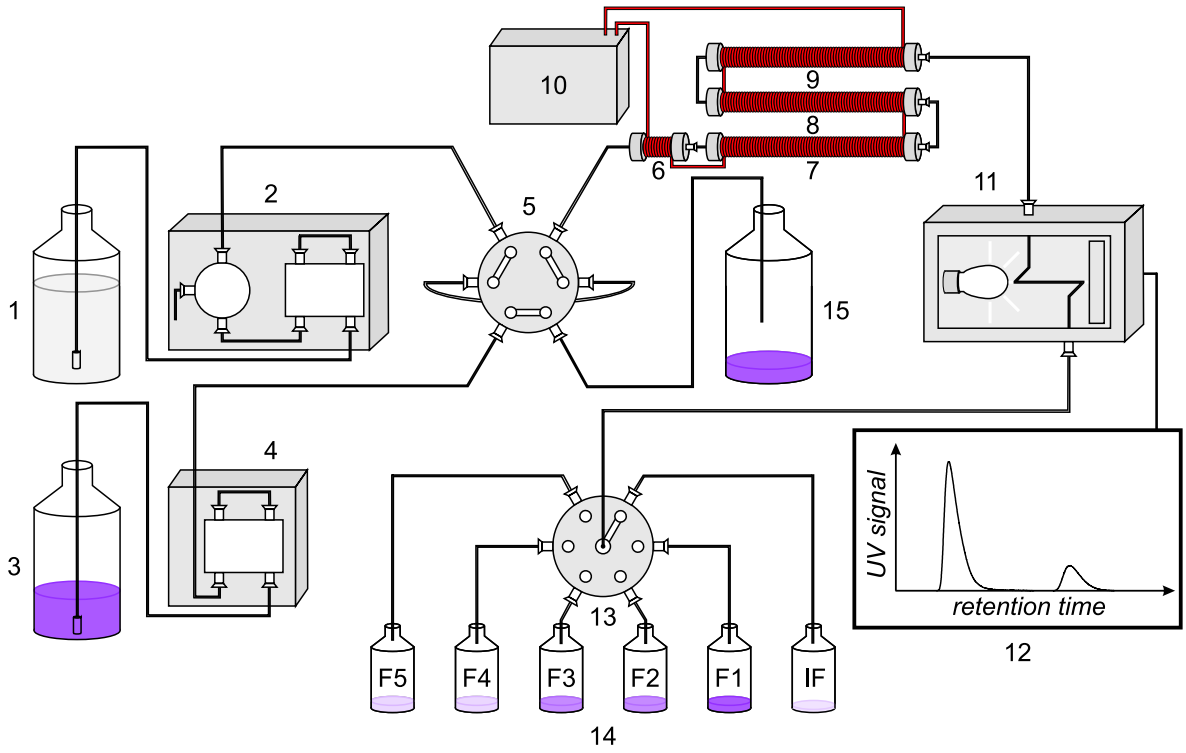

Fig. 27: Schematic diagram of the preparative HPLC setup used to purify N@C_{60}. The mobile phase (toluene) is pumped from the buffer bottle (1) through the injection valve (5) using the high pressure pump (2). The injection valve is used to introduce the C_{60}/N@C_{60} mixture (3) via the injection pump (4). The mobile phase and the fullerene mixture pass the guard column (6) and enter the separation columns A (7), B (8) and C (9) successively and eventually reach the UV detector (11). All columns of the setup are temperature controlled using the thermostat (10). The waste bottle (15) is used to collect overflowing material from the injection system. The collected data is displayed as a chromatogram (12) on the accompanying PC and used by the software to control the fractionation valve (13) in the programmed manner. All fractions are collected in individual bottles (14) with IF being the intermediate and F1 - F5 being the product fractions.

due to the partly overlapping, intensive C_{60} signal. Therefore, the fractionation of the eluate exiting the UV detector has to be performed based on experience and a test run with subsequent analytical determination of the N@C_{60} content in the different collected fractions.[120,125] The final fractionation pattern has then to be adjusted in a way such that a fraction with higher N@C_{60} concentration compared to the starting material is obtained, while the other fractions contain (almost) no N@C_{60}. This process is then repeated several times, until the desired N@C_{60} concentration is reached. In addition to the purification of N@C_{60}, the described process of fractionated eluate collection can be used to isolate other fullerene species as well.
In the present work, the C_{60}/N@C_{60} solution obtained from the flash chromatography process described above (mass concentration about $1\,\mathrm{g\,L^{-1}}$) was processed using the presented preparative HPLC setup running at a mobile phase (toluene) flow rate of $8\,\mathrm{mL\,min^{-1}}$. The column temperature was set to 28.0(1) °C and the UV detector was operating at a wavelength of $\lambda = 280\,\mathrm{nm}$. An

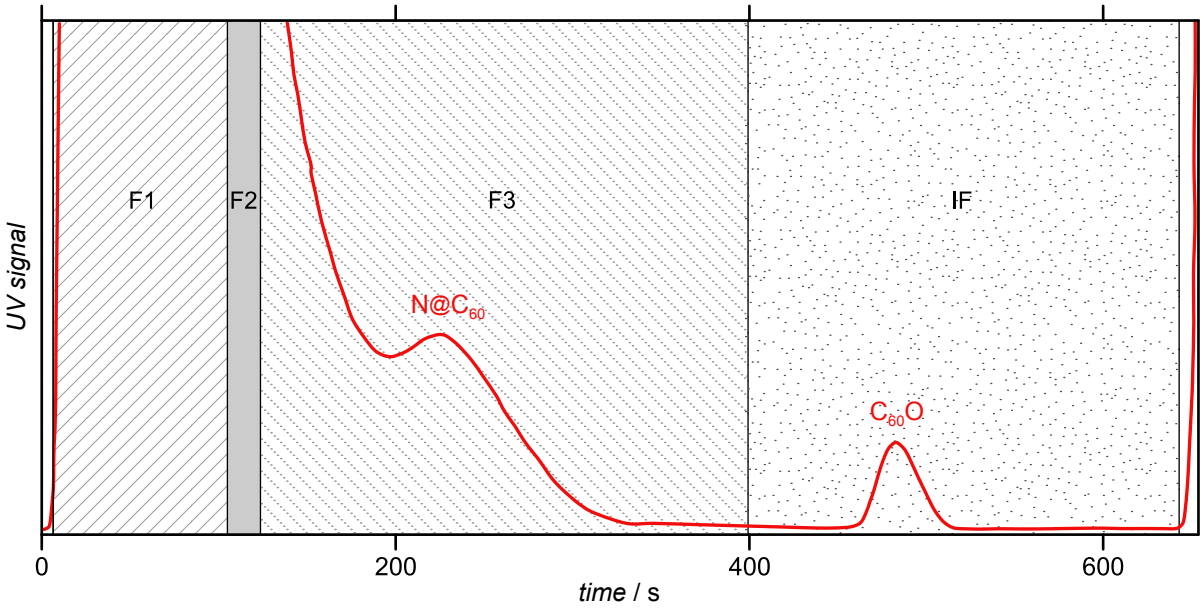

Fig. 28: Schematic diagram of a typical preparative HPLC fractionating pattern. A relative time scale starting shortly before the rise of the C_{60} signal is given. The intensive C_{60} signal was clipped in order to display the other signal components. Fraction F1 contains pure C_{60}, F2 typically shows a composition close to that of the starting material used, F3 contains the $N@C_{60}$ material and IF can be used to collect $C_{60}O$. The rise of the next C_{60} peak is indicated on the far right.

$N@C_{60}$ enrichment factor of up to 15.7 could be obtained using an injection interval of 630 s and collecting three fractions with respective collection times of $t_{F1} = 98\,s$, $t_{F2} = 16\,s$ and $t_{F3} = 270\,s$. However, because the injection interval and the collection times strongly depend on the rate of wear of the used column set and the quality of the starting material, these values can only serve as guidance. For a starting material with $q \approx 1.3 \times 10^{-3}$ the C_{60} peak began to elute 3200 s after the injection of the material was done. The maxima of the $N@C_{60}$ and $C_{60}O$ signals were observed 220 s and 475 s later, respectively. This situation is illustrated in figure 28, which additionally shows that the different fractions were not only of use for enriching $N@C_{60}$ but also to collect the $C_{60}O$ present in the IF fraction. Using the described fractionation process pure C_{60} and $C_{60}O$, as well as $N@C_{60}$ material with $q = 7.8(3) \times 10^{-3}$ was obtained.

7.4. Stability of C_{60} and $N@C_{60}$

The stability of $N@C_{60}$ is not only important for the use as a quantum bit,[118,128,129] but it is also of great interest when it comes to EDMR studies, since an unambiguous assignment of the observed spin resonance signals can only be done if the composition of the material under investigation is known.
Therefore, the stability of both C_{60} and $N@C_{60}$ under thermal and optical exposure was studied prior to this work.[98] In this study it could be clarified that $N@C_{60}$ is stable under intense optical exposure at a wavelength of $\lambda = 532\,nm$ if adequately cooled and that the decomposition of $N@C_{60}$ can be thermally induced at a constant temperature of $T = 423\,K$.[98] Nevertheless, it should be noted that others reported a decomposition temperature as high as 500 K - 550 K

when applying heating rates between 2 K/90 s and 2 K/82 s.[130,131] Besides the decomposition of $N@C_{60}$, which was observed by a decrease in the $N@C_{60}$-related EPR signal area, the occurrence of an additional radical signal with $g = 2.0026(3)$ and $\Delta B_{pp} = 0.113(1)$ mT was found to take place.[98] It could be identified as the paramagnetic species $^{-\bullet}C_{60}-O-O-C_{60}^{\bullet-}$, which can act as precursor in the formation of $C_{120}O$.[97] Hence, two major processes can take place if $N@C_{60}$ is exposed to heat:

1. Decomposition of the $N@C_{60}$ molecule via an escape of the encapsulated nitrogen atom by the formation of a [5,6] or [6,6] aza bridge followed by a nitrogen swing-out that eventually leads to EPR-silent diamagnetic reaction products, as proposed by Mauser *et al.*[132]

2. Formation of fullerene oxygenation products like $C_{60}O$ or $C_{120}O$ via the EPR-active species $^{-\bullet}C_{60}-O-O-C_{60}^{\bullet-}$ as already shown in figure 21.

In principle, the necessary C-C-bond elongation for process number one can also take place via an adiabatic photoreaction with a high activation barrier in the ground state and a low one in the excited state if $T \gtrsim 250$ K.[98,133] As introduced in section 7.1, process number two can be initiated by irradiating fullerene molecules with UV light.[96] The formation of $C_{60}O$ over time could also be observed during the chromatographic purification process done in this work. Even if the corresponding peak was removed in every HPLC cycle, it reappeared after a few days of storage. Hence, for EDMR measurements on pure C_{60} freshly purified material needs to be used.

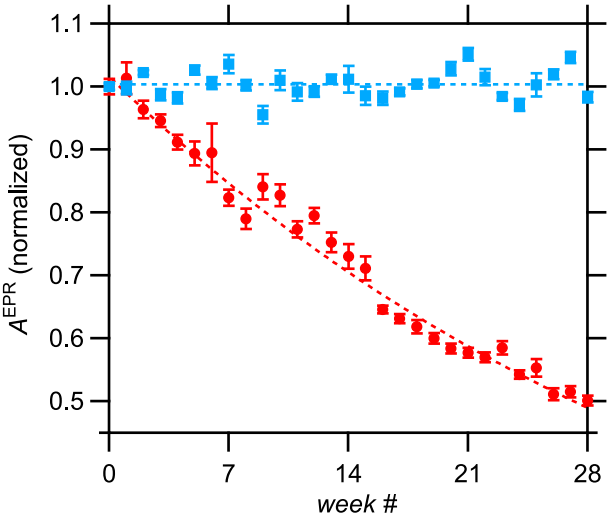

Fig. 29: Long-term stability study of $N@C_{60}$ in solution (red circles) and in the solid state (blue squares). For the solid-state sample, the dotted line shows the average of the EPR area, A^{EPR}. For the liquid sample it shows the used exponential fit, resulting in a time constant of $\tau = 38.3(7)$ weeks.

To asses the long-term stability of $N@C_{60}$, a liquid and a solid sample were prepared. For the liquid sample, 50 µL of an $N@C_{60}$ solution in toluene with $c = 0.119(5)\,\mathrm{g\,L^{-1}}$ and $q = 1.25(7) \times 10^{-3}$ were sealed in a standard EPR quartz glass tube under a protective nitrogen atmosphere. The solid state sample was prepared in a similar manner, using $m = 5.6(5)$ mg of a vacuum dried $N@C_{60}$ material with $q = 3.8(2) \times 10^{-4}$. The area under the resonance signal of both samples was recorded every week for a total period of 28 weeks. Figure 29 shows the results of this stability study. Only variations around the average are observed for the solid state sample, while the EPR area of the material in solution drops to about 50 %. The decay of the $N@C_{60}$ in toluene was analyzed using an exponential fit, resulting in a time constant of $\tau = 38.3(7)$ weeks. One possible explanation for this observation would be the presence or formation of toluene radicals. However, since no additional EPR signals were observed in any of the samples during this study, such solvent-based radicals must be consumed shortly after their formation. Furthermore, the samples were kept in the dark between the measurements and the described $N@C_{60}$ loss could also be observed in samples stored away from light for month, electively ruling out the light-induced formation of toluene radicals as the source of the $N@C_{60}$

decay. Another explanation for the observed decay is the excitation of molecular vibrations in solution, which than lead to the disintegration of the N@C_{60} molecule via the mechanism proposed by Mauser et al.[132] With the discrete phonon dispersion curves reported for solid C_{60},[134] this explanation seems rational since collisions between the molecules in the solid-state can not effectively induce molecular vibrations necessary for the nitrogen escape. In solution, however, this is not the case, which allows for the excitation of intra-molecular vibrations at ambient temperatures. Furthermore, the vibrations allowed in solution could depend on the solvent used as well, as indicated by Morton in his relaxation studies on N@C_{60}.[135] So far, a final decision on what process actually leads to the observed N@C_{60} decay in toluene solutions can not be made without further studies using different solvents or additional analytical methods like Raman spectroscopy.
In summary, the N@C_{60} material is stable if stored as a solid under a protective atmosphere. Thus, all synthesized or HPLC purified material should be vacuum dried for long-term storage instead of storing it in solution. Furthermore, the material has to be stored away from light to prevent the formation of $C_{60}O$ and N@$C_{60}O$.

7.5. Preparation of Fullerene Microcrystals

Various reports regarding the crystallization of fullerene materials are available in the literature.[136–142] Most of them, however, do not aim on providing a detailed theoretical modeling for the crystallization process but are rather focused on empirically opening up ways to new shapes and sizes. So far, no complete and universal description of fullerene crystallizations is available and the observations most likely need to be described by combining different models depending on the experimental conditions (e.g. C_{60} aggregation or nanoparticle-growth according to the model introduced by LaMer).[143–146] The transfer of knowledge and insights gained for a specific crystallization approach to an experiment with altered conditions is therefore difficult.
However, to prepare EDMR samples of fullerene microcrystals using the EDMR gold grid substrates illustrated in figure 11 (see chapter 3, section 3.2) the obtained crystals need to be of a compatible size. Reproduction, as well as optimization experiments, on the crystallization behavior of C_{60} were performed recently by Wieczorek.[125] The three different crystallization methods adapted from his work and the literature that were used in the present thesis are described below:

- **Solvent Evaporation**
  The solvent evaporation method is based on a resulting supersaturation in a fullerene solution due to a slow evaporation of the used solvent. Typically, this results in the formation of wire-like microcrystals.[142] The number of wires formed depends on the concentration of the starting solution.
  For the preparation of the EDMR samples used in this thesis 1.5 mM and 3 mM solutions of pure C_{60} in *m*-xylene were prepared. The solvent was then allowed to slowly evaporate at ambient temperature. Afterwards, the resulting microwires were dispersed in isopropanol and transfered onto suitable EDMR gold grid substrates. Figure 30 d) shows a laser scanning microscope picture of typical obtained C_{60} microwires and figure 30 e) illustrates the resulting ready-to-measure EDMR sample after transferring the microwires.

- **Liquid-Liquid Interfacial Precipitation (LLIP)**
  The liquid-liquid interfacial precipitation method allows for the crystallization to take place at the interface between a good and a poor solvent only.[147,148] This interface is prepared by carefully overlaying a saturated fullerene solution in a good solvent (e.g. benzene) with

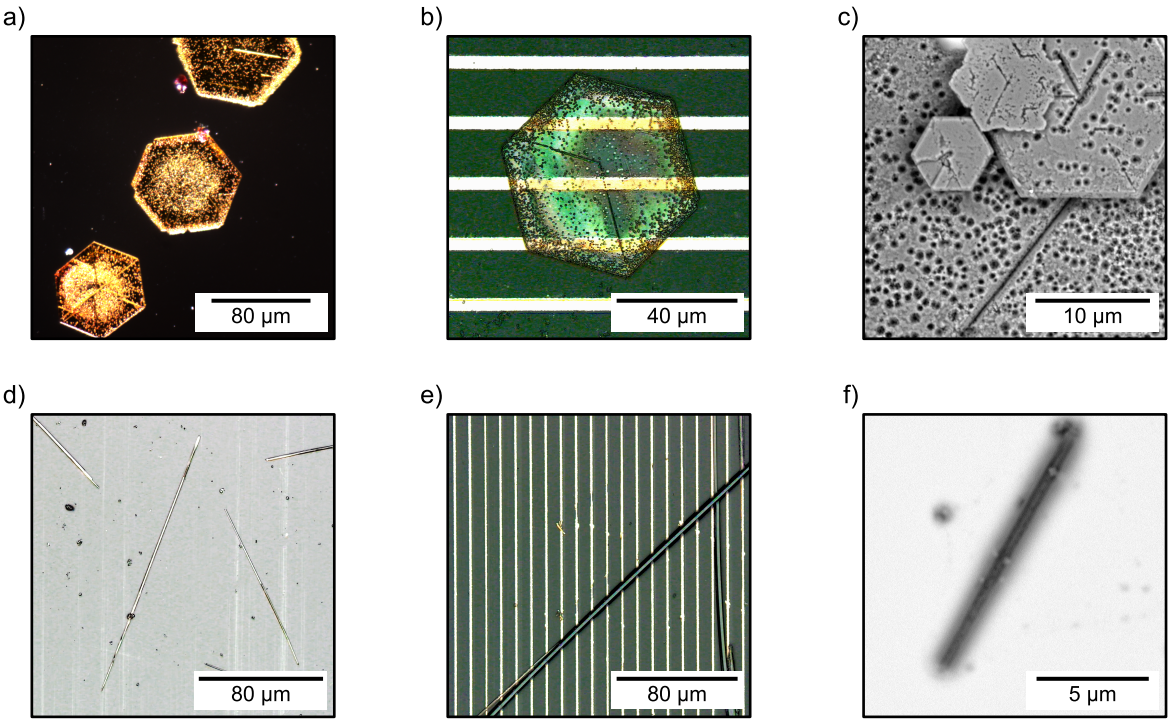

Fig. 30: Micro objects obtained from fullerene materials using different crystallization methods. a) Optical microscope image of the porous hexagonal shaped C_{60} sheets typically obtained via the LLIP method. b) Close-up laser scanning microscope picture of a C_{60} crystal after transferring it onto a test grid structure with a spacing of 20 µm. c) Scanning electron microscope picture of the porous crystal structure obtained using the LLIP method. Additionally, hexagonal shaped crystals of smaller size are visible. d) Laser scanning microscope picture of typical C_{60} microwires obtained using the *m*-xylene evaporation method. e) Laser scanning microscope image of a ready-to-measure EDMR sample with a grid spacing of 10 µm after a few microwires obtained from *m*-xylene evaporation were transfered onto it. f) Scanning electron microscope picture of a typical rod-shaped $C_{60}O$ crystal obtained via the dynLLIP method.

a poor solvent (e.g. isopropanol). In combination with cooling and a short crystallization period this restricts supersaturation to a very narrow region and different shapes and sizes of fullerene crystals – depending on the solvents – can be obtained.[139]
Following the approach described by Shrestha *et al.* for the fabrication of fullerene crystals with bimodal pore architectures,[139] the preparation of the EDMR samples used in this thesis was done starting with a saturated solution of C_{60}/N@C_{60} in a mixture consisting of 1 mL benzene and 1 mL of carbon tetrachloride. 1 mL of the saturated solution was cooled to $\vartheta = 6\,°C$ and then carefully overlaid with 5 mL of cooled isopropanol ($\vartheta = 6\,°C$). The sample was placed inside a refrigerator operating at $\vartheta = 6\,°C$ for a period of 60 min. Afterwards, the sample was gently shaken and then treated in an ultrasonic bath using a power of $P = 110\,W$ for 5 min. Finally, the sample was allowed to crystallize for a period of 20 h to 24 h at $\vartheta = 6\,°C$. The obtained crystals were then removed from the supernatant and thoroughly washed in isopropanol before they were transfered onto suitable EDMR gold

grid substrates. Figure 30 a) shows an optical microscope picture of the porous hexagonal shaped sheets that were typically obtained using this protocol. A close-up laser scanning microscope picture of such a crystal after transferring it onto a test grid structure is given in figure 30 b). Figure 30 c) shows a scanning electron microscope image of the porous crystal surface.

- **Dynamic Liquid-Liquid Interfacial Precipitation (dynLLIP)**
  The dynamic liquid-liquid interfacial precipitation is an advancement of the LLIP method. Unlike the LLIP method, the poor solvent is provided first. A small amount of a fullerene solution in a good solvent is then injected into the vigorously stirred poor one. After a short period of time, the stirrer is stopped and the final crystallization takes place. [140,141] With dynLLIP being a very rapid and easy to perform method, a large parameter space can be investigated in relatively short time, making it the method of choice for materials not crystallized before.
  The dynLLIP method was used in this thesis to prepare microcrystals from a 3.8 mM stock solution of pure $C_{60}O$ in *m*-xylene. 500 µL of the stock solution were injected into 10 mL of vigorously stirred isopropanol and the stirring was continued for 2 min. Afterwards, the stirrer was removed from the solution and the system was allowed to crystallize for about 72 h. The obtained rod-shaped crystals were then transfered to a typical EDMR substrate. Figure 30 f) shows a scanning electron microscope picture of a typical $C_{60}O$ crystal obtained via the dynLLIP method.

In summary, wire-like crystals from pure C_{60}, hexagonal sheet structures from C_{60} and $N@C_{60}$ and rod-like crystals from pure $C_{60}O$, each with dimensions large enough to span the available EDMR grid spacings introduced in chapter 3, section 3.2, were sucessfull prepared. Using a LLIP crystallization approach EDMR samples of $N@C_{60}$ – a material not accessible to evaporation methods due to its temperature sensitivity – could be made.

8. EDMR on C_{60} Microcrystals[†]

Crystalline microstructures offer the possibility to construct model architectures that could be useful for answering fundamental questions in the still developing method of EDMR. For example, one important motivation is to push the sensitivity of EDMR towards fewer spins by miniaturizing the investigated samples and thus constrict the possible carrier pathways. In addition, using a paramagnetic doping-on-demand strategy could be beneficial to gain further insights into the electronic transport in organic materials.
The remainder of this part is thus dedicated to a study on pure and doped fullerene microcrystals in order to enhance the EDMR method in organic materials and devices, e.g. by investigating dipolar couplings between different species inside a given sample. Before we can actually study a paramagnetically doped system, we need to look at the spectroscopic parameters observed in pure C_{60} microcrystals and clarify their origin, especially with respect to fullerene oxidation products, as these are generally difficult to avoid (cf. chapter 7, section 7.4). After some preliminary considerations regarding contact degradation, as well as the influence of bias voltage and illumination on the obtained signal magnitude, the spectroscopic parameters of pure C_{60}

[†]This chapter has partially been taken from the peer-reviewed journal article published in advance: M. Eckardt, J. Behrends, D. Münter, W. Harneit, Compact electrically detected magnetic resonance setup, *AIP Adv.* **2015**, *5*, 047139.

crystals will therefore be presented in this chapter. A comparison with EDMR results obtained on pure $C_{60}O$ material will be the subject of chapter 9.

8.1. Preliminary Considerations

In order to choose the right experimental conditions for the investigation of fullerene microcrystals – especially with respect to the limited availability of $N@C_{60}$ for studies on paramagnetically doped systems – the impact of contact degradation was studied preliminary to the actual EDMR investigations. Furthermore, to facilitate a rapid-investigation process for the delicate organic samples, the bias and illumination conditions giving the best EDMR signal magnitude had to be identified. Both preliminary investigations are briefly described below.

8.1.1. Degradation and Encapsulation

EDMR measurements on organic semiconductors, like the fullerene crystals investigated here, are somewhat difficult due to the fact that the interface between the organic material and the metal contact degrades rather quickly. Generally, degradation under the influence of moisture and oxygen is a common problem in organic semiconductors and electronic devices, such as organic solar cells and light emitting diodes, especially under illumination.[4,5]
Basically, two approaches exist to prevent degradation. The first one is to carry out all experiments inside the protective environment of a glove box where the sample is also prepared. Alternatively, the samples need to be encapsulated, which can be cumbersome in the case of EDMR since the whole device has to fit inside an EPR resonator. Furthermore, the encapsulation process itself may lead to unwanted chemical changes of the device due to interdiffusion of solvents or direct chemical reactions with the encapsulating agent. This is especially a problem for bare organic materials like the microcrystals investigated in this chapter, which are not completely covered by an evaporated metal electrode.
In the present work, biasing a microcrystal sample generally led to an increase of its resistance with time and eventually resulted in a non-conducting sample. Comparing the current-voltage characteristics of freshly prepared samples that were biased, illuminated or stored-only for a period of 90 min revealed that the degradation mainly takes place under the influence of bias or illumination, not due to storage. This suggests that the degradation of the EDMR samples may occur due to a charge and/or light induced polymerization of the fullerene molecules, for which to prevent an encapsulation would may not help completely. Hence, rather than introducing additional chemicals to the sample it was decided to use a rapid-investigation approach, which is possible with the presented benchtop EDMR setup due to the close proximity between the sample preparation equipment and the applied characterization techniques. Typically, the samples were investigated by EDMR only seconds after the final preparation step was completed.
However, due to the gradually degradation process under measuring conditions no quantitative studies on fullerene microcrystals could be conducted. So far, it is unknown if an operation of the benchtop spectrometer inside the protective environment of a glove box – which is technically possible due to its small footprint – would help to slow-down or prevent the observed degradation. Since there may be a thermal component involved in the process it could be beneficial to moderately cool the sample during the measurement using a suitable temperature controlling unit for the MiniScope MS400.

8.1.2. Sample Bias and Illumination

Working with delicate samples it was important to ensure good measuring conditions with respect to the applied sample bias voltage V_{bias} and illumination intensity P_{irr}. One boundary condition for V_{bias} is the occurrence of a sparkover on the EDMR gold grid substrates, which depends on the applied electric field. The maximum field values possible were determined experimentally and the following limits were found (see figure 11 for the definition of the fine structure distance):

- 10 µm fine structure distance: $2.00 \times 10^7\,\mathrm{V\,m^{-1}}$
- 5 µm fine structure distance: $3.40 \times 10^7\,\mathrm{V\,m^{-1}}$
- 3 µm fine structure distance: $4.33 \times 10^7\,\mathrm{V\,m^{-1}}$

Although quantitative experiments were not possible using the fullerene microcrystal samples, as discussed in section 8.1.1, the following qualitative observations when increasing V_{bias} and P_{irr} can be stated. An increase of the SNR could generally be observed with increasing V_{bias} and P_{irr}. When considering the formation of charged fullerene species in the sample due to charge carrier injection via the electrode structure and photoexcitation of the fullerene molecules, it becomes clear that the recombination rate - including the spin-dependent recombination - could somehow depend on these two parameters. Additionally, decreasing the fine structure distance of the EDMR substrates, and hence the path length between the two contacts, can have an influence on the recombination probability in the sample.
In this study the dependence of the EDMR signal area, A^{EDMR}, on the applied illumination intensity was far more pronounced than the one on V_{bias}. Furthermore, it should be noted that without illumination almost no EDMR signal could be observed. This indicates that photogenerated carriers are mainly responsible for the EDMR signal obtained from fullerene microcrystals. In summary, it was found that both sample bias and illumination intensity should be chosen as high as technically possible to obtain intense EDMR signals. This is especially important for observing possible spin-couplings in doped fullerene materials (see chapter 10). Furthermore, no alteration of the spectroscopic parameters was observed, indicating that the species under study did not change as a function of bias voltage or illumination.

8.2. EDMR Results on C_{60} Microcrystals

Using pure C_{60} material obtained from the preparative HPLC process described in chapter 7, section 7.3, wire-like crystals were prepared following the solvent evaporation method introduced in section 7.5. A part of the obtained microwires was transfered to an EDMR substrate with a fine structure distance of 10 µm (cf. figure 11) resulting in the ready-to-measure EDMR sample depicted in figure 30 e). As a first experiment, the current-voltage characteristics of this sample under illumination with $P_{\mathrm{irr}} = 2.2 \times 10^{-1}$ suns was recorded, figure 31 c) shows the obtained result. The non-ohmic behavior expected for C_{60} as an organic semiconductor is clearly visible, showing the sucessfull transfer on and connection to the EDMR substrate's gold electrode structure. Although the investigated sample consisted of only very few fullerene wires, a measurable current signal was obtained.
To determine the spectroscopic parameters of the prepared microwires a similar EDMR sample was prepared and studied using different settings for the magnetic field modulation amplitude at a microwave source power of $P_{\mathrm{MW}} = 100\,\mathrm{mW}$. A single-scan EDMR spectrum of this sample is shown in figure 31 a). As illustrated in figure 31 b), the intrinsic inhomogeneous linewidth could be determined to be $\Delta B_{\mathrm{int}} = 0.30(5)\,\mathrm{mT}$ using Poole's description for a modulation-broadened signal given in equation 5.1.[54] This value is in excellent agreement with earlier investigations

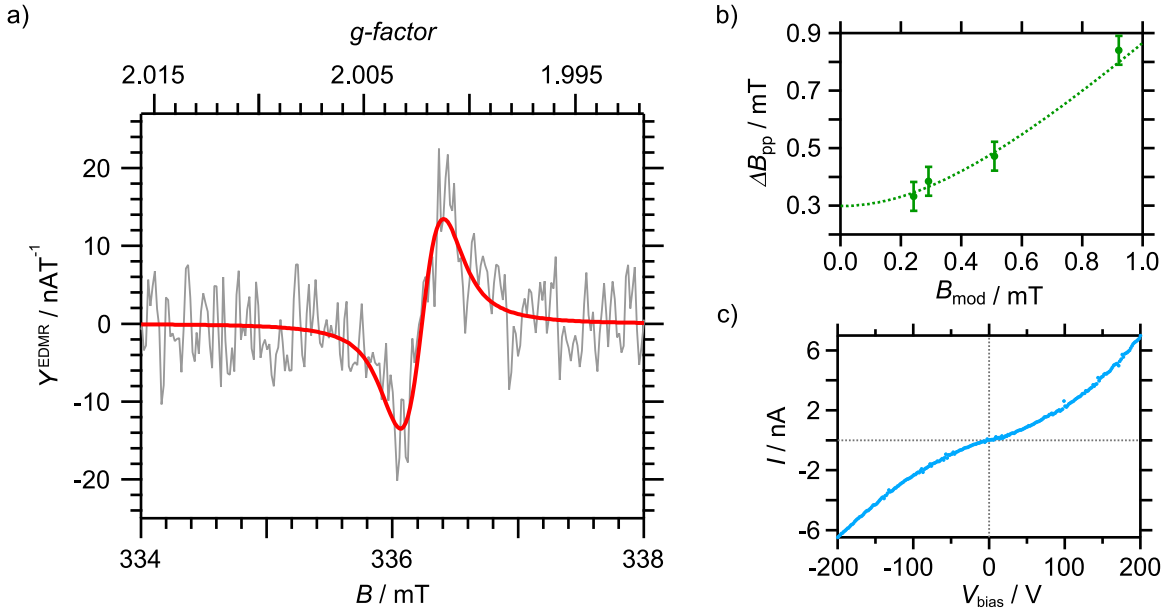

Fig. 31: Experimental results obtained on C_{60} microwires. a) Light-induced EDMR spectrum of C_{60} microwires crystallized from a 3 mM *m*-xylene solution. The data were acquired at $V_{bias} = -150\,V$, $f_{mod} = 625\,Hz$, $B_{mod} = 0.24\,mT$ and $P_{irr} = 2.2 \times 10^{-1}$ suns on a substrate with a spacing of 10 µm. The experimental data were fitted (red line) using a pseudo-Voigt profile, resulting in $g = 2.0022(3)$ and $\Delta B_{pp} = 0.33(5)\,mT$. b) Dependence of the apparent linewidth ΔB_{pp} on B_{mod}. ΔB_{pp} was fitted (dotted line) using Poole's equation for a modulation-broadened linewidth (equation 5.1), yielding an intrinsic linewidth of $\Delta B_{int} = 0.30(5)\,mT$. c) Current-voltage characteristics of the sample shown in figure 30 e) recorded inside the EDMR spectrometer under illumination with $P_{irr} = 2.2 \times 10^{-1}$ suns.

reported by Schäfer *et al.* for C_{60} thin-film samples.[149] An EDMR effect (cf. equation 3.9) of $\xi_{sd}^{EDMR} \approx 8 \times 10^{-5}$ was observed for the sample, which is comparable to that of thin-film devices made from C_{60}.[149,150] For the *g*-factor a value of $g = 2.0022(3)$ was found, in accordance with a value observed in C_{60} thin-film devices studied by pulsed EDMR.[149]

In addition to the experiments on wire-like crystals, measurements were also performed on EDMR samples prepared using porous hexagonal sheets obtained from an LLIP crystallization of C_{60} material as described in section 7.5. As expected, these structures provided results indistinguishable from those obtained for the microwires ($g = 2.0020(3)$, $\Delta B_{pp} = 0.32(5)\,mT$, $\xi_{sd}^{EDMR} \approx 8 \times 10^{-5}$) if measured using comparable experimental conditions including bias voltage, illumination and substrate fine structure distance. This is an important result, since the LLIP method yields a more uniform size distribution than the simple solvent evaporation method and can be easily optimized in order to produce micro-devices or even nano-structures for future works that can help pushing the sensitivity of EDMR towards fewer spins.

So far, the question that remains is what kind of fullerene species is actually observed in EDMR studies on C_{60} at ambient temperature. In CW-EDMR, signals at $g = 2.0017 - 2.0020$ were reported and attributed to spin-dependent recombination of photo-generated, non-geminate charge carrier pairs presuming either a polaron pair as the precursor for the recombination or a defect site formed by impurities.[44,150,151] Another possibility discussed is the spin-dependent recombina-

tion of charge carriers at photo-generated fullerene dimer impurities such as C_{120} or $C_{120}O$.[34,149] However, as will be shown in chapter 9, oxidized C_{60} material possesses a slightly higher g-factor than the one observed here. Additionally, as mentioned in chapter 7, section 7.1, $g = 2.0022$ and $\Delta B_{pp} = 0.3\,\mathrm{mT}$ was observed for the radical $C_{60}^{\bullet+}$ in an EPR study by Reed *et al.*[95] and the negatively charged species $C_{60}^{\bullet-}$ shows a characteristically low g-factor between 1.994 and 2.000 but can not be observed at ambient temperatures due to a strongly temperature dependent signal broadening effect.[92,93]
Hence, the EDMR signal observed in this thesis with $g = 2.0022(3)$ and $\Delta B_{int} = 0.30(5)\,\mathrm{mT}$ is attributed to a spin-dependent recombination of photo-generated $C_{60}^{\bullet+}$. The recombination partner is assumed to be $C_{60}^{\bullet-}$, not visible at ambient temperature. A signal corresponding to $C_{60}O$ or rather its precursor radical $^{-\bullet}C_{60}{-}O{-}O{-}C_{60}^{\bullet-}$ (cf. figure 21) could not be detected in the samples investigated in this study. The presented results on C_{60} microcrystals, however, demonstrate that even a relatively small number of organic semiconductor crystals can be contacted in a simple manner and still deliver sufficient currents for EDMR studies.

9. EDMR on $C_{60}O$ Microcrystals

When storing or processing fullerene materials it is generally difficult to avoid the formation of oxidation products like $C_{60}O$ and $C_{120}O$, as mentioned earlier in this thesis (see chapter 7, section 7.4, as well as figure 21 for details). For this reason, the EDMR investigations on pure C_{60} crystals presented in the previous chapter were carried out on freshly prepared material, purified by HPLC. Nevertheless, it is important to gain some knowledge about the EDMR signature of oxidized materials, since oxidation also occurs on an EDMR sample with time, resulting in questionable signal assignments and interpretations. So far, however, no such EDMR study is available in the literature. With pure $C_{60}O$ material being readily available from the preparative HPLC process done in this work, a first study combining EPR and EDMR on crystals made from this material is presented below.

9.1. EPR Analysis of the Prepared EDMR Samples

As presented in chapter 7, section 7.3, the intermediate fraction collected during the preparative HPLC procedure, used to purify the nitrogen implanted fullerenes, mainly contained $C_{60}O$ (cf. figure 28). By pooling the intermediate fractions of several HPLC runs a solution of $C_{60}O$ in toluene was obtained. Pure $C_{60}O$ material was then prepared using a preparative scale HPLC similar to the one utilized for the $N@C_{60}$ purification, but with only one separation column instead of three and no temperature controlling unit. Due to the rather large retention time differences between C_{60}, $C_{60}O$ and higher fullerenes like C_{70} and C_{120}, the desired material could be obtained using only one purification cycle.
Figure 32 a) shows the result of the HPLC analysis performed on the obtained $C_{60}O$ material. The absence of a signal at a retention time of 490 s confirms the successful remove of C_{60}. The retention time difference between C_{60} and $C_{60}O$ is known to be 53 s when using the HPLC method described in chapter 7, section 7.2.3,[152] resulting in a retention time of 543 s for $C_{60}O$ on our analytical HPLC setup. Additionally, the C_{70} peak with its characteristic retention time of about 789 s is missing (cf. figure 26). As reported earlier, the higher fullerene oxidation product $C_{120}O$ possesses a retention time of about 1200 s on the analytical HPLC setup used,[98] and is clearly not present in the purified material.
As described in chapter 7, section 7.5, rod-shaped crystals were obtained from the purified $C_{60}O$

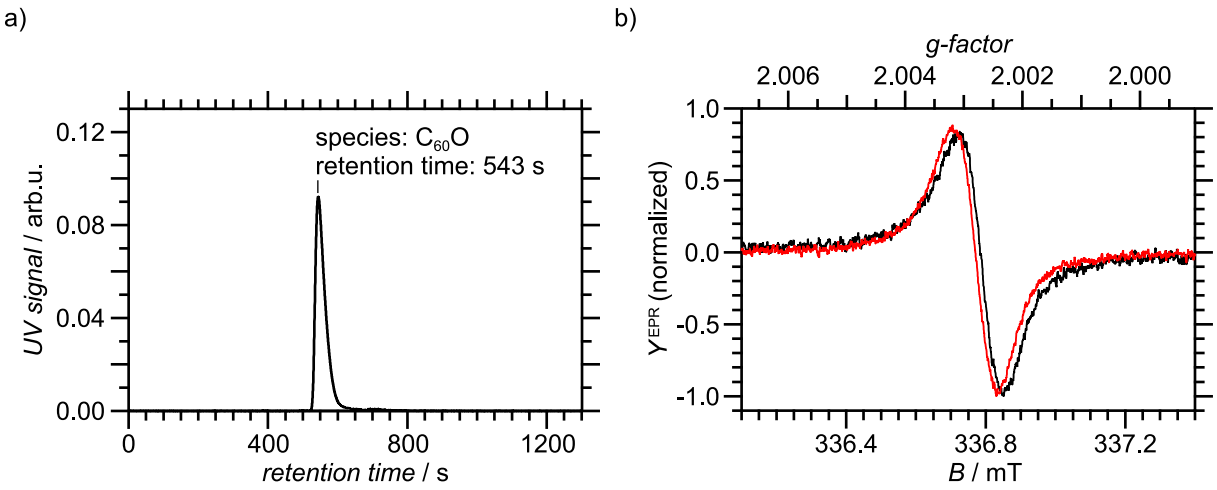

Fig. 32: HPLC and EPR analysis of the purified $C_{60}O$ material. a) HPLC chromatogram illustrating the sucessfull purification of the material with no observable signals corresponding to C_{60}, C_{70}, C_{120} or $C_{120}O$. b) EPR spectra of the purified $C_{60}O$ solution (red) with $g = 2.0028(3)$ and $\Delta B_{pp} = 0.126(1)\,\mathrm{mT}$, as well as the prepared ready-to-measure EDMR sample (black) with $g = 2.0027(3)$ and $\Delta B_{pp} = 0.126(1)\,\mathrm{mT}$. Both samples are indistinguishable within the measurement uncertainties. As discussed in the text, the EPR signal is attributed to secondary products formed by $C_{60}O$, like the paramagnetic precursor $^{-}\cdot C_{60}{-}O{-}O{-}C_{60}{}^{\cdot -}$.[97,98]

material using the dynLLIP method. These crystals were transfered to an EDMR substrate with a fine structure distance of 5 µm (cf. figure 11) to prepare the final EDMR sample. Afterwards, an EPR experiment on the ready-to-measure EDMR sample was performed. Figure 32 b) shows the result of this study together with the corresponding spectrum obtained from the purified $C_{60}O$ solution used for crystallization. As can be seen, both the solution and the prepared microcrystals exhibited identical spectroscopic properties within the measurement uncertainties. This EPR signature is known to belong to the paramagnetic species $^{-}\cdot C_{60}{-}O{-}O{-}C_{60}{}^{\cdot -}$,[97] which acts as a precursor in the formation of $C_{60}O$ (cf. figure 21), and was also observed in the stability study on $N@C_{60}$ mentioned in chapter 7, section 7.4.[98] This signal was not to be expected in the purified $C_{60}O$ material, since the HPLC analysis did not show the presence of any higher fullerenes or higher fullerene oxides. Furthermore, even if the concentration of those species was below the detection limit of the used analytical HPLC setup, they would have been completely separated in the fractionated preparative-scale HPLC process due to their far longer retention times.

However, with the epoxy-ring being the weakest bond in the $C_{60}O$ molecule (due to its high strain), it seems possible that a rupture of an epoxy-bond can occur, resulting in an "open-epoxy-ring" structure. The resulting molecule could then react with another $C_{60}O$ to form $^{-}\cdot C_{60}{-}O{-}O{-}C_{60}{}^{\cdot -}$, or a constitutional isomer thereof. Furthermore, the $C_{60}O$ molecule may be in equilibrium with its EPR-active "open-epoxy-ring" form. Since the discussed secondary products of $C_{60}O$ are structurally related and radical character can well be located on the same part of the molecule, namely the fullerene cage, it seems possible that these structures posses an indistinguishable g-factor and linewidth in the X-band CW-EPR experiments performed in the present work.

9.2. EDMR Results on $C_{60}O$ Microcrystals

The $C_{60}O$ EDMR sample investigated by EPR in the last section was instantaneously studied using EDMR. The bias voltage was set to $V_{\mathrm{bias}} = 210\,\mathrm{V}$, resulting in an average sample current of $I_{\mathrm{sample}} = 468\,\mathrm{nA}$ at a light intensity of $P_{\mathrm{irr}} = 0.5$ suns. Using a modulation frequency of $f_{\mathrm{mod}} = 620\,\mathrm{Hz}$, a field modulation amplitude of $B_{\mathrm{mod}} = 0.3\,\mathrm{mT}$ and a microwave source power of $P_{\mathrm{MW}} = 100\,\mathrm{mW}$, the EDMR spectrum shown in figure 33 could be obtained.
An EDMR effect (cf. equation 3.9) of $\xi_{\mathrm{sd}}^{\mathrm{EDMR}} \approx 4 \times 10^{-6}$ was observed for this sample, which is about a factor of 20 lower than the one obtained for the C_{60} microcrystals presented in chapter 8. Furthermore, a g-factor of 2.0029(3) and a peak-to-peak linewidth of $\Delta B_{\mathrm{pp}} = 0.39(7)\,\mathrm{mT}$ was obtained by fitting the experimental data using a pseudo-Voigt function. Repeated measurements on this and another sample of oxidized fullerenes confirmed the finding of $g \approx 2.0030$ for this type of material.
Comparing these results with the ones obtained on C_{60} microcrystals shows a slight increase of the g-factor for the oxidized fullerene material. Due to the rather large measurement uncertainties for ΔB_{pp}, however, no statement on the influence of the oxidation on the observed linewidth is possible so far. Although the HPLC analysis performed on the final purified $C_{60}O$ material did not show the presence of higher fullerenes or higher fullerene oxides, EPR active species could well have been formed as a secondary product of $C_{60}O$ as discussed in section 9.1. The presence of such species was confirmed in the purified $C_{60}O$ solution, as well as in the prepared microcrystals, as shown in figure 32 b). Giving a general rule of thumb on the g-factor shift when introducing a heteroatom like oxygen in a molecule is difficult due to the comprehensive information that is needed about the involved excited states (e.g. energy, symmetry and occupation) as discussed in chapter 1, section 1.2.1. Nevertheless, comparing the g-factors obtained in the EPR and EDMR experiments suggests a measurement on the same kind of molecule in both cases. Hence, the paramagnetic species originating from $C_{60}O$ seem to be involved in the observed EDMR process. The resulting linewidth is somewhat larger for the EDMR experiment. However, looking at equation 2.23 this is to be expected due to the EDMR pair lifetime T_{pair}. Furthermore, the obtained EDMR spectrum shows a much weaker signal intensity than the corresponding EPR measurement. This can be attributed to the fact that, in contrast to EPR, EDMR is only sensitive to those spins involved in a spin-dependent process.

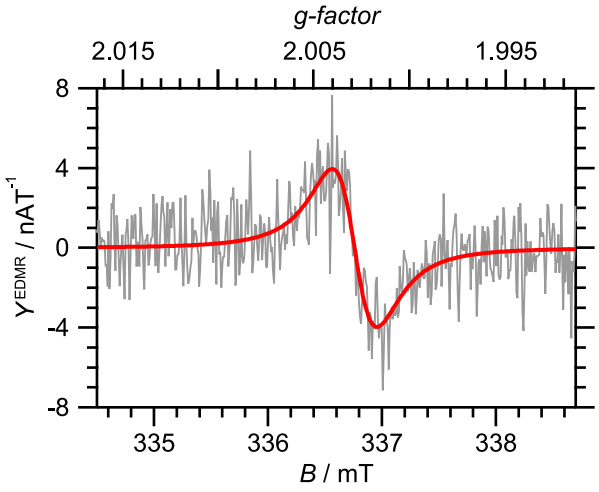

Fig. 33: Light-induced EDMR spectrum of $C_{60}O$ microcrystals recorded at $V_{\mathrm{bias}} = 210\,\mathrm{V}$, $B_{\mathrm{mod}} = 0.3\,\mathrm{mT}$ and $P_{\mathrm{irr}} = 0.5$ suns. Experimental data were fitted (red) using a pseudo-Voigt profile, resulting in $g = 2.0029(3)$ and $\Delta B_{\mathrm{pp}} = 0.39(7)\,\mathrm{mT}$.

In summary, the EDMR signal observed in the prepared $C_{60}O$ microcrystals is tentatively attributed to spin-dependent recombination of photo-generated charge carriers involving a secondary product of $C_{60}O$, which (as discussed in section 9.1) could be an "open-epoxy-ring" form of the molecule, the intermediate $^{-}\cdot C_{60}-O-O-C_{60}{}^{\cdot -}$, or a constitutional isomer thereof. Although, a final proof for the correct assignment of the EDMR signal can not be provided so

far, and $C_{60}O^{\cdot+}$ as well as $C_{60}O^{\cdot-}$ could also be relevant, it seems clear that the oxidation of fullerene molecules can result in a slight shift of the g-factor towards higher values. Thus, an EDMR spectrum obtained on older fullerene material could in fact be a superposition of oxidized and pure material spectra and care must be taken when assigning EPR or EDMR signals. This could, for example, also be the reason for the unusual g-factors of the fullerene material $PC_{61}BM$ reported in the pulsed EDMR study conducted by Morishita *et al.*[11]

10. EDMR on N@C_{60}-Doped Microcrystals

Building on the fullerene microcrystal results presented in chapter 8, we will now turn our attention to the paramagnetic doping of these microstructures. The endohedral fullerene N@C_{60} introduced in chapter 7, section 7.2, with its unique spectroscopic properties ($S = 3/2$, well-resolved hyperfine splitting, very sharp lines in the solid state), is a virtually perfect candidate for such an undertaking. Using the ion implantation technique and preparative HPLC method described in chapter 7, a suitable amount of N@C_{60} material with $q = 7.8(3) \times 10^{-3}$ (see equation 7.4) could be prepared in this work. However, since N@C_{60} cannot be sublimed without disintegration of the molecule,[98,130] a doping by vacuum-deposition is impossible using this material. We will therefore use the experience gained during the EDMR measurements on pure C_{60} and $C_{60}O$ microcrystals obtained from "cold solutions" that were presented in chapters 8 and 9 to investigate EDMR samples of N@C_{60}-doped C_{60} microcrystals in the remainder of this second part of the present thesis.

10.1. EPR Analysis of the Prepared EDMR Samples

N@C_{60}-doped microcrystals of hexagonal shape were prepared from a mixture of C_{60}/N@C_{60} with $q = 7.8(3) \times 10^{-3}$ using the LLIP method as described in chapter 7, section 7.5. Afterwards, the crystals were transfered onto EDMR substrates with a fine structure distance of 5 µm (cf. figure 11), resulting in EDMR samples similar to the test grid shown in figure 30 b). EPR experiments were performed on each ready-to-measure EDMR sample, using the EPR mode of the benchtop EDMR spectrometer presented in part I of this work. To prevent artificial broadening effects, the microwave source power was kept as low as 10 µW and the field modulation amplitude was limited to $B_{\mathrm{mod}} = 10\,\mu\mathrm{T}$. Figure 34 shows a typical result of such an EPR experiment. All investigated samples were indistinguishable within the experimental errors.

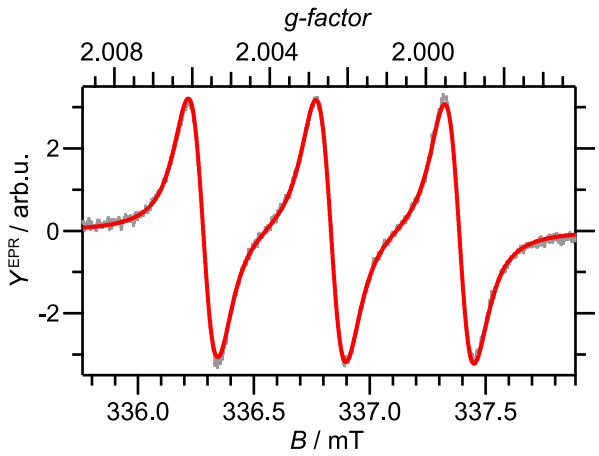

Fig. 34: EPR spectrum of an EDMR sample of N@C_{60}-doped microcrystals. The data were fitted using a three-peak pseudo-Voigt function (red line), resulting in $g = 2.0024(3)$, $\Delta B_{\mathrm{pp}} = 0.13(1)\,\mathrm{mT}$ and a hyperfine splitting of 0.56(1) mT.

As introduced in chapter 7, section 7.2.1 the N@C_{60} spectrum consists of three narrow lines. A g-factor of 2.0024(3) was found for the final EDMR samples and the observed hyperfine interaction can be characterized using an isotropic coupling constant of 0.56(1) mT.

These values are in accordance with the results obtained on toluene solutions of the N@C_{60} raw material, as well as with the results reported by others.[113,117,153] The peak-to-peak linewidth was found to be 0.13(1) mT, which is larger than the value mentioned in chapter 7, section 7.2.1 for N@C_{60} in solution. This is a result of the differences in the relaxation times and spin-interactions of the solid state compared to the liquid samples (cf. chapter 1, sections 1.3.2 and 1.3.3).
It is worth noting that EPR experiments performed on the contacted microcrystals before and after an EDMR study showed no changes in the recorded spectra. Hence, even though the EDMR samples degraded over time and eventually became unmeasurable (see chapter 8, section 8.1.1), the N@C_{60} dopants *per se* were stable under the applied experimental conditions. This observation is particularly important for the use of EDMR as a potential read-out method for molecular quantum bits based on the N@C_{60} material.[34,118,154]

10.2. EDMR Signature of N@C_{60}-Doped Microcrystals

EDMR measurements were performed on two different samples investigated by EPR beforehand (see section 10.1 for sample preparation and EPR results). For each sample, the bias voltage was selected depending on the resulting sample current. In this study, either $V_{\mathrm{bias}} = -100\,\mathrm{V}$ or $V_{\mathrm{bias}} = -200\,\mathrm{V}$, resulting in $I_{\mathrm{sample}} \approx -600\,\mathrm{nA}$, was used. The modulation frequency was set to

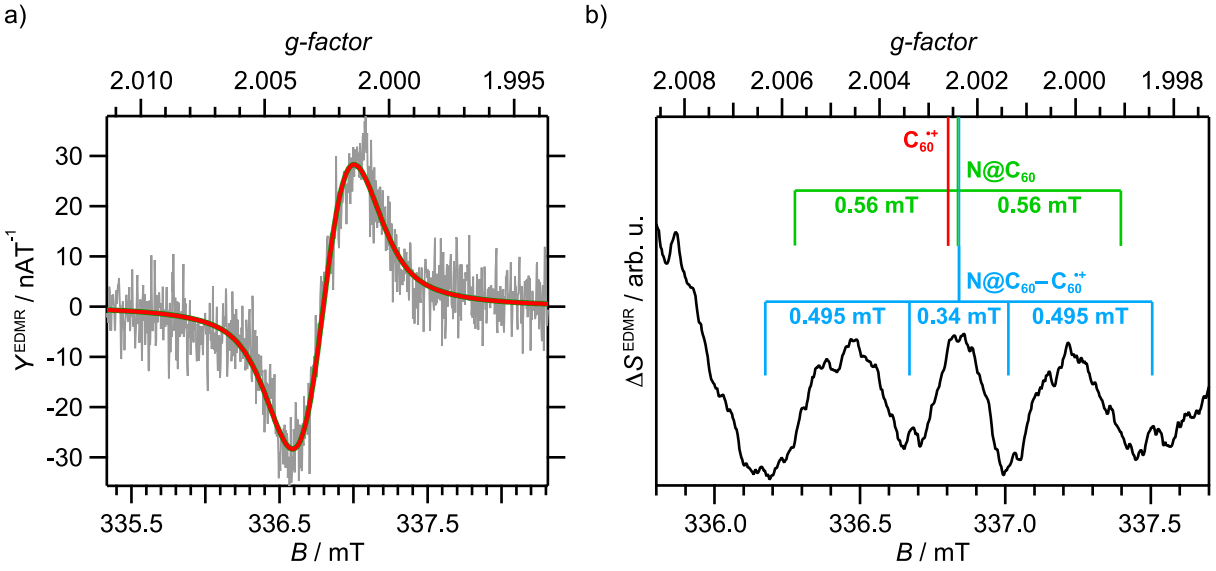

Fig. 35: EDMR results obtained on N@C_{60}-doped microcrystals. a) Light-induced EDMR spectrum of N@C_{60}-doped microcrystals recorded at $V_{\mathrm{bias}} = -100\,\mathrm{V}$, $B_{\mathrm{mod}} = 0.1\,\mathrm{mT}$ and $P_{\mathrm{irr}} = 0.5$ suns. The experimental data were fitted (red line) using a pseudo-Voigt profile, resulting in $g = 2.0026(3)$ and $\Delta B_{\mathrm{pp}} = 0.41(5)\,\mathrm{mT}$. b) Integrated EDMR difference (ΔS^{EDMR}) spectrum (average of two samples) constructed by subtracting the broad resonance due to uncoupled $C_{60}^{\bullet+}$. Also indicated are the line positions for $C_{60}^{\bullet+}$ and neutral N@C_{60} as measured by EDMR in figure 35 a) and EPR in figure 34, respectively.

$f_{\mathrm{mod}} = 620\,\mathrm{Hz}$ and a modulation amplitude of $B_{\mathrm{mod}} = 0.1\,\mathrm{mT}$ was chosen, based on an observed linewidth of $B_{\mathrm{pp}} = 0.13(1)\,\mathrm{mT}$ in the EPR measurements presented in the previous section. A microwave source power of $P_{\mathrm{MW}} = 100\,\mathrm{mW}$ was used and the illumination intensity during the EDMR experiments was set to $P_{\mathrm{irr}} = 0.5$ suns. Figure 35 a) shows the resulting EDMR

spectrum obtained on the same sample whose EPR spectrum is shown in figure 34. The other sample gave a comparable spectrum with spectroscopic parameters that were indistinguishable within the experimental errors. The spectra are dominated by a signal with $g = 2.0026(3)$ and $\Delta B_{\mathrm{pp}} = 0.41(5)\,\mathrm{mT}$, which is attributed to originate from the radical $C_{60}^{\cdot+}$ rather than from an oxidized species due to the facts that the corresponding EPR spectra did not indicate the presence of such species (cf. figure 34), and that only freshly purified material was used (cf. chapters 8 and 9).
Due to the presence of the intense signal caused by uncoupled $C_{60}^{\cdot+}$, a possible N@C_{60}-related structure is difficult to observe. Thus, the broad $C_{60}^{\cdot+}$ resonance signal described by the fit to the experimental data was subtracted from the latter, and the resulting difference spectrum was integrated to give the "integrated difference EDMR signal" ΔS^{EDMR}, in which a possible hyperfine structure or spin-coupling can be more easily identified. This way, a structure superimposed on the dominating $C_{60}^{\cdot+}$ signal could be observed for both EDMR samples. This structure was identical within the experimental uncertainties, and the average of ΔS^{EDMR} of both samples was thus calculated to further improve the SNR. The result of this approach is shown in figure 35 b), which represents a total of 30 EDMR scans with a scan time of $t_{\mathrm{scan}} = 360\,\mathrm{s}$.
A symmetric structure consisting of four lines with distances of 0.495 mT and 0.34 mT can be identified in figure 35 b) as indicated by the blue lines. As a working hypothesis, this structure is attributed to dipolar-coupled N@C_{60}-$C_{60}^{\cdot+}$ spin pairs, and we will further investigate this interpretation in section 10.3. Furthermore, figure 35 b) shows the line position of $C_{60}^{\cdot+}$, which was determined in the EDMR experiment itself, as well as the ones of the N@C_{60} molecule as determined by the EPR measurements presented in section 10.1.

10.3. Dipolar Coupling Between N@C_{60} and $C_{60}^{\cdot+}$

A first spectroscopic evidence for strongly dipolar-coupled pairs in EDMR was presented in section 10.2. Based on the EDMR results obtained on pure C_{60}, as well as oxidized fullerene material (see chapters 8 and 9), the structure observed in the constructed ΔS^{EDMR} spectrum was attributed to N@C_{60}-$C_{60}^{\cdot+}$ spin pairs. We want to further investigate this working hypothesis in this section. In order to capture the essential features, we make the following simplifying assumptions: a) Our sample consists of only few crystals, but with unknown orientation. Additionally, the crystals may contain amorphous parts. Therefore, we will use a powder average approach. b) Although the HOMO of $C_{60}^{\cdot+}$ is not spherically symmetric, we will use a point-dipole approximation. c) While in principle we have an infinitely coupled network of spins, we will treat the sample as consisting of only isolated spin pairs in order to specify a simple Hamiltonian. In this Hamiltonian, we will use only a single coupling constant, even though several of them may be needed for a full description. Thus, the used coupling strength only represents an average of the actual values. With these assumptions, we can set up a simulation using the EasySpin package developed by Stoll *et al.*[155]
Any EasySpin simulation is based on a set of parameters that specify the spin system. As introduced in chapter 1 (section 1.2), the total spin Hamiltonian for a two-spin system consists of the spin Hamiltonian of each constituent plus an additional spin-spin interaction term (see equation 1.9). For the working hypothesis presented in this thesis, the parameters specifying the individual Hamiltonians (like total electron spin, g-factor and isotropic hyperfine coupling constant) for the two spin-pair partners N@C_{60} and $C_{60}^{\cdot+}$ are known either from the literature or from the experiments conducted in this work. Furthermore, some experimental parameters, like temperature and microwave frequency, can be specified in order to facilitate a direct compar-

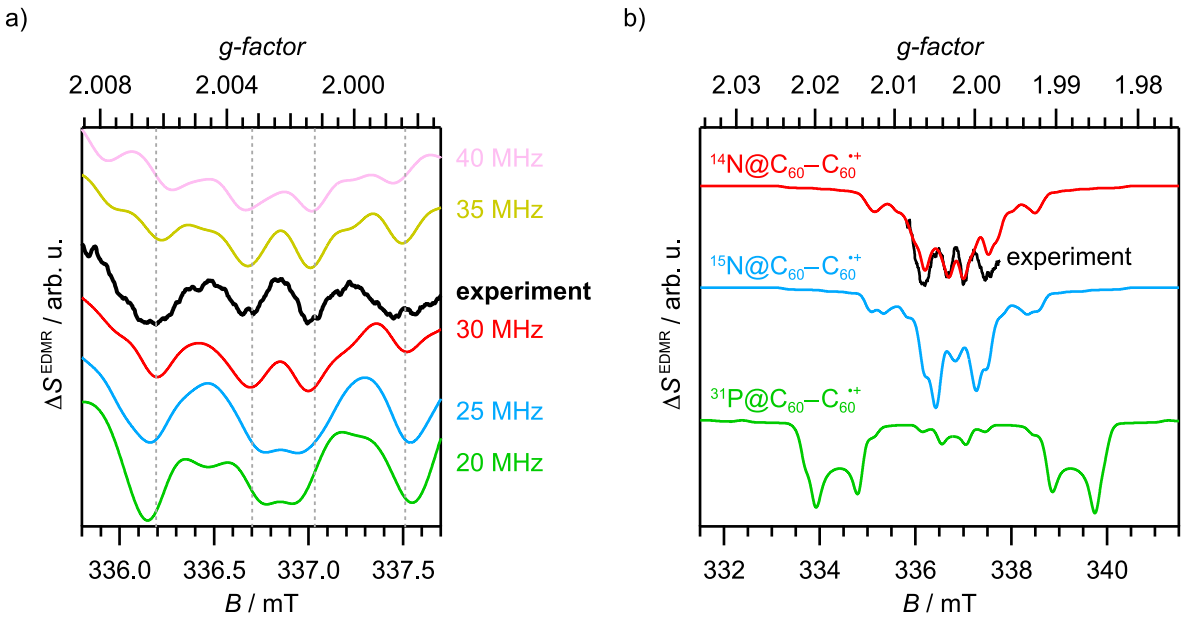

Fig. 36: Dipolar coupling between N@C_{60} and $C_{60}^{\bullet+}$ – simulations versus experiment. a) Experimentally obtained integrated EDMR difference (ΔS^{EDMR}) spectrum taken from figure 35, together with powder spectra simulations obtained for the N@C_{60}-$C_{60}^{\bullet+}$ system using different dipolar-coupling strengths (J_{dd} range: 20 MHz to 40 MHz). The simulations were performed with EasySpin,[155] see text for details about the used parameters. b) Experimentally obtained integrated EDMR difference spectrum taken from figure 35, together with predictions for EDMR spectra of ^{14}N@C_{60}, ^{15}N@C_{60} and ^{31}P@C_{60}, similarly coupled to $C_{60}^{\bullet+}$ with $J_{\mathrm{dd}} = 30$ MHz. The simulated powder spectra were calculated using EasySpin.[155]

ison between experiment and simulation. A summary of the parameters used for the EasySpin simulations can be found in the appendix on page 140 in table A4.

The only unknown term in equation 1.9 is the spin-spin interaction Hamiltonian $\hat{H}_{\mathrm{EE}}$, given by equation 1.26. Assuming no orbital overlap between the nitrogen atom inside an N@C_{60} molecule and a neighboring $C_{60}^{\bullet+}$ – and thus no Heisenberg exchange coupling – the parameter describing the spin-spin interaction in our system is the electron-electron dipole coupling tensor $\boldsymbol{J}_{\mathrm{dd}}$, given by equation 1.29. In order to explore this interaction, simulations were performed using the static values given in table A4 of the appendix, in combination with a coupling constant varying from $J_{\mathrm{dd}} = 20$ MHz to 40 MHz. Figure 36 a) shows the resulting spectra together with the experimental data taken from figure 35 b). While it is rather obvious that the spectra with $J_{\mathrm{dd}} = 20$ MHz, 25 MHz and 40 MHz do not match the experimental data well, a decision between the simulations with $J_{\mathrm{dd}} = 30$ MHz and $J_{\mathrm{dd}} = 35$ MHz is more difficult to make and the actual coupling constant may well be between these two values. The distance between the two coupled spins can be calculated using equation 1.29, resulting in $r_{12}\,(J_{\mathrm{dd}} = 30\,\mathrm{MHz}) = 1.2$ nm and $r_{12}\,(J_{\mathrm{dd}} = 35\,\mathrm{MHz}) = 1.1$ nm, respectively. Thus, the distance between the constituents of the spin pair can be estimated to be somewhere between these values. This is a reasonable result if we take the diameter of a C_{60} fullerene into account, which is about 1 nm. Hence, the two spin-coupled molecules N@C_{60} and $C_{60}^{\bullet+}$ seem to be located next to each other. However, due to an emerging device degradation with time and hence a limited possible number of EDMR scans,

the signal-to-noise ratio is too limited for unambiguous quantitative modeling of the presented data, and a more stable contact scheme needs to be found.
Nevertheless, the performed experiments gave first spectroscopic evidence for strongly dipolar-coupled spin pairs never reported before in EDMR. Firm evidence for the presented hypothesis can be obtained using the proposal shown in figure 36 b). Here, similar paramagnetic dopants were simulated using EasySpin to illustrate the expected structure of the EDMR spectra. The experimental data obtained in this work were added to the graph as well. All spectroscopic parameters necessary to simulate $^{15}N@C_{60}$ and $^{31}P@C_{60}$ were taken from the literature,[113,156] and can be found in the appendix on page 140 (table A4). In principle, $^{15}N@C_{60}$ and $^{31}P@C_{60}$ can be synthesized using the ion implantation technique described in chapter 7, section 7.2.2. Although the starting material for the promising $^{31}P@C_{60}$, phosphane, has to be handled with great caution in a suitable laboratory. The confirmation of the presented dipolar coupling between $N@C_{60}$ and $C_{60}^{\bullet+}$ using such a material would have far-reaching consequences for EDMR research on organic semiconductors, since, up to now, EDMR on organics is hampered by the poor spectral resolution of the method. Using endohedral fullerenes, however, gives rise to a characteristic hyperfine pattern, which is identifiable even on a large and broad background of signals due to other spin species in the sample as indicated by the results presented above.

11. Summary of Part II

In this second part, first the fundamental properties of fullerenes and fullerene materials were introduced in chapter 7. This included the synthesis of $N@C_{60}$, as well as the purification of C_{60}, $C_{60}O$ and $N@C_{60}$. The long-term stability of C_{60} and $N@C_{60}$ was investigated, and microcrystals made from fullerene materials using different crystallization techniques were presented later in that chapter. The developed benchtop EDMR system was used to study organic microcrystals made from pure C_{60} in chapter 8. This was followed by the investigation of oxidized C_{60} material and $N@C_{60}$-doped microcrystals in chapters 9 and 10.

In summary, microcrystals of pure and $N@C_{60}$-doped Buckminsterfullerene C_{60} could be prepared and investigated using the EDMR technique. Furthermore, an EDMR study on crystals obtained from pure $C_{60}O$ material was conducted. While the pure C_{60} material gave $g = 2.0022(3)$ and $\Delta B_{\mathrm{pp}} = 0.33(5)\,\mathrm{mT}$, the $C_{60}O$ microcrystals revealed a slightly higher g-factor of 2.0029(3) and a comparable linewidth.
The EDMR signal observed in pure C_{60} was attributed to a spin-dependent recombination of photo-generated $C_{60}^{\bullet+}$. Its assumed recombination partner, $C_{60}^{\bullet-}$, is known to be too broad for detection at ambient temperature.[93] The presented results on C_{60} microcrystals demonstrate, that even a relatively small number of organic semiconductor crystals can be contacted in a simple manner and still deliver sufficient currents for EDMR detection.
The EDMR signal obtained on the $C_{60}O$ material was tentatively attributed to spin-dependent recombination of photo-generated charge carriers involving a secondary product of $C_{60}O$, which could be an "open-epoxy-ring" form of the molecule, the intermediate $^{-\bullet}C_{60}{-}O{-}O{-}C_{60}^{\bullet-}$, or a constitutional isomer thereof. This illustrates that the oxidation of fullerene molecules can result in a slight shift of the g-factor towards higher values and thus explain the observation of unusual g-factors in oxidized fullerene materials reported by others.[11]
Finally, the most important finding of the EDMR studies presented in this part is by far the evidence for strongly dipolar-coupled spin pairs in $N@C_{60}$-doped material. As a working hypothesis, the observed structure in the corresponding EDMR spectra was attributed to the formation

of dipolar-coupled N@C_{60}-$C_{60}^{\cdot+}$ spin pairs. Although an unambiguous quantitative modeling of the presented data was not possible due to the limited signal-to-noise ratio, a symmetric structure in the obtained spectra is clearly visible. This result illustrates that using microcrystals and paramagnetic doping can significantly enhance the EDMR resolution. Furthermore, a doping-on-demand strategy seems feasible, which could unravel the opposing views as to how the EDMR signal is generated at the microscopic level, which – despite intensive research – continue to be published so far.[8,10,11]

Part III.

EDMR on Organic Solar Cells

Focus and objective: In this part, we will use the compact EDMR setup presented in part I as a tool for organic solar cell device analysis. For the development of photovoltaic devices with optimal efficiency, processes limiting the device performance, like recombination, are of special interest. Since recombination events that macroscopically influence the sample conductivity may alter the spin-dependent current, the EDMR technique is almost predestined for this kind of study. We will combine EDMR with light-dependent current-voltage analysis and try to form a picture of spin-dependent processes that affect the lifetimes and transport of elementary excitations inside organic solar cells under realistic operating conditions. After introducing some basic aspects of organic photovoltaics, we will examine the EDMR signature of head-to-tail regioregular poly(3-hexylthiophene-2,5-diyl) (P3HT) and [6,6]-phenyl-C_{61}-butyric acid methyl ester ($PC_{61}BM$), as these are the components used in the organic solar cells investigated in this work. Afterwards, the observed EDMR signals will be attributed to certain recombination processes and a quantitative EDMR study on fully functional P3HT:$PC_{61}BM$ solar cells under varying bias and illumination conditions will be presented. Finally, an outlook to the investigation of degradation processes in organic photovoltaic devices using the EDMR technique will be given.

The following part of this thesis is currently in preparation for publication in a peer-reviewed journal: M. Eckardt, R. Wieczorek, F. Laquai, W. Harneit, Recombination Spectroscopy for Organic Solar Cells based on Magnetic Resonance, to be submitted to Physical Review. The corresponding chapter is indicated by a †.

12. Introduction to Organic Photovoltaics

While it is doubtless that using photovoltaics to harvest energy from sunlight instead of using up the limited fossil energy sources available on the planet is a must-win-battle in the near future, the cost of this technology still hampers its usage. Despite the far lower efficiency compared to most inorganic solar cells,[6] organic solar cells are promising candidates in this economic challenge. This arises from the fact that organic devices can be processed from solutions at moderate cost by coating or even printing. Furthermore, a wide variety of light-weight and flexibly shaped solar panels can be produced, expanding the possible areas of application.
The origin of the conductivity in organic, or rather carbon-based, semiconductor materials are conjugated double bonds (i.e. the overlap between p_z orbitals not involved in the formation of the σ bond framework of the molecule), which enable a delocalization of charges. If the gap between HOMO and LUMO of the molecule is between 1.5 eV and 3.0 eV it can absorb light in the visible spectrum to drive a transition between these two levels, resulting in a so-called Frenkel exciton (electron-hole pair located on a single molecule), which can be transfered between the molecules by a statistical hopping process (exciton diffusion). This is in stark contrast to inorganic solar cells, where free electron-hole pairs are generated, and also the reason that organic solar cells based on a single material remain below 0.1 % power conversion efficiency.[157] However, a much higher efficiency (about 1 %) was obtained by combining an electron donor and acceptor material in the active layer of the solar cell device.[158] Since then, the power conversion efficiency of polymer solar cells could be increased up to about 11 % by improved donor-acceptor systems and new device geometries.[6]
After introducing device architecture concepts and the current-voltage characteristics of organic solar cells in the following sections, we will have a detailed look on the microscopic processes that eventually lead to the generation of a usable photocurrent in section 12.3.

12.1. Device Architecture and Materials for Organic Solar Cells

Organic solar cells made of a single material sandwiched between two electrodes of different work functions show very low efficiencies.[157] The reason for this is the limited exciton diffusion length in organic materials. Typically, Frenkel excitons generated by the absorption of light can travel about 5 nm and 10 nm in these materials,[159,160] which is much shorter than the few hundred nanometers of device thickness needed for an efficient light absorption.[157] Hence, most of the photogenerated excitons are lost through recombination, limiting charge-carrier generation in this kind of solar cell. The exciton binding energy in organic polymers has been determined experimentally, leading to a value of about 0.4 eV.[161] Introducing a suitable electron acceptor material helps to dissociate these excitons into free charge carriers, since the electron can occupy an energetically lower lying state in the acceptor molecule. This leads to a charge transfer as the electron moves over to the acceptor molecule leaving behind the hole on the donor. Hence, for such a transfer to be successful, the energy difference between the LUMOs of donor and acceptor has to be larger than the exciton binding energy. An example for a widely used electron acceptor material in organic electronics is the Buckminsterfullerene C_{60}, which was introduced in chapter 7, section 7.1.
The donor-acceptor concept first led to the development of planar heterojunction solar cells.[158] This device configuration is illustrated in figure 37 a). An incident photon is absorbed by a donor molecule in the corresponding layer. Subsequently, a Frenkel exciton is generated due to the excitation of an electron from the HOMO to the LUMO. This exciton could then diffuse within the donor layer towards the planar acceptor interface where it dissociates forming free charge carriers. The problem with this device concept again is the rather low exciton diffusion length resulting in a high exciton recombination rate. If, for example, the donor layer needs be 100 nm in thickness to grant for an efficient light harvesting,[157] only 5 % to 10 % of the

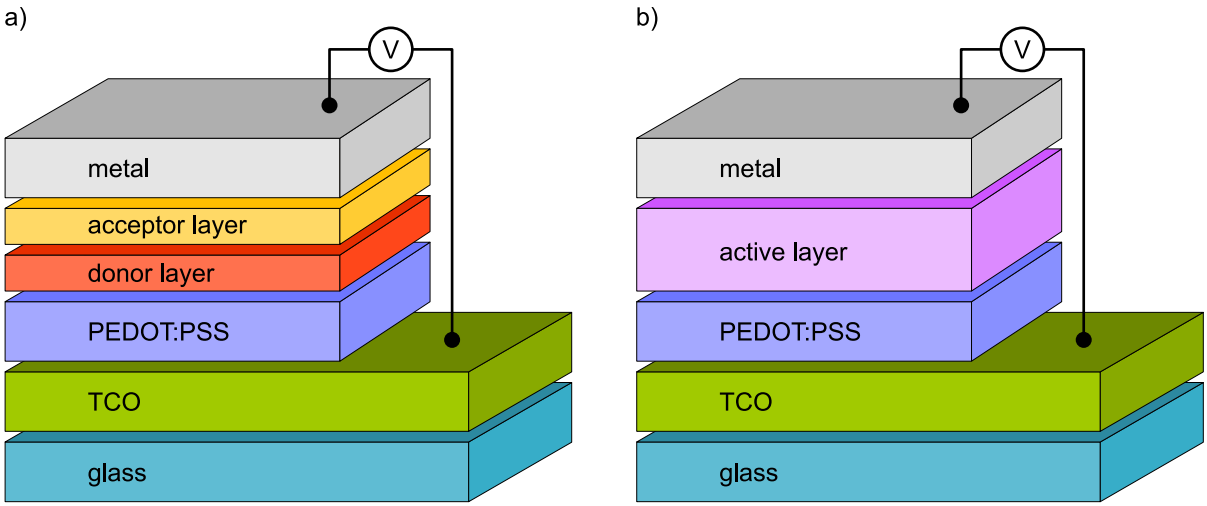

Fig. 37: Device configurations for organic solar cells. a) Planar heterojunction in a bilayer device consisting of an electron donor and acceptor layer. b) In contrast, a donor-acceptor blend forms the active layer in bulk-heterojunction devices. Both configurations use a poly(3,4-ethylenedioxythiophene) polystyrene sulfonate (PEDOT:PSS) interlayer to smooth surface imperfections of the transparent conductive oxide (TCO) electrode and prevent the formation of local shunts.[162] A metallic electrode is used as the top contact.

generated excitons (depending on the actual exciton diffusion length) could reach the donor-acceptor interface. Hence, even though the power conversion efficiency could be increased using a planar donor-acceptor heterojunction compared with the single material cells, this concept has only limited development potential.

A device concept – called bulk heterojunction – accounting for both low exciton diffusion lengths and required absorption layer thickness was introduced by Yu *et al.* in 1995.[163] Figure 37 b) illustrates the general device configuration used in such a solar cell. In contrast to the planar heterojunction approach, the components interpenetrate each other forming a spatially distributed interface. Hence, electron-hole pairs are generated throughout the resulting active layer. Due to their increased disorder the donor-acceptor blends, however, also posses some disadvantages compared to planar heterojunction devices. For example, the percolation of charge carriers to the contacts can be reduced by "dead ends", i.e. donor or acceptor domains that are not in contact with the corresponding electrode. Furthermore, the disorder can lead to the formation of trap states that can act as recombination centers. Hence, a good control of the active layer morphology, e.g. by annealing, is important to obtain efficient devices.[164]

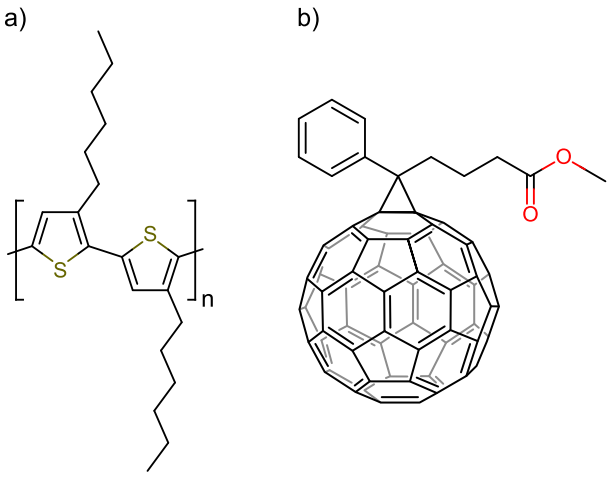

Fig. 38: Chemical structure of a) head-to-tail regioregular P3HT and b) $PC_{61}BM$. While the first one is a commonly used electron donor, the latter is widely applied as an electron acceptor material. P3HT:$PC_{61}BM$ blends are frequently used as active layers in bulk-heterojunction solar cells.

In principle, the donor-acceptor system of bulk-heterojunction solar cells can be tailor-made in order to improve the power conversion efficiency. The two most important donor molecules prepared so far are probably the pathbreaking poly[2-methoxy-5-(2'-ethylhexyloxy)-1,4-phenylenevinylene] (MEH-PPV),[163,165] and the well-studied poly(3-hexylthiophene-2,5-diyl) (P3HT).[166] Figure 38 a) illustrates the structure of the latter. Newer donor materials with higher efficiencies have been introduced in recent years,[167–169] but these systems seem to suffer from a stronger degradation.[170] A comprehensive summary of polymer materials used for organic photovoltaics is, however, outside the scope of this work and more details can be found elsewhere.[166,171]

The acceptor materials of choice are usually based on the fullerenes C_{60} and C_{70}. Figure 38 b) shows the most widely used [6,6]-phenyl-C_{61}-butyric acid methyl ester ($PC_{61}BM$). Several other candidates for possible acceptors were tested in the past, including conjugated polymers, perylenes, and carbon nanotubes, but so far only the derivatives of C_{60} and C_{70} have been reported to yield highly efficient bulk-heterojunction solar cells.[166,171,172] However, a recently conducted study with a nonplanar perylene diimide as the acceptor molecule revealed a device efficiency of 2.77 %, indicating that this material – if further optimized – could be an alternative to fullerenes.[173]

Summarizing the brief introduction to device configurations and materials given in this section, the most promising candidate for a first EDMR study is a bulk-heterojunction solar cell system using P3HT:$PC_{61}BM$ as an active layer, since this system is well-known and sufficiently stable.

12.2. Current-Voltage Characteristics

In section 12.1 we assessed different solar cell systems by their power conversion efficiency η, which in fact is the most important figure of merit in the solar cell literature. In the present section, we will introduce how the power conversion efficiency is connected to other characteristic quantities that are often used in the literature. Figure 39 illustrates typical current-voltage characteristics obtained from organic solar cell devices by sweeping the bias voltage V_{bias} and recording the corresponding sample current density J under illumination, as well as in the dark. Typically,

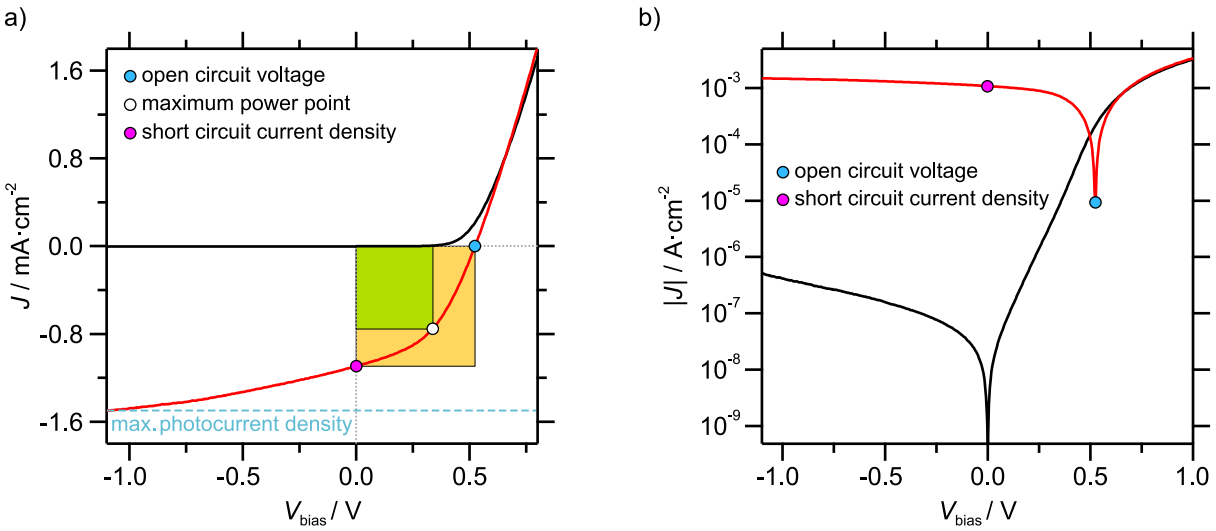

Fig. 39: Schematic current-voltage characteristics of a bulk-heterojunction solar cell. a) Linear and b) semi-logarithmic representation of the same data. As usual in the solar cell literature, the current density $J = I/A_{\mathrm{d}}$ is given instead of the current I for easy comparison between devices with different active area A_{d}. The black line represents the dark current density, the corresponding current density measured under illumination is depicted in red. Open circuit voltage, maximum power point, and short circuit current density are marked by color-coded circles. The photocurrent density in organic solar cells is usually bias dependent, and its maximum is not necessarily reached under short circuit conditions, but at negative V_{bias}. The green rectangle illustrates the maximum obtainable power from the device. Its yellow colored analogue represents the product of the open circuit voltage and the short circuit current density. The area ratio of the green and yellow rectangle defines the so-called fill factor, which is a measure for the "squareness" of the experimentally obtained current-voltage data.

the current density is used in solar cell reports due to the fact that the determined current I depends on the active area A_{d} of the device. Hence, using $J = I/A_{\mathrm{d}}$ makes direct device comparisons much easier. Some important quantities are more easily extracted from a semi-logarithmic representation, as can be seen by comparing figures 39 a) and b), and we will use whatever representation is most appropriate for a particular question in this thesis. Looking at figure 39 we see a typical "rectifying diode behavior" for the dark current density and can identify three prominent points under illumination. These are: the open circuit voltage (V_{OC}), where no net current is flowing trough the external circuit, the maximum power point (MPP), where the device is usually operated, and the short circuit current density (J_{SC}), where the voltage across the device is zero. The latter is equally well represented by the short circuit current

(I_{SC}). Furthermore, it can be seen that the obtainable photocurrent density in an organic solar cell depends somewhat on the bias voltage, with maximum photocurrent density not necessarily reached under short circuit conditions, but at negative V_{bias}.
We can now express the fill factor *FF* of a given solar cell using the prominent points observed in the current-voltage characteristics, as shown in equation 12.1. This is equivalent to calculating the area ratio between the green and yellow rectangle shown in figure 39 a).

$$FF = \frac{V_{MPP}\, J_{MPP}}{V_{OC}\, J_{SC}} \tag{12.1}$$

The power conversion efficiency of the solar cell is then simply given by

$$\eta = \frac{V_{OC}\, J_{SC}\, FF}{P_{in}} \tag{12.2}$$

with P_{in} as the incident light power density. For inorganic p-n junction solar cells, the maximum attainable efficiency is given by the detailed balance limit calculated by Shockley and Queisser based on an analysis of the occurring microscopic processes.[174] However, the situation in organic solar cells is more complicated, and different models for the underlying microscopic processes exist.[175–177] A recently published review on the efficiency of organic bulk-heterojunction solar cells summarized the results obtained from several empirical studies and concluded that an upper efficiency limit of about 15 % should be reachable for state of the art materials and device architectures.[178]
For an ideal inorganic p-n junction, the current-voltage characteristics without illumination is given by the famous Shockley equation

$$J = J_0 \left[\exp\left(\frac{V}{V_{th}} \right) - 1 \right] \tag{12.3}$$

with J_0 as the reverse saturation current density and $V_{th} = k_B\, T/e$ as the thermal voltage.[174,179] For real inorganic solar cells under illumination, this basic equation has to be extended by the diode ideality factor n,[180] the photocurrent density J_{ph},[181] and the parasitic series and parallel resistances R_s and R_p, respectively.[182] Equation 12.4 shows the result of this extension, which is typically used to describe and analyze inorganic photovoltaic devices.[181,183]

$$J = J_0 \left[\exp\left(\frac{V - JR_s}{n\, V_{th}} \right) - 1 \right] - \frac{V - JR_s}{R_p} - J_{ph} \tag{12.4}$$

The diode ideality factor is often discussed to arise from differences in the nature of the dominant recombination process and typically found to lie between one and two, with $n = 1$ for a Langevin-type (band-to-band) and $n = 2$ for a Shockley-Read-Hall (trap-assisted) recombination, respectively.[184–187] The parasitic series resistance R_s describes contact problems such as injection barriers and sheet resistances that act in series with the ideal diode. Effects that lead to additional current paths that circumvent the ideal diode are captured by the parasitic parallel resistance R_p, which is sometimes called "shunt resistance" in the literature.[181,183]
Looking at figure 39 it becomes clear that equation 12.4 does not describe the experimentally obtained data on organic bulk-heterojunction solar cell devices properly. First, the crossing point of dark current density and illuminated curve at around $V_{bias} = 0.7\,V$ is not to be expected from equation 12.4, where the photocurrent density J_{ph} is simply introduced as being a parallel shift of the dark current-voltage data down the current density axis. Furthermore, the voltage-dependent

photocurrent density apparent in the third quadrant of figure 39 a) is unexpected from the diode equation. Thus, as pointed out by Deibel and Dyakonov, applying equation 12.4 to organic solar cells is only possible if the parasitic resistances are - without physically justified foundation - supposed to be voltage and light dependent.[188]
Evidently, organic photovoltaic devices differ fundamentally from their inorganic counterparts, and we shall have a closer look at the processes occurring on the microscopic level in the next section in order to gain a better understanding of the device operation.

12.3. From Light Absorption to Photocurrent

In the previous section, we investigated the typical current-voltage characteristics of an organic bulk-heterojunction solar cell and defined the important quantities V_{OC}, I_{SC} (respectively J_{SC}), as well as the maximum power point. Furthermore, it became clear that the well-known models existing for inorganic semiconductors can not readily be applied to organic photovoltaics. Figure 40 illustrates the microscopic processes involved in the generation of the photocurrent. Starting with the absorption of a photon by a donor molecule, a Frenkel exciton is generated. It should be noted that, even though the majority of the incident light is absorbed by the donor (conjugated polymer), the fullerene acceptor can of course absorb photons too, but the exciton generation rate is much lower compared to the polymer.[188] Subsequently a charge transfer from the fullerene to the polymer could occur, which indeed has been observed experimentally.[189] However, we will focus on the main excitation process taking place on the polymer donor molecule for the remainder of this chapter.

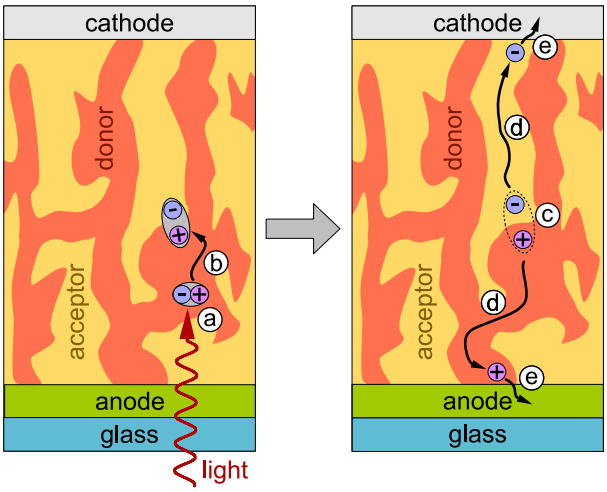

Fig. 40: Sketch of the microscopic processes inside a bulk-heterojunction solar cell. ⓐ A photon is absorbed by the donor, generating a Frenkel exciton. ⓑ The exciton diffuses to the acceptor interface, where it dissociates by transferring the electron to the electronegative acceptor. ⓒ A coulomb-bound electron-hole pair may result in some materials, which is then separated due to the macroscopic electric field inside the device. ⓓ Free charge carriers move towards the corresponding electrodes by a hopping transport. ⓔ The extraction of the charge carriers finally generates the photocurrent.

After its generation, the exciton has to diffuse to the donor/acceptor interface in order to dissociate. With the exciton being neutral, this process can not be driven by any electrical field but is statistically governed. In some materials, the resulting electron-hole pairs may still be bound by Coulomb attraction due to the relatively low dielectric constants of organic materials, which lead to larger screening lengths.[157] As will be discussed in section 12.3.1, the involvement of such Coulomb-bound electron-hole pairs in the photocurrent-generation process, as well as the driving force behind their dissociation into free charge carriers is still under debate.[190–192] The free charge carriers are transported towards their corresponding electrode. This process is aided by the electric field inside the device. However, as can

be deduced from figure 40 "dead ends" may exist in the donor and acceptor phase, preventing some of the charge carriers from finally reaching the electrode. As this is a result of the low order in the device, a higher phase segregation can be beneficial for charge transport. One the other hand, a close proximity between donor and acceptor is needed to efficiently dissociate the excitons, which only posses a traveling distance of about 5 nm to 10 nm.[159,160] Finally, the charges are extracted at the contacts and driven into the external circuit.
In the following sections we will discuss the processes of charge carrier generation, transport, and extraction in more detail. Additionally, section 12.3.3 will introduce some fundamental recombination mechanisms relevant in organic solar cells.

12.3.1. Charge Carrier Generation

The process of charge carrier generation includes the absorption of a photon to yield an exciton and its subsequent dissociation until free charge carriers are obtained. Especially the latter process (cf. step ⓒ in figure 40) is still under debate,[190–192] and may depend on the material system under investigation as discussed below.
The first step of the charge carrier generation process is – without doubt – the absorption of a photon in the active layer of the solar cell. As mentioned earlier, even though the acceptor is also capable of absorbing light, we will focus exclusively on the excitation of the donor as this is the most likely case.[188] Conjugated polymers, like P3HT, used in solar cell applications typically posses absorption coefficients of about $10^7\,\mathrm{m}^{-1}$.[193] Unfortunately, the corresponding absorption bands are quite narrow, leaving most of the solar spectrum uncovered, which leads to their low efficiency compared to inorganic materials like silicon.[157] At the same time, the high absorption coefficients render it possible to manufacture solar cells with an active layer thickness of only a few hundred nanometers compared to several hundreds of micrometers in silicon devices.[157] Hence, significantly lower material amounts can be used for organic devices,[188] making lightweight and flexible structures possible.[194]
Due to the absorption of light, an electron is promoted from the polymers HOMO to its LUMO, resulting in an electron-hole pair located on the same molecule, i.e a Frenkel-type exciton. It was long time argued that the exciton binding energy could be less than $k_\mathrm{B}T$ at ambient temperature,[195,196] thus enabling the direct formation of free electron-hole pairs. However, it is largely agreed today that singlet excitons with binding energies of about 0.4 eV,[161] which is much higher than the 26 meV of thermal energy available at 298 K, are the primary excitations in polymer solar cells.[188,197–199]
In order for the dissociation process to take place, the neutral excitons have to diffuse to the donor/acceptor interface.[200] As introduced in the preceding sections, excitons posses a limited diffusion length of a few nanometers before they are lost - usually by radiative recombination,[188] which led to the development of bulk-heterojunction devices.[163] For the polythiophene/C_{60} heterojunction the exciton diffusion length was determined by photoluminescence experiments revealing a travel distance of only 5 nm,[201] which makes the bulk-heterojunction concept most suitable for this type of donor material. The exciton dissociation itself can only take place if the energy gain due to the transfer of the electron to an electronegative acceptor molecule is larger than the exciton binding energy. The offset between donor LUMO and acceptor LUMO gives a rough estimate for the energy gain, but more exact values need to be obtained experimentally.[188,202] After dissociation, the electron resides on the fullerene donor and the hole on the polymer acceptor molecule. In analogy to crystalline inorganic materials, these carriers are often referred to as the negative and the positive polaron, respectively.[188] The term "polaron

pair" is usually used if a Coulomb-bound pair of polarons is considered.
Generally, depending on whether or not the polarons can overcome their mutual attraction, the result of the exciton dissociation process can either be free polarons or a still coulombically-bound polaron pair. The involvement of the latter in the photocurrent generation process is still under debate in the literature.[190–192] Since organic semiconductors show comparatively low relative dielectric constants (typically between 2 and 4),[157] it seems reasonable that polaron pairs can form due to Coulomb attraction. The possible recombination of such a polaron pair (so-called geminate recombination) will be addressed in section 12.3.3.
In fact, it was found that the charge carrier generation in ladder-type polymers is a two-step process involving the formation and dissociation of bound electron-hole pairs.[203] Over the last decade, it was intensively studied if the same picture also applies to donor-acceptor systems relevant for organic photovoltaics, and the results of these studies indicate that the involvement of polaron pairs may depend on the chosen material system and its morphology.[190–192,204–206] For the regioregular-P3HT:$PC_{61}BM$ system used in this thesis, the experiments performed by Howard *et al.* suggest that less than 20 % of the excitons dissociate into polaron pairs and that more than 80 % form free charge carriers right away.[206] Kniepert *et al.* found no evidence for the involvement of coulombically-bound polaron pairs at all in their study on P3HT:$PC_{61}BM$ solar cells.[191] Thus, step ⓒ in figure 40 seems to be of minor importance for the organic photovoltaic devices investigated in the present work.

12.3.2. Charge Carrier Transport and Extraction

After free polarons have been produced from incident photons (see section 12.3.1), those charge carriers must find their way trough the percolated donor-acceptor layer towards the electrodes in order to get extracted and finally produce a photocurrent. Band transport typically found in crystalline semiconductors can, however, not be considered to take place in organic semiconductors due to the lack of long-range order.[188] Instead, the polarons move by a hopping-like transport from one localized state to the next until they finally reach the semiconductor/electrode interface. Although the donor-acceptor blend in a bulk-heterojunction device is best described as an active layer, the polarons are predominantly transported in their respective phases,[188] namely the acceptor phase for electrons and the donor phase for holes.
The hopping transport from molecule to molecule in a single material can be modeled by the theory of Marcus, which he developed as a mechanism for electron transfer reactions in the mid 1950s, and for which he was awarded the Nobel Prize in Chemistry in 1992.[207,208] The details of this theory are outside the scope of this work, but in a nutshell can be summarized as follows: the hopping rate between to sites is proportional to the absolute square of the transfer integral (overlap of the participating wavefunctions) and further depends on the magnitude of the reorganization energy (related to the polaron relaxation) and the energy difference of the two sites.[188] A very similar hopping rate was later introduced by Miller and Abrahams.[209] Monte Carlo simulations based on these hopping rates are commonly used to describe the charge transport in disordered organic photoconductors,[210] as well as the polaron-pair dissociation in polymer-fullerene blends.[211] Bässler used a hopping-rate-based Monte Carlo approach to develop the so-called Gaussian disorder model, which uses a Gaussian density of states to describe the charge transport.[210]
However, developing a comprehensive model for charge transport in bulk-heterojunction devices is difficult since "dead ends" in the donor or acceptor phase can certainly exist, for instance due to a nanocrystal blocking a carrier path.[188] This can also be observed experimentally, when

investigating the charge carrier mobility of pure P3HT and the blend P3HT:$PC_{61}BM$. It was found that the carrier mobility is governed by the regioregularity of the polymer,[212] its molecular weight,[213–215] as well as the post-processing annealing step.[214,216]
Finally, the photogenerated charges that reach their corresponding electrode can be extracted from the device and driven into the external circuit. As depicted in step ⓔ of figure 40, electrons leave the device through the metal cathode and holes are extracted from the TCO anode (cf. figure 37). This charge extraction, however, can be influenced by imbalanced electron and hole mobilities that lead to a space-charge-limited photocurrent.[217] A reduced surface recombination velocity, or in other words a low charge extraction rate, at one of the contacts can also lead to the formation of a space charge region, which becomes expressed in an S-shaped deformation of the current-voltage characteristics.[188,218]

12.3.3. Charge Carrier Recombination

The recombination of opposite charge carriers was not considered in the presented microscopic device picture so far. However, with recombination loss as a major device performance issue, we will have a closer look at these events in the present section. First of all, we need to distinguish between the so-called geminate and non-geminate recombination processes. The first mentioned process takes place during polaron pair dissociation (see step ⓒ of figure 40) involving opposite charges resulting from the same primary excitation, hence its name. The latter one, on the other hand, happens during charge transport and extraction (see section 12.3.2), between charges that do not have a common precursor state.
A polaron pair resulting from an exciton dissociation at the donor/acceptor interface can either undergo a geminate recombination to the ground state with rate k_r, or dissociate into free polarons with rate k_d. The field-dependent dissociation probability for a polaron pair according to Onsager-Braun theory is then given by equation 12.5.[219,220]

$$P(E) = \frac{k_\mathrm{d}(E)}{k_\mathrm{d}(E) + k_\mathrm{r}} \tag{12.5}$$

However, as discussed in section 12.3.1, experimental results obtained on the P3HT:$PC_{61}BM$ system revealed that the majority of excitons form free charge carriers instead of bound polaron pairs,[191,206] making geminate recombination less significant for the devices investigated in the present thesis. Thus, we will not intensify the discussion about geminate recombination here. A more detailed description of this topic is available elsewhere.[188]
Models for non-geminate recombination in organic photovoltaic devices are mainly based on theories derived for well-understood inorganic semiconductors like amorphous silicon.[221,222] Due to the disorder and corresponding low mobility the situation is somewhat more complicated in organic semiconductors and several modifications to the basic theories have been proposed to explain the experimentally observed behavior. A basic model used in organic solar cell research is the one originally developed by Langevin for the recombination of ions in the gaseous phase.[223] The recombination rate in this theory depends on the likelihood of opposite charges finding each other, and thus on the density of holes p and electrons n, as well as their combined mobility $\mu = \mu_\mathrm{p} + \mu_\mathrm{e}$ as shown in equation 12.6.

$$R_\mathrm{L} = \frac{e\,\mu}{\epsilon}\left(np - n_\mathrm{i}\,p_\mathrm{i}\right) \tag{12.6}$$

Here, e is the elementary charge and ϵ the absolute permitivity of the active layer. The intrinsic charge carrier densities for electrons and holes are given by n_i and p_i, respectively. With the

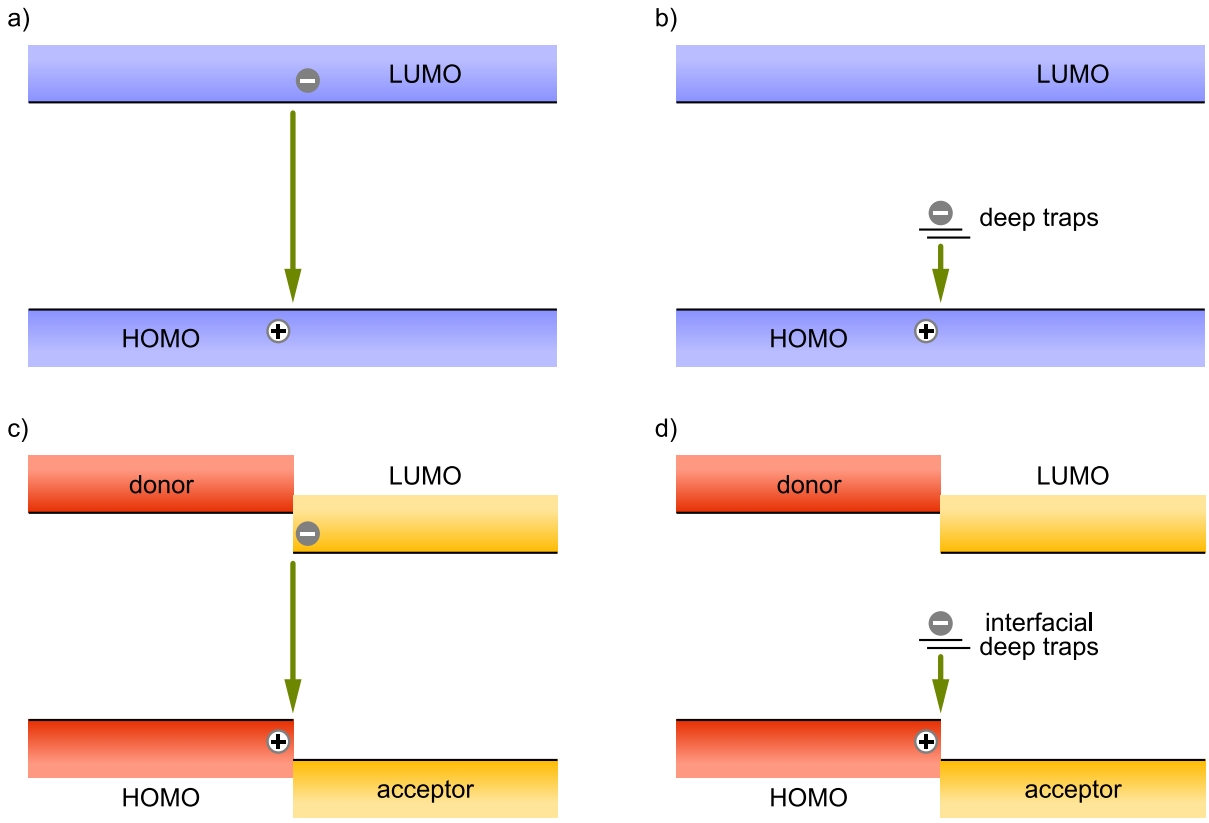

Fig. 41: Langevin and Shockley-Read-Hall recombination in organic semiconductors. a) In the Langevin model, recombination takes place between two mobile charge carriers. The recombination rate is determined by the rather slow approach of the recombination partners, not the very fast annihilation process itself. b) In the Shockley-Read-Hall model, recombination takes place between a stationary charge in a trap state and a mobile carrier. While depicted here for a trapped negative and a mobile positive charge carrier, the opposite is equally possible. Both recombination models can be adapted for bulk-heterojunction solar cells by taking into account that positive polarons reside mainly in the donor phase, while the majority of negative polarons is found in the acceptor material. The result of this adaption is shown in c) for Langevin-type recombination and in d) for the Shockley-Read-Hall process.

definition of the Langevin recombination prefactor

$$\gamma = \frac{e\,\mu}{\epsilon} \tag{12.7}$$

and the assumption that the product of the intrinsic charge carrier densities is much smaller than np, the Langevin recombination rate can be simplified to yield equation 12.8

$$R_{\mathrm{L}} \approx \gamma np \tag{12.8}$$

Figure 41 a) illustrates the Langevin recombination model for an organic semiconductor material. Its adaption to bulk-heterojunction solar cells, were positive polarons reside mainly in the donor phase, while the majority of negative polarons is found in the acceptor material, is depicted in figure 41 c). The recombination rate in this model is determined by the slow approach of the

recombination partners, not the fast annihilation process itself. A bimolecular mechanism, i.e a recombination rate proportional to the square of the electron or hole density (if assuming $n \approx p$), can be anticipated from this picture, as well as from equation 12.8.
The basic Langevin model assumes a homogeneous charge carrier transport with uncorrelated electron and hole densities, which is not necessarily true for low-mobility disordered materials with spatial charge distributions.[187] Thus, it is not surprising that experimentally determined recombination rates for bulk-heterojunction P3HT:$PC_{61}BM$ and other organic photovoltaic devices differ from those calculated using equation 12.8 by several orders of magnitude.[187,199] Hence, a Langevin reduction factor ξ_L needs to be introduced in equation 12.8 in order to obtain quantitative agreement between theory and experiment. Different proposals regarding the reason for the observed reduction where published during the last 20 years. Arkhipov and Adriaenssens, for example, assumed spatial fluctuations in the potential landscape of disordered semiconductors,[224,225] while Nelson introduced a multiple trapping and detrapping of the positive polarons with a thermal activation barrier.[226] Koster *et al.* suggested to use the mobility of the slowest recombination partner instead of the combined mobility of electrons and holes in equation 12.6,[227] and Deibel *et al.* introduced a temperature, electric field, and charge-carrier generation rate dependent reduction factor $\xi_L(T, E, G)$.[228]
Figure 41 b) shows the second recombination mechanism often applied in organic semiconductor research, namely Shockley-Read-Hall (SRH) recombination.[229,230] As illustrated in figure 41 d), this model can be adapted to better reflect the situation in bulk-heterojunction solar cells as well. In contrast to the Langevin model, only one charge carrier is considered to be mobile. The other recombination partner is trapped at a recombination center in the effective band gap. Thus, the name trap-assisted recombination is often used for this mechanism. The SRH recombination rate is given by

$$R_{SRH} = \frac{np - n_i^2}{\tau_n \left[p + n_i \exp\left(\frac{E_i - E_t}{k_B T}\right)\right] + \tau_p \left[n + n_i \exp\left(\frac{E_t - E_i}{k_B T}\right)\right]} \tag{12.9}$$

with $\tau_n = 1/(\sigma_n v_n N_t)$ and $\tau_p = 1/(\sigma_p v_p N_t)$ as the electron and hole lifetime, respectively.[183] In this model, free charge carriers (densities: n and p) are trapped and released from trap states of energy E_t and density N_t. The capture cross section, describing the capture probability for a carrier moving at velocity v_n or v_p is denoted σ_n and σ_p, respectively. The intrinsic charge carrier density is given by n_i and the intrinsic energy level is symbolized by E_i. For a negligible intrinsic charge carrier density ($np \gg n_i^2$) and if mainly one carrier type is trapped, say electrons ($\tau_n \gg \tau_p$), and with the further assumption that the trap states are located mostly in the middle of the effective band gap ($E_i = E_t$), equation 12.9 can be simplified to yield equation 12.10.

$$R_{SRH} \approx \frac{n}{\tau_n} \tag{12.10}$$

Hence, the SRH recombination process is of pseudo-first order, and thus considered to be monomolecular, under these constraints.[187]
For steady-state current-voltage experiments, a connection between the order of the recombination (Δ) and the diode ideality factor n (see equation 12.4) is sometimes discussed.[231,232] Deibel *et al.* studied the order of decay of mobile charge carriers in P3HT:$PC_{61}BM$ solar cells and formulated the relationship shown in equation 12.11.[232]

$$\Delta = \frac{2}{n} \tag{12.11}$$

For the recombination of two mobile charge carriers $\Delta = 2$ and hence $n = 1$ is assumed. Accordingly, $\Delta = 1$ and $n = 2$ is expected in case of trap-assisted (SRH) recombination.[187,232] Equation 12.12 illustrates the determination of the "dark ideality factor", which can be deduced from equation 12.3 after introducing non-ideal diode behavior.[184]

$$n_{\mathrm{d}} = \left(V_{\mathrm{th}} \frac{\mathrm{d} \ln \left[J \left(V \right) \right]}{\mathrm{d}V} \right)^{-1} \tag{12.12}$$

In analogy to n_{d}, the "light ideality factor" introduced by Kirchartz *et al.* can be calculated for a device under illumination,[184] as shown in equation 12.13.

$$n_{\mathrm{l}} = \left(V_{\mathrm{th}} \frac{\mathrm{d} \ln \left[J \left(V_{\mathrm{rev}} \right) \right]}{\mathrm{d}V_{\mathrm{OC}}} \right)^{-1} \tag{12.13}$$

Here, the current measured at strong reverse bias, $J \left(V_{\mathrm{rev}} \right)$, is used, which corresponds to the maximum photocurrent (cf. figure 39). With the ideality factor being easily available from standard current-voltage characteristics, an estimate for the dominating recombination type in a specific device seems possible.[187]

13. EDMR on Fully Functional Organic Photovoltaic Devices†

Having introduced the foundations of organic photovoltaics in chapter 12, we now turn to a study of fully functional solar cells by EDMR. First, we will motivate this study by illustrating some benefits that EDMR may provide to the very active field of organic solar cell research. Afterwards, the device configuration used in this work will be introduced, together with the typical current-voltage characteristics obtained from these samples. We will discuss the spectroscopic informations contained in EDMR and attribute the observed signals to certain species and recombination processes relevant for the operation of the device. In the last part, we will then enlarge upon this and quantitatively relate the recombination currents measured by EDMR with the loss current available from the current-voltage characteristics of the sample in section 13.4.

13.1. Benefits of Solar Cell EDMR

The device performance of organic solar cells was greatly improved over the years. Starting with less than 0.1 % power conversion efficiency for a typical device based on a single organic material,[157] modern cells today provide efficiencies of about 11 %.[6] This development was driven mostly by improved donor-acceptor systems and new device geometries.[188]
However, some microscopic processes that are at the heart of organic photovoltaics, like charge carrier recombination, are still not fully understood. For further progress, it is necessary to develop a quantitative picture of the recombination inside a device and to overcome these processes, since they represent the dominant loss pathway in today's bulk-heterojunction devices.[178] Structural and energetic disorder, low charge carrier mobility and the presence of traps is what makes organic solar cells complex.[187] Hence, theories and models are still evolving, especially on the molecular level. Although the theoretical understanding of charge carrier recombination has made progress, tools providing a direct view on recombination events at a molecular-level

†Parts of this chapter are currently in preparation for publication in a peer-reviewed journal: M. Eckardt, R. Wieczorek, F. Laquai, W. Harneit, Recombination Spectroscopy for Organic Solar Cells based on Magnetic Resonance, to be submitted to Physical Review.

are of great interest. Optical spectroscopies require often rather high illumination levels, which may not represent standard device operating conditions accurately. Spin-sensitive methods like EPR promise to provide a more detailed insight into device operation. The widespread light-induced electron paramagnetic resonance (LEPR) gives a spectroscopic fingerprint that helps identifying different polaronic species. It is, however, limited to thick molecular films that may not have the same micro-morphology as functional solar cells, and is usually performed without electrodes and hence confined to zero applied bias voltage. Additionally, standard EPR is not able to distinguish between charge carriers that are just trapped somewhere in the device without influencing the photocurrent generation and those that actually contribute. This is where the much less widespread technique of EDMR can excel. By incorporating optical and electrical bias conditions, EDMR can provide insights into fully functional organic semiconductor devices. An EDMR experiment can in principle identify which kind of charge carrier is involved in a particular transport event by the spectroscopic fingerprint of the transport data. Additionally, the compact EDMR system introduced in part I of this work can be situated next to the device fabrication, allowing for a rapid analysis of semiconductor devices.[233]
In recent years, a growing number of EDMR studies on organic solar cells has been reported in the literature.[8,10,150,234,235] For $PC_{61}BM$-polymer based organic solar cells, EDMR has led to two observations that seem to be in conflict: At low temperatures and with strong illumination, a clear bimolecular recombination signature featuring both $PC_{61}BM$ and polymer-related signals has been observed.[10] At ambient temperature, dark EDMR was reported to show only a polymer signal with two components of differing linewidth, which was interpreted in terms of a "bipolaron blocking" effect,[8] or a bipolar injection,[11] but these interpretations are still controversial.[236,237] Interestingly, the applied electrical bias conditions in organic semiconductor EDMR are often dissimilar, e.g. OLED-mode at 15 K,[7] forward bias at ambient-temperature,[8] short-circuit at 5 K,[9] or reverse bias at 10 K,[10] and the dependence of EDMR on the operating regimes of a solar cell have not yet been studied systematically.
As will be shown in the following sections, EDMR results obtained on photovoltaic devices depend strongly on both electrical and light biasing conditions. The method can thus be the perfect tool to bridge the gap between spectroscopy and quantitative electrical analysis, paving the way to a deeper understanding of organic solar cells.

13.2. Device Configuration and Current-Voltage Analysis

The experiments presented in this part were carried out on two P3HT:$PC_{61}BM$ bulk-heterojunction solar cells with an active area of 2.3 mm × 2.9 mm. Both solar cell devices were prepared at the Max Planck Institute for Polymer Research in Mainz, Germany by the Research Group for Organic Optoelectronics headed by Prof. Dr. Frédéric Laquai.
The solar cell devices are based on the ITO substrates presented in chapter 3, section 3.2 and the used standard preparation procedure for a sample was as follows: ITO-coated glass substrates (2.5 mm × 57.5 mm, Präzisions Glas & Optik GmbH, Germany) were patterned by wet etching, cleaned by a multi-step ultrasonic treatment with different solvents, and plasma-etched in argon for 15 min. Afterwards, a PEDOT:PSS layer (Clevios P, Heraeus) was spin-coated onto these substrates and annealed for 30 min at 120 °C. A mixture of 7.2 mg P3HT (Sepiolid P200, regioregularity > 98 %, BASF), 4.8 mg $PC_{61}BM$ (∼ 99 %, Aldrich) and 600 µL of chlorobenzene was prepared and stirred at 80 °C for more than 12 h in a nitrogen-filled glove box. The P3HT:$PC_{61}BM$ layer (70 nm) was spin-coated and the samples were directly loaded into an evaporation chamber were the aluminum electrode (100 nm) was deposited. The resulting

sample design is depicted in figure 42. Both samples were annealed at 120 °C for a period of 20 min and then encapsulated using a quartz glass slide glued with Norland Optical Adhesive 68 (Norland Products, USA). To prevent degradation, the prepared devices were stored in a nitrogen atmosphere and only removed from the glove box when performing current-voltage or EDMR experiments. All current-voltage characteristics were recorded directly inside the EDMR spectrometer with the sample positioned and contacted as depicted in figure 9 (page 27) and 10 (page 28), respectively. This way, near simultaneous current-voltage and EDMR measurements were possible, without the need for sample repositioning. Figure 43 a) shows the result of the electrical characterization for the first P3HT:$PC_{61}BM$ solar cell sample (sample A). The dark current grows exponentially with applied bias voltage V_{bias}, characterized by a dark ideality factor $n_{\mathrm{d}} = 2.0(1)$ (cf. equation 12.12), until saturation occurs at higher voltages due to an effective series resistance. The maximum photocurrent $I_{\mathrm{ph,\,max}}$ (determined at $V_{\mathrm{bias}} = -0.9\,\mathrm{V}$) grows linearly with increasing light intensity P_{irr}, thus shifting the current-voltage curve vertically and leading to a logarithmic increase in the open circuit voltage V_{OC} characterized by a light ideality factor of $n_{\mathrm{l}} = 1.9(1)$ (cf. equation 12.13), as depicted in figure 43 b).

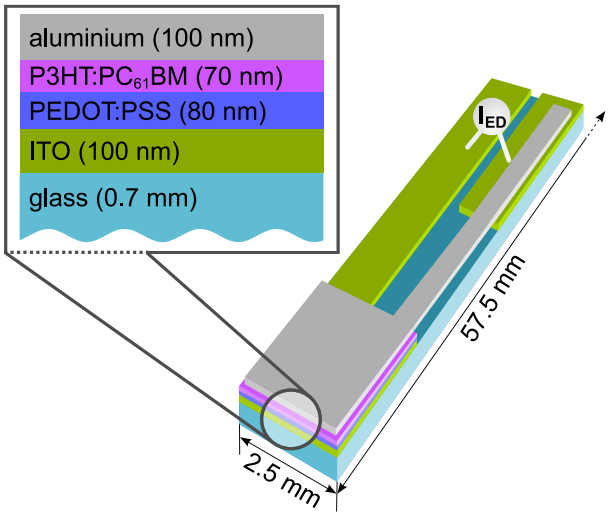

Fig. 42: Device configuration of the organic solar cells used in this thesis. The basic ITO/glass substrate design is shown in figures 10 d) and 11 on pages 28 and 29.

The voltage-dependent photocurrent I_{ph} can be further analyzed by subtracting the dark curve from the current-voltage curves with illumination. The result of this operation is displayed in figure 43 c). For every illumination level a pronounced point can be identified were the curvature of I_{ph} changes (inflection point, IP). This increase in the slope of I_{ph} near a "point of optimal symmetry" was also discussed by Limpinsel *et al.*[238] The photocurrent at this point is still negative for all irradiation levels, but a sign change can be anticipated at even lower illumination. It is worth noting that in the conducted experiments, the photocurrent is almost strictly proportional to the illumination level over the entire bias voltage range up to the IP, as can be seen in figure 43 d). Limpinsel *et al.* have explained the IP with a quasi flatband condition that occurs within the sample at voltage levels far lower than the built-in voltage due to band bending. This bending is expected for low-mobility semiconductors as a consequence of carrier injection and leads to highly charged contact regions and a homogenized charge distribution in the bulk.[238] Consequently, at this bias point the recombination is expected to be fairly strong, and the photocurrent is produced mainly by the contact regions that still provide a drift field for the extraction of photo-generated carriers. The importance of the drift field for successful generation and extraction of photo-induced carriers can be read off from the high symmetry of the photocurrent around the IP. As discussed later (see section 13.4), it turns out that this voltage level is also a good scaling variable for voltage-dependent EDMR.

The second investigated solar cell sample (sample B) showed similar current-voltage characteristics and ideality factors n_{dark} and n_{light}. Furthermore, both samples revealed comparable fill

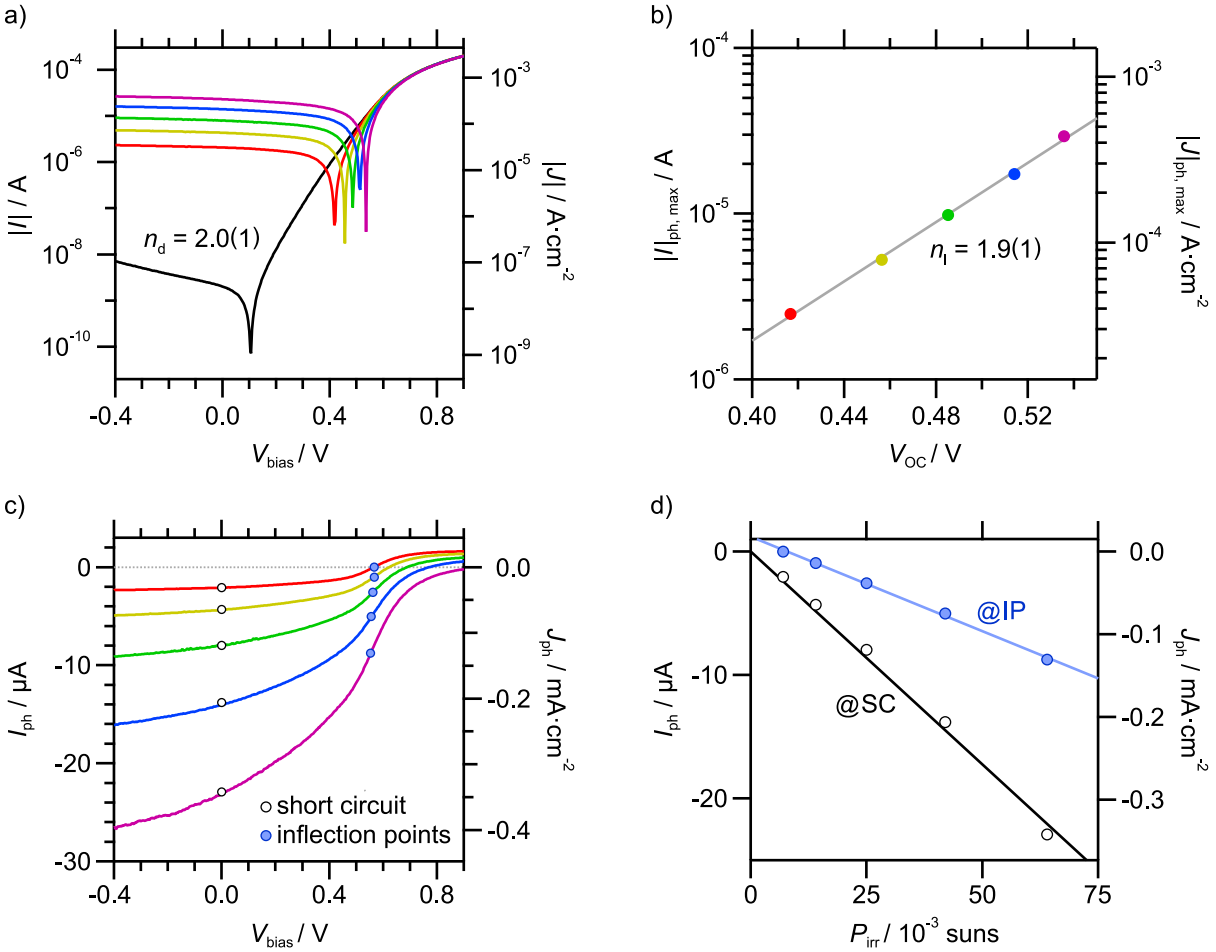

Fig. 43: Electrical characteristics of P3HT:$PC_{61}BM$ solar cell sample A. a) Current-voltage characteristics of the device without illumination (black), as well as with weak illumination (color code: red $= 7 \times 10^{-3}$ suns, yellow $= 1.4 \times 10^{-2}$ suns, green $= 2.5 \times 10^{-2}$ suns, blue $= 4.2 \times 10^{-2}$ suns, purple $= 6.4 \times 10^{-2}$ suns). The dark ideality factor $n_\mathrm{d} = 2.0(1)$ was determined according to equation 12.12 by fitting the dark values in the range $V_\mathrm{bias} = 0.25\,\mathrm{V} - 0.50\,\mathrm{V}$. b) Maximum photocurrent $I_{\mathrm{ph,\,max}}$ extracted from I at $V_\mathrm{bias} = -0.9\,\mathrm{V}$ versus open circuit voltage V_OC for the different light intensities. The data were fitted according to equation 12.13 (gray line) resulting in a light ideality factor of $n_\mathrm{l} = 1.9(1)$. c) Voltage-dependent photocurrent I_ph obtained by subtracting the dark curve from the current-voltage curves with illumination. The lines are color-coded as before. Circles mark the short circuit and inflection point conditions for each trace. d) Dependence of the photocurrent I_ph at short-circuit (SC) and inflection point (IP) conditions on the illumination intensity P_irr, both data sets were linearly fitted (lines). The photocurrent is almost strictly proportional to the illumination level over the entire bias voltage range up to the inflection point.

factors of $FF = 0.52$ (sample A) and $FF = 0.56$ (sample B) at weak light illumination with an intensity of $P_\mathrm{irr} = 7 \times 10^{-3}$ suns, as well as inflection points $V_\mathrm{IP} \approx 0.56\,\mathrm{V}$ (sample A) and $V_\mathrm{IP} \approx 0.54\,\mathrm{V}$ (sample B).

13.3. Basic EDMR Spectroscopy

After introducing the device configuration, as well as presenting the current-voltage analysis results of the P3HT:$PC_{61}BM$ solar cell samples in the previous section, we will now proceed with basic EDMR spectroscopy on this system. Here, our focus is on the identification and assignment of the observed species, which is a necessary foundation for the bias and light dependent EDMR study presented in section 13.4. All EDMR experiments on organic solar cells shown in this thesis were performed with the benchtop spectrometer presented in part I using a microwave source power of $P_{\mathrm{MW}} = 100\,\mathrm{mW}$, a modulation amplitude of $B_{\mathrm{mod}} = 0.2\,\mathrm{mT}$, and a modulation frequency of $f_{\mathrm{mod}} = 620\,\mathrm{Hz}$.

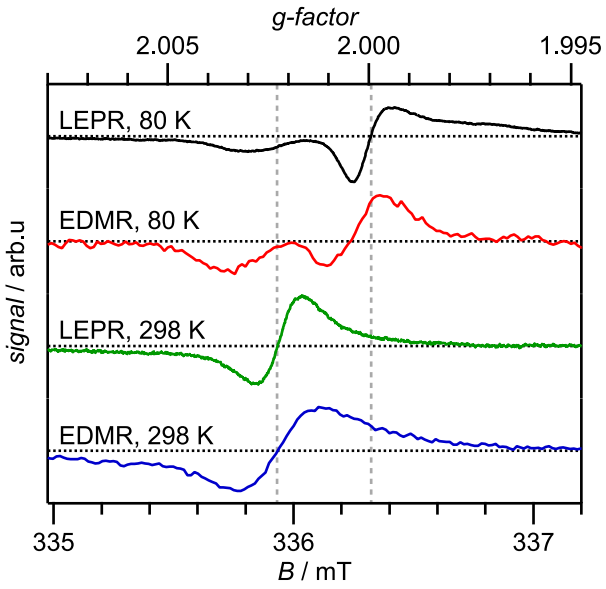

Fig. 44: LEPR and EDMR of a P3HT:$PC_{61}BM$ blend at high and low temperatures. All LEPR experiments were performed on a mixture of P3HT and $PC_{61}BM$ in a standard EPR quartz glass tube at $P_{\mathrm{irr}} = 2.2 \times 10^{-1}$ suns. The EDMR experiments were done using solar cell sample B at $V_{\mathrm{bias}} = 0\,\mathrm{V}$. The light intensity was set to $P_{\mathrm{irr}} = 2.2 \times 10^{-1}$ suns and $P_{\mathrm{irr}} = 2.5 \times 10^{-2}$ suns for the 80 K and 298 K experiment, respectively. A P3HT related signal at $g \approx g_{\mathrm{s}}$ is observed in all measurements. The typical $PC_{61}BM$ signal at $g \approx 2.000$ is only visible in the 80 K experiments. A slight shift between LEPR and EDMR is observed, as discussed in the text.

As introduced in chapter 2, EDMR is based on the detection of spin-dependent transitions that alter the sample's conductivity. The concept of the spin pair and an EDMR rate equation model were discussed in the same chapter (see section 2.2). In the context of organic photovoltaic devices two different kinds of spin pairs exist: the first one is made up from polarons of opposite charge (P^+/P^-), the second one from polarons of the same charge (P^+/P^+ or P^-/P^-). A spin pair formed by two unlike polarons can recombine only from a spin singlet configuration. In the absence of microwaves, this leads to an excess of triplet pairs under steady-state conditions. Under spin resonance, excess triplets are converted to singlets and may recombine, which reduces the total number of such carrier pairs. In the noted case, this leads to a reduction of the device current. If, in contrast, the spin pair is unipolar the steady-state pairs may have reduced mobility since polarons with the same spin cannot occupy the same hopping transport level. Therefore, the device current can be increased under spin resonance, as it will remove a "bipolaronic blocking".[8] This scenario is especially expected near interfaces of a contact, as it is otherwise implausible to have coulombically repellent pair states.[11]

At this point, it is useful to take a closer look at the signal that results from the fullerene component used in many organic solar cells including the ones investigated here, $PC_{61}BM$. Own experimental results obtained on a P3HT:$PC_{61}BM$ blend (LEPR) and solar cell sample B (EDMR) are illustrated in figure 44. The low temperature measurements were carried out using the available dewar for the MiniScope MS400 system. The solar cell sample was enclosed in a shortened EPR quartz glass tube and contacted using a suitable clamping adapter. Finally,

the EPR tube was sealed with hot-melt adhesive. The $PC_{61}BM$ related signal ($g \approx 2.000$) is only observed in the low temperature measurements and vanishes at ambient temperatures. The second signal visible in figure 44 at $g \approx g_s$ is related to P3HT and discussed in more detail below. The slight signal shift between LEPR and EDMR visible in figure 44 has also been observed by others but remains unexplained at the moment.[10]

C_{60} – which is the parent compound of $PC_{61}BM$ – has been studied extensively in the 1990s. As mentioned earlier (cf. chapter 7, section 7.1), the fulleride anion $C_{60}^{\bullet -}$ has a characteristically low g-factor between 1.994 and 2.000, which is caused by a strong delocalization of the electron wave function.[92,239] The linewidth of this species is excessively broad at ambient temperatures,[92,93] which can be explained as a result of energetically close ($\sim 10\,\mathrm{meV}$) molecular orbital states (belonging to a Jahn-Teller split t_{1u} state) that can be populated.[93,240] This leads to a rapid configuration-sampling and hence to low values for T_1 and T_2. LEPR studies on $PC_{61}BM$ reported by others suggest a similar behavior for this material.[241] Furthermore, no $PC_{61}BM$ related signal was observed in a recently reported EDMR study on polymer-fullerene blend solar cells at ambient temperature.[8]

In summary, it is concluded here that the negatively charged $PC_{61}BM$ polaron is effectively invisible in EDMR and LEPR at ambient temperatures. However, this can not be taken as a proof for the non-involvement of a $PC_{61}BM^{\bullet -}$ radical in spin-dependent processes, i.e. it may still be part of a spin pair but too broad for excitation and detection (cf. part I, equation 2.19).

The second resonance at $g \approx g_s$ observed in all measurements (cf. figure 44) is easily assigned to positive polarons in P3HT. It has been observed in EPR studies of P3HT alone,[242] as well as mixed with $PC_{61}BM$.[170,243] However, detailed EDMR spectra of the P3HT:$PC_{61}BM$ solar cells used in this study revealed not one signal corresponding to P3HT but two as shown in figure 45 a) for solar cell sample A with illumination and bias set to $V_{bias} = V_{OC}$. The first signal component (signal #1) with $g_1 = 2.0021(3) \approx g_s$ and $\Delta B_{pp,1} = 0.37(5)\,\mathrm{mT}$ is assigned to mobile $P3HT^{\bullet +}$ polarons as just discussed.

The pronounced shoulder on the low field site with $g_2 = 2.006(1)$ and $\Delta B_{pp,2} = 0.5(2)\,\mathrm{mT}$ shows up faintly in an earlier EPR study of neat P3HT but was not unequivocally identified.[244] In an own EDMR control experiment conducted on pristine commercial P3HT (see appendix on page 141, figure A7), no sign of a signal at $g_2 = 2.006(1)$ was found. Instead, a signal with $g_{2'} = 2.0026(3)$ and $\Delta B_{pp,2'} \approx 1\,\mathrm{mT}$ was observed, which is assigned here to a P3HT internal process such as bipolaronic blocking of accumulated holes or recombination of oppositely charged P3HT polarons. Upon addition of small amounts of $PC_{61}BM$ or even unsubstituted C_{60}, however, the g_2 signal clearly emerges (cf. figure A7 in the appendix on page 141). This leads to the conclusion that the signal at $g_2 = 2.006(1)$ represents an interfacial deep trap state that is due to additive-induced molecular disorder, i.e. $PC_{61}BM$ may induce stacking faults in adjacent P3HT crystallites.

The two EDMR signals described so far were observed both at reverse (rev) and forward (fwd) bias condition. A third P3HT-related EDMR resonance is detected under forward bias only. This component can best be visualized by taking the difference between normalized spectra at forward and reverse bias as shown in figure 45 b). This comparatively weak signal is characterized by $g_3 = 2.0025(3)$ and $\Delta B_{pp,3} \approx 1.3\,\mathrm{mT}$, which is compatible with the broad signal observed in pristine commercial P3HT as mentioned above ($g_{2'} = 2.0026(3)$ and $\Delta B_{pp,2'} \approx 1\,\mathrm{mT}$). More details about the procedure used to visualize signal #3 can be found in the appendix on page 142 in figure A8.

In summary, at least three distinct Lorentzian peaks related to P3HT are observed in X-band EDMR on P3HT:$PC_{61}BM$ solar cell devices at 298 K: A narrow signal characterized by

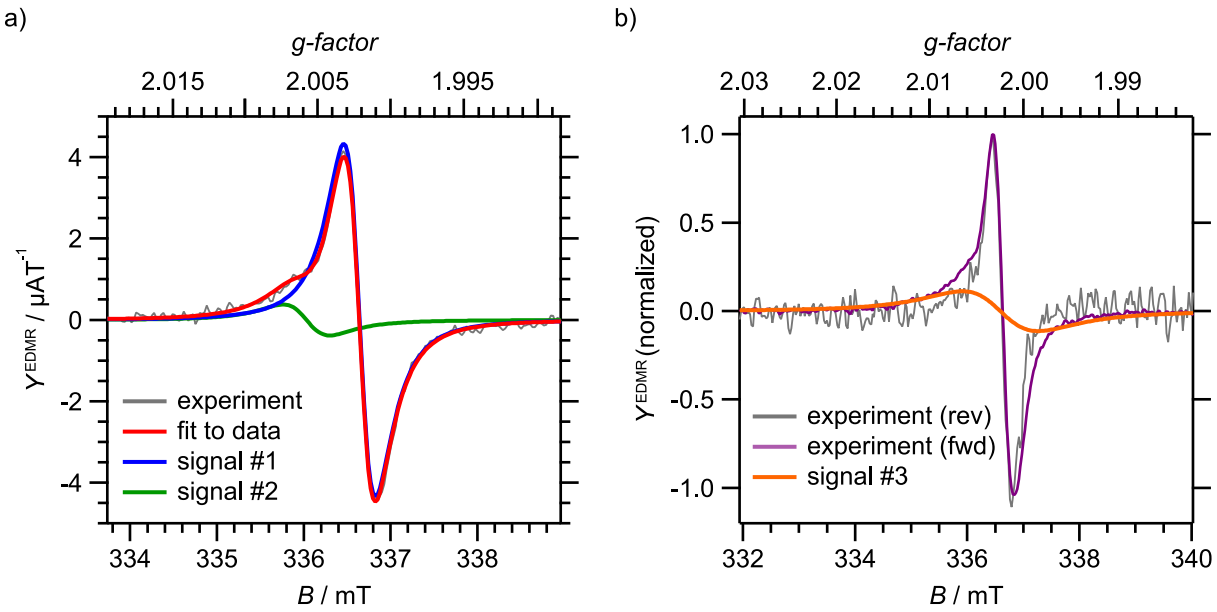

Fig. 45: Detailed EDMR spectra of solar cell sample A under illumination recorded at ambient temperature. a) EDMR spectrum obtained at $V_{\mathrm{bias}} = V_{\mathrm{OC}}$ using a light intensity of $P_{\mathrm{irr}} = 4.2 \times 10^{-2}$ suns. The deconvolution of the experimental data revealed signals at $g_1 = 2.0021(3)$ and $g_2 = 2.006(1)$ with corresponding linewidths (Lorentzian shape) of $\Delta B_{\mathrm{pp},1} = 0.37(5)\,\mathrm{mT}$ and $\Delta B_{\mathrm{pp},2} = 0.5(2)\,\mathrm{mT}$, respectively. Both signals originate from P3HT as discussed in the text. b) EDMR signals recorded at different applied bias. Data are normalized and averaged around $V_{\mathrm{bias}} = -0.2\,\mathrm{V}$ (rev) and $V_{\mathrm{bias}} = 0.5\,\mathrm{V}$ (fwd), for details see figure A8 a) of the appendix on page 142. A broad resonance (signal #3) with $g_3 = 2.0025(3)$ and $\Delta B_{\mathrm{pp},3} \approx 1.3\,\mathrm{mT}$ is revealed by fitting the difference between the fwd and rev spectra. Details of this procedure are given in the appendix on page 142 and illustrated in figure A8 b).

Tab. 5: EDMR signal components and corresponding spin-dependent processes observed in P3HT:$PC_{61}BM$ solar cell sample A (cf. figures 45 and 46). Note that the negatively charged $PC_{61}BM$ polaron involved in process ⓓ is effectively invisible in EDMR at 298 K (cf. figure 44). Hence, no signal corresponding to that species is given here.

Signal #	g-factor	ΔB_{pp}/mT	Species	Process in Fig. 46
1	2.0021(3)	0.37(5)	mobile P^{+}_{P3HT}	ⓐ, ⓑ, ⓒ, ⓓ
2	2.006(1)	0.5(2)	trap state $P^{\mathrm{T}}_{\mathrm{P3HT}}$	ⓒ
3	2.0025(3)	~ 1.3	localized P^{+}_{P3HT} mobile P^{-}_{P3HT}	ⓐ ⓑ

$g_1 = 2.0021(3)$ and $\Delta B_{\mathrm{pp},1} = 0.37(5)\,\mathrm{mT}$, a pronounced low-field shoulder with $g_2 = 2.006(1)$ and $\Delta B_{\mathrm{pp},2} = 0.5(2)\,\mathrm{mT}$, and a weak resonance at $g_3 = 2.0025(3)$ with $\Delta B_{\mathrm{pp},3} \approx 1.3\,\mathrm{mT}$.

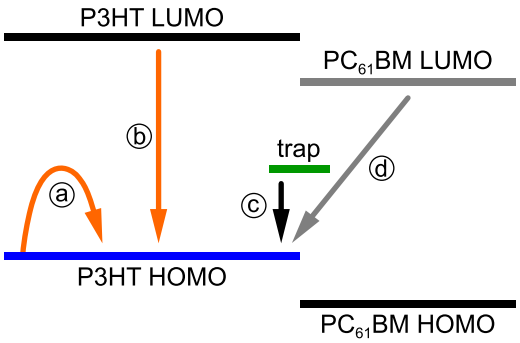

Fig. 46: Microscopic picture of spin-dependent processes inside a P3HT:$PC_{61}BM$ solar cell. ⓐ "bipolaronic blocking " involving a mobile P^+_{P3HT} and a localized P^+_{P3HT}, ⓑ ambipolar polaron recombination between a mobile P^+_{P3HT} and a mobile P^-_{P3HT}, ⓒ SRH recombination involving a deep level trap state, drawn here at the interface and ⓓ direct $PC_{61}BM$/P3HT recombination, see text for details.

Having identified the spins taking part in the various EDMR signals, we can now discuss their relation to the recombination processes inside the photovoltaic device. Figure 46 illustrates the microscopic interpretation of the spin-dependent processes inside a P3HT:$PC_{61}BM$ solar cell. Since all signals are quantitatively independent, an assignment to spin pairs involved in a single process cannot be based on CW-EDMR intensities. Pulsed EDMR (pEDMR) studies, which are not possible with the MiniScope MS400 system, are thus needed to identify the spin partners.[8,10,11]

Based on the conducted control experiment on pristine P3HT (see appendix on page 141) the broad difference line (signal #3) was assigned to a process internal to the P3HT phase. As discussed above, this may either be ⓐ a "bipolaronic blocking " involving a mobile P^+_{P3HT} and a localized P^+_{P3HT} or ⓑ an ambipolar polaron recombination between a mobile P^+_{P3HT} and a mobile P^-_{P3HT}. In either case, the mobile P^+_{P3HT} is involved as a partner and hence these processes contribute to signal #1. Process ⓒ involves, again, the mobile P^+_{P3HT} and the possibly interface-related deep trap state P^T_{P3HT} with resonance at g_2 (signal #2). Finally, the negatively charged $PC_{61}BM$ polaron involved in process ⓓ, whose pair partner is the mobile P^+_{P3HT} polaron as well, cannot be observed at 298 K and is thus effectively invisible in the solar cell experiments conducted in the present work. It should be noted that the P^+_{P3HT} polaron (signal #1) takes part in all discussed processes, which involve different partner spins (cf. figure 46). Its intensity therefore represents the sum of several recombination events.

The spectroscopic properties and the assignments of the three distinct EDMR peaks to the species and corresponding spin-dependent processes inside the P3HT:$PC_{61}BM$ solar cell device are summarized in table 5 on page 95.

13.4. Bias and Light Dependent EDMR

In the last section, it became evident that the voltage bias applied during a measurement can significantly alter the EDMR spectrum of a P3HT:$PC_{61}BM$ solar cell sample. As was illustrated in figure 45 b), the broad resonance signal #3 with $g_3 = 2.0025(3)$ and $\Delta B_{\mathrm{pp},3} \approx 1.3\,\mathrm{mT}$ was only observed under forward bias conditions. The ubiquitous signals #1 and #2, introduced in figure 45 a), are influenced by the chosen bias voltage as well. This becomes clear when looking at EDMR spectra recorded at different voltage bias but using a constant illumination intensity (see figure 47). For the three experiments with $V_{\mathrm{bias}} = 0\,\mathrm{mV}$, $V_{\mathrm{bias}} = 533\,\mathrm{mV}$ (equal to the inflection point voltage V_{IP} introduced in section 13.2) and $V_{\mathrm{bias}} = 900\,\mathrm{mV}$ the total signal

intensity changes significantly. Additionally, a shift and growth of signal #2 with respect to signal #1 is observed. Hence, the different components of an EDMR spectrum may depend on electrical biasing in different ways. This illustrates why carefully checking the bias voltage during EDMR measurements is important when comparing different results. In fact, it is well possible that studies about the very same material or system come to different conclusions if different bias points are chosen.

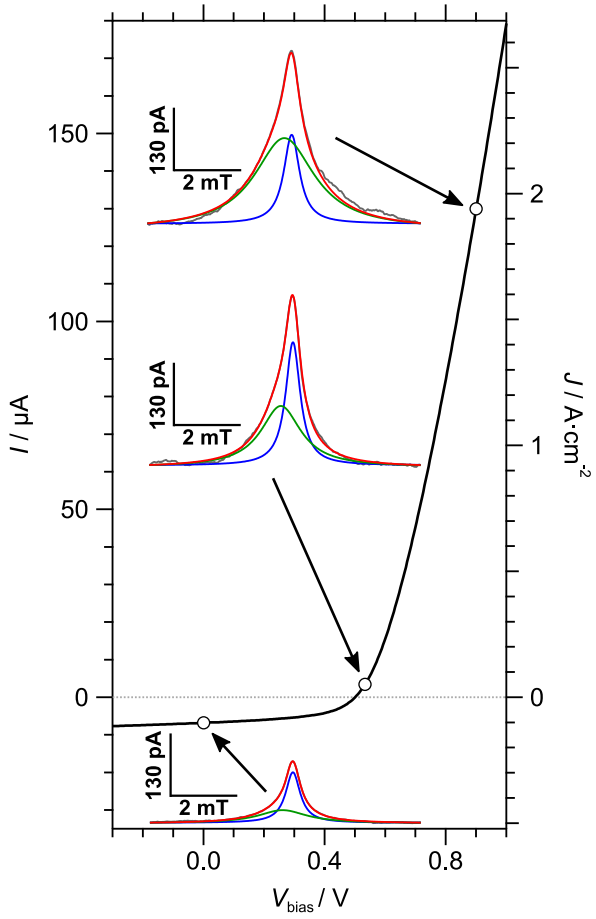

Fig. 47: EDMR absorption spectra (S^{EDMR} vs. B, cf. figure 2 on page 15) of solar cell sample B illuminated with 2.5×10^{-2} suns at different points of the corresponding current-voltage characteristics (black line). All inset spectra are scaled the same way for easy comparison. The deconvolution of the experimental data was done in analogy to figure 45 a) and the same color code applies. Note the change in total signal intensity, as well as the shift and growth of the green component (signal #2) with respect to the blue one (signal #1).

We now proceed to an evaluation of the EDMR signal strengths by systematically varying both optical and electronic operation conditions for solar cell sample A. Due to a limited SNR at 298 K, the most easily quantifiable $\mathrm{P}^{+}_{\mathrm{P3HT}}$ signal at $g_1 = 2.0021(3)$ (signal #1) will be used for this study. Since the linewidth of this Lorentzian-shaped signal changes only marginally with bias or illumination, it is equally possible to use the amplitude of S^{EDMR}, which is the spin-dependent EDMR current ΔI^{EDMR}, or the area of the signal component. In this section, the former approach is chosen since this avoids spurious noise due to baseline instability and yields the EDMR current in physical units of amperes. In the EDMR literature on photoconductors,[44,245] it is customary to discuss the EDMR effect $\xi_{\mathrm{sd}}^{\mathrm{EDMR}} = \Delta I^{\mathrm{EDMR}}/I_{\mathrm{sample}}$ (cf. equation 3.9) rather than the spin-dependent EDMR current. However, since the EDMR effect is a relative measure it makes no sensible prediction for the open circuit case in a solar cell where the total current I_{sample} is zero and hence $\xi_{\mathrm{sd}}^{\mathrm{EDMR}}$ diverges. For the bias and light dependent EDMR study presented here, the electrical bias value was varied between $V_{\mathrm{bias}} = -0.27\,\mathrm{V}$ and $V_{\mathrm{bias}} = 0.80\,\mathrm{V}$ and light intensities between $P_{\mathrm{irr}} = 7.0 \times 10^{-3}$ suns and $P_{\mathrm{irr}} = 6.4 \times 10^{-2}$ suns were used. Additionally, two EDMR experiments in the dark were carried out to complement the data with illumination.

Figure 48 a) shows the obtained results for the spin-dependent EDMR current ΔI^{EDMR} together with the observed signal phase shift $\Delta\varphi^{\mathrm{EDMR}}$ measured in the lock-in technique. The most striking feature is that two different EDMR regions can clearly be distinguished. In the bias regime below about 0.3 V, ΔI^{EDMR} strongly depends on the light intensity P_{irr}, suggesting

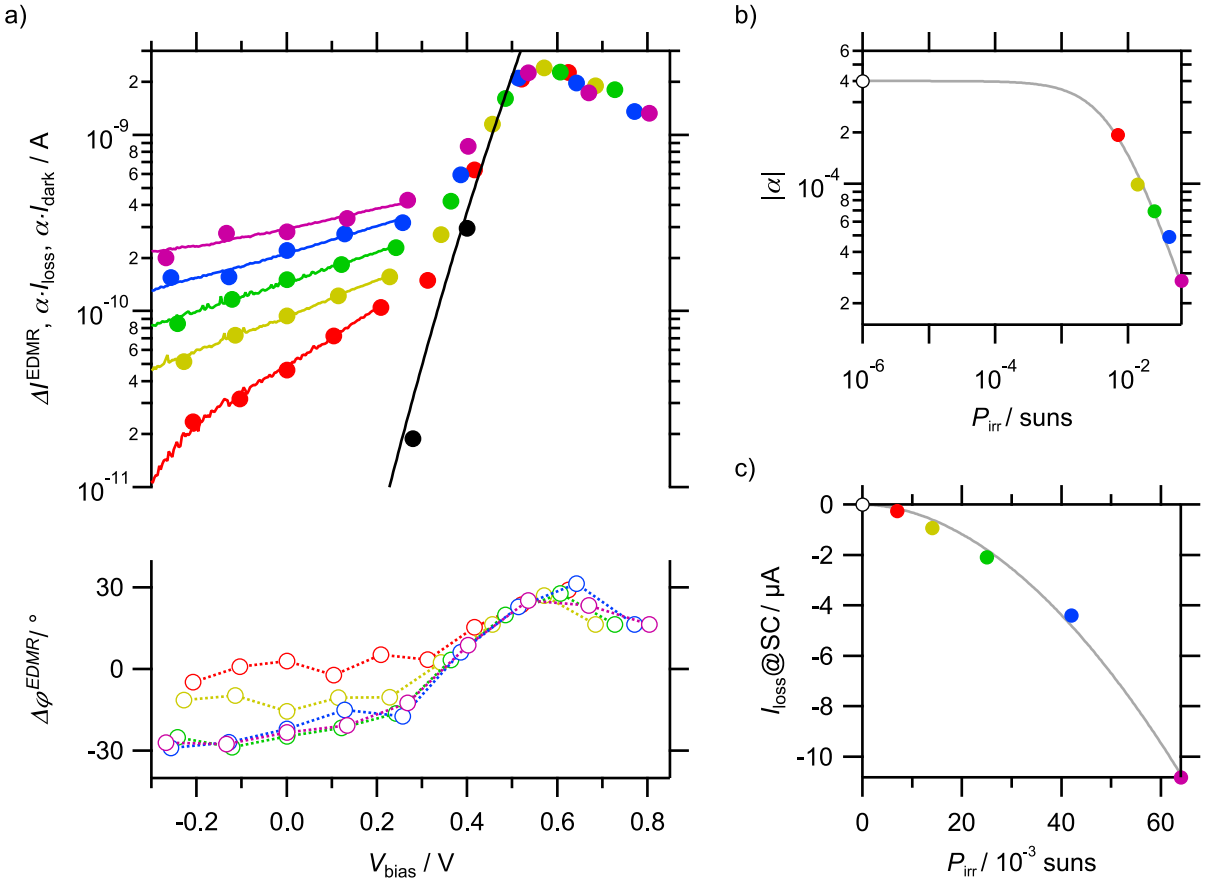

Fig. 48: Results of the bias and light dependent EDMR study on solar cell sample A. a) Spin-dependent EDMR current ΔI^{EDMR} (closed circles) and signal phase shift $\Delta\varphi^{\mathrm{EDMR}}$ (open circles with dotted lines as guides to the eye) vs. applied bias V_{bias} at weak illumination intensities (color code: black = dark, red = 7×10^{-3} suns, yellow = 1.4×10^{-2} suns, green = 2.5×10^{-2} suns, blue = 4.2×10^{-2} suns, purple = 6.4×10^{-2} suns). The corresponding loss currents I_{loss} for $V_{\mathrm{bias}} \lesssim 0.3\,\mathrm{V}$ (cf. equation 13.1) scaled by the EDMR visibility function α (see equation 13.2), as well as the dark current I_{dark} scaled by α are shown as lines using the same color code. b) Dependence of the visibility function α on the applied light intensity P_{irr} (closed circles, same color code as before). The gray line is a fit to the experimental data using equation 13.6, resulting in $P_0 = 6.2(6) \times 10^{-3}$ suns and $\kappa = 1.1(1)$. c) Dependence of the loss current I_{loss} (cf. equation 13.1) determined at short-circuit condition (SC) on the applied light intensity P_{irr} (closed circles, same color code as before). The gray line is a power-law fit revealing $I_{\mathrm{loss}} \propto P_{\mathrm{irr}}^{1.9(1)}$.

that the recombination of photo-generated carriers dominates the spin-dependent EDMR current in this regime. A different recombination process then takes over at forward bias, where the EDMR current is basically independent of illumination but strongly bias-dependent. Between about 0.3 V and 0.5 V, the bias dependence of ΔI^{EDMR} is very nearly exponential. The signal phase shift gives a first indication of how to properly interpret the course of ΔI^{EDMR}. Although the absolute value of the phase is arbitrary due to experimental reasons, a strong difference in reverse and forward directions is apparent. The relative phase shift is about 60°, thus not a

sign change, and rather corresponds to a change from resistive to capacitive impedance. This suggests that the EDMR-detected recombination takes place at different locations in the sample, e.g. in the volume ("resistive", at reverse bias) or near the contact interfaces ("capacitive", at forward bias). This is in line with the observation that ΔI^{EDMR} is strongly photo-dependent at reverse-bias, while the data points in forward direction fall on a single curve with a maximum at $V_{\mathrm{bias}} \approx 0.56\,\mathrm{V}$, equal to the inflection points of the current-voltage characteristics observed for this sample (cf. section 13.2).
A more quantitative picture of the loss processes inside the P3HT:$PC_{61}BM$ solar cell device can be obtained by relating the loss current I_{loss}, which is defined as the difference between the expected generation current $I_{\mathrm{gen}} = qGLA$ (with charge q, averaged generation rate G, active layer thickness L and active area A) and the actual photo-current I_{ph},

$$I_{\mathrm{loss}} = I_{\mathrm{gen}} - I_{\mathrm{ph}} \tag{13.1}$$

directly to the obtained EDMR data points. In the photo-dependent regime where $V_{\mathrm{bias}} \lesssim 0.3\,\mathrm{V}$, quantitative coincidence between the spin-dependent EDMR current ΔI^{EDMR} and I_{loss} can be obtained by introducing a bias-independent scaling function α (equation 13.2) to account for the illumination-dependent EDMR sensitivity, as illustrated in figure 48 a).

$$\Delta I^{\mathrm{EDMR}}\big|_{V_{\mathrm{bias}} \lesssim 0.3\,\mathrm{V}} = \alpha \cdot I_{\mathrm{loss}} = \alpha \cdot (I_{\mathrm{gen}} - I_{\mathrm{ph}}) \tag{13.2}$$

With ΔI^{EDMR} and I_{ph} being available from EDMR and current-voltage experiments, respectively, equation 13.2 was used for curve fitting, yielding the parameters I_{gen} and α. It should be noted that I_{gen} was in good agreement with the maximum photocurrent $I_{\mathrm{ph,\,max}}$, as expected for a complete charge carrier extraction at strong reverse bias ($V_{\mathrm{bias}} = -0.9\,\mathrm{V}$). Furthermore, figure 48 a) shows that the dark current I_{dark} can be scaled using α to roughly reach coincidence with the corresponding ΔI^{EDMR} values as well. The values of α and I_{loss} depend on the used light intensity P_{irr} as depicted in figures 48 b) and 48 c), respectively. Their physical meaning will be discussed in the following paragraph.
On general grounds, the EDMR signal can be considered to be affected by three probabilities

$$\frac{\Delta I^{\mathrm{EDMR}}}{I_{\mathrm{loss}}} = \eta_{\mathrm{vis}}\left(P_{\mathrm{irr}}\right) \cdot \eta_{\mathrm{rec}} \cdot \eta_{\mathrm{ex}} \equiv \alpha\left(P_{\mathrm{irr}}\right) \tag{13.3}$$

which are the visibility η_{vis} of the process, the probability for a spin-dependent recombination η_{rec}, and the excitation efficiency of the resonance line η_{ex}. The latter two terms depend on spin relaxation times, as well as on SRH parameters like trap density and emission probability but are usually assumed to be independent of illumination. The visibility, on the other hand, is related to the effective spin-dependence of the total current and can be written as a ratio of probabilities

$$\eta_{\mathrm{vis}}\left(P_{\mathrm{irr}}\right) = \frac{\Pi_{\mathrm{SDR}}\left(P_{\mathrm{irr}}\right)}{\Pi_{\mathrm{SDR}}\left(P_{\mathrm{irr}}\right) + \Pi_{\mathrm{NSDR}}\left(P_{\mathrm{irr}}\right)} \tag{13.4}$$

with Π_{SDR} and Π_{NSDR} as the probabilities for a charge carrier to take part in an observed spin-dependent process or in a non-spin-dependent process, respectively. For example, using equations 2.18 and 2.20 of the rate equation model introduced in chapter 2, section 2.2, we could identify η_{vis}, η_{rec} and η_{ex} as shown in equation 13.5.

$$S^{\mathrm{EDMR}} = \underbrace{-\frac{f\tau}{\left(1+\frac{d}{r}\right)+f\tau}}_{\eta_{\mathrm{vis}}} \cdot \underbrace{\frac{\left(\frac{\varrho}{r}\right)^2 + \pi\left(\frac{\varrho}{r}\right)\left(1+\frac{d}{r}\right)}{1+\frac{r}{d}\left(1-\left(\frac{\varrho}{r}\right)^2\right)+\left(1+\frac{d}{r}\right)\left(1+2\,\frac{W_0}{d}\right)}}_{\eta_{\mathrm{rec}}} \cdot \underbrace{\frac{W_{\mathrm{MW}}}{W_1+W_{\mathrm{MW}}}}_{\eta_{\mathrm{ex}}} \tag{13.5}$$

For photogenerated carriers, where a photon generates an electron and a hole, the Langevin recombination rate R_{L} is proportional to P_{irr}^{β} with $\beta = 2$ (cf. equation 12.8) and the SRH recombination rate is characterized by $R_{\mathrm{SRH}} \propto P_{\mathrm{irr}}^{\beta}$ with $\beta = 1$ (cf. equation 12.10). As shown in figure 48 b), the α values obtained for the different illumination levels can be fitted using equation 13.6.

$$\alpha \propto \frac{1}{1 + \left(\frac{P_{\mathrm{irr}}}{P_0}\right)^{\kappa}} \tag{13.6}$$

A comparison with equation 13.4 reveals that P_0 equals the light intensity where $\Pi_{\mathrm{SDR}} = \Pi_{\mathrm{NSDR}}$ and that κ is connected to the above introduced probabilities by: $\Pi_{\mathrm{NSDR}}/\Pi_{\mathrm{SDR}} \propto P_{\mathrm{irr}}^{\kappa}$. Taking into account that, in general, the light dependence of the spin-dependent and spin-independent process are different, it becomes clear that $\kappa = \beta_{\mathrm{NSDR}} - \beta_{\mathrm{SDR}}$. For the data shown in figure 48 b), it was found that $P_0 = 6.2(6) \times 10^{-3}$ suns and that $\kappa = 1.1(1)$. This suggests - in a simple picture - that the non-spin-dependent recombination is bimolecular (Langevin type), while the spin-dependent process is monomolecular (SRH type). Furthermore, we find that the non-spin-dependent process outweighs the spin-dependent one for light intensities above about 6×10^{-3} suns. It should be noted that the effectively quadratic illumination dependence of the loss current ($I_{\mathrm{loss}} \propto P_{\mathrm{irr}}^{1.9(1)}$) shown in figure 48 c) is not apparent from the photocurrent, which scales as $I_{\mathrm{ph}} \propto P_{\mathrm{irr}}$ as depicted in figure 43 d) (both values were determined at short-circuit condition to exclude effects introduced by an external electric field). This is due to the fact that the losses are still small compared to the total current flowing through the sample. Hence, using just the light-dependence of the photo-current as a measure for the "reaction order" of the recombination in a solar cell device may not be very meaningful. Rather, the light dependence of the loss current has to be analyzed. Here, it is concluded that bimolecular recombination dominates already at fairly low illumination levels in the investigated solar cells.
We have shown that there are several recombination paths visible in the EDMR spectrum of a P3HT:$PC_{61}BM$ solar cell and that their relative and absolute amplitude strongly depends on electrical and optical bias conditions. Furthermore, a quantitative correlation of the spin-dependent EDMR currents with the losses in photocurrent at voltages below $V_{\mathrm{bias}} \lesssim 0.3\,\mathrm{V}$, and with the injection-related dark current above that was found. As discussed above, the observed signal phase shift suggests two distinct recombination regimes. If we assume the observed course of ΔI^{EDMR} with V_{bias} to result from a superposition of two processes that do not influence each other, i.e. one EDMR signal ΔI_{p} due to photo recombination and another one ΔI_{i} related to the recombination of the injected charge carriers, as summarized in equation 13.7, a reconstruction of both constituents becomes possible.

$$\Delta I^{\mathrm{EDMR}} = \Delta I_{\mathrm{i}} + \Delta I_{\mathrm{p}} \tag{13.7}$$

In this approach, the photo recombination signal over the whole experimental range is given by

$$\Delta I_{\mathrm{p}} = \alpha \cdot (I_{\mathrm{gen}} - I_{\mathrm{ph}}) \tag{13.8}$$

in analogy to equation 13.2. Here, the necessary values for α and I_{gen} were taken from the fits mentioned above (cf. figure 48). Figure 49 a) shows the result of this reconstruction together with the experimentally obtained EDMR data points. The spin-dependent EDMR current signal due to injected charge carriers is then given by equation 13.9.

$$\Delta I_{\mathrm{i}} = \Delta I^{\mathrm{EDMR}} - \Delta I_{\mathrm{p}} \tag{13.9}$$

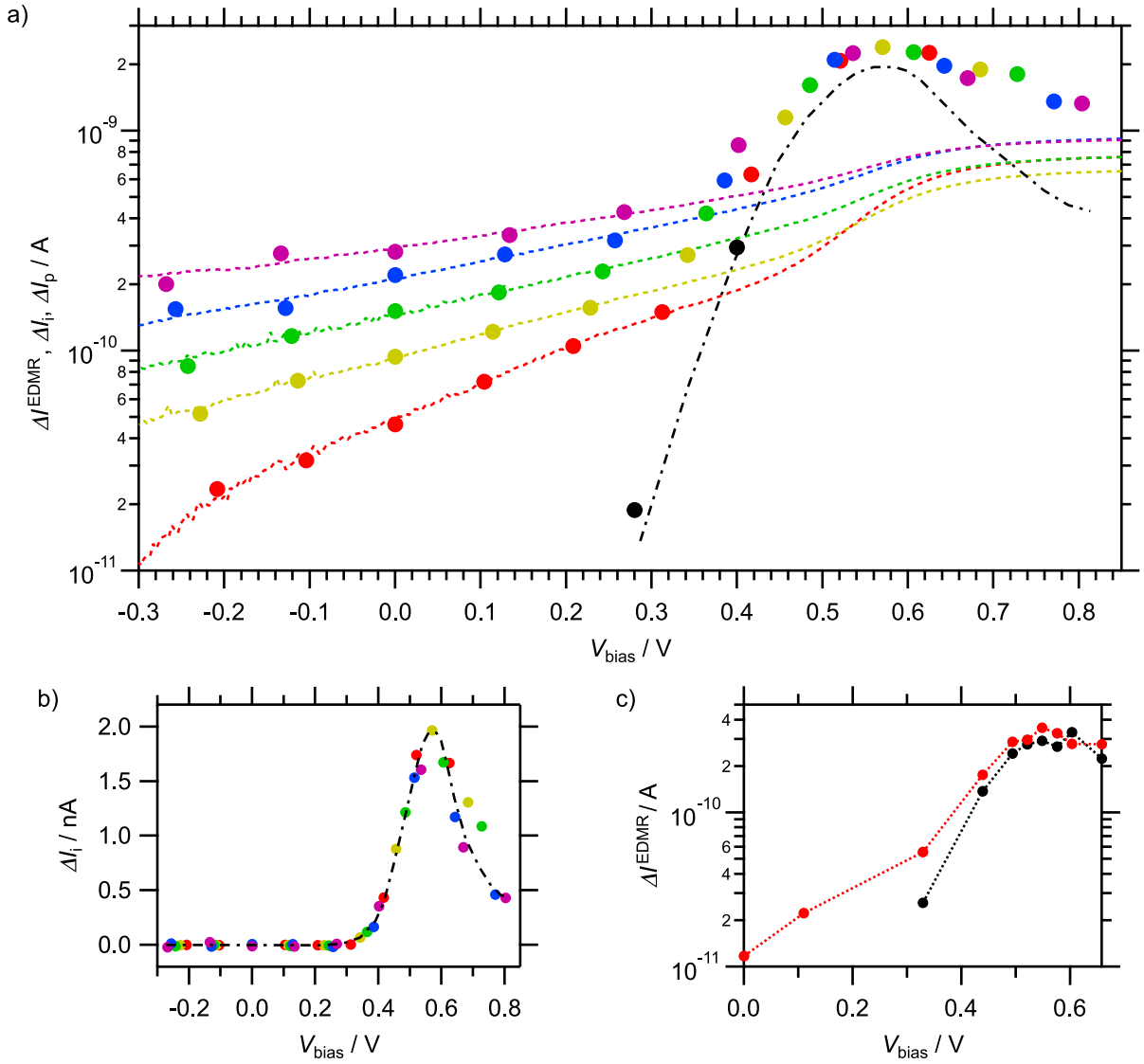

Fig. 49: Superposition approach for signal reconstruction in bias and light dependent EDMR. a) Experimentally determined spin-dependent EDMR currents ΔI^{EDMR} (closed circles) for solar cell sample A and reconstructed spin-dependent EDMR currents ΔI_{p} due to photo recombination calculated using equation 13.8 (dashed lines with color code: red $= 7 \times 10^{-3}$ suns, yellow $= 1.4 \times 10^{-2}$ suns, green $= 2.5 \times 10^{-2}$ suns, blue $= 4.2 \times 10^{-2}$ suns, purple $= 6.4 \times 10^{-2}$ suns). The dash-dotted black line shows the reconstruction for the spin-dependent EDMR current ΔI_{i} due to injected charge carriers. b) Reconstruction of the EDMR signal ΔI_{i} due to injected charge carriers: The closed circles (same color code as before) represent the data points obtained using equation 13.9. The dash-dotted black line shows the corresponding regression curve that was inserted in part a) of this figure. c) Direct comparison of the EDMR results without (black) and with illumination at $P_{\mathrm{irr}} = 7 \times 10^{-3}$ suns (red) for solar cell sample B. The dotted lines are guides to the eye. Note the very similar trend of ΔI^{EDMR} compared to part a) of this figure, see text for more details.

Figure 49 b) illustrates the result of this reconstruction, which is added to figure 49 a) as well. The presented superposition approach is further supported by a direct comparison between EDMR experiments with and without illumination carried out on solar cell sample B, which is shown in figure 49 c). As for the reconstruction done for sample A, the data points with and without illumination obtained on sample B fall on a single curve for $V_{\mathrm{bias}} \gtrsim 0.45\,\mathrm{V}$. Due to a lack in SNR, the course of ΔI^{EDMR} for $V_{\mathrm{bias}} \gtrsim 0.54\,\mathrm{V}$ remains somewhat unclear and no reliable statement can be made on whether the signal really runs through a maximum and significantly drops afterwards, or just reaches a more or less constant saturation value.
In general, the EDMR measurements on solar cell samples A and B gave similar results, albeit with different magnitude especially for the contact-related dark current components near the inflection points around $V_{\mathrm{bias}} \approx 0.55\,\mathrm{V}$, as can be seen by comparing figures 49 a) and c). At present, it is believed that this may be due to unintended differences in the sample preparation, most probably in the final annealing stage that determines the front contact micromorphology. It is worth noting that at the maximum power points (around $V_{\mathrm{bias}} \approx 0.35\,\mathrm{V}$), the EDMR signal in both samples turns out to be influenced by injected and photogenerated carriers, underlining the importance of bulk and interface properties for the design and construction of efficient organic solar cells.

14. Outlook: Investigation of Degradation Processes

Basic EDMR spectroscopy on photovoltaic devices based on P3HT:$PC_{61}BM$, as well as a more quantitative picture of the loss processes inside such a solar cell device were presented in the preceding chapter. It was shown how EDMR can be used in addition to standard current-voltage characteristics to gain a deeper understanding of the recombination processes inside fully functional organic solar cells. However, an important topic that hinders the widespread use of organic photovoltaics, not addressed so far, is the often rapidly occurring device degradation. Due to the rather unsystematic degradation conditions used for the sample discussed in this chapter, the following study only gives an outlook on how EDMR can be utilized in order to enhance our understanding of degradation processes. Nevertheless, it will support the results presented in the preceding chapter, obtained on the same device prior to degradation, and pave the way for more complex investigations on degraded devices.

Numerous studies have been conducted in order to understand the phenomenon of device degradation in organic photovoltaic devices and extensive resumes on this topic can be found in the literature.[5,246,247] At this point, we will only briefly list some of the results that are important with respect to the EDMR experiments conducted in the present work.
It is known that degradation processes can effect the different regions and materials of a polymer solar cell. For example, the active layer can undergo a chemical degradation by means of photobleaching or photooxidation.[248–250] Furthermore, the interfaces at the top and bottom contacts are known to degrade as well,[251–253] eventually leading to S-shaped current-voltage characteristics with significantly reduced short circuit currents.[218] For the P3HT:$PC_{61}BM$ devices investigated in this thesis, the aluminum top contact may oxidize, forming an interface that is only poorly permeable for charge carriers, i.e. a blocking contact, which significantly reduces the device performance.[254] This degradation of the metal/organic interface typically proceeds more rapidly than the degradation of the active layer.[255]
To obtain EDMR results on a degraded system, solar cell sample A was stored under atmospheric conditions for several weeks. Afterwards, its current-voltage characteristics were recorded in

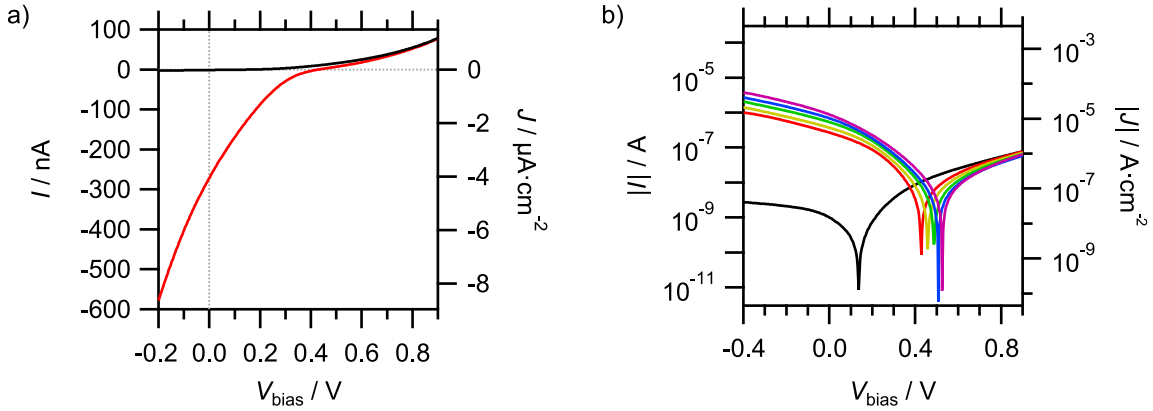

Fig. 50: Current-voltage characteristics of solar cell sample A after degradation. a) Observed shape of the current-voltage characteristics in the dark (black line) and with illumination (red line, $P_{\mathrm{irr}} = 7 \times 10^{-3}$ suns). The change of the course of the data with respect to the theoretical behavior, illustrated in figure 39 a) (see page 81), is often referred to as S-shaped or "kinked". This behavior is typical for a blocking contact with restricted charge transport over the material interfaces.[218] b) Current-voltage characteristics without illumination (black), as well as with illumination at different intensities (color code: red $= 7 \times 10^{-3}$ suns, yellow $= 1.4 \times 10^{-2}$ suns, green $= 2.5 \times 10^{-2}$ suns, blue $= 4.2 \times 10^{-2}$ suns, purple $= 6.4 \times 10^{-2}$ suns). Note the drastic reduction of the sample current I at forward bias compared to the results obtained at the same device prior to degradation, shown in figure 43 a) (see page 92).

the dark and with illumination at different light intensities. The EDMR data were collected near simultaneously, using identical conditions as in sections 13.3 and 13.4 ($P_{\mathrm{MW}} = 100\,\mathrm{mW}$, $B_{\mathrm{mod}} = 0.2\,\mathrm{mT}$, $f_{\mathrm{mod}} = 620\,\mathrm{Hz}$).

Figure 50 a) shows the recorded current-voltage characteristics of the degraded solar cell. The S-shape or "kink" is typical for a blocking contact with restricted charge transport over the material interfaces.[218] The changes in the current-voltage characteristics of solar cell sample A are especially noticeable when comparing the degraded device shown in figure 50 b) and the healthy sample displayed in figure 43 a). The current obtained at short circuit conditions goes down by about 87 % to 96 %, depending on the chosen light intensity. Generally, the current measured at reverse bias seems to be less affected compared to the one determined at strong forward bias, which drops by more than three orders of magnitude. Hence, the contact barrier almost suppresses the injection current that is typically dominating the first quadrant of the current-voltage characteristics.

EDMR measurements on the degraded solar cell sample, shown in figure 51, revealed three distinct Lorentzian peaks related to P3HT: A narrow signal visible at both forward and reverse bias (signal #1), a pronounced low-field shoulder visible only at reverse bias (signal #2), and a broad resonance visible at forward bias only (signal #3). Within the measurement uncertainties, the obtained values for the g-factors and linewiths are in good accordance with the ones observed earlier on the healthy device (cf. figure 45, section 13.3). It is thus concluded that the degradation does not change the species actively involved in the spin-dependent processes observed in the P3HT:$PC_{61}BM$ device and we will continue to use the same naming (numbering) scheme for the signals.

We will now proceed to a bias and light dependent study on the degraded device. As for

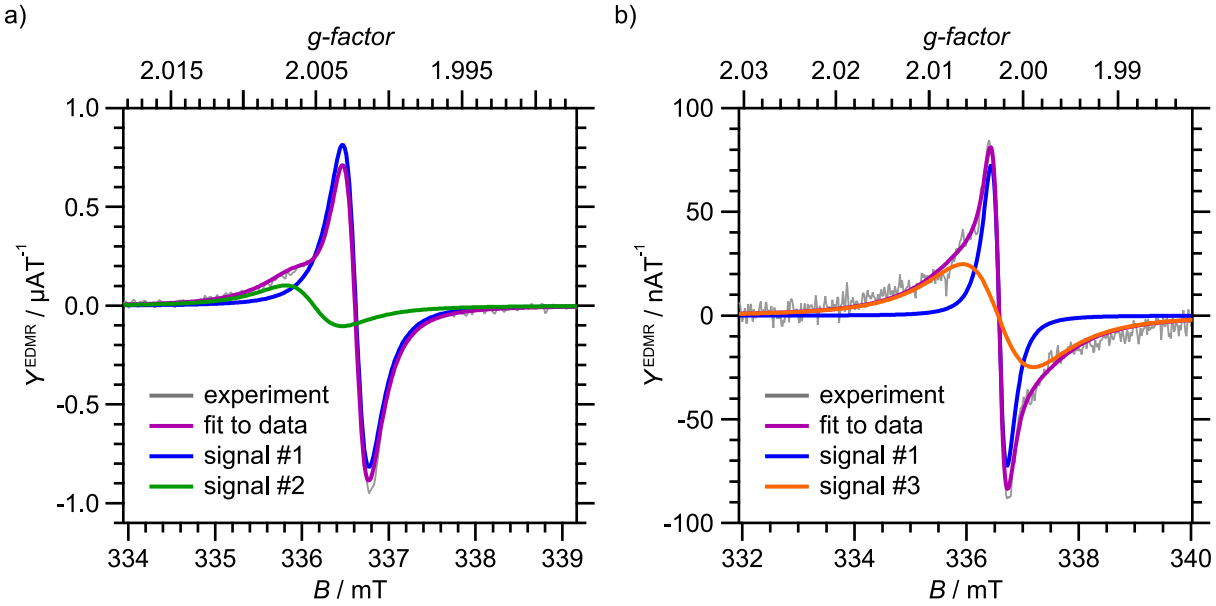

Fig. 51: EDMR spectra of solar cell sample A after degradation. The device was illuminated at a light intensity of $P_{\mathrm{irr}} = 2.5 \times 10^{-2}$ suns. a) EDMR spectrum recorded at reverse bias ($V_{\mathrm{bias}} = -0.9\,\mathrm{V}$). The deconvolution of the experimental data revealed signals at $g_1 = 2.0023(3)$ and $g_2 = 2.0051(5)$ with corresponding linewidths (Lorentzian shape) of $\Delta B_{\mathrm{pp},1} = 0.30(5)\,\mathrm{mT}$ and $\Delta B_{\mathrm{pp},2} = 0.6(2)\,\mathrm{mT}$, respectively. b) EDMR spectrum obtained at forward bias ($V_{\mathrm{bias}} = 0.9\,\mathrm{V}$). The deconvolution of the experimental spectrum revealed signals at $g_1 = 2.0026(3)$ and $g_3 = 2.0027(3)$ with corresponding linewidths (Lorentzian shape) of $\Delta B_{\mathrm{pp},1} \approx 0.3\,\mathrm{mT}$ and $\Delta B_{\mathrm{pp},3} \approx 1.3\,\mathrm{mT}$, respectively.

the healthy sample, the most easily quantifiable $\mathrm{P}^{+}_{\mathrm{P3HT}}$ signal at $g_1 = 2.0023(3)$ (signal #1) will be used for this study. The electrical bias value was varied between $V_{\mathrm{bias}} = -0.27\,\mathrm{V}$ and $V_{\mathrm{bias}} = 1.07\,\mathrm{V}$ and light intensities between $P_{\mathrm{irr}} = 7.0 \times 10^{-3}$ suns and $P_{\mathrm{irr}} = 6.4 \times 10^{-2}$ suns were used. Figure 52 shows the obtained results for the spin-dependent EDMR current ΔI^{EDMR} together with the observed signal phase shift $\Delta\varphi^{\mathrm{EDMR}}$ measured in the lock-in technique. As for the healthy samples, two EDMR regions can clearly be distinguished. While the signal in the bias regime $V_{\mathrm{bias}} \lesssim 0.3\,\mathrm{V}$ basically depends only on the light intensity, a strongly bias-dependent region showing almost no dependence on illumination is found for $V_{\mathrm{bias}} \gtrsim 0.3\,\mathrm{V}$. If compared to the results obtained on the same device before degradation, presented in figure 48 a), a larger ΔI^{EDMR} signal is found for $V_{\mathrm{bias}} \lesssim 0.3\,\mathrm{V}$. The spin-dependent EDMR current is still light-dependent, but increased by almost an order of magnitude. Furthermore, the dependence on the voltage bias seems to be less pronounced for the degraded sample in this regime. For $V_{\mathrm{bias}} \gtrsim 0.3\,\mathrm{V}$, the spin-dependent EDMR currents before and after device degradation are in stark contrast. The striking increase of ΔI^{EDMR} corresponding to the injection of charge carriers, visible in the healthy device under forward biasing conditions, is completely missing. Instead, all data points seem to collapse in a minimum around $V_{\mathrm{bias}} \approx 0.6\,\mathrm{V}$, which is slightly above the individual open circuit conditions. The course of the signal phase shift $\Delta\varphi^{\mathrm{EDMR}}$ with V_{bias} differs significantly from the one observed for the healthy device shown in figure 48 a). Qualitatively, its inflection seems to have changed, which could be related to the observed suppression of the superimposed injection-current-related EDMR signal component in the degraded

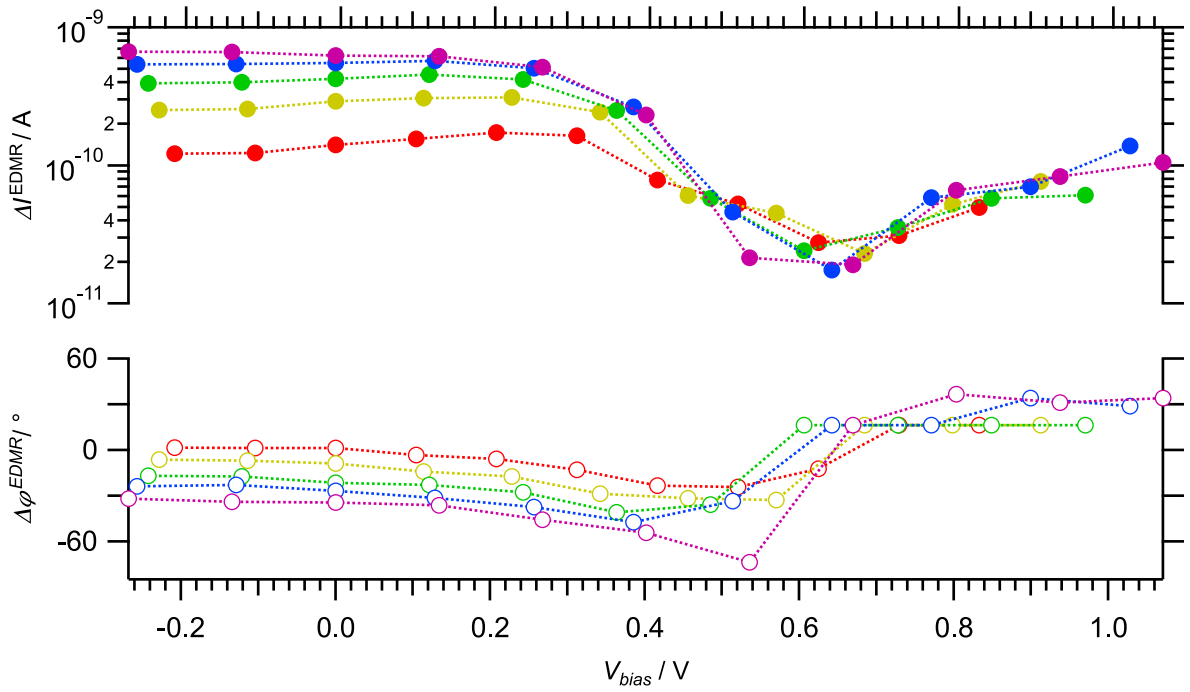

Fig. 52: Bias and light dependent EDMR study on solar cell sample A after degradation. Spin-dependent EDMR current ΔI^{EDMR} (closed circles) and signal phase shift $\Delta\varphi^{\mathrm{EDMR}}$ (open circles) vs. applied bias voltage V_{bias} at weak illumination (dotted lines are guides to the eye, color code: red $= 7 \times 10^{-3}$ suns, yellow $= 1.4 \times 10^{-2}$ suns, green $= 2.5 \times 10^{-2}$ suns, blue $= 4.2 \times 10^{-2}$ suns, purple $= 6.4 \times 10^{-2}$ suns).

device. Systematic studies on degraded devices are needed in order to investigate the origin of the signal minimum and to unravel the details of the change in the course of the signal phase shift.

The above discussed observations are in accordance with a degradation that takes place at one of the contacts, presumably the top contact made from aluminum metal. The EDMR data at $V_{\mathrm{bias}} \lesssim 0.3\,\mathrm{V}$ indicate that the charge carrier generation (cf. chapter 12, section 12.3.1) still takes place in the bulk of the device. Because charge carrier transport and extraction are somewhat hindered, we find an enhanced recombination signal compared to the data recorded prior to degradation. For the region where $V_{\mathrm{bias}} \gtrsim 0.3\,\mathrm{V}$ the missing injection-related component suggests that an injection barrier has formed (presumably by the oxidation of the aluminum contact).

In summary, this brief study on a degraded P3HT:$PC_{61}BM$ solar cell supports the argument that the EDMR-detected recombination takes place at different locations in the sample, i.e. in the volume at reverse bias and near the contact interfaces at forward bias. The observation of signal #3 in the forward bias regime is in accordance with the takeover of a different recombination mechanism like "bipolaronic blocking", which becomes favorable due to the hampered charge carrier extraction.

These results pave the way for more complex studies on degraded devices, e.g. "live degradation experiments" that analyze the temporal evolution of the degradation process. This could be done by introducing oxygen into the resonance cavity on demand, while taking EDMR snapshots in defined intervals. Investigating devices that were encapsulated in different ways in such a study could support the development of long-term-stable organic solar cells. Another promising type of

investigation is "degradation pinpointing", which could identify where the degradation processes actually happen. By selectively altering one of the contacts, one could figure out which electrode is degrading under certain conditions and change the contact or interface design in order to suppress this process. Additionally, degradation processes at the heterojunction in the bulk could be monitored by incorporating paramagnetic dopants, like the N@C_{60} molecule used in part II of the present thesis.

15. Summary of Part III

In this third part, first the fundamentals of organic photovoltaics including device architecture, charge carrier generation and recombination, as well as typical current-voltage characteristics were introduced in chapter 12. This was followed by a basic EDMR study on fully functional organic photovoltaic devices, as well as a bias and light dependent EDMR study in chapter 13. Finally, an outlook on how the application of EDMR – as a tool for the investigation of device degradation – can help to understand the processes that eventually lead to a failure of the solar cell was given in chapter 14.

In summary, it could be shown in this part that EDMR can act as a bridge between spectroscopic methods like EPR and LEPR and the "classic" device analysis protocols like the current-voltage characteristics. The EDMR technique can identify the charge carriers involved in spin-dependent processes by means of their magnetic resonance fingerprint. Three distinct signals were observed in the P3HT:$PC_{61}BM$ solar cell devices at 298 K: the first signal with $g_1 = 2.0021(3)$ and $\Delta B_{\mathrm{pp},1} = 0.37(5)\,\mathrm{mT}$ was assigned to mobile P^{+}_{P3HT} polarons, the second signal with $g_2 = 2.006(1)$ and $\Delta B_{\mathrm{pp},2} = 0.5(2)\,\mathrm{mT}$ was identified to be a possibly interface-related deep trap state $P^{\mathrm{T}}_{\mathrm{P3HT}}$, and the third signal with $g_3 = 2.0025(3)$ and $\Delta B_{\mathrm{pp},3} \approx 1.3\,\mathrm{mT}$ is related to a process internal to the P3HT phase, which may either be a "bipolaronic blocking" or an ambipolar polaron recombination between a mobile P^{+}_{P3HT} and a mobile P^{-}_{P3HT}.
The electrical detection scheme used in EDMR assures a quantitative relation between the physical processes inside the device and the observed signal strengths. Here, it was shown that the relative and absolute amplitude of the observed signals strongly depends on both electrical and optical biasing conditions. Focusing on the signal component related to the mobile P^{+}_{P3HT} polaron, two regions in the course of the spin-dependent EDMR current with applied bias voltage could clearly be distinguished in this work. While the spin-dependent current is strongly illumination-dependent below $V_{\mathrm{bias}} \approx 0.3\,\mathrm{V}$, the recombination signal becomes dominated by injected charge carriers above that. Furthermore, a quantitative correlation of the spin-dependent EDMR currents with the losses in the photocurrent for bias voltages below about 0.3 V, and with the injection-related dark current above that was found. The EDMR visibility function introduced in this context was successfully related to the probability ratio between spin-independent and spin-dependent recombination via its illumination dependence. We found that the spin-independent recombination is a bimolecular process (Langevin type) and that the spin-dependent recombination is monomolecular in nature (Shockley-Read-Hall type). Additionally, the light intensity at which the probabilities for a charge carrier to take part in the non-spin-dependent or in the spin-dependent process are equal was found to be as low as about 6×10^{-3} suns. Above this level, bimolecular recombination of the Langevin-type dominates the losses in the investigated solar cell devices.
Assuming that the observed course of ΔI^{EDMR} with V_{bias} is a result of a superposition of two processes that do not influence each other, i.e. one EDMR signal due to photo recombination and

another one related to the recombination of injected charge carriers, both constituents could be reconstructed. The presented superposition approach was further supported by a direct comparison between EDMR experiments with and without illumination. The solar cell operation near the maximum power point seems to be strongly impacted by recombination of both injected and photogenerated carriers, underlining the importance of bulk and interface properties for the design and construction of organic solar cells.
Finally, the brief degradation study presented at the end of this part indicated a way to use EDMR as a tool for monitoring degradations processes. By designing suitable experiments, i.e. studying degradation in real time by introducing oxygen in the resonance cavity or altering a specific contact or contact interface by incorporating paramagnetic dopants like $N@C_{60}$, the EDMR method could be used to unravel processes that lead to early device failures in a more systematic way.

Summary

The present thesis is dedicated to the analytical technique of electrically detected magnetic resonance (EDMR) and its application to organic semiconductors. The main goals of this work were to a) implement a flexible benchtop EDMR system that can be used by researchers working in the field of material sciences as an easy to handle tool and b) to investigate the species and processes that are actively involved in spin-dependent recombination events inside organic semiconductor materials and fully functional organic photovoltaic devices in order to support solar cell optimizations.

In the first part, a compact setup for measuring electrically detected magnetic resonance of semiconductor devices that yields consistent and highly reproducible results is presented. The introduced setup allows the study of processes in dark EDMR, as well as under illumination both at ambient and low temperatures. Most importantly, the system is capable of nearly simultaneous collection of EDMR and current-voltage data, opening up the way to rapid research cycles and measurement series. Hence, the developed spectrometer can be used for complete semiconductor device characterization at different operating conditions. Due to its small footprint, the unit is highly mobile and can in particular be operated inside cleanrooms or even glove boxes, which is beneficial for studies on organic materials and devices that degrade rather quickly.
Using a standard silicon solar cell for a detailed comparison with a typical "large-scale" setup, we could show that the EDMR spectra recorded with the new setup are quantitatively comparable in all spectroscopic dimensions with those obtained in a state-of-the-art spectrometer.

In the second part, the benefits of close proximity between device fabrication and spectroscopic characterization possible with the new benchtop EDMR setup were used to record EDMR spectra of microcrystals made from pure and N@C_{60}-doped Buckminsterfullerene and the C_{60} oxidation product $C_{60}O$. With these studies, we introduced a class of samples – namely organic microcrystals – to EDMR that was not investigated so far, due to its delicate nature.
The EDMR signal observed in pure C_{60} was attributed here to a spin-dependent recombination of photo-generated $C_{60}^{\bullet+}$. Its assumed recombination partner, $C_{60}^{\bullet-}$, is known to be too broad for detection at ambient temperature,[93] and thus effectively invisible in the recorded spectra. The presented results on C_{60} microcrystals demonstrate that even a relatively small number of organic semiconductor crystals can be contacted in a simple manner and still deliver sufficient currents for an EDMR detection. The scalable crystallization approach presented in this part opens up a way to further extent the sensitivity of the method towards fewer spins.
The EDMR signal obtained on the $C_{60}O$ material was tentatively attributed to spin-dependent recombination of photo-generated charge carriers involving a secondary product of $C_{60}O$, which may be an "open-epoxy-ring" form of the molecule, the intermediate $^{-}\bullet C_{60}{-}O{-}O{-}C_{60}^{\bullet-}$, or a constitutional isomer thereof. Within this study, we could show that the oxidation of fullerene molecules can result in a slight shift of the g-factor towards higher values, which could explain the observation of unusual g-factors in oxidized fullerene materials reported by others.[11]
The most important finding of the EDMR studies presented in this part is by far the evidence for strongly dipolar-coupled spin pairs in N@C_{60}-doped material. As a working hypothesis, we attribute the observed structure in the corresponding EDMR spectra to the formation of dipolar-coupled N@C_{60}-$C_{60}^{\bullet+}$ spin pairs. Although an unambiguous quantitative modeling of the presented data is not possible due to the limited signal-to-noise ratio, a symmetric structure in the obtained spectra is clearly visible. The performed experiments give a first spectroscopic

evidence for strongly dipolar-coupled spin pairs, never reported before in EDMR. This result illustrates that using microcrystals and paramagnetic doping can significantly enhance the EDMR resolution. Furthermore, a doping-on-demand strategy seems feasible, which could unravel the opposing views as to how the EDMR signal is generated at the microscopic level, which – despite intensive research – continue to be published so far.[8,10,11] The confirmation of the presented dipolar coupling between N@C_{60} and $C_{60}^{\bullet+}$ would have far-reaching consequences for EDMR research on organic semiconductors since, up to now, EDMR on organics is hampered by the poor spectral resolution of the method. Using endohedral fullerenes, however, gives rise to a characteristic hyperfine pattern, which is identifiable even on a large and broad background of signals due to other spin species in the sample, as indicated by the results presented in this work.

The third part of this work is devoted to the investigation of spin-dependent recombination events in P3HT:$PC_{61}BM$ solar cell devices. We could show that the EDMR technique can distinguish between charge carriers involved in different spin-dependent processes by means of their magnetic resonance fingerprint and identify three distinct peaks in the EDMR spectra. These signals are related to P3HT and were attributed to mobile P^{+}_{P3HT} polarons, deep trap states P^{T}_{P3HT} and P3HT internal processes like "bipolaronic blocking " or ambipolar polaron recombination between a mobile P^{+}_{P3HT} and a mobile P^{-}_{P3HT} in this work.
We have shown that the relative and absolute amplitude of the observed signals strongly depends on the electrical and optical biasing conditions. Focusing on the signal component related to the mobile P^{+}_{P3HT} polaron, two regions in the course of the spin-dependent EDMR current with applied bias voltage could clearly be distinguished: the spin-dependent current is strongly illumination-dependent below $V_{bias} \approx 0.3\,V$ (photo regime) and becomes dominated by injected charge carriers above that.
Furthermore, we were able to quantitatively correlate the spin-dependent EDMR currents with the losses in the photocurrent for bias voltages below about 0.3 V, and with the injection-related dark current above that by introducing an illumination-dependent EDMR visibility function. This scaling function is related to the probability ratio between spin-independent and spin-dependent recombination. A quantitative analysis of the values obtained for the visibility function revealed that the spin-independent recombination in our experiments is a bimolecular process (Langevin type), while the observed spin-dependent recombination is monomolecular in nature (Shockley-Read-Hall type). Additionally, we found that bimolecular recombination of the Langevin-type dominates the losses in the investigated solar cell devices for light intensities above about 6×10^{-3} suns. This important result shows, that EDMR can act as a bridge between spectroscopic methods like EPR and LEPR and the "classic" device analysis protocols like the current-voltage characteristics. Using EDMR, a direct observation of loss processes inside photovoltaic devices under realistic operating conditions becomes possible.
Finally, a brief degradation study was presented, indicating how EDMR could be used for monitoring degradation processes in organic photovoltaic devices. In this study, we found that the injection-current-related EDMR signal component is suppressed, most probably due to the oxidation of the aluminum top contact, and that the charge carrier generation still takes place in the bulk of the solar cell. By designing suitable experiments, i.e. studying degradation in real time by introducing oxygen in the resonance cavity ("live degradation") or altering a specific contact or contact interface ("degradation pinpointing"), the EDMR method could be used to gain a deeper understanding of device degradation, enabling solar cell researchers to design material systems with longer lifetimes and higher conversion efficiencies.

References

[1] M. Jacob, Organic Semiconductors: Past, Present and Future, *Electronics* **2014**, *3*(4), 594–597.

[2] S. R. Forrest, The path to ubiquitous and low-cost organic electronic appliances on plastic, *Nature* **2004**, *428*(6986), 911–918.

[3] M. Berggren, D. Nilsson, N. D. Robinson, Organic materials for printed electronics, *Nat. Mater.* **2007**, *6*(1), 3–5.

[4] P. E. Burrows, V. Bulovic, S. R. Forrest, L. S. Sapochak, D. M. McCarty, M. E. Thompson, Reliability and degradation of organic light emitting devices, *Appl. Phys. Lett.* **1994**, *65*(23), 2922–2924.

[5] N. Grossiord, J. M. Kroon, R. Andriessen, P. W. M. Blom, Degradation mechanisms in organic photovoltaic devices, *Org. Electron.* **2012**, *13*(3), 432–456.

[6] M. A. Green, K. Emery, Y. Hishikawa, W. Warta, E. D. Dunlop, Solar cell efficiency tables (version 47), *Prog. Photovoltaics Res. Appl.* **2016**, *24*(1), 3–11.

[7] D. R. McCamey, S.-Y. Lee, S.-Y. Paik, J. M. Lupton, C. Böhme, Spin-dependent dynamics of polaron pairs in organic semiconductors, *Phys. Rev. B* **2010**, *82*(12), 125206.

[8] J. Behrends, A. Schnegg, K. Lips, E. A. Thomsen, A. K. Pandey, I. D. W. Samuel, D. J. Keeble, Bipolaron Formation in Organic Solar Cells Observed by Pulsed Electrically Detected Magnetic Resonance, *Phys. Rev. Lett.* **2010**, *105*(17), 176601.

[9] D. R. McCamey, H. A. Seipel, S.-Y. Paik, M. J. Walter, N. J. Borys, J. M. Lupton, C. Böhme, Spin Rabi flopping in the photocurrent of a polymer light-emitting diode, *Nat. Mater.* **2008**, *7*(9), 723–728.

[10] A. J. Kupijai, K. M. Behringer, F. G. Schaeble, N. E. Galfe, M. Corazza, S. A. Gevorgyan, F. C. Krebs, M. Stutzmann, M. S. Brandt, Bipolar polaron pair recombination in polymer/fullerene solar cells, *Phys. Rev. B* **2015**, *92*(24), 245203.

[11] H. Morishita, W. J. Baker, D. P. Waters, R. Baarda, J. M. Lupton, C. Böhme, Mechanisms of spin-dependent dark conductivity in films of a soluble fullerene derivative under bipolar injection, *Phys. Rev. B* **2014**, *89*(12), 125311.

[12] P. Zeeman, Ueber einen Einfluss der Magnetisirung auf die Natur des von einer Substanz emittirten Lichtes, *Verh. Phys. Ges. Berlin* **1896**, *15*(7), 128–130.

[13] W. Gerlach, O. Stern, Der experimentelle Nachweis der Richtungsquantelung im Magnetfeld, *Z. Phys.* **1922**, *9*(1), 349–352.

[14] G. E. Uhlenbeck, S. Goudsmit, Ersetzung der Hypothese vom unmechanischen Zwang durch eine Forderung bezüglich des inneren Verhaltens jedes einzelnen Elektrons, *Naturwissenschaften* **1925**, *13*(47), 953–954.

[15] G. E. Uhlenbeck, S. Goudsmit, Spinning Electrons and the Structure of Spectra, *Nature* **1926**, *117*(2938), 264–265.

[16] P. J. Mohr, B. N. Taylor, D. B. Newell, CODATA recommended values of the fundamental physical constants: 2010, *Rev. Mod. Phys.* **2012**, *84*(4), 1527–1605.

[17] J. E. Wertz, J. R. Bolton, *Electron Spin Resonance: Elementary Theory and Practical Applications*, Chapman and Hall, London, **1986**.

[18] A. Abragam, M. H. L. Pryce, Theory of the Nuclear Hyperfine Structure of Paramagnetic Resonance Spectra in Crystals, *Proc. R. Soc. Lond. A* **1951**, *205*(1080), 135–153.

[19] A. Schweiger, G. Jeschke, *Principles of Pulse Electron Paramagnetic Resonance*, Oxford University Press, New York, **2001**.

[20] J.-M. Spaeth, J. Niklas, R. Bartram, *Structure Analysis of Point Defects in Solids: An Introduction to Multiple Magnetic Resonance Spectroscopy*, Springer Series in Solid-State Sciences 43, Springer, Heidelberg, **1992**.

[21] J. A. Weil, J. R. Bolton, *Electron Paramagnetic Resonance: Elementary Theory and Practical Applications*, 2nd ed., John Wiley & Sons, Hoboken, **2006**.

[22] A. Carrington, A. D. McLachlan, *Introduction to Magnetic Resonance : with Applications to Chemistry and Chemical Physics*, Chapman and Hall, London, **1979**.

[23] K. Scheffler, H. B. Stegmann, *Elektronenspinresonanz: Grundlagen und Anwendung in der organischen Chemie*, Springer, Heidelberg, **1970**.

[24] F. K. Kneubühl, Line Shapes of Electron Paramagnetic Resonance Signals Produced by Powders, Glasses, and Viscous Liquids, *J. Chem. Phys.* **1960**, *33*(4), 1074–1078.

[25] A. J. Stone, Gauge Invariance of the g Tensor, *Proc. R. Soc. A Math. Phys. Eng. Sci.* **1963**, *271*(1346), 424–434.

[26] A. J. Stone, g tensors of aromatic hydrocarbons, *Mol. Phys.* **1964**, *7*(4), 311–316.

[27] A. J. Stone, g factors of aromatic free radicals, *Mol. Phys.* **1963**, *6*(5), 509–515.

[28] M. T. Jones, T. C. Kuechler, S. Metz, The Effects of Orbital Degeneracy and Near Degeneracy upon the g-Values of Organic Free Radicals, *J. Magn. Reson.* **1973**, *10*(2), 149–155.

[29] R. E. Moss, A. J. Perry, g -factor deviations in degenerate aromatic hydrocarbon radicals: the benzene anion, *Mol. Phys.* **1971**, *22*(5), 789–798.

[30] R. A. Rouse, M. T. Jones, Modification of Stone's Theory of g-Factors for Aromatic Hydrocarbon Free Radicals to Include Quadratic Terms, *J. Magn. Reson.* **1975**, *19*(3), 294–302.

[31] B. R. McGarvey, The Isotropic Hyperfine Interaction, *J. Phys. Chem.* **1967**, *71*(1), 51–66.

[32] G. Jeschke, Determination of the Nanostructure of Polymer Materials by Electron Paramagnetic Resonance Spectroscopy, *Macromol. Rapid Commun.* **2002**, *23*(4), 227–246.

[33] F. Bloch, Nuclear Induction, *Phys. Rev.* **1946**, *70*(7-8), 460–474.

[34] W. Harneit, C. Böhme, S. Schäfer, K. Hübener, K. Fostiropoulos, K. Lips, Room Temperature Electrical Detection of Spin Coherence in C_{60}, *Phys. Rev. Lett.* **2007**, *98*(21), 216601.

[35] T. Herring, S.-Y. Lee, D. R. McCamey, P. Taylor, K. Lips, J. Hu, F. Zhu, A. Madan, C. Böhme, Experimental discrimination of geminate and non-geminate recombination in a-Si:H, *Phys. Rev. B* **2009**, *79*(19), 195205.

[36] C. C. Lo, F. R. Bradbury, A. M. Tyryshkin, C. D. Weis, J. Bokor, T. Schenkel, S. A. Lyon, Suppression of microwave rectification effects in electrically detected magnetic resonance measurements, *Appl. Phys. Lett.* **2012**, *100*(6), 063510.

[37] D. R. McCamey, K. J. van Schooten, W. J. Baker, S.-Y. Lee, S.-Y. Paik, J. M. Lupton, C. Böhme, Hyperfine-Field-Mediated Spin Beating in Electrostatically Bound Charge Carrier Pairs, *Phys. Rev. Lett.* **2010**, *104*(1), 017601.

[38] M. Stutzmann, M. S. Brandt, M. W. Bayerl, Spin-dependent processes in amorphous and microcrystalline silicon: a survey, *J. Non. Cryst. Solids* **2000**, *266-269*, 1–22.

[39] R. Maxwell, A. Honig, Neutral-Impurity Scattering Experiments in Silicon with Highly Spin-Polarized Electrons, *Phys. Rev. Lett.* **1966**, *17*(4), 188–190.

[40] D. Lepine, Spin-Dependent Recombination on Silicon Surface, *Phys. Rev. B* **1972**, *6*(2), 436–441.

[41] H. Dersch, L. Schweitzer, J. Stuke, Recombination processes in a-Si:H: Spin-dependent photoconductivity, *Phys. Rev. B* **1983**, *28*(8), 4678–4684.

[42] D. Kaplan, I. Solomon, N. Mott, Explanation of the large spin-dependent recombination effect in semiconductors, *J. Phys. Lettres* **1978**, *39*(4), 51–54.

[43] C. Böhme, K. Lips, Theory of time-domain measurement of spin-dependent recombination with pulsed electrically detected magnetic resonance, *Phys. Rev. B* **2003**, *68*(24), 245105.

[44] T. Eickelkamp, S. Roth, M. Mehring, Electrically detected magnetic resonance in photoexcited fullerenes, *Mol. Phys.* **1998**, *95*(5), 967–972.

[45] A. Barabanov, V. Lvov, O. Tretyak, About the Mechanisms of Spin-Dependent Recombination in Semiconductors, *Phys. Status Solidi B* **1998**, *207*(2), 419–427.

[46] R. Haberkorn, W. Dietz, Theory of spin-dependent recombination in semiconductors, *Solid State Commun.* **1980**, *35*(6), 505–508.

[47] F. Rong, W. Buchwald, E. Poindexter, W. Warren, D. J. Keeble, Spin-Dependent Shockley-Read Recombination of Electrons and Holes in Indirect-Band-Gap Semiconductor p-n Junction Diodes, *Solid-State Electron.* **1991**, *34*(8), 835–841.

[48] K. Lips, C. Lerner, W. Fuhs, Semiclassical model of electrically detected magnetic resonance in undoped a-Si:H, *J. Non. Cryst. Solids* **1996**, *198-200*, 267–270.

[49] B. Movaghar, B. Ries, L. Schweitzer, Theory of the resonant and non-resonant photoconductivity changes in amorphous silicon, *Philos. Mag. Part B* **1980**, *41*(2), 159–167.

[50] Z. Xiong, D. J. Miller, General expression for the electrically detected magnetic resonance signal from semiconductors, *Appl. Phys. Lett.* **1993**, *63*(3), 352–354.

[51] P. Kanschat, ESR and spin-dependent recombination in microcrystalline silicon (original thesis in German: ESR und spinabhängige Rekombination in mikrokristallinem Silizium), PhD thesis, Philipps-Universität Marburg, Germany, **2000**.

[52] A. Abragam, B. Bleaney, *Electron Paramagnetic Resonance of Transition Ions*, Clarendon Press, Oxford, **1970**.

[53] C. Böhme, *Dynamics of spin-dependent charge carrier recombination*, Cuvillier Verlag, Göttingen, **2003**.

[54] C. P. Poole, *Electron Spin Resonance: A Comprehensive Treatise on Experimental Techniques*, 2nd ed., Wiley, New York, **1983**.

[55] D. R. Lide (Ed.), *CRC Handbook of Chemistry and Physics*, 90th ed., CRC Press, Boca Raton, Florida, **2009**.

[56] S.-Y. Lee, S. Paik, D. R. McCamey, C. Böhme, Modulation frequency dependence of continuous-wave optically/electrically detected magnetic resonance, *Phys. Rev. B* **2012**, *86*(11), 115204.

[57] C. Yang, E. Ehrenfreund, F. Wang, T. Drori, Z. Vardeny, Spin-dependent kinetics of polaron pairs in organic light-emitting diodes studied by electroluminescence detected magnetic resonance dynamics, *Phys. Rev. B* **2008**, *78*(20), 205312.

[58] A. Neumann, Operation Hints for the MiniScope MS100 - MS300, Manual, Magnettech GmbH, Berlin, **2009**.

[59] D. W. Marquardt, An Algorithm for Least-Squares Estimation of Nonlinear Parameters, *J. Soc. Ind. Appl. Math.* **1963**, *11*(2), 431–441.

[60] A. Nelson, Australian Nuclear Science and Technology Organisation, GenCurveFit for IGOR Pro, *http://www.igorexchange.com/project/gencurvefit,* **2007-2014**.

[61] K. Price, R. Storn, Differential Evolution, *Dr Dobb's J.* **1997**, *April*, 18–24.

[62] R. Storn, K. Price, Differential Evolution – A Simple and Efficient Heuristic for Global Optimization over Continuous Spaces, *J. Glob. Optim.* **1997**, *11*(4), 341–359.

[63] M. Wormington, C. Panaccione, K. M. Matney, D. K. Bowen, Characterization of structures from X-ray scattering data using genetic algorithms, *Phil. Trans. R. Soc. Lond. A* **1999**, *357*(1761), 2827–2848.

[64] C. J. Chen, *Physics of Solar Energy*, John Wiley & Sons, Hoboken, **2011**.

[65] J. Behrends, A. Schnegg, C. Böhme, S. Haas, H. Stiebig, F. Finger, B. Rech, K. Lips, Recombination and transport in microcrystalline pin solar cells studied with pulsed electrically detected magnetic resonance, *J. Non. Cryst. Solids* **2008**, *354*(19-25), 2411–2415.

[66] C. Meier, J. Behrends, C. Teutloff, O. Astakhov, A. Schnegg, K. Lips, R. Bittl, Multifrequency EDMR applied to microcrystalline thin-film silicon solar cells., *J. Magn. Reson.* **2013**, *234*, 1–9.

[67] W. Böttler, V. Smirnov, J. Hüpkes, F. Finger, Texture-etched ZnO as a versatile base for optical back reflectors with well-designed surface morphologies for application in thin film solar cells, *Phys. Status Solidi A* **2012**, *209*(6), 1144–1149.

[68] A. Schnegg, J. Behrends, M. Fehr, K. Lips, Pulsed electrically detected magnetic resonance for thin film silicon and organic solar cells., *Phys. Chem. Chem. Phys.* **2012**, *14*(42), 14418–14438.

[69] J. Behrends, Spin-dependent Transport and Recombination in Solar Cells studied by Pulsed Electrically Detected Magnetic Resonance, PhD thesis, Freie Universität Berlin, Germany, **2009**.

[70] M. Stutzmann, D. K. Biegelsen, Electron-spin-lattice relaxation in amorphous silicon and germanium, *Phys. Rev. B* **1983**, *28*(11), 6256–6261.

[71] O. Astakhov, R. Carius, Y. Petrusenko, V. Borysenko, D. Barankov, F. Finger, Defects in thin film silicon at the transition from amorphous to microcrystalline structure, *Phys. Status Solidi – Rapid Res. Lett.* **2007**, *1*(2), R77–R79.

[72] F. Finger, L. B. Neto, R. Carius, T. Dylla, S. Klein, Paramagnetic defects in undoped microcrystalline silicon, *Phys. Status Solidi C* **2004**, *1*(5), 1248–1254.

[73] P. Kanschat, K. Lips, W. Fuhs, Identification of non-radiative recombination paths in microcrystalline silicon (μc-Si:H), *J. Non. Cryst. Solids* **2000**, *266-269*, 524–528.

[74] J. C. Randel, F. C. Niestemski, A. R. Botello-Mendez, W. Mar, G. Ndabashimiye, S. Melinte, J. E. P. Dahl, R. M. K. Carlson, E. D. Butova, A. A. Fokin, P. R. Schreiner, J.-C. Charlier, H. C. Manoharan, Unconventional molecule-resolved current rectification in diamondoid–fullerene hybrids, *Nat. Commun.* **2014**, *5*, 4877.

[75] H. W. Kroto, J. R. Heath, S. C. O'Brien, R. F. Curl, R. E. Smalley, C_{60}: Buckminsterfullerene, *Nature* **1985**, *318*(6042), 162–163.

[76] H. W. Kroto, The stability of the fullerenes C_n, with n = 24, 28, 32, 36, 50, 60 and 70, *Nature* **1987**, *329*(6139), 529–531.

[77] M. Dresselhaus, G. Dresselhaus, P. Eklund, *Science of Fullerenes and Carbon Nanotubes*, Academic Press, San Diego, **1996**.

[78] C. S. Yannoni, P. P. Bernier, D. S. Bethune, G. Meijer, J. R. Salem, NMR determination of the bond lengths in C_{60}, *J. Am. Chem. Soc.* **1991**, *113*(8), 3190–3192.

[79] R. D. Johnson, C. S. Yannoni, H. C. Dorn, J. R. Salem, D. S. Bethune, C_{60} Rotation in the Solid State: Dynamics of a Faceted Spherical Top, *Science* **1992**, *255*(5049), 1235–1238.

[80] D. Bonifazi, A. Kiebele, M. Stöhr, F. Cheng, T. Jung, F. Diederich, H. Spillmann, Supramolecular Nanostructuring of Silver Surfaces via Self-Assembly of [60]Fullerene and Porphyrin Modules, *Adv. Funct. Mater.* **2007**, *17*(7), 1051–1062.

[81] G. Schull, R. Berndt, Orientationally Ordered (7 x 7) Superstructure of C_{60} on Au(111), *Phys. Rev. Lett.* **2007**, *99*(22), 226105.

[82] M. Nimmrich, M. Kittelmann, P. Rahe, W. Harneit, A. J. Mayne, G. Dujardin, A. Kühnle, Influence of charge transfer doping on the morphologies of C_{60} islands on hydrogenated diamond C(100)-(2 x 1), *Phys. Rev. B* **2012**, *85*(3), 035420.

[83] H. Park, J. Park, A. K. L. Lim, E. H. Anderson, A. P. Alivisatos, P. L. McEuen, Nanomechanical oscillations in a single-C_{60} transistor, *Nature* **2000**, *407*, 57–60.

[84] C. B. Winkelmann, N. Roch, W. Wernsdorfer, V. Bouchiat, F. Balestro, Superconductivity in a single-C_{60} transistor, *Nat. Phys.* **2009**, *5*(12), 876–879.

[85] W. Krätschmer, L. D. Lamb, K. Fostiropoulos, D. R. Huffman, Solid C_{60}: a new form of carbon, *Nature* **1990**, *347*(6291), 354–358.

[86] A. Hirsch, M. Brettreich, *Fullerenes: Chemistry and Reactions*, Wiley-VCH, Weinheim, **2005**.

[87] J. B. Howard, J. T. McKinnon, Y. Makarovsky, A. L. Lafleur, M. E. Johnson, Fullerenes C_{60} and C_{70} in flames, *Nature* **1991**, *352*(6331), 139–141.

[88] A. Rosén, B. Wästberg, Calculations of the ionization thresholds and electron affinities of the neutral, positively and negatively charged C_{60} - "follene-60", *J. Chem. Phys.* **1989**, *90*(4), 2525–2526.

[89] C. A. Reed, R. D. Bolskar, Discrete Fulleride Anions and Fullerenium Cations, *Chem. Rev.* **2000**, *100*(3), 1075–1120.

[90] Q. Xie, E. Perez-Cordero, L. Echegoyen, Electrochemical detection of C_{60}^{6-} and C_{70}^{6-}: Enhanced stability of fullerides in solution, *J. Am. Chem. Soc.* **1992**, *114*(10), 3978–3980.

[91] L. Echegoyen, L. E. Echegoyen, Electrochemistry of Fullerenes and Their Derivatives, *Acc. Chem. Res.* **1998**, *31*(9), 593–601.

[92] S. S. Eaton, G. R. Eaton, EPR Spectra of C_{60} Anions, *Appl. Magn. Reson.* **1996**, *11*(2), 155–170.

[93] G. Völkel, A. Pöppl, J. Simon, J. Hoentsch, S. Orlinskii, H. Klos, B. Gotschy, Evidence of the Jahn-Teller splitting of C_{60}^{-} in C_{60}-tetraphenylphosphoniumchloride from an electron-spin-relaxation study, *Phys. Rev. B* **1995**, *52*(14), 10188–10193.

[94] R. Haddon, L. Brus, K. Raghavachari, Electronic structure and bonding in icosahedral C_{60}, *Chem. Phys. Lett.* **1986**, *125*(5-6), 459–464.

[95] C. A. Reed, K.-C. Kim, R. D. Bolskar, L. J. Mueller, Taming Superacids: Stabilization of the Fullerene Cations HC_{60}^{+} and $C_{60}^{\cdot+}$, *Science* **2000**, *289*(5476), 101–104.

[96] J. M. Wood, B. Kahr, S. H. Hoke, L. Dejarme, R. G. Cooks, D. Ben-Amotz, Oxygen and Methylene Adducts of C_{60} and C_{70}, *J. Am. Chem. Soc.* **1991**, *113*(15), 5907–5908.

[97] P. Paul, K.-C. Kim, D. Sun, P. D. W. Boyd, C. A. Reed, Artifacts in the Electron Paramagnetic Resonance Spectra of C_{60} Fullerene Ions: Inevitable $C_{120}O$ Impurity, *J. Am. Chem. Soc.* **2002**, *124*(16), 4394–4401.

[98] M. Eckardt, R. Wieczorek, W. Harneit, Stability of C_{60} and N@C_{60} under thermal and optical exposure, *Carbon* **2015**, *95*, 601–607.

[99] S. Lebedkin, S. Ballenweg, J. Gross, R. Taylor, W. Krätschmer, Synthesis of $C_{120}O$: A New Dimeric [60]Fullerene Derivative, *Tetrahedron Lett.* **1995**, *36*(28), 4971–4974.

[100] R. Taylor, M. P. Barrow, T. Drewello, C_{60} degrades to $C_{120}O$, *Chem. Commun.* **1998**, (22), 2497–2498.

[101] P. Paul, R. D. Bolskar, A. M. Clark, C. A. Reed, The origin of the 'spike' in the EPR spectrum of C_{60}^-, *Chem. Commun.* **2000**, *2*(14), 1229–1230.

[102] X. Camps, A. Hirsch, Efficient cyclopropanation of C_{60} starting from malonates, *J. Chem. Soc. Perkin Trans. 1* **1997**, *8*(11), 1595–1596.

[103] C. C. Henderson, P. A. Cahill, $C_{60}H_2$: Synthesis of the Simplest C_{60} Hydrocarbon Derivative, *Science* **1993**, *259*(5103), 1885–1887.

[104] A. A. Gakh, A. A. Tuinman, J. L. Adcock, R. A. Sachleben, R. N. Compton, Selective Synthesis and Structure Determination of $C_{60}F_{48}$, *J. Am. Chem. Soc.* **1994**, *116*(2), 819–820.

[105] P. J. Fagan, J. C. Calabrese, B. Malone, Metal Complexes of Buckminsterfullerene (C_{60}), *Acc. Chem. Res.* **1992**, *25*(3), 134–142.

[106] J. C. Hummelen, B. W. Knight, F. LePeq, F. Wudl, J. Yao, C. L. Wilkins, Preparation and Characterization of Fulleroid and Methanofullerene Derivatives, *J. Org. Chem.* **1995**, *60*(3), 532–538.

[107] J. R. Heath, S. C. O'Brien, Q. Zhang, Y. Liu, R. F. Curl, F. K. Tittel, R. E. Smalley, Lanthanum Complexes of Spheroidal Carbon Shells, *J. Am. Chem. Soc.* **1985**, *107*(25), 7779–7780.

[108] F. D. Weiss, J. L. Elkind, S. C. O'Brien, R. F. Curl, R. E. Smalley, Photophysics of Metal Complexes of Spheroidal Carbon Shells, *J. Am. Chem. Soc.* **1988**, *110*(13), 4464–4465.

[109] E. W. Godly, R. Taylor, Nomenclature and Terminology of Fullerenes: A Preliminary Survey, *Pure Appl. Chem.* **1997**, *69*(7), 1411–1434.

[110] A. Bondi, van der Waals Volumes and Radii, *J. Phys. Chem.* **1964**, *68*(3), 441–451.

[111] J. C. Slater, Atomic Radii in Crystals, *J. Chem. Phys.* **1964**, *41*(10), 3199–3204.

[112] M. Saunders, R. J. Cross, H. A. Jimenez-Vazquez, R. Shimshi, A. Khong, Noble Gas Atoms Inside Fullerenes, *Science* **1996**, *271*(5256), 1693–1697.

[113] T. Almeida Murphy, T. Pawlik, A. Weidinger, M. Höhne, R. Alcala, J.-M. Spaeth, Observation of Atomlike Nitrogen in Nitrogen-Implanted Solid C_{60}, *Phys. Rev. Lett.* **1996**, *77*(6), 1075–1078.

[114] A. Weidinger, B. Pietzak, M. Waiblinger, K. Lips, B. Nuber, A. Hirsch, Study of N@C_{60} and P@C_{60}, *AIP Conf. Proc.* **1998**, *442*, 363–367.

[115] B. Pietzak, M. Waiblinger, T. Almeida Murphy, A. Weidinger, M. Höhne, E. Dietel, A. Hirsch, Properties of endohedral N@C_{60}, *Carbon* **1998**, *36*(5-6), 613–615.

[116] J. A. Larsson, J. C. Greer, W. Harneit, A. Weidinger, Phosphorous trapped within buckminsterfullerene, *J. Chem. Phys.* **2002**, *116*(18), 7849.

[117] A. Weidinger, M. Waiblinger, B. Pietzak, T. Almeida Murphy, Atomic nitrogen in C_{60}:N@C_{60}, *Appl. Phys. A: Mater. Sci. Process.* **1998**, *66*(3), 287–292.

[118] W. Harneit, Fullerene-based electron-spin quantum computer, *Phys. Rev. A* **2002**, *65*(3), 032322.

[119] C. Meyer, Endohedral Fullerenes for Quantum Computing, PhD thesis, Freie Universität Berlin, Germany, **2003**.

[120] M. Eckardt, Assessing and optimizing the stability of N@C_{60} for the use as a quantum bit (original thesis in German: Untersuchung und Optimierung der Stabilität von N@C_{60} für die Verwendung als Quantenbit), Diploma thesis, Johannes Gutenberg-Universität Mainz, Germany, **2013**.

[121] H. Kobayashi, T. Ueda, K. Miyakubo, T. Eguchi, A. Tani, Spin–Spin Interaction of TEMPO Molecular Chains Formed in an Organic One-Dimensional Nanochannel as Studied by Electron Spin Resonance (ESR), *Bull. Chem. Soc. Jpn.* **2007**, *80*(4), 711–720.

[122] K. Kimata, T. Hirose, K. Moriuchi, K. Hosoya, T. Araki, N. Tanaka, High-Capacity Stationary Phases Containing Heavy Atoms for HPLC Separation of Fullerenes, *Anal. Chem.* **1995**, *67*(15), 2556–2561.

[123] R. Kellner, J.-M. Mermet, M. Otto, M. Valcárcel, H. M. Widmer (Eds.), *Analytical Chemistry: A Modern Approach to Analytical Science*, 2nd ed., Wiley-VCH, Weinheim, **2004**.

[124] W. A. Scrivens, P. V. Bedworth, J. M. Tour, Purification of gram quantities of C_{60}. A new inexpensive and facile method, *J. Am. Chem. Soc.* **1992**, *114*(20), 7917–7919.

[125] R. Wieczorek, Investigations regarding the separation of fullerene mixtures and the crystallization of C_{60} (original thesis in German: Untersuchungen zur Auftrennung von Fullerengemischen und zur Kristallisation von C_{60}), Diploma thesis, Johannes Gutenberg-Universität Mainz, Germany, **2014**.

[126] B. Gödde, Synthesis and spectroscopy of enriched nitrogen endohedral fullerenes (original thesis in German: Synthese und Spektroskopie angereicherter stickstoffendohedraler Fullerene), PhD thesis, Technische Universität Darmstadt, Germany, **2001**.

[127] P. Jakes, Chromatographic method for the complete isolation of the nitrogen endohedral fullerenes N@C_{60} and N@C_{70} and their EPR spectra in liquid crystals (original thesis in German: Chromatographische Methode zur vollständigen Isolierung der stickstoffendohedralen Fullerene N@C_{60} und N@C_{70} sowie deren EPR-Spektren in Flüssigkristallen), PhD thesis, Technische Universität Darmstadt, Germany, **2005**.

[128] R. M. Brown, A. M. Tyryshkin, K. Porfyrakis, E. M. Gauger, B. W. Lovett, A. Ardavan, S. A. Lyon, G. A. D. Briggs, J. J. L. Morton, Coherent State Transfer between an Electron and Nuclear Spin in ^{15}N@C_{60}, *Phys. Rev. Lett.* **2011**, *106*(11), 110504.

[129] J. J. L. Morton, A. M. Tyryshkin, A. Ardavan, S. C. Benjamin, K. Porfyrakis, S. A. Lyon, G. A. D. Briggs, Bang-bang control of fullerene qubits using ultra-fast phase gates, *Nat. Phys.* **2006**, *2*, 40–43.

[130] M. Waiblinger, K. Lips, W. Harneit, A. Weidinger, E. Dietel, A. Hirsch, Thermal stability of the endohedral fullerenes N@C_{60}, N@C_{70}, and P@C_{60}, *Phys. Rev. B* **2001**, *64*(15), 159901.

[131] S. Tóth, D. Quintavalle, B. Náfrádi, L. Korecz, L. Forró, F. Simon, Enhanced thermal stability and spin-lattice relaxation rate of N@C_{60} inside carbon nanotubes, *Phys. Rev. B* **2008**, *77*(21), 214409.

[132] H. Mauser, A. Hirsch, N. J. R. van Eikema Hommes, T. Clark, B. Pietzak, A. Weidinger, L. Dunsch, Stabilization of Atomic Nitrogen Inside C_{60}, *Angew. Chemie Int. Ed.* **1997**, *36*(24), 2835–2838.

[133] P. Zhou, Z.-h. Dong, A. M. Rao, P. C. Eklund, Reaction mechanism for the photopolymerization of solid fullerene C_{60}, *Chem. Phys. Lett.* **1993**, *211*(4-5), 337–340.

[134] J. Yu, R. K. Kalia, P. Vashishta, Phonon dispersion and density of states of solid C_{60}, *Appl. Phys. Lett.* **1993**, *63*(23), 3152–3154.

[135] J. J. L. Morton, Electron Spins in Fullerenes as Prospective Qubits, PhD thesis, University of Oxford, England, **2005**.

[136] A. Masuhara, Z. Tan, M. Ikeshima, T. Sato, H. Kasai, H. Oikawa, H. Nakanishi, Cyclic transformation in shape and crystal structure of C_{60} microcrystals, *CrystEngComm* **2012**, *14*(22), 7787–7791.

[137] M. Sathish, K. Miyazawa, J. P. Hill, K. Ariga, Solvent Engineering for Shape-Shifter Pure Fullerene (C_{60}), *J. Am. Chem. Soc.* **2009**, *131*(18), 6372–6373.

[138] L. K. Shrestha, J. P. Hill, T. Tsuruoka, K. Miyazawa, K. Ariga, Surfactant-Assisted Assembly of Fullerene (C_{60}) Nanorods and Nanotubes Formed at a Liquid-Liquid Interface, *Langmuir* **2013**, *29*(24), 7195–7202.

[139] L. K. Shrestha, Y. Yamauchi, J. P. Hill, K. Miyazawa, K. Ariga, Fullerene Crystals with Bimodal Pore Architectures Consisting of Macropores and Mesopores., *J. Am. Chem. Soc.* **2013**, *135*(2), 586–589.

[140] Z. Tan, A. Masuhara, H. Kasai, H. Nakanishi, H. Oikawa, Multibranched C_{60} Micro/Nanocrystals Fabricated by Reprecipitation Method, *Jpn. J. Appl. Phys.* **2008**, *47*(2), 1426–1428.

[141] A. Masuhara, Z. Tan, H. Kasai, H. Nakanishi, H. Oikawa, Fullerene Fine Crystals with Unique Shapes and Controlled Size, *Jpn. J. Appl. Phys.* **2009**, *48*(5), 050206.

[142] L. Wang, B. Liu, D. Liu, M. Yao, Y. Hou, S. Yu, T. Cui, D. Li, G. Zou, A. Iwasiewicz, B. Sundqvist, Synthesis of Thin, Rectangular C_{60} Nanorods Using m-Xylene as a Shape Controller, *Adv. Mater.* **2006**, *18*(14), 1883–1888.

[143] Q. Ying, J. Marecek, B. Chu, Slow aggregation of buckminsterfullerene (C_{60}) in benzene solution, *Chem. Phys. Lett.* **1994**, *219*(3-4), 214–218.

[144] A. D. Bokare, A. Patnaik, Microscopic diffusion model applied to C_{60} fullerene fractals in carbon disulphide solution, *J. Chem. Phys.* **2003**, *119*(8), 4529.

[145] L. Wei, J. Yao, H. Fu, Solvent-Assisted Self-Assembly of Fullerene into Single-Crystal Ultrathin Microribbons as Highly Sensitive UV-Visible Photodetectors, *ACS Nano* **2013**, *7*(9), 7573–7582.

[146] V. K. LaMer, R. H. Dinegar, Theory, Production and Mechanism of Formation of Monodispersed Hydrosols, *J. Am. Chem. Soc.* **1950**, *72*(11), 4847–4854.

[147] H. Kasai, H. S. Nalwa, H. Oikawa, S. Okada, H. Matsuda, N. Minami, A. Kakuta, K. Ono, A. Mukoh, H. Nakanishi, A Novel Preparation Method of Organic Microcrystals, *Jpn. J. Appl. Phys.* **1992**, *31*(Part 2, No. 8A), L1132–L1134.

[148] K. Miyazawa, Y. Kuwasaki, A. Obayashi, M. Kuwabara, C_{60} nanowhiskers formed by the liquid–liquid interfacial precipitation method, *J. Mater. Res.* **2002**, *17*(1), 83–88.

[149] S. Schäfer, K. Hübener, W. Harneit, C. Böhme, K. Fostiropoulos, H. Angermann, J. Rappich, J. Behrends, K. Lips, Thin film engineering for $N@C_{60}$ quantum computers: Spin detection and device patterning approaches, *Solid State Sci.* **2008**, *10*(10), 1314–1321.

[150] I. Hiromitsu, Y. Kaimori, M. Kitano, T. Ito, Spin-dependent recombination of photoinduced carriers in phthalocyanine/C_{60} heterojunctions, *Phys. Rev. B* **1999**, *59*(3), 2151–2163.

[151] M. S. Brandt, Spin-dependent transport and recombination in semiconductors (original thesis in German: Spinabhängiger Transport und Rekombination in Halbleitern), PhD thesis, Universität Stuttgart, Germany, **1992**.

[152] Nacalai Tesque Inc., COSMOSIL Application Data, *Application No.: AP-1237*.

[153] S. Abe, G. Sato, T. Kaneko, T. Hirata, R. Hatakeyama, K. Yokoo, S. Ono, K. Omote, Y. Kasama, Effects of Ion Energy Control on Production of Nitrogen–C_{60} Compounds by Ion Implantation, *Jpn. J. Appl. Phys.* **2006**, *45*(10B), 8340–8343.

[154] J. E. Grose, E. S. Tam, C. Timm, M. Scheloske, B. Ulgut, J. J. Parks, H. D. Abruña, W. Harneit, D. C. Ralph, Tunnelling spectra of individual magnetic endofullerene molecules, *Nat. Mater.* **2008**, *7*(11), 884–889.

[155] S. Stoll, A. Schweiger, EasySpin, a comprehensive software package for spectral simulation and analysis in EPR, *J. Magn. Reson.* **2006**, *178*(1), 42–55.

[156] C. Knapp, N. Weiden, H. Kass, K.-P. Dinse, B. Pietzak, M. Waiblinger, A. Weidinger, Electron paramagnetic resonance study of atomic phosphorus encapsulated in [60]fullerene, *Mol. Phys.* **1998**, *95*(5), 999–1004.

[157] P. W. M. Blom, V. D. Mihailetchi, L. J. A. Koster, D. E. Markov, Device Physics of Polymer:Fullerene Bulk Heterojunction Solar Cells, *Adv. Mater.* **2007**, *19*, 1551–1566.

[158] C. W. Tang, Two-layer organic photovoltaic cell, *Appl. Phys. Lett.* **1986**, *48*(2), 183–185.

[159] J. J. M. Halls, R. H. Friend, The Photovoltaic Effect in a Poly(p-phenylenevinylene) / Perylene Heterojunction, *Synth. Met.* **1997**, *85*(1-3), 1307–1308.

[160] D. E. Markov, E. Amsterdam, P. W. M. Blom, A. B. Sieval, J. C. Hummelen, Accurate Measurement of the Exciton Diffusion Length in a Conjugated Polymer Using a Heterostructure with a Side-Chain Cross-Linked Fullerene Layer, *J. Phys. Chem. A* **2005**, *109*(24), 5266–5274.

[161] R. N. Marks, J. J. M. Halls, D. D. C. Bradley, R. H. Friend, A. B. Holmes, The photovoltaic response in poly(p-phenylene vinylene) thin-film devices, *J. Phys. Condens. Matter* **1994**, *6*(7), 1379–1394.

[162] R. Bechara, J. Petersen, V. Gernigon, P. Lévêque, T. Heiser, V. Toniazzo, D. Ruch, M. Michel, PEDOT:PSS-free organic solar cells using tetrasulfonic copper phthalocyanine as buffer layer, *Sol. Energy Mater. Sol. Cells* **2012**, *98*, 482–485.

[163] G. Yu, J. Gao, J. C. Hummelen, F. Wudl, A. J. Heeger, Polymer Photovoltaic Cells: Enhanced Efficiencies via a Network of Internal Donor-Acceptor Heterojunctions, *Science* **1995**, *270*(5243), 1789–1791.

[164] F. Padinger, R. Rittberger, N. Sariciftci, Effects of Postproduction Treatment on Plastic Solar Cells, *Adv. Funct. Mater.* **2003**, *13*(1), 85–88.

[165] N. S. Sariciftci, D. Braun, C. Zhang, V. I. Srdanov, A. J. Heeger, G. Stucky, F. Wudl, Semiconducting polymer-buckminsterfullerene heterojunctions: Diodes, photodiodes, and photovoltaic cells, *Appl. Phys. Lett.* **1993**, *62*(6), 585–587.

[166] G. Dennler, M. C. Scharber, C. J. Brabec, Polymer-Fullerene Bulk-Heterojunction Solar Cells, *Adv. Mater.* **2009**, *21*(13), 1323–1338.

[167] N. Blouin, A. Michaud, D. Gendron, S. Wakim, E. Blair, R. Neagu-Plesu, M. Belletête, G. Durocher, Y. Tao, M. Leclerc, Toward a Rational Design of Poly(2,7-Carbazole) Derivatives for Solar Cells, *J. Am. Chem. Soc.* **2008**, *130*(2), 732–742.

[168] S. H. Park, A. Roy, S. Beaupré, S. Cho, N. Coates, J. S. Moon, D. Moses, M. Leclerc, K. Lee, A. J. Heeger, Bulk heterojunction solar cells with internal quantum efficiency approaching 100%, *Nat. Photonics* **2009**, *3*(5), 297–302.

[169] Z. He, C. Zhong, S. Su, M. Xu, H. Wu, Y. Cao, Enhanced power-conversion efficiency in polymer solar cells using an inverted device structure, *Nat. Photonics* **2012**, *6*(9), 593–597.

[170] J. Niklas, K. L. Mardis, B. P. Banks, G. M. Grooms, A. Sperlich, V. Dyakonov, S. Beaupré, M. Leclerc, T. Xu, L. Yu, O. G. Poluektov, Highly-efficient charge separation and polaron delocalization in polymer-fullerene bulk-heterojunctions: a comparative multi-frequency EPR and DFT study., *Phys. Chem. Chem. Phys.* **2013**, *15*(24), 9562–9574.

[171] C. J. Brabec, S. Gowrisanker, J. J. M. Halls, D. Laird, S. Jia, S. P. Williams, Polymer-Fullerene Bulk-Heterojunction Solar Cells, *Adv. Mater.* **2010**, *22*(34), 3839–3856.

[172] H. Hoppe, N. S. Sariciftci, Polymer Solar Cells, *Adv. Polym. Sci.* **2008**, *214*, 1–86.

[173] S. Rajaram, R. Shivanna, S. K. Kandappa, K. S. Narayan, Nonplanar Perylene Diimides as Potential Alternatives to Fullerenes in Organic Solar Cells, *J. Phys. Chem. Lett.* **2012**, *3*(17), 2405–2408.

[174] W. Shockley, H. J. Queisser, Detailed Balance Limit of Efficiency of p-n Junction Solar Cells, *J. Appl. Phys.* **1961**, *32*(3), 510–519.

[175] J. Nelson, J. Kirkpatrick, P. Ravirajan, Factors limiting the efficiency of molecular photovoltaic devices, *Phys. Rev. B* **2004**, *69*(3), 035337.

[176] L. J. A. Koster, E. C. P. Smits, V. D. Mihailetchi, P. W. M. Blom, Device model for the operation of polymer/fullerene bulk heterojunction solar cells, *Phys. Rev. B* **2005**, *72*(8), 085205.

[177] T. Kirchartz, B. E. Pieters, K. Taretto, U. Rau, Electro-optical modeling of bulk heterojunction solar cells, *J. Appl. Phys.* **2008**, *104*(9), 094513.

[178] M. Scharber, N. Sariciftci, Efficiency of bulk-heterojunction organic solar cells, *Prog. Polym. Sci.* **2013**, *38*(12), 1929–1940.

[179] W. Shockley, The Theory of p-n Junctions in Semiconductors and p-n Junction Transistors, *Bell Syst. Tech. J.* **1949**, *28*(3), 435–489.

[180] H. J. Queisser, Forward Characteristics and Efficiencies of Silicon Solar Cells, *Solid. State. Electron.* **1962**, *5*(1), 1–10.

[181] S. M. Sze, *Physics of Semiconductor Devices*, Wiley-Interscience, **1969**.

[182] M. B. Prince, Silicon Solar Energy Converters, *J. Appl. Phys.* **1955**, *26*(5), 534–540.

[183] J. Nelson, *The Physics of Solar Cells*, Imperial College Press, **2003**.

[184] T. Kirchartz, B. E. Pieters, J. Kirkpatrick, U. Rau, J. Nelson, Recombination via tail states in polythiophene:fullerene solar cells, *Phys. Rev. B* **2011**, *83*(11), 115209.

[185] S. R. Cowan, W. L. Leong, N. Banerji, G. Dennler, A. J. Heeger, Identifying a Threshold Impurity Level for Organic Solar Cells: Enhanced First-Order Recombination Via Well-Defined $PC_{84}BM$ Traps in Organic Bulk Heterojunction Solar Cells, *Adv. Funct. Mater.* **2011**, *21*(16), 3083–3092.

[186] G. A. H. Wetzelaer, M. Kuik, H. T. Nicolai, P. W. M. Blom, Trap-assisted and Langevin-type recombination in organic light-emitting diodes, *Phys. Rev. B* **2011**, *83*(16), 165204.

[187] G. Lakhwani, A. Rao, R. H. Friend, Bimolecular Recombination in Organic Photovoltaics, *Annu. Rev. Phys. Chem.* **2014**, *65*(1), 557–581.

[188] C. Deibel, V. Dyakonov, Polymer-Fullerene Bulk Heterojunction Solar Cells, *Rep. Prog. Phys.* **2010**, *73*, 096401.

[189] S. Cook, R. Katoh, A. Furube, Ultrafast Studies of Charge Generation in PCBM:P3HT Blend Films following Excitation of the Fullerene PCBM, *J. Phys. Chem. C* **2009**, *113*(6), 2547–2552.

[190] T. Strobel, C. Deibel, V. Dyakonov, Role of Polaron Pair Diffusion and Surface Losses in Organic Semiconductor Devices, *Phys. Rev. Lett.* **2010**, *105*(26), 266602.

[191] J. Kniepert, M. Schubert, J. C. Blakesley, D. Neher, Photogeneration and Recombination in P3HT/PCBM Solar Cells Probed by Time-Delayed Collection Field Experiments, *J. Phys. Chem. Lett.* **2011**, *2*(7), 700–705.

[192] A. A. Bakulin, A. Rao, V. G. Pavelyev, P. H. M. van Loosdrecht, M. S. Pshenichnikov, D. Niedzialek, J. Cornil, D. Beljonne, R. H. Friend, The Role of Driving Energy and Delocalized States for Charge Separation in Organic Semiconductors, *Science* **2012**, *335*(6074), 1340–1344.

[193] Y. Kim, S. Cook, S. M. Tuladhar, S. A. Choulis, J. Nelson, J. R. Durrant, D. D. C. Bradley, M. Giles, I. McCulloch, C.-S. Ha, M. Ree, A strong regioregularity effect in self-organizing conjugated polymer films and high-efficiency polythiophene:fullerene solar cells, *Nat. Mater.* **2006**, *5*(3), 197–203.

[194] A. J. Heeger, 25th Anniversary Article: Bulk Heterojunction Solar Cells: Understanding the Mechanism of Operation, *Adv. Mater.* **2014**, *26*(1), 10–28.

[195] K. Pakbaz, C. H. Lee, A. J. Heeger, T. W. Hagler, D. McBranch, Nature of the primary photoexcitations in poly(arylene-vinylenes), *Synth. Met.* **1994**, *64*(2-3), 295–306.

[196] D. Moses, A. Dogariu, A. J. Heeger, Ultrafast detection of charged photocarriers in conjugated polymers, *Phys. Rev. B* **2000**, *61*(14), 9373–9379.

[197] R. Kersting, U. Lemmer, M. Deussen, H. J. Bakker, R. F. Mahrt, H. Kurz, V. I. Arkhipov, H. Bässler, E. O. Göbel, Ultrafast Field-Induced Dissociation of Excitons in Conjugated Polymers, *Phys. Rev. Lett.* **1994**, *73*(10), 1440–1443.

[198] M. Deussen, M. Scheidler, H. Bässler, Electric field-induced photoluminescence quenching in thin-film light-emitting diodes based on poly(phenyl-p-phenylene vinylene), *Synth. Met.* **1995**, *73*(2), 123–129.

[199] F. Laquai, D. Andrienko, R. Mauer, P. W. M. Blom, Charge Carrier Transport and Photogeneration in P3HT:PCBM Photovoltaic Blends, *Macromol. Rapid Commun.* **2015**, *36*(11), 1001–1025.

[200] L. W. Barbour, R. D. Pensack, M. Hegadorn, S. Arzhantsev, J. B. Asbury, Excitation Transport and Charge Separation in an Organic Photovoltaic Material: Watching Excitations Diffuse to Interfaces, *J. Phys. Chem. C* **2008**, *112*(10), 3926–3934.

[201] M. Theander, A. Yartsev, D. Zigmantas, V. Sundström, W. Mammo, M. R. Andersson, O. Inganäs, Photoluminescence quenching at a polythiophene/C_{60} heterojunction, *Phys. Rev. B* **2000**, *61*(19), 12957–12963.

[202] C. Deibel, D. Mack, J. Gorenflot, A. Schöll, S. Krause, F. Reinert, D. Rauh, V. Dyakonov, Energetics of excited states in the conjugated polymer poly(3-hexylthiophene), *Phys. Rev. B* **2010**, *81*(8), 085202.

[203] D. Hertel, E. V. Soh, H. Bässler, L. J. Rothberg, Electric field dependent generation of geminate electron–hole pairs in a ladder-type π-conjugated polymer probed by fluorescence quenching and delayed field collection of charge carriers, *Chem. Phys. Lett.* **2002**, *361*(1-2), 99–105.

[204] V. D. Mihailetchi, L. J. A. Koster, J. C. Hummelen, P. W. M. Blom, Photocurrent Generation in Polymer-Fullerene Bulk Heterojunctions, *Phys. Rev. Lett.* **2004**, *93*(21), 216601.

[205] J. G. Müller, J. M. Lupton, J. Feldmann, U. Lemmer, M. C. Scharber, N. S. Sariciftci, C. J. Brabec, U. Scherf, Ultrafast dynamics of charge carrier photogeneration and geminate recombination in conjugated polymer:fullerene solar cells, *Phys. Rev. B* **2005**, *72*(19), 195208.

[206] I. A. Howard, R. Mauer, M. Meister, F. Laquai, Effect of morphology on ultrafast free carrier generation in polythiophene:fullerene organic solar cells, *J. Am. Chem. Soc.* **2010**, *132*(42), 14866–14876.

[207] R. A. Marcus, On the Theory of Oxidation-Reduction Reactions Involving Electron Transfer. I, *J. Chem. Phys.* **1956**, *24*(5), 966–978.

[208] R. A. Marcus, Electron transfer reactions in chemistry. Theory and experiment, *Rev. Mod. Phys.* **1993**, *65*(3), 599–610.

[209] A. Miller, E. Abrahams, Impurity Conduction at Low Concentrations, *Phys. Rev.* **1960**, *120*(3), 745–755.

[210] H. Bässler, Charge Transport in Disordered Organic Photoconductors a Monte Carlo Simulation Study, *Phys. Status Solidi B* **1993**, *175*(1), 15–56.

[211] C. Deibel, T. Strobel, V. Dyakonov, Origin of the Efficient Polaron-Pair Dissociation in Polymer-Fullerene Blends, *Phys. Rev. Lett.* **2009**, *103*, 036402.

[212] R. Mauer, M. Kastler, F. Laquai, The Impact of Polymer Regioregularity on Charge Transport and Efficiency of P3HT:PCBM Photovoltaic Devices, *Adv. Funct. Mater.* **2010**, *20*(13), 2085–2092.

[213] R. J. Kline, M. D. McGehee, E. N. Kadnikova, J. Liu, J. M. J. Fréchet, Controlling the Field-Effect Mobility of Regioregular Polythiophene by Changing the Molecular Weight, *Adv. Mater.* **2003**, *15*(18), 1519–1522.

[214] A. Zen, J. Pflaum, S. Hirschmann, W. Zhuang, F. Jaiser, U. Asawapirom, J. P. Rabe, U. Scherf, D. Neher, Effect of Molecular Weight and Annealing of Poly(3-hexylthiophene)s on the Performance of Organic Field-Effect Transistors, *Adv. Funct. Mater.* **2004**, *14*(8), 757–764.

[215] C. Goh, R. J. Kline, M. D. McGehee, E. N. Kadnikova, J. M. J. Fréchet, Molecular-weight-dependent mobilities in regioregular poly(3-hexyl-thiophene) diodes, *Appl. Phys. Lett.* **2005**, *86*(12), 122110.

[216] V. D. Mihailetchi, H. X. Xie, B. de Boer, L. J. A. Koster, P. W. M. Blom, Charge Transport and Photocurrent Generation in Poly(3-hexylthiophene): Methanofullerene Bulk-Heterojunction Solar Cells, *Adv. Funct. Mater.* **2006**, *16*(5), 699–708.

[217] V. D. Mihailetchi, J. Wildeman, P. W. M. Blom, Space-Charge Limited Photocurrent, *Phys. Rev. Lett.* **2005**, *94*(12), 126602.

[218] A. Wagenpfahl, D. Rauh, M. Binder, C. Deibel, V. Dyakonov, S-shaped current-voltage characteristics of organic solar devices, *Phys. Rev. B* **2010**, *82*(11), 115306.

[219] L. Onsager, Initial Recombination of Ions, *Phys. Rev.* **1938**, *54*(8), 554–557.

[220] C. L. Braun, Electric field assisted dissociation of charge transfer states as a mechanism of photocarrier production, *J. Chem. Phys.* **1984**, *80*(9), 4157–4161.

[221] W. B. Jackson, Role of bimolecular recombination in picosecond photoinduced absorption of hydrogenated amorphous silicon, *Philos. Mag. Lett.* **1989**, *60*(6), 277–282.

[222] E. A. Schiff, Diffusion-controlled bimolecular recombination of electrons and holes in a-Si:H, *J. Non. Cryst. Solids* **1995**, *190*(1-2), 1–8.

[223] P. Langevin, Recombinaison et mobilites des ions dans les gaz, *Ann. Chim. Phys.* **1903**, *28*, 433–530.

[224] G. J. Adriaenssens, V. I. Arkhipov, Non-Langevin recombination in disordered materials with random potential distributions, *Solid State Commun.* **1997**, *103*(9), 541–543.

[225] V. I. Arkhipov, G. J. Adriaenssens, Kinetics of low-temperature charge-carrier recombination in disordered hopping systems, *J. Phys. Condens. Matter* **1997**, *9*(32), 6869–6876.

[226] J. Nelson, Diffusion-limited recombination in polymer-fullerene blends and its influence on photocurrent collection, *Phys. Rev. B* **2003**, *67*(15), 155209.

[227] L. J. A. Koster, V. D. Mihailetchi, P. W. M. Blom, Bimolecular recombination in polymer/fullerene bulk heterojunction solar cells, *Appl. Phys. Lett.* **2006**, *88*(5), 052104.

[228] C. Deibel, A. Wagenpfahl, V. Dyakonov, Origin of reduced polaron recombination in organic semiconductor devices, *Phys. Rev. B* **2009**, *80*(7), 075203.

[229] W. Shockley, W. T. Read, Statistics of the Recombination of Holes and Electrons, *Phys. Rev.* **1952**, *87*(5), 835–842.

[230] R. N. Hall, Electron-Hole Recombination in Germanium, *Phys. Rev.* **1952**, *87*(2), 387.

[231] T. Kirchartz, J. Nelson, Meaning of reaction orders in polymer:fullerene solar cells, *Phys. Rev. B* **2012**, *86*(16), 165201.

[232] C. Deibel, D. Rauh, A. Foertig, Order of decay of mobile charge carriers in P3HT:PCBM solar cells, *Appl. Phys. Lett.* **2013**, *103*(4), 043307.

[233] M. Eckardt, J. Behrends, D. Münter, W. Harneit, Compact electrically detected magnetic resonance setup, *AIP Adv.* **2015**, *5*(4), 047139.

[234] F. Kraffert, R. Steyrleuthner, C. Meier, R. Bittl, J. Behrends, Transient electrically detected magnetic resonance spectroscopy applied to organic solar cells, *Appl. Phys. Lett.* **2015**, *107*(4), 043302.

[235] B. Z. Tedlla, F. Zhu, M. Cox, B. Koopmans, E. Goovaerts, Spin-dependent photophysics in polymers lightly doped with fullerene derivatives: Photoluminescence and electrically detected magnetic resonance, *Phys. Rev. B* **2015**, *91*(8), 085309.

[236] C. Böhme, J. M. Lupton, Challenges for organic spintronics, *Nat. Nanotechnol.* **2013**, *8*(9), 612–615.

[237] J. Behrends, I. D. W. Samuel, A. Schnegg, D. J. Keeble, Persistent spin coherence and bipolarons, *Nat. Nanotechnol.* **2013**, *8*(12), 884–885.

[238] M. Limpinsel, A. Wagenpfahl, M. Mingebach, C. Deibel, V. Dyakonov, Photocurrent in bulk heterojunction solar cells, *Phys. Rev. B* **2010**, *81*(8), 085203.

[239] T. Kato, T. Kodama, T. Shida, Spectroscopic studies of the radical anion of C_{60}. Detection of the fluorenscence and reinvestigation of the ESR spectrum, *Chem. Phys. Lett.* **1993**, *205*(4-5), 405–409.

[240] T. Kato, T. Kodama, M. Oyama, S. Okazaki, T. Shida, T. Nakagawa, Y. Matsui, S. Suzuki, H. Shiromaru, K. Yamauchi, Y. Achiba, ESR and optical studies of the radical anion of C_{60}, *Chem. Phys. Lett.* **1991**, *186*(1), 35–39.

[241] V. Dyakonov, G. Zoriniants, M. Scharber, C. Brabec, R. Janssen, J. C. Hummelen, N. S. Sariciftci, Photoinduced charge carriers in conjugated polymer–fullerene composites studied with light-induced electron-spin resonance, *Phys. Rev. B* **1999**, *59*(12), 8019–8025.

[242] A. Aguirre, P. Gast, S. Orlinskii, I. Akimoto, E. J. J. Groenen, H. El Mkami, E. Goovaerts, S. van Doorslaer, Multifrequency EPR analysis of the positive polaron in I_2-doped poly(3-hexylthiophene) and in poly[2-methoxy-5-(3,7-dimethyloctyloxy)]-1,4-phenylenevinylene, *Phys. Chem. Chem. Phys.* **2008**, *10*(47), 7129–7138.

[243] O. G. Poluektov, S. Filippone, N. Martín, A. Sperlich, C. Deibel, V. Dyakonov, Spin Signatures of Photogenerated Radical Anions in Polymer-[70]Fullerene Bulk Heterojunctions: High Frequency Pulsed EPR Spectroscopy, *J. Phys. Chem. B* **2010**, *114*(45), 14426–14429.

[244] A. Sperlich, H. Kraus, C. Deibel, H. Blok, J. Schmidt, V. Dyakonov, Reversible and Irreversible Interactions of Poly(3-hexylthiophene) with Oxygen Studied by Spin-Sensitive Methods, *J. Phys. Chem. B* **2011**, *115*(46), 13513–13518.

[245] K. Lips, P. Kanschat, D. Will, C. Lerner, W. Fuhs, ESR and transport in microcrystalline silicon, *J. Non. Cryst. Solids* **1998**, *227-230*, 1021–1025.

[246] M. Jørgensen, K. Norrman, F. C. Krebs, Stability/degradation of polymer solar cells, *Sol. Energy Mater. Sol. Cells* **2008**, *92*(7), 686–714.

[247] A. Turak, Interfacial degradation in organic optoelectronics, *RSC Adv.* **2013**, *3*(18), 6188–6225.

[248] M. Manceau, A. Rivaton, J.-L. Gardette, Involvement of Singlet Oxygen in the Solid-State Photochemistry of P3HT, *Macromol. Rapid Commun.* **2008**, *29*(22), 1823–1827.

[249] M. Manceau, A. Rivaton, J.-L. Gardette, S. Guillerez, N. Lemaître, The mechanism of photo- and thermooxidation of poly(3-hexylthiophene) (P3HT) reconsidered, *Polym. Degrad. Stab.* **2009**, *94*(6), 898–907.

[250] H. Hintz, H.-J. Egelhaaf, L. Lüer, J. Hauch, H. Peisert, T. Chassé, Photodegradation of P3HT-A Systematic Study of Environmental Factors, *Chem. Mater.* **2011**, *23*(2), 145–154.

[251] K. Kawano, R. Pacios, D. Poplavskyy, J. Nelson, D. D. C. Bradley, J. R. Durrant, Degradation of organic solar cells due to air exposure, *Sol. Energy Mater. Sol. Cells* **2006**, *90*(20), 3520–3530.

[252] A. Sharma, G. Andersson, D. A. Lewis, Role of humidity on indium and tin migration in organic photovoltaic devices, *Phys. Chem. Chem. Phys.* **2011**, *13*(10), 4381–4387.

[253] M. T. Lloyd, D. C. Olson, P. Lu, E. Fang, D. L. Moore, M. S. White, M. O. Reese, D. S. Ginley, J. W. P. Hsu, Impact of contact evolution on the shelf life of organic solar cells, *J. Mater. Chem.* **2009**, *19*(41), 7638–7642.

[254] M. Glatthaar, M. Riede, N. Keegan, K. Sylvester-Hvid, B. Zimmermann, M. Niggemann, A. Hinsch, A. Gombert, Efficiency limiting factors of organic bulk heterojunction solar cells identified by electrical impedance spectroscopy, *Sol. Energy Mater. Sol. Cells* **2007**, *91*(5), 390–393.

[255] M. O. Reese, A. J. Morfa, M. S. White, N. Kopidakis, S. E. Shaheen, G. Rumbles, D. S. Ginley, Pathways for the degradation of organic photovoltaic P3HT:PCBM based devices, *Sol. Energy Mater. Sol. Cells* **2008**, *92*(7), 746–752.

List of Figures

List of Tables

List of Appendices

Appendix A: EDMR Control Center Interface

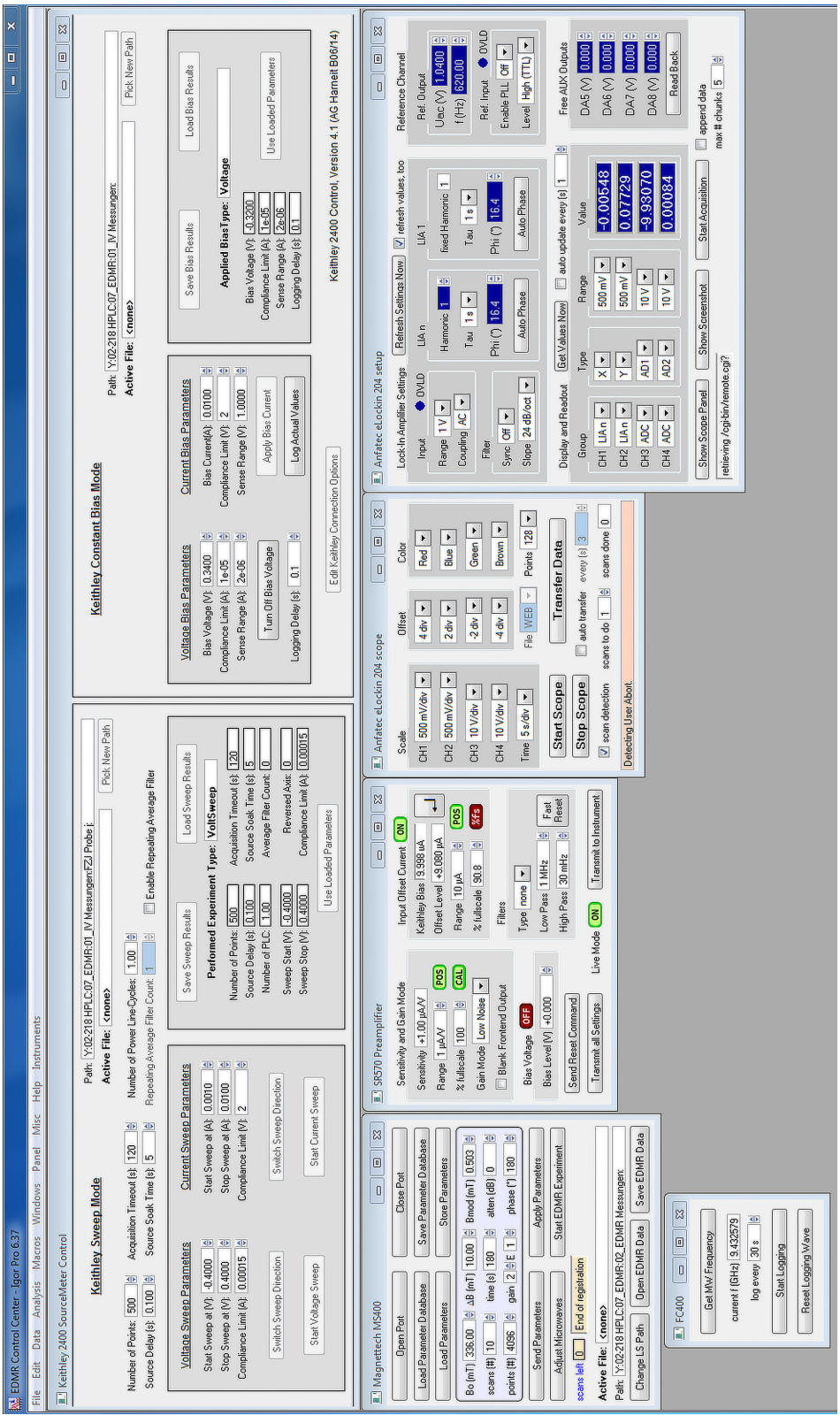

Fig. A1: Screenshot of the EDMR Control Center interface (upper part).

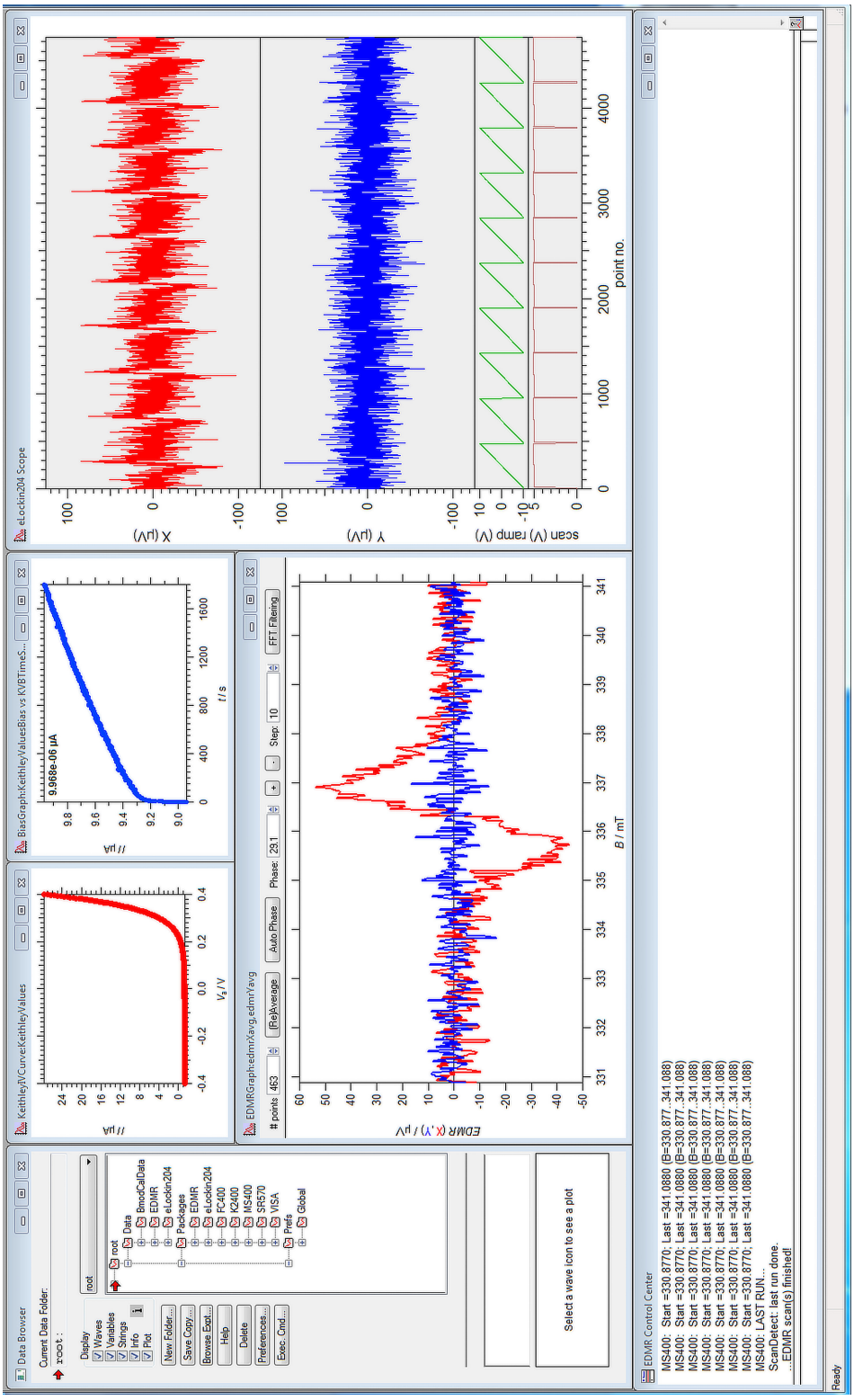

Fig. A2: Screenshot of the EDMR Control Center interface (lower part).

Appendix B: EDMR Control Center Saved Data File Content

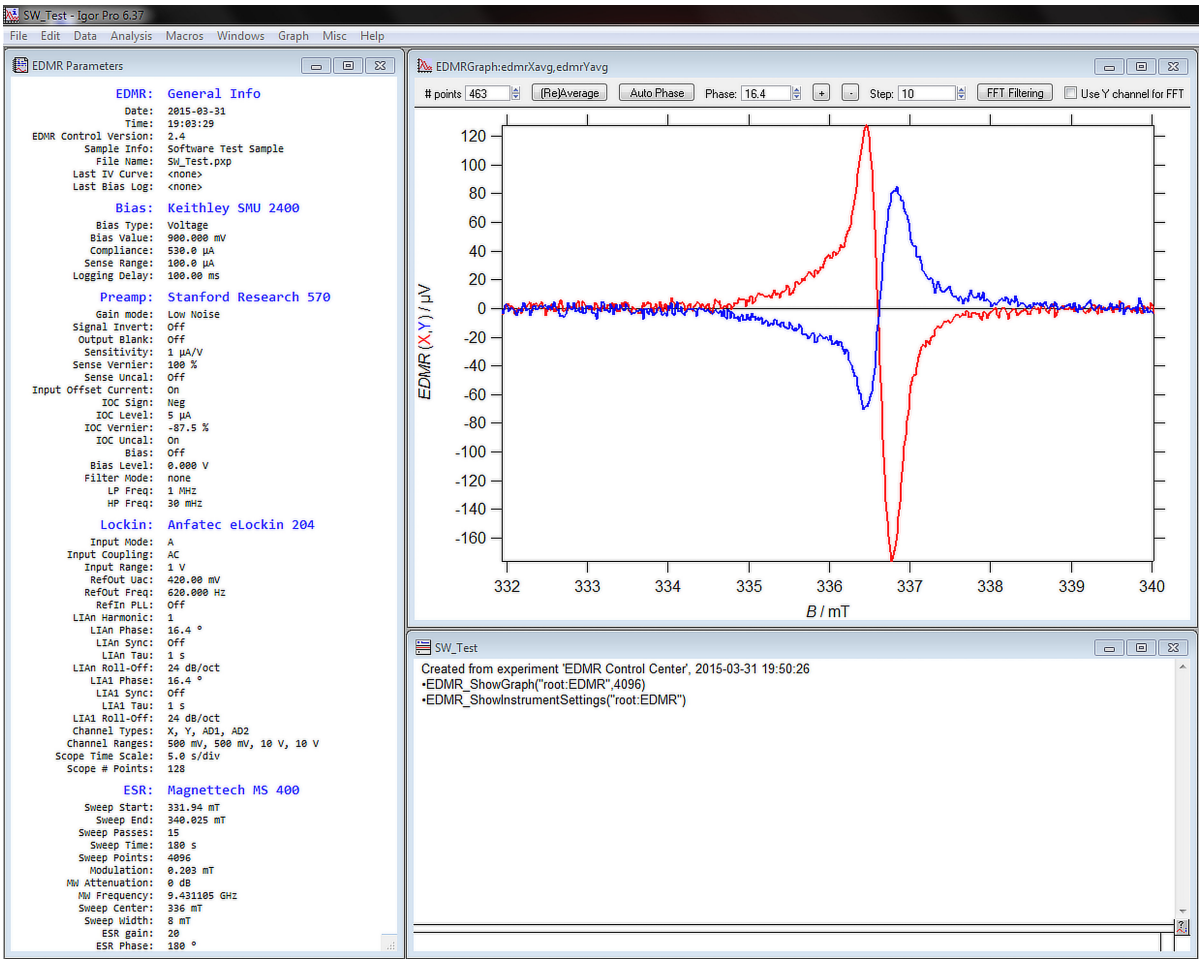

Fig. A3: Screenshot of an opened *.pxp file saved by the EDMR Control Center. The data file written by the EDMR Control Center contains two functions that are automatically called with the correct parameters on the first file opening: *EDMR_ShowGraph()* and *EDMR_ShowInstrumentSettings()*. The latter creates an overview of all instrument settings used during the measurement, while the first one is responsible for building a graph window similar to the one used by the EDMR Control Center software (*EDMR-Graph*). Here, the same operations as described in chapter 3, section 3.3.1 are available to the user - namely *(Re)Average*, *Auto Phase* and *FFT Filtering*.

Data included in the saved *.pxp file:

- Individual EDMR raw data for all scans (x- and y-channel)
- Individual magnetic field ramps & microwave frequencies
- Averaged x- and y-channel data incl. corresponding magnetic fields
- All sample current values recorded during the experiment
- All instrument settings used for the experiment
- Operator note given at the end of the measurement

Appendix C: EDMR Analysis Toolbox Software Demo

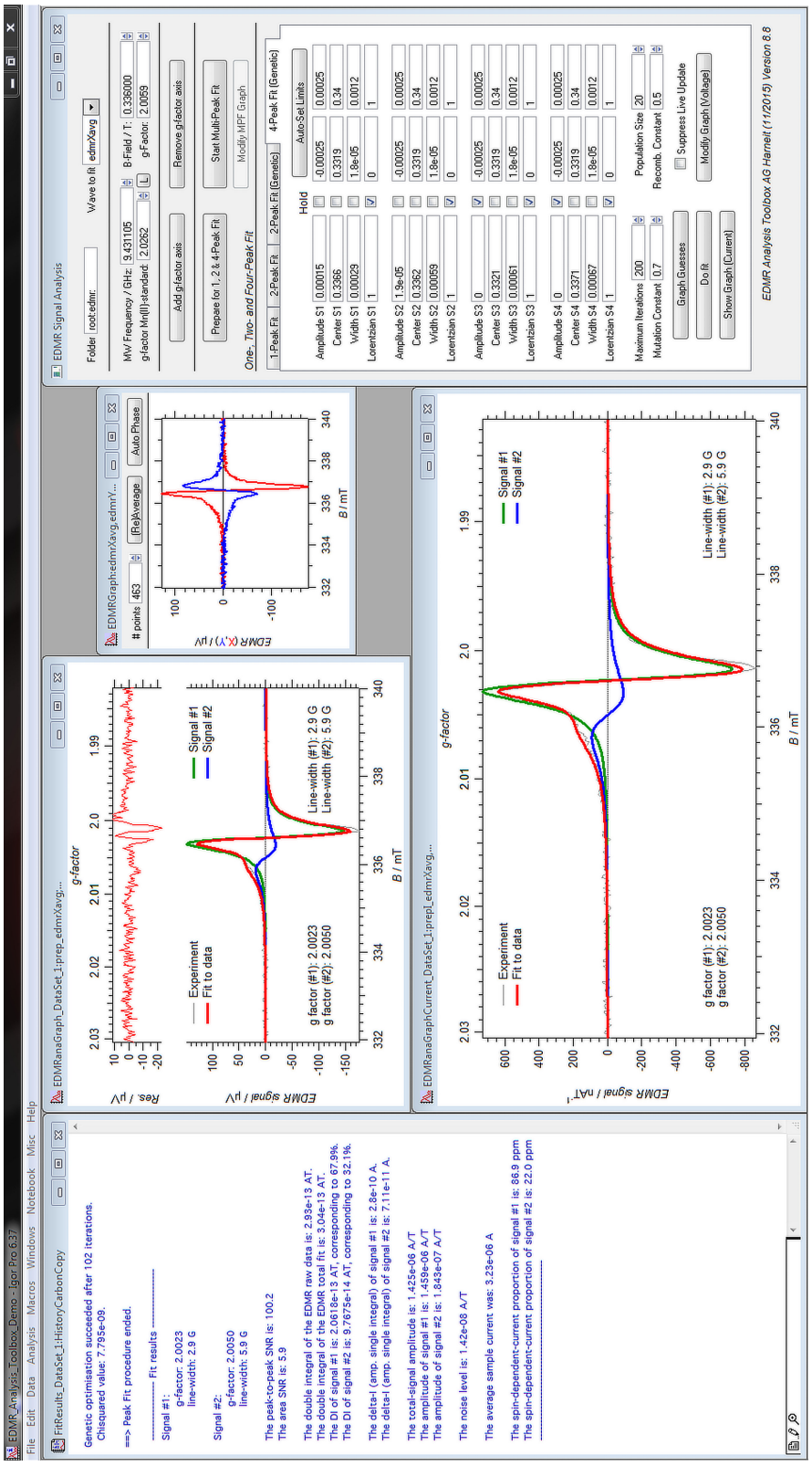

Fig. A4: Screenshot of the EDMR Analysis Toolbox performing a two-peak fit of the x-channel.

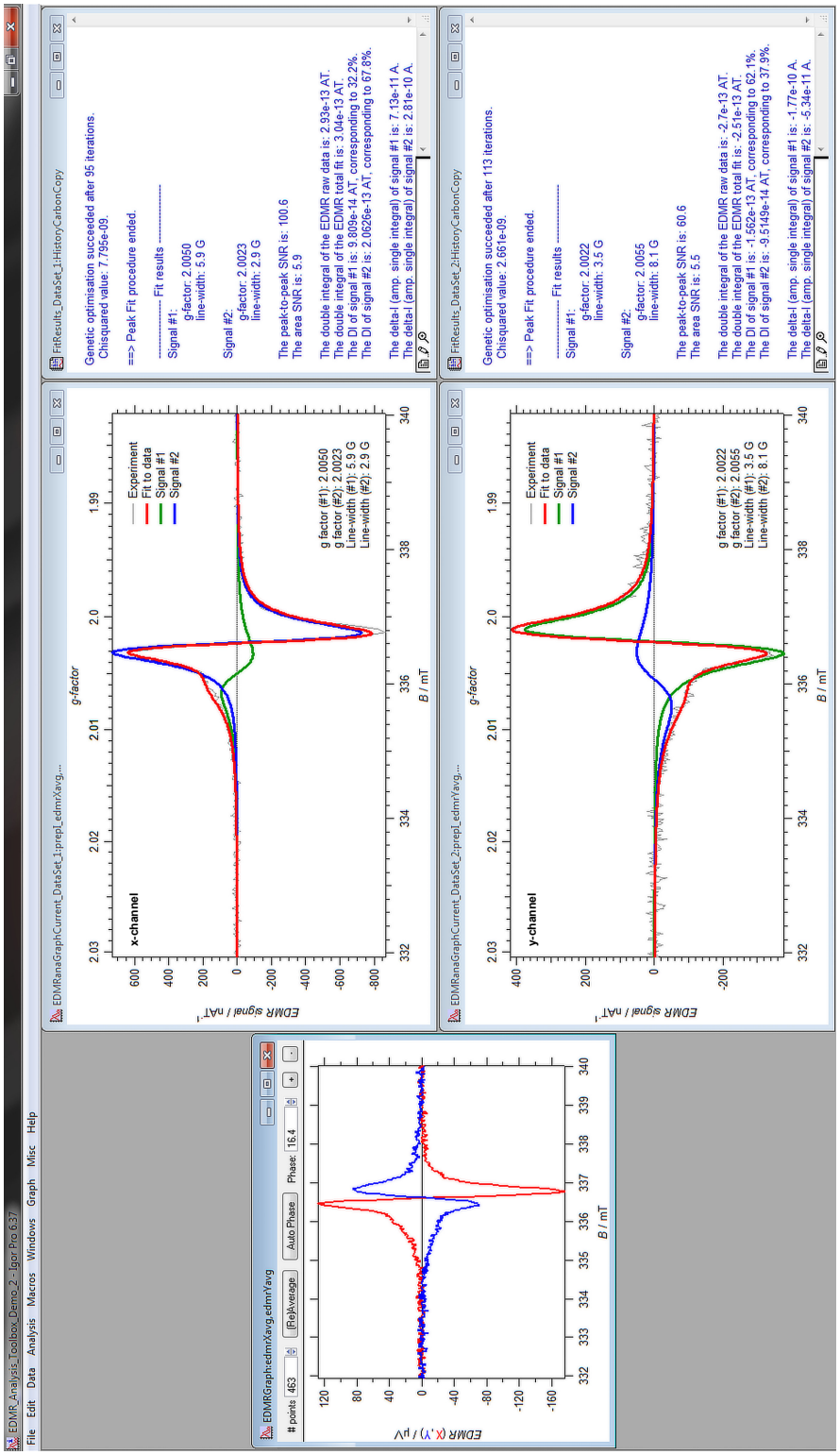

Fig. A5: Screenshot of the EDMR Analysis Toolbox performing a two-peak fit on both x- and y-channel data. Separate graph and result windows are generated for each channel making direct comparisons easy. All results are stored together in a single file.

Appendix D: Light Source Intensity Calibration Data

Tab. A1: Calibration data for the used Schott KL 2500 LCD halogen cold light source. The equivalent light intensity P_{irr} in suns, with one sun corresponding to a standard illumination of $1\,\mathrm{kW\,m^{-2}}$,[64] is given for each *Level* and *Aperture* setting of the light source.

Level Setting	*Aper*ture Setting	*Light Intensity* P_{irr} / suns	*Level* Setting	*Aperture* Setting	*Light Intensity* P_{irr} / suns
1	A	7.0×10^{-3}	4	A	2.4×10^{-2}
1	B	1.4×10^{-2}	4	B	4.8×10^{-2}
1	C	2.5×10^{-2}	4	C	8.7×10^{-2}
1	D	4.2×10^{-2}	4	D	1.4×10^{-1}
1	E	6.4×10^{-2}	4	E	2.2×10^{-1}
2	A	1.1×10^{-2}	5	A	3.7×10^{-2}
2	B	2.1×10^{-2}	5	B	7.3×10^{-2}
2	C	3.8×10^{-2}	5	C	1.3×10^{-1}
2	D	6.3×10^{-2}	5	D	2.2×10^{-1}
2	E	9.6×10^{-2}	5	E	3.3×10^{-1}
3	A	1.6×10^{-2}	6	A	5.5×10^{-2}
3	B	3.3×10^{-2}	6	B	1.1×10^{-1}
3	C	5.8×10^{-2}	6	C	2.0×10^{-1}
3	D	9.8×10^{-2}	6	D	3.3×10^{-1}
3	E	1.5×10^{-1}	6	E	5.0×10^{-1}

The calibration data given here were determined using an increment for each *Level* and *Aperture* setting of the KL 2500 LCD obtained by recording spectra for nine different combinations covering *Level* settings 1 to 4 and 6, as well as *Aperture* settings A to E and calculating the corresponding spectral count rate for each combination by integrating over the wavelength range from 339 nm to 1025 nm.

A commercial silicon-based solar cell (Osram SFH2400) in combination with a LOT Oriel sun simulator and a Czibula & Grundmann RS-OD-1 reference solar cell was used to convert the relative unit of measure into the corresponding effective light intensity in suns present at the sample location in the benchtop EDMR setup. More details about the calibration procedure can be found in part I, chapter 4, section 4.3.

Appendix E: Composition of the Ion Implantation Setup

The implantation setup used to synthesis N@C_{60} was lab-build during this thesis – mainly using equipment already available from an earlier production of the molecule in the Harneit research group. The setup's main chamber vacuum is maintained using an Edwards STP-A803C turbomolecular pump (TMP) with accompanying SCU 800 controller unit in combination with an Edwards nXDS15i scroll pump as the backing pump. The nitrogen plasma is produced by a HFQ 1303-3 ion source (JE PlasmaConsult) together with a suitable RF generator (PFG 300 RF, Hüttinger) and the necessary power supply units for the screen voltage (MCN 350-1250, F.u.G. Elektronik), the acceleration voltage (MCN 350-650, F.u.G. Elektronik) and the magnetic coil current (NTN 700-35, F.u.G. Elektronik). The nitrogen flow can be controlled using a mass flow controller unit (GFC171, Aalborg Instruments & Controls). Furthermore, the setup has a lock (incl. assoc. vacuum equipment), allowing for easy target exchange and fullerene harvest. In case of a mains failure, the main TMP is protected using an uninterrupted power supply (UPS) unit. The temperature at the build-in boron nitride effusion cell is controlled via an Eurotherm 2408 PID, an Inficon quartz crystal microbalance monitors the fullerene evaporation.

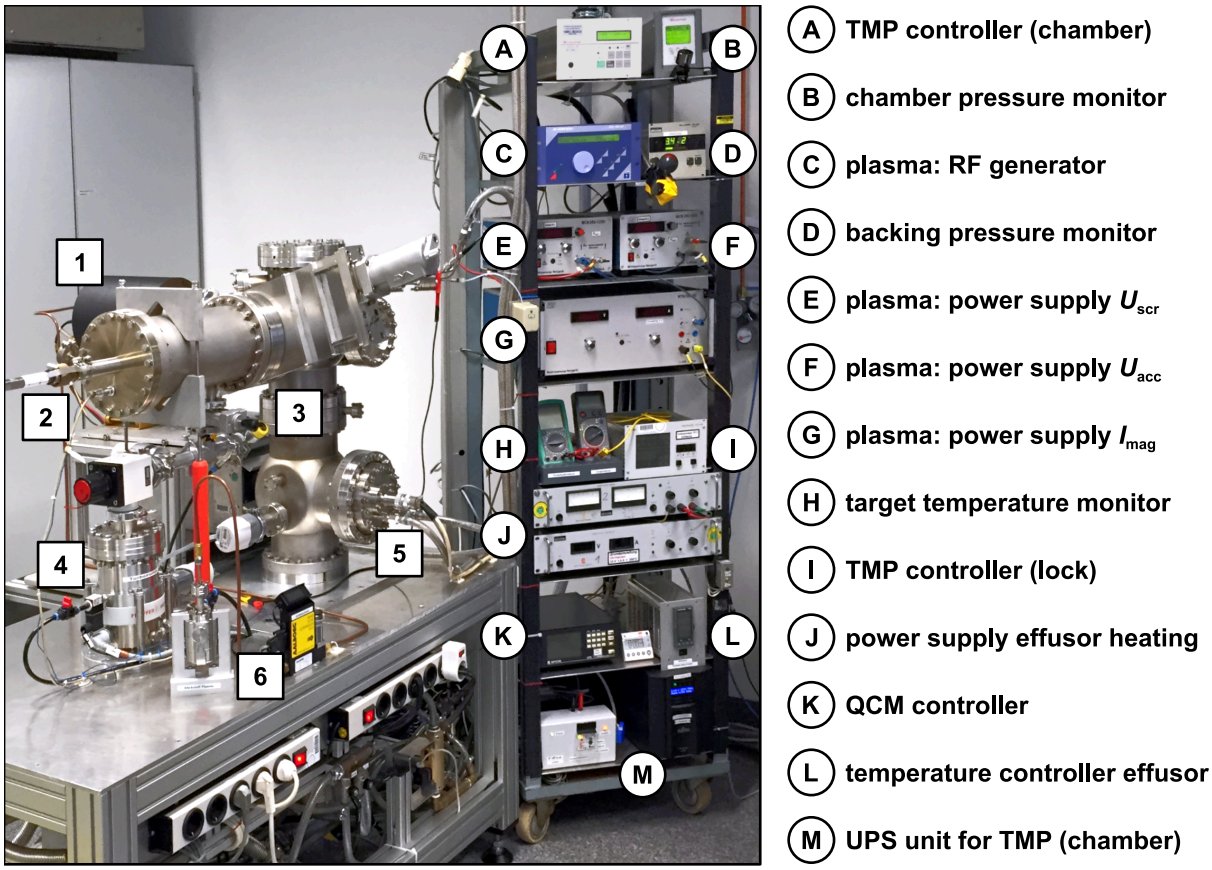

Fig. A6: Picture of the ion implantation setup used for the synthesis of N@C_{60}. Due to the point of view, the main turbomolecular pump (TMP), the backing pump, the plasma RF matching system and the quartz crystal microbalance (QCM) are not visible.

Appendix F: Composition of the HPLC Setups

Tab. A2: Equipment used in the analytical HPLC setup. The system was lab-build.

Component	Description
high-pressure pump	Merck-Hitachi L6000
injection valve	6-port-3-channel valve with Knauer K6
sample loop	20 µL
guard column	Buckyprep 4.6 mm × 10.0 mm
separation column	Buckyprep 4.6 mm × 250 mm
detector	Knauer Variable Wavelength Monitor

Tab. A3: Equipment used in the preparative HPLC setup. The system was lab-build.

Component	Description
high-pressure pump	Knauer Smartline 1000
injection pump	Knauer K-120
injection valve	6-port-3-channel valve with Knauer K6
sample loop	2.35 mL
guard column	Buckyprep 10.0 mm × 20.0 mm
separation column A	Buckyprep 20.0 mm × 250 mm
separation column B	Buckyprep 20.0 mm × 250 mm
separation column C	Buckyprep 20.0 mm × 250 mm
detector	Knauer K-2001
fractionation valve	7-port-1-channel valve with Knauer K6
temperature control	Thermo Haake DC 10 in combination with a resona technics Coolstar SC-550

Appendix G: EasySpin Simulation Parameters

Tab. A4: EasySpin parameters used for N@C_{60}-$C_{60}^{\cdot+}$ and P@C_{60}-$C_{60}^{\cdot+}$ simulations. The replacement character X represents ^{14}N,^{15}N, or ^{31}P.

Parameter	Value	Source / Comment
$S_{X@C_{60}}$	$3/2$	Almeida Murphy *et al.*[113], Knapp *et al.*[156]
$S_{C_{60}^{\cdot+}}$	$1/2$	chapter 10, section 10.2, figure 35 a)
$g_{X@C_{60}}$	2.0024	chapter 10, section 10.1, figure 34
$g_{C_{60}^{\cdot+}}$	2.0026	chapter 10, section 10.2, figure 35 a)
$a_{iso}\left(^{14}N@C_{60}\right)$	0.56 mT	Almeida Murphy *et al.*[113]
$a_{iso}\left(^{15}N@C_{60}\right)$	0.79 mT	Almeida Murphy *et al.*[113]
$a_{iso}\left(^{31}P@C_{60}\right)$	4.92 mT	Knapp *et al.*[156]
ΔB_{pp}	0.15 mT	best empirical fit to the experimental data
temperature	298.15 K	experiments done at ambient temperature

Note:
EasySpin simulations of EDMR samples were performed using the solid-state CW-EPR function *pepper* of EasySpin version 5.1.0 running in MATLAB R2013a. In order to facilitate a direct comparison between the experimental data and the simulations, all EasySpin calculations were performed using the microwave frequency observed in the experiment illustrated in figure 35 a) ($\nu_{MW} = 9.4402$ MHz).

Appendix H: Species Identification in Solar Cell EDMR

The study of EDMR active species in P3HT:$PC_{61}BM$ solar cells was done using fully functional devices as described in chapter 13, section 13.3. However, some resonances are more difficult to assign to a species and experiments on pristine P3HT (Sigma-Aldrich, purity > 99.9 % trace metals basis, regioregularity > 98 %), as well as on $PC_{61}BM$-doped P3HT material at 80 K were performed in addition to standard device EDMR. These experiments are described in the following. The pristine commercial P3HT was drop casted from a toluene solution onto an

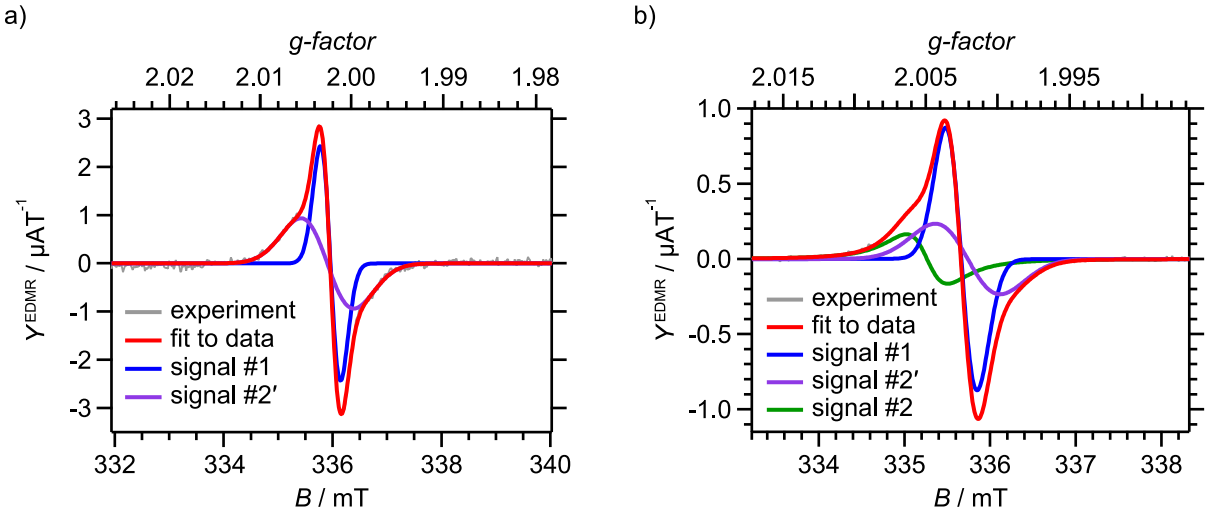

Fig. A7: Supplementary EDMR spectra for species identification. a) EDMR of pristine commercial P3HT drop casted from toluene solution and annealed at 150 °C on an EDMR gold grid substrate with a fine structure distance of 3 µm, recorded at 80 K using $V_{bias} = 40$ V, $B_{mod} = 0.1$ mT, $f_{mod} = 620$ Hz and $P_{MW} = 100$ mW without illumination. The deconvolution of the obtained signal revealed two components with $g_1 = 2.0023(3)$, $\Delta B_{pp,1} = 0.37(5)$ mT and $g_{2'} = 2.0026(3)$, $\Delta B_{pp,2'} = 0.97(5)$ mT. b) EDMR of P3HT doped with trace amounts of $PC_{61}BM$. The sample preparation, as well as the instrument settings were the same as for the pristine P3HT sample. The deconvolution of the obtained signal revealed three components with $g_1 = 2.0025(3)$, $\Delta B_{pp,1} = 0.37(5)$ mT, $g_{2'} = 2.0021(3)$, $\Delta B_{pp,2'} = 0.76(5)$ mT, and $g_2 = 2.0049(3)$, $\Delta B_{pp,2} = 0.48(5)$ mT. The low-field shoulder at g_2 is thus related to the addition of trace amounts of $PC_{61}BM$.

EDMR gold grid substrate with a fine structure distance of 3 µm (see figure 11 on page 29) and annealed at 150 °C for 60 s. Likewise, a sample doped with trace amounts of $PC_{61}BM$ was prepared. The samples were enclosed in shortened EPR quartz glass tubes and contacted using a suitable clamping adapter. Finally, the EPR tubes were sealed with hot-melt adhesive and studied at about 80 K using the available dewar unit for the MiniScope MS400 system filled with liquid nitrogen. Looking at figure A7 one can clearly see that the shoulder (green line) at $g_2 = 2.0049(3)$ only emerges after the addition of trace amounts of $PC_{61}BM$. Similar results were obtained when using unsubstituted C_{60} as the dopant (not shown). This suggests that the additional signal in figure A7 b) represents an interfacial deep trap state resulting from additive-induced molecular disorder, i.e. the $PC_{61}BM$ may induce stacking faults in the adjacent P3HT. Signal #2′ belongs to a P3HT internal process such as bipolaronic blocking of accumulated holes or recombination of oppositely charged P3HT polarons, since it is visible in spectra of pure P3HT material as well.

At forward bias conditions, the investigated P3HT:$PC_{61}BM$ solar cell samples show an additional signal that can best be visualized by taking the difference between normalized spectra at forward and reverse bias. To obtain a suitable SNR for this analysis, the ten EDMR datasets around

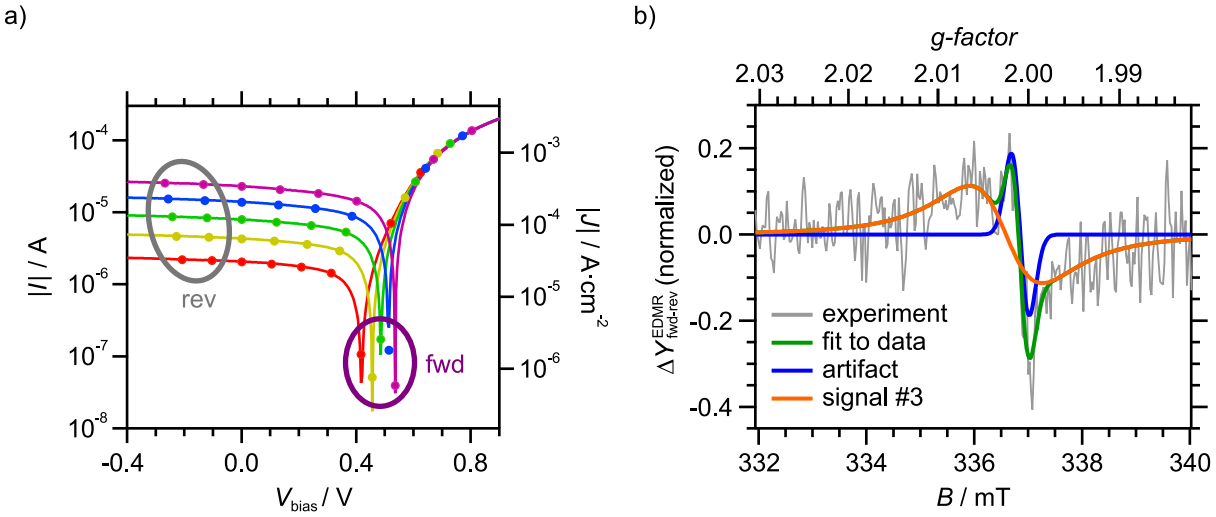

Fig. A8: Visualization procedure for the P3HT-related signal #3. a) Current-voltage characteristics of solar cell sample A taken from figure 43 a), the symbols indicate points at which EDMR data were collected. Circled areas mark datasets averaged to give the forward (fwd) and reverse (rev) EDMR spectra shown in figure 45 b) on page 95. b) Difference spectrum of the normalized EDMR forward and reverse datasets calculated using equation A.1. The experimental data were fitted by a combination of a Lorenzian-line (signal #3) and a Voigt-line (artifact) characterized by $g_3 = 2.0025(3)$ with $\Delta B_{\mathrm{pp},3} \approx 1.3\,\mathrm{mT}$ and $g_{\mathrm{artifact}} = 2.0009(3)$ with $\Delta B_{\mathrm{pp,artifact}} \approx 0.3\,\mathrm{mT}$, respectively.

$V_{\mathrm{bias}} = -0.2\,\mathrm{V}$ marked by a gray circle in figure A8 a), were normalized and averaged to yield the reverse signal (rev) used for figure 45 b). The five EDMR datasets around $V_{\mathrm{bias}} = 0.5\,\mathrm{V}$ (circled in purple) were treated likewise to yield the forward signal (fwd). The calculated difference of the normalized forward and reverse datasets

$$\Delta Y^{\mathrm{EDMR}}_{\mathrm{fwd\text{-}rev}} = \mathrm{fwd} - \mathrm{rev} \tag{A.1}$$

is shown in figure A8 b). The resulting data were fitted using a combination of a Lorentzian line (signal #3) and a pseudo-Voigt line (artifact). These components are characterized by $g_3 = 2.0025(3)$ with $\Delta B_{\mathrm{pp},3} \approx 1.3\,\mathrm{mT}$ and $g_{\mathrm{artifact}} = 2.0009(3)$ with $\Delta B_{\mathrm{pp,artifact}} \approx 0.3\,\mathrm{mT}$. The latter could in principle be a true signal with spectroscopic parameters not reported for the P3HT:$PC_{61}BM$ system so far. However, it could also be an artifact resulting from slight g-factor shifts between the subtracted spectra. Due to the yet unclear origin, this component will be omitted in the further course of our signal analysis. The characteristics of the broad signal #3, on the other hand, fit well with the resonance labeled as signal #2′ in pristine P3HT (cf. figure A7). It is thus concluded that these two signals are of the same origin. Hence, signal #3 is assigned to a P3HT internal process such as bipolaronic blocking of accumulated holes or recombination of oppositely charged P3HT polarons in the P3HT:$PC_{61}BM$ devices and added to the plot shown in figure 45 b).

Curriculum Vitae (educational)

[redacted]

[redacted]

Publications

4 M. Eckardt, R. Wieczorek, F. Laquai, W. Harneit, Recombination Spectroscopy for Organic Solar Cells based on Magnetic Resonance, in preparation.

3 M. Eckardt, R. Wieczorek, W. Harneit, Stability of C_{60} and $N@C_{60}$ under thermal and optical exposure, *Carbon* **2015**, 95, 601-607.

2 M. Eckardt, J. Behrends, D. Münter, W. Harneit, Compact electrically detected magnetic resonance setup, *AIP Adv.* **2015**, 5(4), 047139.

1 M. Schreiber, M. Eckardt, S. Klassen, H. Adam, M. Nalbach, L. Greifenstein, F. Kling, M. Kittelmann, R. Bechstein, A. Kühnle, How deprotonation changes molecular self-assembly - an AFM study in liquid environment, *Soft Matter* **2013**, 9(29), 7145-7149.

Talks and Poster Presentations

4 M. Eckardt, F. Laquai, R. Wieczorek, W. Harneit, Recombination Spectroscopy on Organic Photovoltaic Devices and Paramagnetically Doped Organic Semiconductors, *MRS Fall Meeting*, Boston, **2015**.

3 M. Eckardt, R.Wieczorek, C. Meyer, W. Harneit, Electrically detected magnetic resonance on nanoscopic devices, *SPP1601 Annual Meeting*, Schwerte, **2014**.

2 M. Eckardt, W. Harneit, Electrically detected mangnetic resonance of fullerene nanostructures, 2nd SPP1601 Young Researchers' Workshop, CJD Bonn, **2014**

1 M. Eckardt, A. Kühnle, W. Harneit, Scalable quantum computing - from endohedral fullerenes to quantum registers, *1st YRN Workshop*, CENIDE Duisburg-Essen, **2013**.